UNIVERSITÀ DI PAVIA

SCUOLA DI ALTA FORMAZIONE DOTTORALE

MACRO-AREA SCIENZE E TECNOLOGIE

Dottorato di Ricerca in Scienze della Terra e dell'ambiente

Mara Murri

From Raman elastic geobarometry to impact structures: the role of oriented stresses

Anno Accademico 2018-2019
Ciclo XXXII

Coordinatore
Prof. Roberto Sacchi

Tutor
Prof. Maria Chiara Domeneghetti

Co-tutor(s)
Prof. Boriana Mihailova, Prof. Mauro Prencipe, Dott. Ross John Angel

TABLE OF CONTENTS

PREFACE

The aim of this PhD Thesis is to shed light on processes occurring in the deep Earth (e.g. subduction, exhumation) and on its surface (e.g. impact shock events) using mineral physics and crystallography tools to investigate ultra-high-pressure metamorphic (UHPM) rocks and impact shocked minerals with a focus study on the effects of non-hydrostatic stresses on quartz and diamond since both are strictly related to shock impact environments as well as common minerals in UHPM rocks.

In particular, with my PhD research I have contributed to the practical development of the host-inclusion Raman elastic geobarometry (which involves measuring the stress in mineral inclusions in order to determine the conditions at which they were entrapped by their hosts) under the supervision of Dott. Angel (one of my co-supervisor). At the beginning of my PhD, the state of the art was restricted to a model for elastically-isotropic host and inclusion crystals, but no mineral is elastically isotropic. Therefore, I had no means of measuring the in-situ stress and strain gradients within inclusions. Prof. Mihailova (one of my co-supervisors) introduced me to the concept of phonon-mode Grüneisen tensors, which relate shifts in Raman modes from a crystal to their elastic strains. Then I worked with Prof. Prencipe (also a co-supervisor) to develop a method of determining the values of the tensor components from *ab initio* HF/DFT simulations. Provided the guidelines from Prof. Prencipe I applied these methods to quartz performing about 60 full HF/DFT simulations over a period of a year. I organised the results and developed the analyses to determine the values of the tensor components, and then I collected new Raman data in temperature on a free quartz crystal in order to test the phonon-mode Grüneisen tensors at high temperatures. Then I also collaborated with some colleagues in collecting Raman data on natural host inclusion systems to validate both the method, the concepts and the actual values that I determined. The results that I achieved are now published in three papers (i.e. Chapters 2,3 and 4).

In the meantime, I carried out two other projects: one on the characterization of shock defect features in impact diamonds, and one on Fe^{2+}-Mg cation exchange and cooling rates of lava flows (Chapter 5 and Appendix I, II and III). I'm studying impact diamonds from the Popigai crater with other colleagues mainly from London and Budapest in order to (i) understand the peculiarities of their structure and (ii) to be able to constrain the possible formation conditions of these carbon materials since could be relevant in the framework of industrial applications. In particular, I carried

out X-ray diffraction (XRD) analyses on 36 impact diamonds. I prepared the samples for the Transmission Electron Microscopy (TEM) and Raman spectroscopy analyses and I participated at the TEM data collection in order to choose the appropriate area on the grains from which get the fast Fourier transforms and high resolution TEM images. I was hosted several times over these three years at the University College London to discuss and develop this project.

For the geothermometry project I performed structural refinements with chemical constraints from the X-ray diffraction data collected on synthetic clino- and orthopyroxenes in order to validate the intracrystalline geothermometry. Moreover, I carried out the same analyses on clinopyroxenes from Theo's Flow lava. The aim of this study was to shed light on the thermal history and emplacement mechanisms of this lava flow. I determined the closure temperatures and the cooling rates for each sample. Then I carried out rheology experiments at the University of Perugia under the supervision of Dott. Vetere and Prof. Perugini and finite difference simulations at the University of Padova under the supervision of Prof. Faccenda in order to test and validate the acquired data and give a possible scenario for the formation of Theo's Flow lava (Ontario, Canada).

This PhD Thesis is organized into seven chapters and four appendices:

Chapter 1 is a brief discussion on all the main aspects related to the presence of non-hydrostatic stresses from the deep Earth to impact structures. Therefore, the main concepts behind the stress-strain relationship in the framework of the elastic geobarometry method on isotropic and anisotropic host-inclusion systems and of the impact cratering processes will be presented.

Chapter 2 is the paper entitled *"Stress, strain and Raman shifts"* by Ross J. Angel, Mara Murri, Boriana Mihailova and Matteo Alvaro. It is a theoretical paper focused on the concept of the phonon-mode Grüneisen tensor applied to develop the Raman elastic geobarometry method with the aim to determine the strains from the Raman wavenumber shifts for host-inclusion systems (e.g. quartz in garnet) by means of *ab initio* Hartree-Fock/Density Functional Theory simulations. A computer program "stRAinMAN" has also been written to calculate the changes in phonon wavenumbers from strains as well as the strains from measured changes in phonon wavenumbers. The most important application is the determination of strains in crystals by using Raman spectroscopy to measure changes in phonon wavenumbers relative to an unstrained crystal. This

paper was submitted to the international peer-reviewed journal Zeitschrift für Kristallographie-Crystalline Materials on 3rd July 2018, accepted on 23rd August 2018 and published in the February issue 2019 (vol. 234 pp. 129-140).

Chapter 3 is the paper entitled *"Raman elastic geobarometry for anisotropic mineral inclusions"* by Mara Murri, Mattia L. Mazzucchelli, Nicola Campomenosi, Andrey V. Korsakov, Mauro Prencipe, Boriana Mihailova, Marco Scambelluri, Ross J. Ange1 and Matteo Alvaro. It is a letter dedicated to the application of the Raman elastic geobarometry (i.e. the concept of the phonon-mode Grüneisen tensor coupled with the elastic geobarometry theory) to natural samples. It highlights the importance of studying the elastic properties of host-inclusion pairs under hydrostatic and non-hydrostatic stress fields to determine their formation conditions and to understand how the system behaves from depths to Earth's surface during exhumation processes. In particular, it reports an example of a quartz in garnet host-inclusion system within an eclogite xenolith from Mir pipe kimberlite. It shows how to deal with anisotropic inclusions such as quartz (trigonal symmetry) in order to determine its entrapment conditions. This paper was submitted to the international peer-reviewed journal American Mineralogist on 10th May 2018, accepted on 31st May 2018 and published in the November issue 2018 (vol. 103 pp. 1869-1872).

Chapter 4 is the paper entitled *"The effects of non-hydrostatic stress on the structure and properties of alpha-quartz"* by Mara Murri, Matteo Alvaro, Ross J. Angel, Mauro Prencipe and Boriana Mihailova. It is a detailed crystallographic paper focused on the investigation of the structure, properties, and vibrational Raman modes of quartz under deviatoric stress conditions. Moreover, this paper describes how they change with the imposed state of strain to predict and understand the real behavior of quartz under conditions of deviatoric stress that are ubiquitous in rocks. This paper was submitted to the international peer-reviewed journal Physics and Chemistry of Minerals on 2nd October 2018, accepted on 18th December 2018 and published in the May issue 2019 (vol. 46, pp 487–499).

Chapter 5 is the paper entitled *"Quantifying hexagonal stacking in diamond"* by Mara Murri, Rachael L. Smith, Kit McColl, Martin Hart, Matteo Alvaro, Adrian P. Jones, Péter Németh, Christoph G. Salzmann, Furio Corà, Maria C. Domeneghetti, Fabrizio Nestola, Nikolay V. Sobolev, Sergey A. Vishnevsky, Alla M. Logvinova, Paul F. McMillan. With the support of the

Barringer Family Company award, impact diamonds from the Popigai impact site (Siberia, Russia) containing hexagonal features in their X-ray diffraction patterns were studied to develop a systematic protocol for understanding and assigning specific hexagonality attributes to the mineral designated as "lonsdaleite" among natural, artificially shocked and synthetic samples. Their hexagonal features interpreted as a deviation from the standard cubic structure of diamond were characterized using multiple techniques (i.e. High-Resolution X-ray diffraction, High Resolution Transmission Electron Microscopy, micro Raman spectroscopy and Density Functional Theory calculations) in order to also understand how the deviatoric stresses deform the crystallographic structures not only into the deep Earth, but also during catastrophic impact events. Investigation of mineral structures retrieved from their host rocks (e.g. meteorites and planetary bodies) provides fundamental information on planetary-scale geological processes including impact cratering processes. This paper was submitted to the international peer-reviewed journal Scientific Reports on 29th April 2019, accepted on 11th June 2019 and published online in the July issue 2019 (vol. 9, pp 10334).

The conclusions of this PhD Thesis together with future activities and projects related to the present PhD topics are discussed in **Chapter 6**.

Appendices I, II, III report the results of the study that I started during my Master Thesis and carried out over the three years of my PhD as a side project dedicated to the intracrystalline geothermometry on pyroxenes. In the framework of my master's project I carried out high temperature *ex situ* experiments (i.e. high-temperature annealing and quenching experiments) followed by X-ray diffraction measurements to investigate the Fe^{2+}-Mg exchange reaction in pyroxenes at high temperature. These experiments are extremely relevant for geothermometric and geospeedometric investigation of Earth and other planetary materials because the determination of the closure temperature and cooling rate from clino- and orthopyroxenes occurring in terrestrial and extra-terrestrial minerals can be used to infer the thermal history of their host rocks. I validated the intracrystalline geothermometry method applying it to synthetic clino- and orthopyroxene single crystals (**Appendix I:** M. Murri, F. Cámara, J. Adam, M.C. Domeneghetti, M. Alvaro (2018). *Intracrystalline "geothermometry" assessed on clino and orthopyroxene bearing synthetic rocks*. Geochimica et Cosmochimica Acta, 227, 133-142.) in order to determine the closure temperatures and cooling rates of Theo's Flow lava (Canada) from which I could infer the timing

of magma emplacement (**Appendix II:** M. Murri, M.C. Domeneghetti, A. M. Fioretti, F. Nestola, F. Vetere, D. Perugini, A. Pisello, M. Faccenda, M. Alvaro. *Cooling history and emplacement of a pyroxenitic lava as proxy for understanding Martian lava flows.* Scientific Reports). Moreover, the intracrystalline geothermometry has also been validated against rheology experiments under dynamic conditions (**Appendix III:** F. Vetere, M. Murri, M. Alvaro, M. C. Domeneghetti, S. Rossi, A. Pisello, D. Perugini, F. Holtz (2019). *Viscosity of Pyroxenite Melt and its Evolution during Cooling.* Journal of Geophysical Research – Planets, 124, 1451-1469) to prove that they can influence the thermal state and emplacement mechanism for these lavas (Theo's Flow).

Appendix IV reports the supplementary materials cited in all the articles presented in this dissertation.

Appendix V lists the other activities that I carried out during the three years of my PhD.

1. INTRODUCTION

1.1 ORIENTED STRESSES: from the deep Earth to impact structures

In the past 40 years, the largest part of the development of experimental methods, protocols and apparatus used by the mineral physics community has been aimed to maintain hydrostatic conditions while performing experiments at extreme conditions (e.g. high pressure and high temperature conditions) in order to study the thermoelastic properties of several mineral phases. At the same time, a growing community of petrologists, geophysicists and crystallographers started to interpret many Earth and planetary processes, from subduction to impact cratering, in terms of oriented (non-hydrostatic) stresses. These recent hypotheses are also supported by the fact that, as showed by several studies (e.g. Korsakov et al. 2009; Briggs and Ramdas 1977; Bassett 2006, Kenichi 1999; Weinberger et al. 2008; Duffy et al. 1999) and by our calculations performed using *ab initio* Hartree- Fock /Density Functional Theory (HF/DFT) (e.g. Murri et al. 2018; Murri et al. 2019; Stangarone et al. 2019), many properties and processes (e.g. formation and migration of defects, ordering processes, crystal growth and lattice preferred orientation) for minerals subject to oriented stresses (e.g. host-inclusion systems) can differ significantly from those under isotropic (hydrostatic) stresses commonly determined in many research studies to obtain calibrations of the Raman wavenumber shifts and/or equations of state as a function of pressure and temperature (e.g. Schmidt and Zimann 2010; Schmidt et al. 2013; Schiedl et al. 2016). Thus, entire phase diagrams (e.g. mineral phase transitions, reaction border) must be considerably re-thought. However, it is difficult to calibrate non-hydrostatic stresses in routine experiments because of the presence of stress gradients, not only in the "pressure transmitting medium" but also across the entire sample, that cannot be measured independently (e.g. Zhao et al. 2010 and references therein). Therefore, both theoretical and experimental approaches for understanding the crystal structures and their elastic response under oriented stresses have to be revised with the aim to shed light not only on how non-hydrostatic stresses may influence the elastic response of mineral inclusions entrapped in their mineral hosts, but also to properly interpret the preserved structural changes observed in minerals and related to the stresses (e.g. uniaxial, non-hydrostatic) generated by impacts. Indeed, an impact shock event can be interpreted in terms of uniaxial compression and/or oriented stresses applied to minerals at high temperature for which the theoretical and experimental techniques have never been coherently developed yet.

Therefore, I have contributed to a relevant development of (i) the elasticity theory that was carried out to interpret the "stress-T" (i.e. stress and/or pressure – temperature) evolution of the lattice parameters for mineral phases entrapped in other hosts minerals during subduction or UHP metamorphism processes and (ii) the investigation of the deformation features (e.g. stacking disorder, Salzmann et al. 2015; Jones et al. 2016) recorded in minerals that have experienced shock impact events and thus highly oriented stress fields in impact sites.

1.2 ELASTIC GEOBAROMETRY

Non-hydrostatic stresses can arise from kinematic non-elastic processes, such as plate motion or local deformation, and from elastic interactions between different mineral phases.

Subduction zones located at convergent plate margins are the major geodynamic sites that primarily affect plate tectonics and transport of crustal material deep into the Earth's mantle. However, the mechanisms that take part in the downwards transport of crustal material during subduction and its exhumation back to the Earth's surface are still poorly understood and controversial (Figure 1). This is because the history of subduction cannot be obtained either from real-time geophysical and seismic data, which only provide static snapshots of subduction zones today, nor from the classical geothermobarometric approach, which can only be applied to mineral pairs that attained chemical equilibrium (Rosenfeld and Chase 1961).
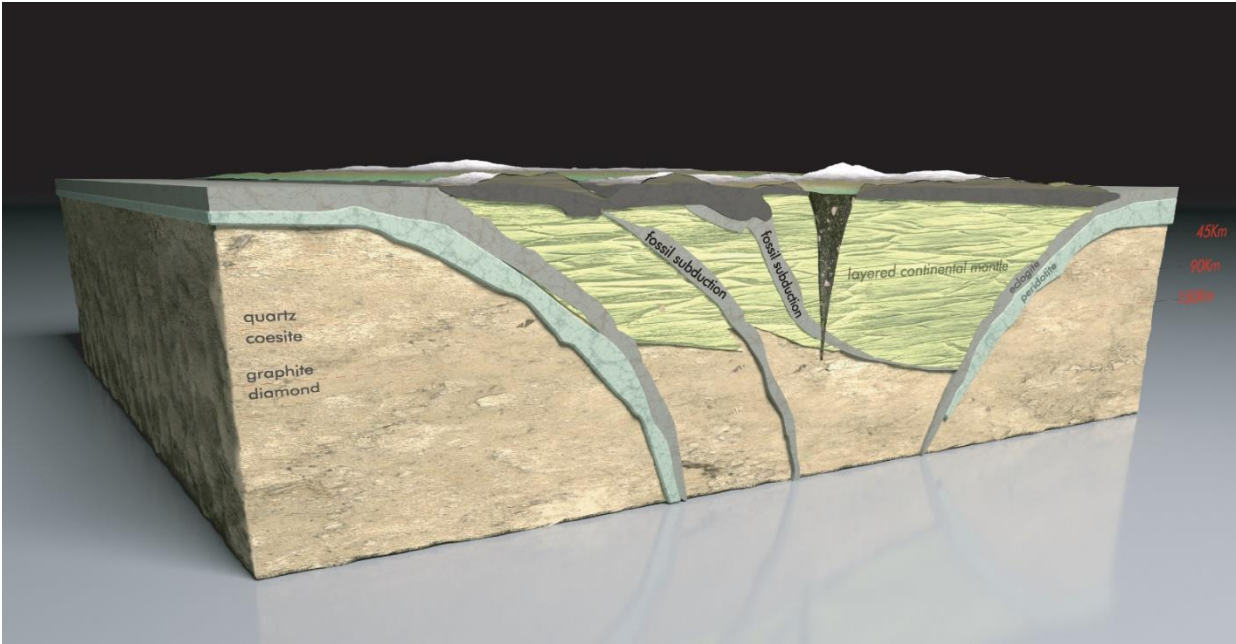
Figure 1. Schematic representation of a subduction zone (modified after Alvaro et al. 2020)

The only solution is to study UHPM terrains that have been subducted and subsequently brought up to the Earth's surface on which they are exposed and accessible (Figure 2). These rocks are the keys to understand what happened during the downward and upwards transport by investigating their mineral phases in order to determine their history in terms of pressure and temperature. The determination of the formation conditions (e.g. *P-T*, see Chapter 6) for such minerals would allow us to characterize regions into the Earth or in other planetary bodies that are still inaccessible (e.g. Rosenfeld and Chase 1961).
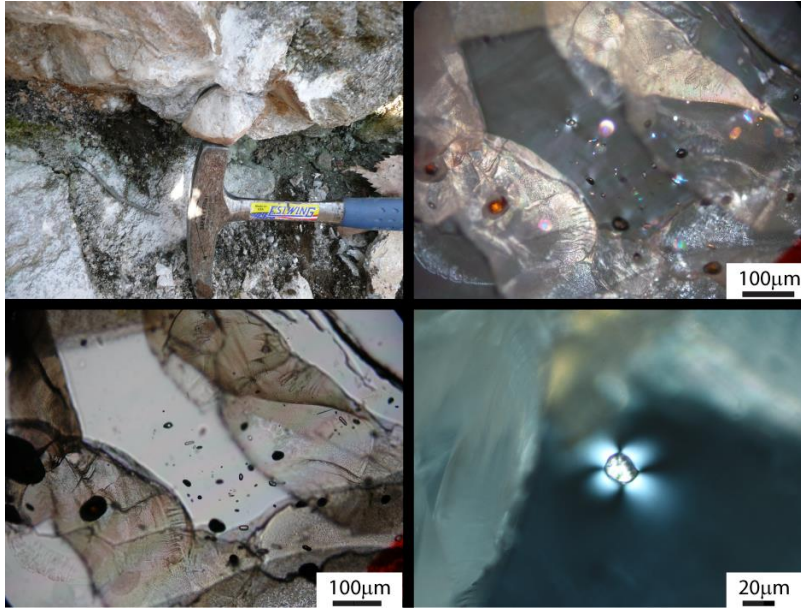
Figure 2. Host- inclusion systems from UHPM rocks (optical images courtesy of Nicola Campomenosi)

An exhumation process acts by transporting a mineral from a depth to the Earth's surface. This means that the mineral is subject to different pressure and temperature conditions until reaching the surface (i.e. from *P-T* of its origin to room *P-T* at the Earth's surface). The subduction mechanism works in the same way but in the opposite direction (i.e. from room *P-T* to *P-T* at depth into the Earth).

Physical constraints, such as physical confinement, often play a fundamental role in generating non-hydrostatic stress fields from the macro (e.g. subduction channels; e.g. Mancktelow 1995, 2008; Raimbourg and Kimura 2008) to the micro scale (e.g. grain or sub-grain). Indeed, elastic interactions between minerals can also raise very significant non-hydrostatic stresses when, for example, a mineral is completely entrapped inside a different one as in host-inclusion systems (e.g. Howell 2012; Moulas et al. 2013). Because the compressibility (β) and thermal expansion (α) of the two phases will differ, a change in pressure and temperature would lead to free grains of the free phases undergoing different amounts of strain. The difference in strain is dependent on one side upon the thermoelastic properties of the mineral itself and on the other upon the mutual confinement that limits the strains that can occur. Therefore, additional non-uniform stress fields, as a purely elastic phenomenon, are developed within the constrained host-inclusion system, while no plastic deformation or brittle failure are required.

Such stress fields can give rise to either over- or under-pressure with respect to the external pressure, whether or not the external pressure is lithostatic. Indeed, when the formed host-inclusion system starts its travel from depth to the Earth's surface two possible phenomena can occur. The first one having the inclusion pushing against the cavity of the host when it is softer than the host (i.e. over pressure), while the second case is when the inclusion is shrunk because it is stiffer with respect to the entrapping mineral (i.e. under pressure) (Angel et al. 2015). For the first case, the contrast in the elastic properties between the two-phases system can show up as birefringent haloes around the inclusion phase pointing to the fact that the host-inclusion interface is deformed (i.e. it is subject to strains) and thus is storing some precious information related to their origin (e.g. Rosenfeld and Chase 1961; Zhang 1998; Angel et al. 2014b). The stored message is a residual pressure that is still acting on the inclusion and that, if determined, can be used to calculate the entrapment conditions by means of the elastic geobarometry method (see Alvaro et al. 2020). Elasticity theory provides just an alternative method of barometry which does not rely on the chemistry of the rock, nor on whether chemical equilibrium has been attained at either the local or rock scale. Therefore, the measured elastic signal is not primarily dependent on cation exchange between mineral pairs and affected by the exhumation path. Further, mineral inclusions are encapsulated and protected by the host mineral that acts as an "inert container" allowing them to be the only marker and evidence of UHPM since the rest of the rock can be 'overprinted' (i.e. converted to an assemblage of minerals characteristic of lower *P,T* conditions) during its exhumation path. Thus, mineral inclusions carry a signature of processes occurring at great depth and their characterization can provide a precise picture of the stress-*T* conditions of entrapment if coupled with conventional thermobarometry methods to have temperature estimates. A series of such points can provide a complete picture of the exhumation path and in some cases the prograde path, and in particular whether significant non-lithostatic deviatoric stresses were present in collision zones and during subduction.

This concept has been known for a long time (Rosenfeld and Chase 1961) and has been extensively applied (e.g. Izraeli et al. 1999; Nestola et al. 2011; Howell 2012) and developed in the last five years passing from the assumptions of linear elasticity (e.g. Zhang 1998) to the *non-linear* elasticity theory (Angel et al. 2014a, 2015) with the incorporation of realistic equations of state into the classic inclusion elasticity solutions (Goodier 1933; Eshelby 1957) by using the host-

inclusion isomeke (see below for a detailed explanation) as a basis that provides satisfactory quantitative modelling of host-inclusion systems.

The key concepts are that (i) at the moment of entrapment both the host and the inclusion are at the same *P-T* condition with no significant stress or temperature gradients across the host and the inclusion and both phases continue to experience the external pressure whether or not that is lithostatic, (ii) they share the same fractional volume (i.e. the inclusion fits perfectly the cavity inside the host with no left space at their interface) and (iii) they have different thermoelastic properties (see Figure 3).
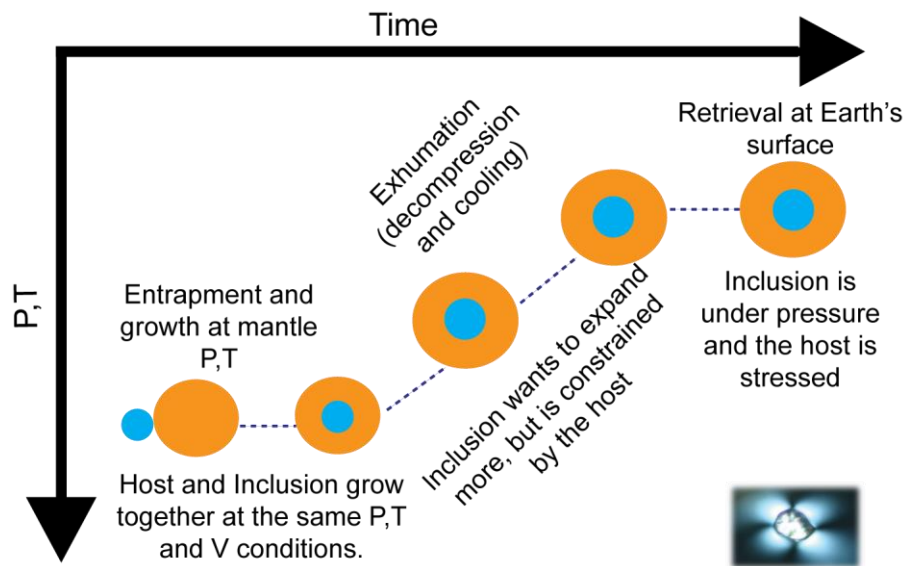
Figure 3. *P-T- t* history for a host-inclusion system with the inclusion softer with respect to the host.

Moreover, to have exact solutions for geologically relevant ranges of pressure and temperature (e.g. Angel et al. 2014b) a single isolated spherical isotropic inclusion entrapped in a different elastically isotropic host has to be considered. The inclusion will still exhibit isotropic stress from the isotropic strain, and the behavior will be the same as for a crystal in a fluid pressure medium (i.e. under hydrostatic pressure regimes) as this is the simplest case. Under these conditions there is only a single possible path in *P-T* space, the entrapment isomeke, along which the stress and the strain remains uniform across the host-inclusion system and the stress is equal to the external pressure.

The entrapment isomeke is defined by the volume thermal expansivities and compressibilities of the host and inclusion phases (Eq. 1):

$$\frac{\delta P}{\delta T} = \frac{\alpha_I - \alpha_H}{\beta_I - \beta_H}$$

(1)

An isomeke is never a straight line in *P-T* space because the thermal expansion and compressibility of the two phases are complex and different functions of *P* and *T*. The calculations of isomekes and residual inclusion pressures, as for all EoS calculations, are already developed and incorporated into the software package EosFit7-c (Angel et al. 2014b). Because along the entrapment isomeke the host and inclusion are at the same pressure, it provides a basis for the calculation of their mutual elastic relaxation from classical methods (e.g. Goodier 1933).

This approach provides a realistic calculation of the deviations from lithostatic pressures that can be developed through elastic interactions between elastically isotropic minerals under metamorphic conditions.

However, another complication arises from the fact that no minerals are perfectly elastically isotropic and therefore the stress fields around the inclusions are non-hydrostatic. Thus, the stress state and the structural changes of the inclusion phase (e.g. quartz in garnet) will be different from the hydrostatic behaviour (e.g. Briggs and Ramdas 1977; Korsakov et al. 2009). Moreover, the amount of the deviatoric stress around the inclusion is also a function of (i) its anisotropy (i.e. zircon is more anisotropic than quartz, see Zaffiro et al. 2019), (ii) its orientation with respect to the host (see Mazzucchelli et al. 2019 for a detailed explanation), (iii) its shape and (iv) whether the inclusion is elastically isolated or, as is often the case, close to other inclusions or to the surface of the host grain (e.g. Campomenosi et al. 2018 and Mazzucchelli et al. 2018).

1.3 IMPACT CRATERING PROCESS AND STACKING DISORDER IN IMPACT DIAMONDS

Impact cratering is one of the most common geological process of the Solar System that plays an important role in shaping solar system bodies and surfaces. Cosmic impacts can catastrophically destroy Solar system bodies or form new ones [e.g. the Moon (Hartmann and Davis 1975)] and change their surface geochemistry. Moreover, when they occur on the Earth's surface they can

generate abrupt climate changes and mass extinctions, and allow the formation of hydrocarbons reservoirs, and biological niches (Osinski et al. 2008). On Earth, impact structures are not preserved for long because they are continually obliterated by tectonic activity, erosion, burial, weathering, volcanic resurfacing and vegetation. When a large enough projectile (>50 m in diameter for stony and >20 m for iron meteorites) passes through the atmosphere without a significant deceleration and disruption it reaches the Earth's surface at hypervelocity (>11 km/s) and produces high-pressure shock waves that radiate into the target at velocities of 5–8 km/s causing pressures, temperatures and strains several orders of magnitude higher than that reached by endogenic metamorphism. The occurrence of unique features (shock effects) in the impactites (Stöffler and Grieve 2007), caused by the energy released by the impact, is nowadays the most important criterion to establish the impact origin of a crater which is very often under debate especially from small impact craters(1-10 km). Shock metamorphism of rocks and minerals caused by the impact of a solid body travelling at hypervelocity (i.e. velocity > 1 km/s) or due to the detonation of nuclear explosives is characterized by pressures higher than 10 GPa and T up to 4000°C (Figure 4).
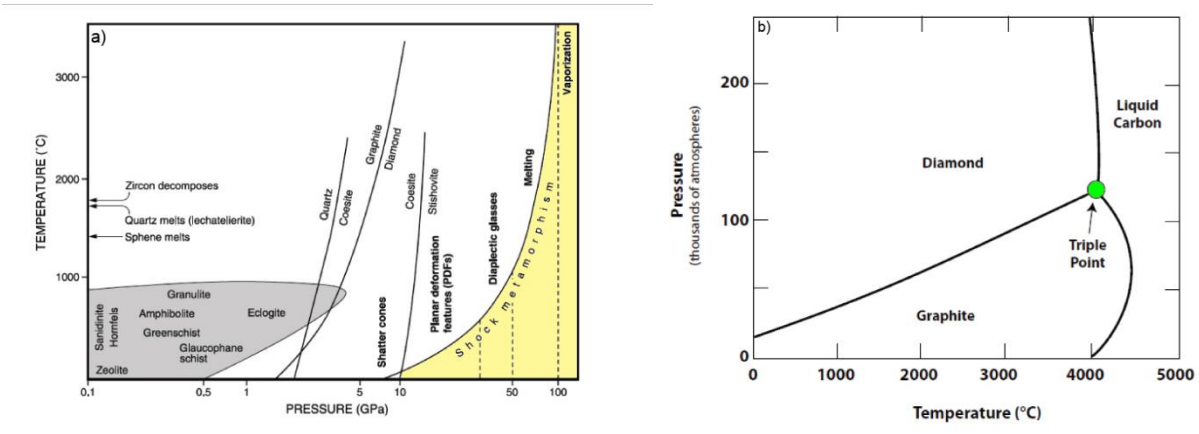
Figure 4. **(a)** Pressure and temperature ranges of endogenic and shock metamorphism modified after French (1998) and **(b)** phase diagram for carbon phases modified after Hazen et al. (2013)

For example, the energy released from an impact occurring on the Earth's surface as calculated even for a small impact crater (e.g. Barringer or Meteor crater, 1.8 km in diameter) appears to be 3 orders of magnitude higher than the Hiroshima atomic bomb. These enormous oriented stresses [e.g. 624 GPa have been calculated for Popigai crater in Siberia (Masaitis 1998)] and the very short duration can cause unique irreversible changes to rocks and minerals [e.g. deformations, phase transformations, melting and vaporization (e.g. Langenhorst 2002)] and are far higher than P and T conditions to transform graphite into diamond (4.5 GPa at 1000°C) in the Earth's mantle and are also enough to induce deformation in the newly formed diamonds (e.g. Masaitis 1998; Stöffler and Grieve 2007; Németh et al. 2014 and Salzmann et al. 2015).

Shock-induced changes in minerals have been reported for many rock-forming minerals (e.g. French 1998; Németh et al. 2014; Ferriere and Osinski 2013). Upon impact shock metamorphism, graphite can transform into diamond as suggested by the graphite-diamond textural relationship within shocked rocks from Ries Crater in Germany. Shock formation stresses can vary substantially according to the porosity of the rock and the nature of graphite (degree of crystallinity, Ferriere and Osinski 2013). For the rocks from Ries Crater it has been suggested that diamond is formed from graphite by shock-induced solid-state phase transformation during shock compression occurring at pressures of about 30-40 GPa (El Goresy et al. 2001). Because of its peculiar chemical and mechanical properties diamond can survive catastrophes (e.g. explosive nucleosynthesis or disruption of planetary bodies), being the only marker of extreme shock events occurring either in outer space collisions or on the Earth's surface (Jones et al. 2016). All types of diamond contain puckered layers of carbon atoms with six-membered rings in the armchair configuration. The difference between cubic (CD) and hexagonal diamond (HD) lies in how these layers are stacked on top of each other to build up the three-dimensional crystal structure (Figure 5).
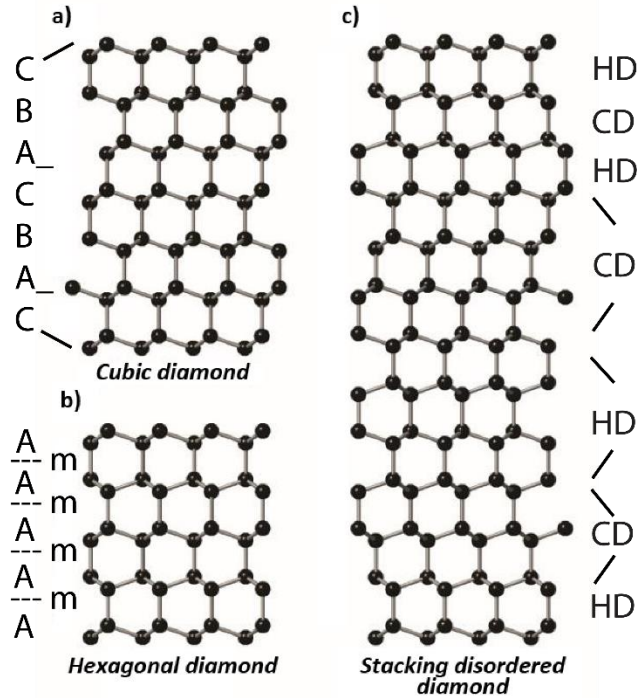
Figure 5. Schematic representation of the crystal structure along the hexagonal *a axis* for cubic **(a)**, hexagonal **(b)** and stacking disordered **(c)** diamond modified after Salzmann et al. (2015).

In CD, identical layers are stacked on top of each other with a shift halfway across the diagonal of a six-membered ring (armchair type). Whereas, in HD, each layer is the mirror image of the previous one (boat type). Commonly, impact diamond samples can contain mixtures of interlaced cubic (c) and hexagonal (h) stacking in variable quantities (e.g. Koeberl et al. 1997; Masaitis 1998; Salzmann et al. 2015; Jones et al. 2016, Murri et al. 2017, 2019).

The first discovery of impact diamonds in meteorite fragments occurred in the Meteor crater in Arizona more than 100 years ago in an iron meteorite, named Canyon Diablo (Foote 1891 and Barringer 1905). These impact diamonds were polycrystalline, and they formed because of a shock transformation from a carbon-rich precursor phase included in the iron meteorite (Jones et al. 2016 and references therein). The second finding of impact shocked diamonds took place in the Popigai crater (Masaitis et al. 1972), where they formed in the target rocks rich in carbon phases (Koeberl et al. 1997 and Masaitis 1998).

"Lonsdaleite", a metastable form of tetrahedrally (sp^3-) bonded carbon, was found for the first time in the Canyon Diablo meteorite and it has always been ascribed as the hexagonal high-pressure polymorph of cubic diamond (Frondel and Marvin 1967) and considered a possible marker of

shock events (Bundy and Kasper 1967 and Hanneman et al. 1967). "Lonsdaleite" takes its name in honor of the crystallographer Professor K. Lonsdale to indicate a new natural mineral (Frondel and Marvin 1967). It has features belonging to both graphite and diamond, because it has a hexagonal symmetry, like that of graphite, but it has a sp^3 hybridization for C atoms like that of diamond. It has a wurtzite-like (i.e. ZnS-type) structure and a density almost identical to that of the cubic diamond (i.e. 3.51g/cm^3). The unit cell parameters are $a = b = 2.51$Å and $c = 4.12$ Å (Németh et al. 2014). The cubic and hexagonal structures are very similar one to another because both are formed by layers of C with six-membered rings in the armchair configuration, the difference is in how these layers are interlaced (Salzmann et al. 2015).

Dense forms of carbon with structural features ascribed to hexagonal symmetry and assigned to "Lonsdaleite" were first synthesized by Bundy and Kasper (1967) at temperatures greater than 1000° and a static pressure of about 130 kbar from a graphite starting material. Then, it has been synthesized under various conditions, such as: HP experiments in a wide range of temperatures (Utsumi and Yagi 1991; Utsumi et al. 1994), chemical vapor deposition (CVD) (e.g. Fayette et al. 1995 and Chiem et al. 2003) and HP-HT experiments (e.g Kraus et al. 2016; Shiell et al. 2016). Therefore, the stability field of "Lonsdaleite" is still unknown and its formation mechanism as well as its structural characterization is under debate. In synthesis experiments, it is often found together with cubic diamond and graphite with only a unique exception for the synthetic sample by Shiell et al. (2016) that is made up of almost pure (90%) "Lonsdaleite".The presence of "Lonsdaleite" in natural impact diamonds has been interpreted as the result of a shock transformation from graphite (e.g. Jones et al. 2016 and references therein). Moreover, natural "individual crystals" of "Lonsdaleite" were first reported by Shumilova et al. (2011), whereas its occurrence in polycrystalline natural impact diamonds from Popigai crater was reported by several literature studies (e.g. Koeberl et al. 1997; Masaitis 1998; Jones et al. 2016; Yelisseyev et al. 2016).

However, only a systematic statistical investigation, through a multidisciplinary approach, of the "fingerprint" provided by the deformation in diamonds can provide fundamental information about the structural features related to the stacking disorder and about the nature of the stacking disorder itself. Indeed, results from Murri et al. (2019) clearly indicate that these classic examples of lonsdaleite-containing impact diamonds are best described as materials containing intergrowths of cubic and hexagonally stacked layers at the nanoscale.

1.4 THE SHOWDOWN BETWEEN TIME, SPACE AND DEFORMATION REGIMES.

The presence of oriented stresses in various geological settings needs to be discussed further in order to understand the subtle similarities between the most catastrophic events occurring at surface of our planet and those acting at depth. The key to unravel the mechanisms to generate oriented stresses is the comprehension of the complex interplay between deformation regimes at different time and length scales.

Indeed, the first step is to focus on the deformation mechanisms occurring in mineral phases. In the first part of this thesis I show how to shed light on deformation processes occurring in the context of subduction zones though the investigation of host-inclusion systems from UHPM rocks. In this scenario, the deformation, in the purely elastic regime, is revealed by the birefringent haloes around the entrapped mineral. This implies that once the physical constraint (e.g. pressure exerted by the host) is removed also the preserved pressure in the inclusion disappears and the inclusion will behave as a free crystal. However, the residual pressure on the inclusion has to be preserved to allow calculating the entrapment conditions. Because experimental determination of the residual pressure in host-inclusion system when the inclusion is anisotropic is extremely challenging, I carried out *ab initio* HF/DFT calculations on alpha-quartz under different strain conditions (e.g. hydrostatic, anisotropic, uniaxial, isotropic stress regimes) to reproduce the observations on natural samples (e.g. similar deformation regimes). This in turns allowed me to further explore (i) the concept of the phonon-mode Grüneisen tensor in the framework of the elastic geobarometry and (ii) the response of common silicate inclusions under different stress/deformation regimes occurring in geological processes such as subduction and exhumation (see Chapter 2, 3 and 4).

The second part of this thesis is dedicated to shock deformation mechanisms which act on the crystal structure of minerals present in the target rocks as well as in meteorite or other planetary bodies. In this case preserved traces of deformation are also detected, but they occur on free crystals in the rock matrix and the agent responsible of their presence is already gone. Shock events last for an undetectable time with respect to subduction, exhumation processes or crystal growth mechanisms, producing plastic and brittle deformations on the mineral that then will be the only witnesses of the occurred event.

The investigation of shock features in the structure of minerals that experienced such events is fundamental in order to be able to reconstruct the pressure and temperature environments at the

moment of the impact and also their associate gradients. For this purpose, in Chapter 5 is reported the study on impact shocked diamonds from Popigai crater (Siberia, Russia). Analyses and measurements on shocked impact diamonds are not straightforward and sometimes it is not easy to understand their preserved deformation features. Therefore, I performed X-ray diffraction measurements contributing to develop a protocol to characterize them in a framework of a multi technical approach.

Having the possibility to study and model how these mineral phases behave in such geological settings is a unique opportunity that allowed me to understand processes that act in deep regions below the Earth's crust, so far away from my everyday life, as well as for those occurred million years before my existence (Popigai impact event dates at 35 Ma, Bottomley et al. 1997).

References

Alvaro, M., Mazzucchelli, M.L., Angel, R.J., Murri, M., Campomenosi, N., Scambelluri, M., Nestola, F., Korsakov, A., Tomilenko, A.A., Marone, F., Morana, M. (2020) Fossil subduction recorded by quartz from the coesite stability field, Geology, in press.

Angel, R.J., Gonzalez-Platas, J., and Alvaro, M. (2014a) EosFit7c and a Fortran module (library) for equation of state calculations. Zeitschrift für Kristallographie-Crystalline Materials, 229, 405-419.

Angel, R.J., Mazzucchelli, M.L., Alvaro, M., Nimis, P., and Nestola, F. (2014b) Geobarometry from host-inclusion systems: The role of elastic relaxation. American Mineralogist, 99, 2146-2149.

Angel, R. J., Nimis, P., Mazzucchelli, M. L., Alvaro, M., and Nestola, F. (2015) How large are departures from lithostatic pressure? Constraints from host–inclusion elasticity. Journal of Metamorphic Geology, 33(8), 801-813.

Barringer, D. M. (1905) Coon Mountain and its crater. Proceedings of the Academy of Natural Sciences of Philadelphia, 861-886.

Bassett, W. A. (2006) Deviatoric stress: a nuisance or a gold mine?. Journal of Physics: Condensed Matter, 18(25), S921.

Bottomley, R., Grieve, R., York, D., and Masaitis, V. (1997) The age of the Popigai impact event and its relation to events at the Eocene/Oligocene boundary. Nature, 388(6640), 365.

Briggs, R.J., and Ramdas, A.K. (1977) Piezospectroscopy of the Raman spectrum of α-quartz. Physical Review B, 16, 3815-3826.

Bundy, F. P., and Kasper, J. S. (1967) Hexagonal diamond—a new form of carbon. The Journal of Chemical Physics, 46(9), 3437-3446.

Campomenosi, N., Mazzucchelli, M.L., Mihailova, B.D., Scambelluri, M., Angel, R.J, Nestola, F., Reali, A., and Alvaro, M. (2018) How geometry and anisotropy affect residual strain in host inclusion system: coupling experimental and numerical approaches. American Mineralogist, 103(12), 2032-2035.

Chiem, C. V., Seo, H. K., Ansari, S. G., Kim, G. S., Seo, J. M., and Shin, H. S. (2003) Lonsdaleite diamond growth on reconstructed Si (100) by hot-filament chemical vapour deposition (HFCVD). Korean Journal of Chemical Engineering, 20(6), 1154-1157.

Duffy, T.S., Shen, G., Shu, J., Mao, H.K., Hemley, R.J. and Singh, A.K. (1999). Elasticity, shear strength, and equation of state of molybdenum and gold from x-ray diffraction under nonhydrostatic compression to 24 GPa. Journal of Applied Physics, 86(12), pp.6729-6736.

Eshelby, J.D. (1957) The determination of the elastic field of an ellipsoidal inclusion, and related problems: Royal Society of London Proceedings, ser. A, v. 241, p. 376–396.

Fayette, L., Mermoux, M., Marcus, B., Brunet, F., Germi, P., Pernet, M., Abello, L., Lucazeau, G. and Garden, J. (1995) Analysis of the fine structure of the Raman line and of X-ray reflection profiles for textured CVD diamond films. Diamond and Related Materials, 4(11), 1243-1250.

Ferrière, L., and Osinski, G. R. (2013) Shock metamorphism. Impact Cratering: Processes and Products, GR Osinski, E. Pierazzo, Eds.(John Wiley & Sons, 2012), 106-124.

Foote, A. E. (1891) ART. XLIV.--A New Locality for Meteoric Iron with a Preliminary Notice of the Discovery of Diamonds in the Iron. American Journal of Science (1880-1910), 42(251), 413.

French, B. M. (1998) Traces of catastrophe: A handbook of shock-metamorphic effects in terrestrial meteorite impact structures.

Frondel, C., and Marvin, U. B. (1967) Lonsdaleite, a hexagonal polymorph of diamond. Nature, 214(5088), 587.

Goodier, J.N. (1933) Concentration of stress around spherical and cylindrical inclusions and flaws. Journal of Applied Mechanics, v. 55, p. 39–44.

Goresy, A. E., Gillet, P., Chen, M., Künstler, F., Graup, G., and Stähle, V. (2001) In situ discovery of shock-induced graphite-diamond phase transition in gneisses from the Ries Crater, Germany. American Mineralogist, 86(5-6), 611-621.

Hanneman, R. E., Strong, H. M., and Bundy, F. P. (1967) Hexagonal diamonds in meteorites: implications. Science, 155(3765), 995-997.

Hartmann, W. K., and Davis, D. R. (1975) Satellite-sized planetesimals and lunar origin. Icarus, 24(4), 504-515.

Hazen, R. M., Downs, R. T., Jones, A. P., and Kah, L. (2013). Carbon mineralogy and crystal chemistry. Reviews in Mineralogy and Geochemistry, 75(1), 7-46.

Howell, D. (2012). Strain-induced birefringence in natural diamond: a review. European Journal of Mineralogy, 24(4), 575-585.

Izraeli, E. S., Harris, J. W., and Navon, O. (1999) Raman barometry of diamond formation. Earth and Planetary Science Letters, 173(3), 351-360.

Jones, A.P., McMillan, P.F., Salzmann, C.G., Alvaro, M., Nestola, F., Prencipe, M., Dobson, D., Hazael, R., and Moore, M. (2016) Structural characterization of natural diamond shocked to 60 GPa; implications for Earth and planetary systems. Lithos, 265, 214-221.

Kenichi, T. (1999) Absence of the c/a anomaly in Zn under high pressure with a helium-pressure medium. Physical Review B, 60(9), 6171.

Koeberl, C., Masaitis, V. L., Shafranovsky, G. I., Gilmour, I., Langenhorst, F., and Schrauder, M. (1997) Diamonds from the Popigai impact structure, Russia. Geology, 25(11), 967-970.

Korsakov, A.V., Perraki, M., Zhukov, V.P., De Gussem, K., Vandenabeele, P., and Tomilenko, A.A. (2009) Is quartz a potential indicator of ultrahigh-pressure metamorphism? Laser Raman spectroscopy of quartz inclusions in ultrahigh-pressure garnets. European Journal of Mineralogy, 21(6), 1313-1323.

Kraus, D., Ravasio, A., Gauthier, M., Gericke, D.O., Vorberger, J., Frydrych, S., Helfrich, J., Fletcher, L.B., Schaumann, G., Nagler, B. and Barbrel, B. (2016) Nanosecond formation of diamond and lonsdaleite by shock compression of graphite. Nature Communications, 7, 10970.

Langenhorst, F. (2002) Shock metamorphism of some minerals: Basic introduction and microstructural observations. Bulletin of the Czech Geological Survey, 77(4), 265-282.

Mancktelow, N. S. (1995) Non-lithostatic pressure during sediment subduction and the development and exhumation of high pressure metamorphic rocks. Journal of Geophysical Research: Solid Earth, 100(B1), 571-583.

Mancktelow, N. S. (2008) Tectonic pressure: Theoretical concepts and modelled examples. Lithos, 103(1-2), 149-177.

Masaitis, V. L., Futergendler, S. I., & Gnevushev, M. A. (1972) Diamonds in impactites of the Popigai meteorite crater. Zapiski Vsesouznogo Mineralogicheskogo Obstchestva, 101, 108-113.

Masaitis, V. L. (1998) Popigai crater: Origin and distribution of diamond-bearing impactites. Meteoritics & Planetary Science, 33(2), 349-359.

Mazzucchelli, M.L., Burnley, P., Angel, R.J., Morganti, S., Domeneghetti, M.C., Nestola, F., and Alvaro, M. (2018) Elastic geothermobarometry: Corrections for the geometry of the host-inclusion system. Geology, 46(3), 231-234.

Mazzucchelli, M.L., Reali, A., Morganti, S., Angel, R.J. and Alvaro, M., 2019. Elastic geobarometry for anisotropic inclusions in cubic hosts. Lithos, 350, p.105218.

Moulas, E., Podladchikov, Y. Y., Aranovich, L. Y., & Kostopoulos, D. (2013). The problem of depth in geology: When pressure does not translate into depth. Petrology, 21(6), 527-538.

Murri, M., Jones, A.P., McMillan, P.F., Salzmann, C.G., Alvaro, M., Domeneghetti, M.C., Nestola, F., Prencipe, M., Dobson, D., Hazael, R., Moore, M., Vishnevsky, S., Logvinova, A.M., Sobolev, N.V. (2017) Structure characterization of impact natural diamond from Popigai crater. 80th Annual Meeting of the Meteoritical Society.

Murri, M., Mazzucchelli, M.L., Campomenosi, N., Korsakov, A.V., Prencipe, M., Mihailova, B., Scambelluri, M., Angel, R.J., and Alvaro, M. (2018) Raman elastic geobarometery for anisotropic mineral inclusions. American Mineralogist, 103, 1869-1872.

Murri M., Alvaro M., Angel R.J., Prencipe M., Mihailova B.D. (2019). The effects of non-hydrostatic stress on the structure and properties of alpha-quartz. Physics and Chemistry of Minerals, 46(5), 487-499.

Murri, M., Smith, R.L., McColl, K., Hart, M., Alvaro, M., Jones, A.P., Németh, P., Salzmann, C.G., Corà, F., Domeneghetti, M.C., Nestola, F., Sobolev N.V., Vishnevsky S.A., Logvinova A.M., McMillan P.F. 2019. Quantifying hexagonal stacking in diamond. Scientific reports, 9(1), p.10334.

Németh, P., Garvie, L. A., Aoki, T., Dubrovinskaia, N., Dubrovinsky, L., and Buseck, P. R. (2014) Lonsdaleite is faulted and twinned cubic diamond and does not exist as a discrete material. Nature communications, 5, 5447.

Nestola, F., Nimis, P., Ziberna, Longo, L. M., Marzoli, A. Harris, J.W., Manghnani, M.H., and Fedortchouk, Y. (2011) First crystal-structure determination of olivine in diamond: Composition and implications for provenance in the Earth's mantle. Earth and Planetary Science Letters 305, no. 1-2, 249-255.

Osinski, G. R., Grieve, R. A. F., Collins, G. S., Marion, C., and Sylvester, P. (2008) The effect of target lithology on the products of impact melting. Meteoritics & Planetary Science, 43(12), 1939-1954.

Raimbourg, H., and Kimura, G. (2008) Non-lithostatic pressure in subduction zones. Earth and Planetary Science Letters, 274(3-4), 414-422.

Rosenfeld, J.L., and Chase, A.B. (1961) Pressure and temperature of crystallization from elastic effects around solid inclusion minerals? American Journal of Science, 259, 519-541.

Salzmann, C. G., Murray, B. J. and Shephard, J. J. (2015) Extent of stacking disorder in diamond. Diamond and Related Materials, 59, 69-72.

Scheidl, K.S., Kurnosov, A., Trots, D.M., Boffa Ballaran, T., Angel, R.J., and Miletich, R. (2016) Extending the single-crystal quartz pressure gauge up to hydrostatic pressure of 19 GPa. Journal of Applied Crystallography, 49, 2129-2137.

Schmidt, C., and Ziemann, M.A. (2000) In-situ Raman spectroscopy of quartz: A pressure sensor for hydrothermal diamond-anvil cell experiments at elevated temperatures. American Mineralogist, 85, 1725-1734.

Schmidt C., Steele-MacInnis M., Watenphil A., and Wilke M. (2013) Calibration of zircon as a Raman spectroscopic pressure sensor to high temperatures and application to water-silicate melt systems. American Mineralogist, 98, 643-650.

Shiell, T. B., McCulloch, D. G., Bradby, J. E., Haberl, B., Boehler, R., and McKenzie, D. R. (2016) Nanocrystalline hexagonal diamond formed from glassy carbon. Scientific Reports, 6, 37232.

Shumilova, T. G., Mayer, E., and Isaenko, S. I. (2011) Natural monocrystalline lonsdaleite. In Doklady Earth Sciences (Vol. 441, No. 1, pp. 1552-1554). SP MAIK Nauka/Interperiodica.

Stangarone, C., Angel, R. J., Prencipe, M., Campomenosi, N., Mihailova, B., and Alvaro, M. (2019) Measurement of strains in zircon inclusions by Raman spectroscopy. European Journal of Mineralogy.

Stöffler, D., Grieve, R. A. F., Fettes, D., and Desmons, J. (2007) Impactites. Metamorphic rocks: A classification and glossary of terms, recommendations of the International Union of Geological Sciences, 82-92.

Utsumi, W., and Yagi, T. (1991) Formation of hexagonal diamond by room temperature compression of graphite. Proceedings of the Japan Academy, Series B, 67(9), 159-164.

Utsumi, W., Yamakata, M., Yagi, T., and Shimomura, O. (1994) In situ X-ray diffraction study of the phase transition from graphite to hexagonal diamond under high pressures and high temperatures. In AIP Conference Proceedings (Vol. 309, No. 1, pp. 535-538). AIP.

Weinberger, M. B., Tolbert, S. H. and Kavner, A. (2008) Osmium metal studied under high pressure and nonhydrostatic stress. Physical Review Letters 100, 045506.

Yelisseyev, A. P., Afanasiev, V. P., Panchenko, A. V., Gromilov, S. A., Kaichev, V. V., and Saraev, A. A. (2016) Yakutites: Are they impact diamonds from the Popigai crater?. Lithos, 265, 278-291.

Zaffiro, G., Angel, R. J., and Alvaro, M. (2019) Constraints on the Equations of State of stiff anisotropic minerals: rutile, and the implications for rutile elastic barometry. Mineralogical Magazine, 83(3), pp.339-347.

Zhang, Y. (1998) Mechanical and phase equilibria in inclusion–host systems. Earth and Planetary Science Letters, 157,209-222.

Zhao, J., Angel, R.J., and Ross, N.L. (2010) Effects of deviatoric stresses in the diamond-anvil pressure cell on single crystal samples. Journal of Applied Crystallography, 43, 743-751.

2. STRESS, STRAIN AND RAMAN SHIFTS

Ross J. Angel[1], Mara Murri[1], Boriana D. Mihailova[2], Matteo Alvaro[1]

[1]*Department of Earth and Environmental Sciences, University of Pavia, Via A. Ferrata, 1 I-27100 4 Pavia, Italy*
[2]*Department of Earth Sciences, University of Hamburg, Grindelallee 48, D-20146 Hamburg, Germany*

ABSTRACT

The concept of the phonon-mode Grüneisen tensor is reviewed as method to determine the elastic strains across crystals from the changes in the wavenumbers of Raman-active phonon modes relative to an unstrained crystal. The symmetry constraints on the phonon-mode Grüneisen tensor are discussed and the consequences for which combinations of strains can be determined by this method are stated. A computer program for Windows, stRAinMAN, has been written to calculate strains from changes in Raman (or other phonon) mode wavenumbers, and vice-versa. It can be downloaded for free from www.rossangel.net

INTRODUCTION

The measurement of elastic strains in crystals has many applications, including the determination of thermal expansion coefficients and compressibilities, the characterization of structural phase transitions and crystals under non-hydrostatic stress states inside diamond-anvil cells (DACs), as well as the stress states of individual crystal grains within a rock or ceramic composite. When the sample crystal is uniformly stressed, for example when it is under hydrostatic pressure inside a fluid pressure medium, then the strains are uniform across the sample, and they can be determined by measuring the unit-cell parameters of the crystal and comparing them to those of an unstrained reference crystal. This is the basis of using diffraction measurements to determine the thermal expansion and equations of state of minerals.

However, if a crystal is surrounded by other solid material it is subjected to strains imposed upon it by the thermal expansion and compressibility of the host material. The simplest case to consider is a spherical or ellipsoidal-shaped single crystal trapped as an inclusion inside an elastically-isotropic host crystal. When the pressure (*P*) or the temperature (*T*) changes, the host crystal will impose a uniform isotropic strain on the inclusion. If the inclusion crystal is elastically anisotropic

it will therefore develop different normal stresses in different directions. Therefore, the inclusion will not be under hydrostatic pressure. This deviatoric stress state will be the same at all points within the inclusion (Eshelby 1957), and there will be no strain gradients across the inclusion. The strain in such inclusions can therefore be measured by conventional X-ray diffraction (XRD) techniques. However, when the same inclusion is faceted, the edges and corners act as stress concentrators and the stress and strain will change across the inclusion volume (e.g. Campomenosi et al. 2018; Mazzucchelli et al. 2018; Murri et al. 2018). Strain gradients also exist across crystals in DACs when the pressure medium becomes non-hydrostatic. In both cases, the strain gradients give rise to broadening of Bragg reflections in the diffraction pattern (e.g. Angel et al. 2007; Zhao and Ross 2015), and the measured unit-cell parameters are some average of all of the various strained unit cells within the part of the sample that is within the X-ray beam. To follow the strain gradients it is therefore necessary to reduce the probed sample volume. This can be done with synchrotron-based XRD where the intensity of the source allows small volumes of the sample to be probed (e.g. Levine et al. 2015; Sørensen et al. 2012). However, synchrotron XRD is a rather expensive method and cannot be routinely applied to the many grains or inclusions that must be measured in even a single geological study of one small field area. Raman spectroscopy provides a practical alternative which is economically-accessible to most laboratories. Raman spectrometers coupled to microscopes can obtain spectra from volumes of just a few μm^3 of individual minerals within polished sections and allow the Raman shifts of multiple lines to be mapped across the volume of an inclusion a few 10's of microns across (e.g. Murri et al. 2018; Zhukov and Korsakov 2015).

The Raman shifts from inclusions are normally interpreted as the result of the inclusion being under a hydrostatic pressure. Consequently, the Raman shifts measured from inclusions are directly converted into a hydrostatic pressure (e.g. Kohn 2014), using pressure-wavenumber calibration curves established from hydrostatic DAC experiments. However, it is a common misconception implicit in such an analysis that Raman shifts directly measure stress or pressure, as can be easily illustrated. First, let us assume that the change $\Delta\omega^m$ in the wavenumber of a phonon mode m is indeed proportional to the applied normal stresses as:

$$\Delta\omega^m = a_1^m\sigma_1 + a_2^m\sigma_2 + a_3^m\sigma_3 \qquad (1)$$

With the a_i^m representing coefficients of proportionality that depend on the mode m and the direction in the crystal, but not on the magnitude of any of the stresses σ_i. This approach implicitly assumes that the effects of three simultaneous stresses along the X, Y, and Z axes is equal to the sums of the effects of the individual uniaxial stresses. Basic physical insight shows that this cannot be true. A uniaxial stress along X leads to expansion in Y and Z for normal materials with positive Poisson ratio, whereas simultaneous compression along X and Y must lead to shortening along both X and Y which is a completely different physical state. Therefore, the structural effect of compression along X and Y simultaneously is not the sum of compression along X and Y separately. As phonon modes of a crystal depend on the structure and bonding within the crystal, it is clear that these two different stress states must give rise to different Raman shifts, in contradiction to the premise behind Equation (1).

Second, at ambient pressure, heating a crystal does not change its stress state but its strain state; therefore, the observed changes of the Raman peak positions at different temperatures are the direct result of the strain tensor ε induced by temperature change ΔT. Similarly, in *in-situ* high-pressure experiments the observed changes in the phonon wavenumbers are the direct result of strain, which is induced by pressure P. Further, for many modes in many minerals, the phonon-wavenumber changes induced by reducing the temperature or increasing the pressure are the same for the same decrease in volume. For example, if the shifts of the most intense Raman peak of quartz at ca. 464 cm^{-1} is plotted against the unit-cell volume, then both the high-pressure and the low- and high-temperature data fall on a single trend (Murri et al. 2018). This clearly demonstrates that the wavenumber of this Raman-active mode of quartz is determined not directly by the pressure or the temperature, but is solely a function of the strains induced by changes in P or T. The effects of P and T on the Raman peak positions are therefore indirect; a change in P or T changes the unit-cell parameters and volume and this change (or strain) determines the change in the wavenumber of the Raman-active mode.

The concept was first established by Grüneisen (Grüneisen 1926) for isotropic solids. He defined what is now known as the thermal or thermodynamic Grüneisen parameter which relates the change in internal energy of an isotropic solid to the change in its pressure along an isochor.

From an atomistic point of view, the Grüneisen parameter represents the response of lattice dynamics (atomic vibrations) as opposed to the response of lattice statics (atomic equilibrium positions) to temperature change or stress, and it is determined by the anharmonicity of the crystal potential due to phonon-phonon interactions (Ziman 1960). If the anharmonicity in the potential is relatively small then the Grüneisen parameter remains approximately constant with either *P* or *T*. Grüneisen was clearly aware that the thermodynamic Grüneisen parameter was a tensor quantity in non-isotropic solids related to the anisotropic thermal expansion, the heat capacity and the elastic moduli. The details are laid out in (Key 1967) and discussed for the mineral olivine, for example, in (Kroll et al. 2014). Since the entropy of a solid depends explicitly on the lattice vibrations (phonon modes) (e.g. Barron et al. 1982; Cantrell 1980; Ziman 1960) it is possible to relate the macroscopic thermodynamic Grüneisen parameter to the microscopic phonon-mode Grüneisen tensors that define the relative wavenumber changes induced by the tensorial strain imposed on the crystal. In this paper we apply this idea to the specific problem of determining the strains in a crystal by measuring changes in the Raman shifts compared to those in an unstrained crystal. We first review the concept of the phonon-mode Grüneisen tensor and introduce a new approach to uniquely determine strains in crystals by measurements of Raman shifts. This has an immediate application, for example, in the measurement of strains in natural inclusions in order to provide estimates of the *P* and *T* at which they were entrapped deep within the Earth (e.g. Angel et al. 2014; Kohn 2014; Zhang 1998). The final section describes a new computer program, stRAinMAN, which is freely available and can be used to calculate strains of crystals from measured Raman shifts and vice-versa.

THEORY
Strains

Strains describe the change in shape and size of a physical object relative to an initial undeformed reference state. In this paper we are concerned with small elastic strains in crystals. 'Elastic' means that when the external field or force creating the strains, such as pressure, temperature or stress, is removed then the single crystal returns to its original size and shape. Plastic deformation and brittle failure, which both lead to permanent changes in size or shape, are explicitly excluded from this analysis. Elastic strains fall into two types, normal strains related to changes in length, and shear strains which do not change linear dimensions of the sample.

For crystals it is easiest to define strains in terms of the changes in their unit-cell parameters. The exact relationships between the strains and the cell parameters depend on the orientation with respect to the crystal axes of the Cartesian axes used to describe the strains. The conventional orientation for crystal classes of orthorhombic or higher symmetry is the natural one of having the Cartesian axes parallel to the crystallographic axes, thus **X** // **a** and **Z** // **c**. Then (except for the hexagonal system) the infinitesimal normal strain components ε_{11}, ε_{22} and ε_{33} define the changes in the cell parameters a, b, and c, for example $\varepsilon_{11} = {da}/{a}$, , where da is a very small change in the a cell parameter. The shear strains are related to changes in unit cell angles, for example ε_{13} is related to the change in angle between the a and c axes. In monoclinic and triclinic systems there are several widely-used different conventions for orienting the Cartesian axes of the tensor relative to the crystal axes, and the expressions for the strain components in terms of the unit-cell parameters are different in each case. Explicit equations for different conventions are given in (Carpenter et al. 1998) and (Cámara et al. 2009), and general equations in (Zotov 1990) and (Schlenker et al. 1978), for example. The strain tensor by definition excludes rigid-body rotations (Nye 1957) so it is symmetric, $\varepsilon_{ij} = \varepsilon_{ji}$ i, j = 1, 2, 3.

Phonon-mode Grüneisen tensor

The fractional change in the wavenumber, $\frac{-\Delta\omega^m}{\omega_0^m}$ of a phonon mode m in a crystal as a result of a strain $\boldsymbol{\varepsilon}$ is determined by a second-rank symmetric tensor, the phonon-mode Grüneisen tensor $\boldsymbol{\gamma^m}$ (Barron et al. 1982; Cantrell 1980; Ziman 1960):

$$\frac{-\Delta\omega^m}{\omega_0^m} = \boldsymbol{\gamma^m} : \boldsymbol{\varepsilon} \tag{2}$$

The ":" in Equation (2) indicates a double-scalar product between the two tensors, which can be written out in a full form as:

$$\frac{-\Delta\omega^m}{\omega_0^m} = \gamma_{11}^m \varepsilon_{11} + \gamma_{22}^m \varepsilon_{22} + \gamma_{33}^m \varepsilon_{33} + + \gamma_{23}^m \varepsilon_{23} + \gamma_{32}^m \varepsilon_{32} + + \gamma_{13}^m \varepsilon_{13} + \gamma_{31}^m \varepsilon_{31} + \gamma_{12}^m \varepsilon_{12} + \gamma_{21}^m \varepsilon_{21} \tag{3}$$

Both tensors are symmetric and therefore $\varepsilon_{ij} = \varepsilon_{ji}$ and $\gamma_{ij}^m = \gamma_{ij}^m$ for each pair of non-diagonal elements, so:

$$\frac{-\Delta\omega^m}{\omega_0^m} = \gamma_{11}^m \varepsilon_{11} + \gamma_{22}^m \varepsilon_{22} + \gamma_{33}^m \varepsilon_{33} + 2\gamma_{23}^m \varepsilon_{23} + 2\gamma_{13}^m \varepsilon_{13} + 2\gamma_{12}^m \varepsilon_{12} \tag{4}$$

For ease of notation we can reduce these tensors to a vector form in which the double-scalar product in Equation (2) becomes a scalar product of two vectors that represent the $\boldsymbol{\gamma^m}$ and the $\boldsymbol{\varepsilon}$ tensors. Under the Voigt (Voigt 1910) convention used here for strains, the normal strain components are equal in magnitude to the diagonal components of the tensor, e.g. $\varepsilon_1 = \varepsilon_{11}$, while the shear strains ε_4, ε_5 and ε_6 are one-half of the values of the corresponding tensor components ε_{23}, ε_{13}, ε_{12}. Therefore, if we set γ_4^m, γ_5^m and γ_6^m equal to the values of the corresponding tensor components γ_{23}, γ_{13} and γ_{12}, we obtain:

$$\frac{-\Delta\omega^m}{\omega_0^m} = \gamma_1^m \varepsilon_1 + \gamma_2^m \varepsilon_2 + \gamma_3^m \varepsilon_3 + \gamma_4^m \varepsilon_4 + \gamma_5^m \varepsilon_5 + \gamma_6^m \varepsilon_6 \qquad (5)$$

The introduction of a factor of ½ into the strain vector components and not into the Grüneisen vector components avoids factors of 2 appearing for the terms with subscripts $i = 4,5,6$ in the matrix version (5) of the tensor equation (2). The same convention works for the vector expression for the elastic energy of a solid (Nye 1957). The values of γ_i^m are different for different modes, indicated here by the superscript m. In general, each phonon mode is characterized by its wavenumber ω, wavevector $\mathbf{k}$, and polarization (transverse optical (TO) vs longitudinal optical (LO)). However, only modes at the Brilloiun-zone centre can be measured by Raman spectroscopy and therefore m represents in fact the wavenumber of non-polar modes (e.g. A1 in quartz) as well as the wavenumber of the corresponding TO and LO components of a polar mode (e.g. ETO and ELO in quartz). Thus γ_1^{464} for quartz relates the wavenumber of the 464 cm^{-1} mode of quartz to the applied ε_1 strain.

This relationship means that the changes in the Raman peak positions depend on all of the strains in three dimensions experienced by the crystal, not just the volume change. The negative sign on the left-hand side of Equations 2-5 is a convention introduced to make the values of γ_i^m positive for most phonon modes in most materials (e.g. Ziman 1960). With this convention, Equation (5) predicts that positive strains normally lead to a decrease in the phonon wavenumbers, and vice-versa. This is consistent with the general observation that, in the absence of phase transitions, Raman shifts increase with increasing hydrostatic pressure due to the development of negative strains and decrease with increasing temperature due to the development of positive strains.

The changes in phonon-mode wavenumbers induced by a temperature change ΔT can be calculated from (5) by recalling that in matrix form the strain is related to the thermal expansion tensor by:

$$\alpha_i \Delta T = \varepsilon_i \tag{6}$$

So that we can write (5) as:

$$\frac{-\Delta\omega^m}{\omega_0^m} = (\gamma_1^m \alpha_1 + \gamma_2^m \alpha_2 + \gamma_3^m \alpha_3 + \gamma_4^m \alpha_4 + \gamma_5^m \alpha_5 + \gamma_6^m \alpha_6)\Delta T \tag{7}$$

Or, similarly, the direct effect of pressure on phonon mode wavenumbers can be written directly in terms of the compressibility $\beta_i = -\varepsilon_i/\Delta P$:

$$\frac{\Delta\omega^m}{\omega_0^m} = (\gamma_1^m \beta_1 + \gamma_2^m \beta_2 + \gamma_3^m \beta_3 + \gamma_4^m \beta_4 + \gamma_5^m \beta_5 + \gamma_6^m \beta_6)\Delta P \tag{8}$$

Note that this means the phonon wavenumbers are not expected to be linear in either T or P, because the values of the thermal expansion and compressibility of a crystal change with T and P respectively. In the absence of strong anharmonicity in the crystal interatomic potentials one can assume that $\gamma_i^m = constant$ for each i = 1,…,6. That means that the response of lattice dynamics (phonons) follows the response of the static lattice (atomic equilibrium positions) to changes in temperature or pressure. In this case, the use of the phonon-mode Grüneisen parameters has several advantages over using empirical polynomial functions in P and T to describe the variation in peak shifts (e.g. Ashley et al. 2017; Schmidt and Ziemann 2000). First, the phonon-mode Grüneisen tensor has a sound physical basis and reflects the underlying physics that Raman shifts due to changes in P and T are not independent from each other. Second, they account for deviatoric strains as required, for example, in the analysis of host-inclusion systems, with the same approach as used for hydrostatic pressure. Third, quite often less coefficients are needed to describe the phonon wavenumbers than are required for higher-order polynomials in P and T.

Symmetry constraints

 We explore the symmetry constraints on the Grüneisen tensor in some detail because they have significant consequences for which individual strains can, and which cannot, be determined through the measurements of the shifts of Raman active modes of a crystal. These limitations arise

because we are using scalars $\frac{-\Delta\omega^m}{\omega_0^m}$ to determine the values of the components of a strain tensor via a property tensor. This is in contrast to measurements to determine, for example, strains from the applied stresses via elasticity theory. In elasticity, the relevant property tensor is the compliance tensor, s_{ijkl}, and if the stresses σ_{ij} are known, then the strains can be calculated directly from the tensor equation relating stress to strain. The closer analogy in elasticity for the Grüneisen concept would be to determine the strains from the known stresses by measuring the work done on the system dW, which is the double scalar product of the stress and the change in strains, $d\varepsilon_{ij}$, thus dW = $\sigma : d\varepsilon = \sigma_{ij} : d\varepsilon_{ij}$ (Nye 1957).

The reformulation of Equation (5) in terms of the thermal expansion and compressibility tensors (Equations 7, 8) indicates that the phonon-mode Grüneisen tensor is subject to the same symmetry constraints on its component values as other second-rank property tensors. This can be proved algebraically by requiring that $\frac{-\Delta\omega^m}{\omega_0^m}$ does not change when the symmetry operators of the crystal are applied as a transformation. The physical picture is that if symmetry-equivalent strains are applied separately to a crystal, one must obtain the same shift in mode wavenumbers: a strain ε_1 applied to a tetragonal crystal must result in the same $\frac{-\Delta\omega^m}{\omega_0^m}$ as a strain ε_2. If this were not true, the symmetry-equivalent a- and b-axes of the tetragonal crystal could be distinguished by experiment. For convenience, the constraints imposed by the symmetry on the components of the phonon-mode Grüneisen tensor are summarised in Table 1. For triclinic crystals all six components γ_i^m can be non-zero and have different values. For monoclinic crystals with the diad axis set along the y-axis, $\gamma_4{}^m = \gamma_6{}^m = 0$, so:

$$\frac{-\Delta\omega^m}{\omega_0^m} = \gamma_1^m\varepsilon_1 + \gamma_2^m\varepsilon_2 + \gamma_3^m\varepsilon_3 + \gamma_5^m\varepsilon_5 \tag{9}$$

In all crystals with orthorhombic symmetry or higher, $\gamma_4^m = \gamma_5^m = \gamma_6^m = 0$, and the wavenumber shifts become governed by:

$$\frac{-\Delta\omega^m}{\omega_0^m} = \gamma_1^m\varepsilon_1 + \gamma_2^m\varepsilon_2 + \gamma_3^m\varepsilon_3 \tag{10}$$

The Grüneisen tensor concept can also be used to predict the consequences for Raman spectra of small strains imposed on a crystal that break its symmetry. For example, a shear strain ε_5 applied to an orthorhombic crystal will cause the β unit-cell angle to deviate from 90°, thereby breaking the orthorhombic lattice symmetry. However, if ε_5 is close to zero, such a symmetry change will only have a very small effect on the relative wavenumber shifts because the additional "monoclinic term" $\gamma_5^m \varepsilon_5$ will be negligibly small with respect to the "orthorhombic one" given by Equation (10). Therefore $\Delta\omega^m \sim 0$ for small symmetry-breaking strains. However, if the symmetry-breaking strain exceeds a certain threshold value, then the wavenumber change of the lower-symmetry phase will become different from that predicted by the Grüneisen tensor of the higher-symmetry phase. This "pseudo-symmetry" approach certainly holds under conditions where the Grüneisen tensor components do not depend on strains. This is completely analogous to the concept of infinitesimal strains and constant coefficients used in linear elasticity theory (e.g. Nye 1957) in which the elastic compliance tensor conforms to the original symmetry of the undeformed crystal, but can predict the strains arising from small stresses that break the symmetry. For Grüneisen tensors, as for elasticity, it remains for experiments to determine the range of strains for which the linear approximation represented by this approach (Equations 5-10) remains valid. This approach is not expected to apply to structural phase transitions, where the associated anharmonicity may change the values of the γ_i^m significantly.

For all uniaxial crystals (tetragonal, trigonal, hexagonal) in the standard setting $\gamma_1^m = \gamma_2^m$ and the relationship (10) is further reduced to:

$$\frac{-\Delta\omega^m}{\omega_0^m} = \gamma_1^m(\varepsilon_1 + \varepsilon_2) + \gamma_3^m \varepsilon_3 \tag{11}$$

Note that in a uniaxial crystal even if the strains ε_1 and ε_2 are not equal, the change in phonon wavenumbers depends only on their sum $\varepsilon_1 + \varepsilon_2$ and not their individual values. Conversely, a measurement of the change in the Raman shift of two vibrational modes of a uniaxial crystal can be used to determine $\varepsilon_1 + \varepsilon_2$ and ε_3, if the values of the γ_i^m are known. Measurement of further vibrational modes can only reduce the uncertainty in the values of $\varepsilon_1 + \varepsilon_2$ and ε_3 but cannot ever allow the value of ε_1 to be determined separately from ε_2.

For cubic crystals and isotropic materials $\gamma_1^m = \gamma_2^m = \gamma_3^m$, and the other components are zero. Further, for small strains, the sum of the normal strains $\varepsilon_1+\varepsilon_2+\varepsilon_3$ is the fractional volume change, or the volume strain $\frac{\Delta V}{V}$. Thus, for cubic crystals, the Raman shift depends only upon the total volume change and not the values of the individual strain components:

$$\frac{-\Delta\omega^m}{\omega_0^m} = \gamma_1^m(\varepsilon_1 + \varepsilon_2 + \varepsilon_3) = \gamma_1^m \frac{\Delta V}{V} \tag{12}$$

It follows that the measurement, for example by Raman spectroscopy, of the change in the wavenumber of a single vibrational mode in a cubic crystal is sufficient to determine the volume change of the crystal. However, by analogy with the case of uniaxial crystals, if a cubic crystal is under unequal strains with $\varepsilon_1 \neq \varepsilon_2 \neq \varepsilon_3$, the symmetry of the phonon-mode Grüneisen tensor means that it is not possible to determine the individual strain components (Eqn. 12), no matter how many Raman lines are measured. Equation (12) also predicts that if the strains of a cubic crystal are purely deviatoric so that $\varepsilon_1+\varepsilon_2+\varepsilon_3=0$, there will be no change in the phonon wavenumbers, provided that the strains are infinitesimal.

Table 1. Symmetry constraints on the mode Grüneisen tensor in vector notation.

Crystal system	Vector	
	Independent values	Constraints
Triclinic	$\gamma_1^m, \gamma_2^m, \gamma_3^m, \gamma_4^m, \gamma_5^m, \gamma_6^m$	*none*
Monoclinic, b-unique	$\gamma_1^m, \gamma_2^m, \gamma_3^m, \gamma_5^m$	$\gamma_4^m = \gamma_6^m = 0$
Monoclinic, c-unique	$\gamma_1^m, \gamma_2^m, \gamma_3^m, \gamma_6^m$	$\gamma_4^m = \gamma_5^m = 0$
Orthorhombic	$\gamma_1^m, \gamma_2^m, \gamma_3^m$	$\gamma_4^m = \gamma_5^m = \gamma_6^m = 0$
Tetragonal, Trigonal, Hexagonal	γ_1^m, γ_3^m	$\gamma_1^m = \gamma_2^m$ $\gamma_4^m = \gamma_5^m = \gamma_6^m = 0$
Cubic	γ_1^m	$\gamma_1^m = \gamma_2^m = \gamma_3^m$ $\gamma_4^m = \gamma_5^m = \gamma_6^m = 0$

Determining Phonon-Mode Grüneisen Components

For cubic crystals the single symmetrically-independent value $\gamma_1^m = \gamma_2^m = \gamma_3^m$ for each mode can be determined from the change of the mode wavenumber with pressure if the bulk modulus $K = -V \frac{\partial P}{\partial V}$ is known:

$$\gamma_1^m = K \cdot \frac{1}{\omega^m} \frac{\partial \omega^m}{\partial P} \tag{13}$$

Note that K is not a constant, but is a function of P and T. Therefore, a more correct approach is to plot the wavenumber of the phonon mode against volume, and to use Equation (12) to determine the value of γ_1^m. For non-cubic crystals, one can define a similar quantity, the volume Grüneisen parameters γ_V^m of a mode:

$$\gamma_V^m = \frac{-\Delta\omega^m}{\omega_0^m} \bigg/ \frac{\Delta V}{V} \qquad (14)$$

This can be determined from the measured shift in wavenumber with pressure, $\frac{1}{\omega^m}\frac{\partial\omega^m}{\partial P}$, known as the 'phonon compressibility' (Pina-Binvignat et al. 2018), and the measured volume change with pressure. Consideration of Equation (8) shows that values of γ_V^m are related to the values of the components of the phonon-mode Grüneisen tensor by:

$$\gamma_V^m = K(\gamma_1^m\beta_1 + \gamma_2^m\beta_2 + \gamma_3^m\beta_3 + \gamma_4^m\beta_4 + \gamma_5^m\beta_5 + \gamma_6^m\beta_6) \qquad (15)$$

with the appropriate simplifications for symmetries higher than triclinic.

In crystals of lower than cubic symmetry the determination of the components of the phonon-mode Grüneisen tensor for even a single vibrational mode is not easy to achieve experimentally, because it requires different strain states to be imposed on a crystal. It is therefore not sufficient to measure the Raman shifts under hydrostatic pressure, because this generates a single strain state. Consider a uniaxial crystal, like quartz. The symmetry constraints reduce Equation 8 to:

$$\frac{\Delta\omega^m}{\omega_0^m} = (2\gamma_1^m\beta_1 + \gamma_3^m\beta_3)\Delta P \qquad (16)$$

If the change in mode wavenumber $\Delta\omega^m$ is measured as a function of pressure change ΔP, then all that can be determined is $\frac{\Delta\omega^m}{\Delta P} = (2\gamma_1^m\beta_1 + \gamma_3^m\beta_3)\omega_0^m$. Even if the values of the compressibilities β_1 and β_3 are known, it is not possible to determine the *two* values of γ_1^m and γ_3^m from the *just one* value of $\frac{\Delta\omega^m}{\Delta P}$. Only if $\gamma_1^m = \gamma_3^m$, which is the case in cubic minerals, can their values be determined from hydrostatic compression experiments. An equation exactly analogous to (16) can be written for a temperature change ΔT at constant pressure, with the implication that the values of γ_1^m and γ_3^m cannot be determined independently.

Therefore, in order to determine the values of γ_i^m in non-cubic crystals it is necessary to generate several different sets of strain conditions. This has been done successfully on quartz, by applying uniaxial stresses of up to 0.5 GPa, to determine both phonon-mode Grüneisen components for various Raman active modes (Barron et al. 1982; Briggs and Ramdas 1977). The limited fracture strength of silicate crystals however limits the deviatoric stress and strain levels that can be applied to quite low levels, limiting the precision with which the values of γ_i^m can be determined. And, such experiments cannot be performed under significant tension, except via shock wave techniques (Gallivan and Gupta 1995). One possibility is that reproducible deviatoric stress at GPa levels can be applied to single crystals by using non-hydrostatic pressure media (Zhao et al. 2010), and this is an avenue currently under exploration.

A practical alternative is to use computer simulations of the crystal based on density-functional theory (DFT) to calculate the Raman spectra (e.g. Prencipe 2012; Zicovich-Wilson et al. 2004) under a range of deviatoric strains (Murri et al. 2018; Özkan and Jamieson 1978). The strains applied in the simulations are not limited by the physical fragility of the crystal and can be arbitrarily large, and any combination of strains both positive in tension and negative in compression can be applied provided that the structure remains dynamically stable. If the simulations are performed over a grid of strains, then a contour plot of the phonon wavenumber on this grid immediately indicates the relationship between the phonon-mode shift and the strains. An example is provided by Figure 1a, for the 969 cm^{-1} Raman line of zircon, which illustrates several important principles about Raman shifts in minerals. First, the contour lines are parallel and equally-spaced, which means that the phonon-mode Grüneisen components are independent of the strains and their values can be determined from fitting a planar surface to the calculated shifts. Second, the contour lines of constant Raman shift are not parallel to the isochors, which for tetragonal zircon would be lines of constant $2\varepsilon_1+\varepsilon_3$. Therefore, in contrast to cubic minerals, but in agreement with Equation (11), the shift of the 969 cm^{-1} line of zircon does not indicate the volume strain. Figure 1b is the same map replotted as a function of stress rather than strain, using the room P,T elastic tensor of zircon (Brown 1996) and shows that the contours are not parallel to lines of constant mean stress, $(2\sigma_1+\sigma_3)/3$. Therefore, the Raman shift of this line does not provide a measurement of mean stress. Lastly, the contour maps for different phonon modes have very different patterns of contour lines. As an extreme example, Figure 1c is a map of the 223 cm^{-1}

mode whose contour lines have positive slopes indicating that one of the two mode Grüneisen components is negative. A fit of this data with Equation (11) yields $\gamma_1^{223} = -0.27$ and $\gamma_3^{223} = 1.32$. A similar analysis of DFT simulations of quartz (Murri et al. 2018) gave values of the phonon-mode Grüneisen tensor components that are in good agreement with those obtained by direct Raman spectroscopic measurements of uniaxially stressed quartz crystals (Barron et al. 1982; Briggs and Ramdas 1977) and that correctly predict Raman shifts from the strains of inclusion crystals in natural garnet crystals measured by XRD (Murri et al. 2018).
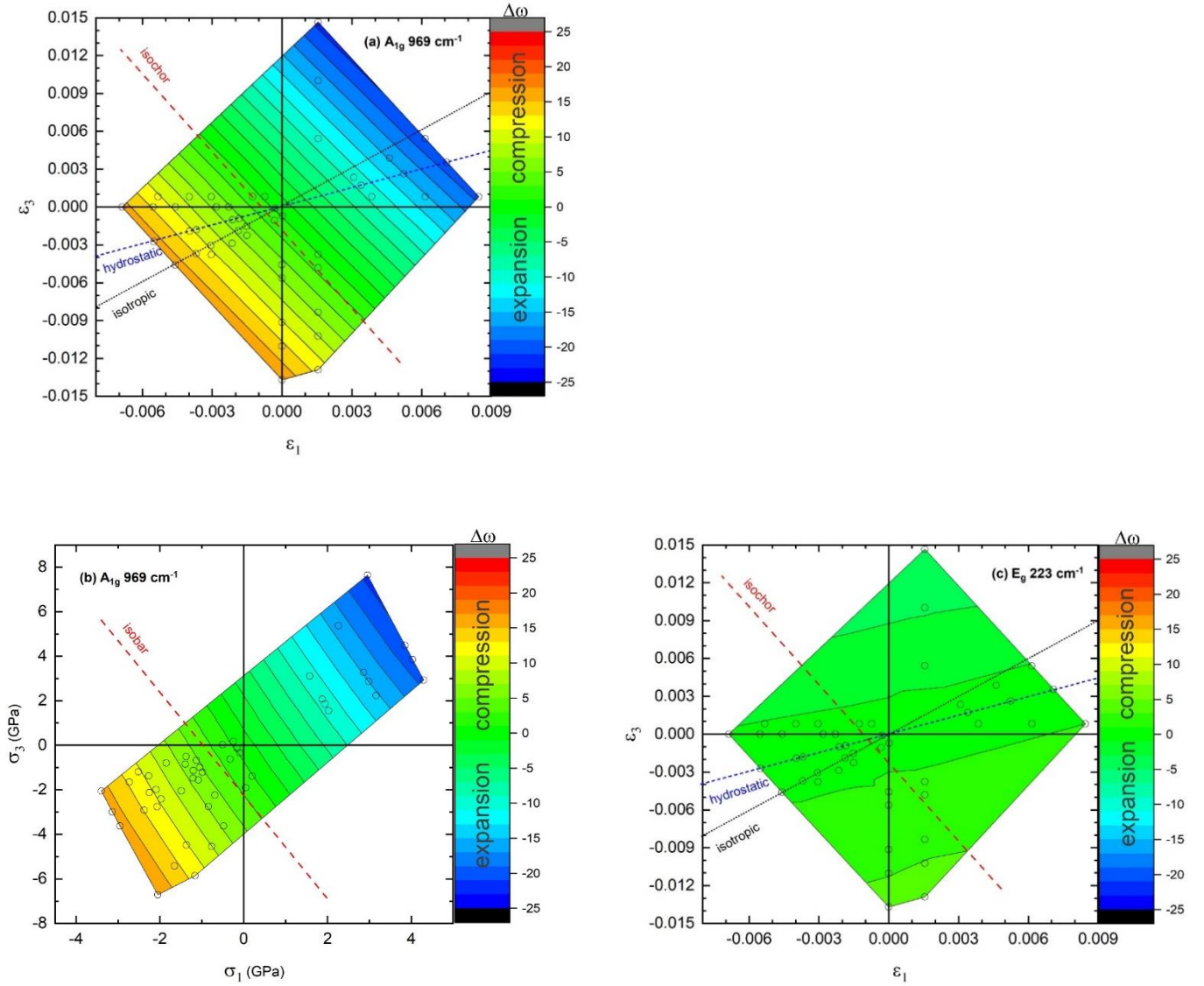
Figure 1. Variation of Raman shift of phonon modes of zircon, calculated by HF-DFT simulations (Stangarone et al. 2019). (a) The 969 cm^{-1} mode plotted as a function of strains exhibits parallel, equally-spaced contours indicating the that components $\gamma_1^{969} = 1.17$ and $\gamma_3^{969} = 1.26$ of the mode Grüneisen tensor are constant. The contours are not parallel to isochors. (b) Neither are the iso-shift contours parallel to isobars, lines of equal mean stress $(2\sigma_1 + \sigma_3)/3$.
(c) A contour plot of the 223 cm^{-1} mode which has $\gamma_1^{223} = -.27$ and $\gamma_3^{223} = 1.32$.

IMPLEMENTATION

We have written a computer program, stRAinMAN, that calculates the changes in phonon wavenumbers from strains as well as the strains from measured changes in phonon wavenumbers, by applying Equation (5) with the symmetry constraints that we have described above. The program name emphasises its most important application, which is the determination of strains in

crystals by using Raman spectroscopy to measure changes in phonon wavenumbers relative to an unstrained crystal. However, the program can be used for any phonon mode in a crystal whether or not it is Raman- or infrared-active.

The program has a graphical user interface (GUI) consisting of a number of tabs (Figure 2), most of which are comprised of an upper area for user input and a lower information window which displays results as well as warning and error messages from the program. Tabs for calculations only become active when the necessary information about the phonon-mode Grüneisen parameters have been loaded to the program. These are loaded from a file via a file browser launched from the *Load Grueneisen* tab (Figure 2). The structure of the input file follows that of *crystallographic information files (cif)*, because it is a very flexible text file format which allows information to be explicitly labelled by text flags (e.g. Rodriguez-Carvajal and González-Platas 2003) making it easily-read by both humans and computer programs, and editable by the simplest text editors. For the stRAinMAN program we have introduced a new set of *cif* data names to describe the parameters of phonon-mode Grüneisen tensors, which are listed in Table 2. An example file with the phonon-mode Grüneisen tensor components of quartz is given in Table 3. By using the *cif* syntax and structure we are also able to make use of standard *cif* data names to specify the crystal system of the mineral, and the file can be read by any program that is *cif*-compliant. If the crystal system is specified, then the stRAinMAN program applies the appropriate symmetry constraints to the components of the Grüneisen tensor that we have described above. For the example of trigonal quartz (Table 3), the program will set $\gamma_2^m = \gamma_1^m$ and $\gamma_4^m = \gamma_5^m = \gamma_6^m = 0$ for all the modes input. If any tensor components listed in the Grüneisen file violate the symmetry constraints, or if a symmetry-required component is not listed, then a warning is issued to the user. The input file must also contain the value of ω_0^m for each mode because Equation (5) defines the fractional change of the wavenumber of the mode, not the absolute value of the shift. The units used for wavenumbers are not defined by Equation (5), and therefore any units can be used in the program. However, the input and output formats in stRAinMAN are designed to optimally display wavenumbers in the most commonly-used units for Raman spectroscopy, namely cm^{-1}.
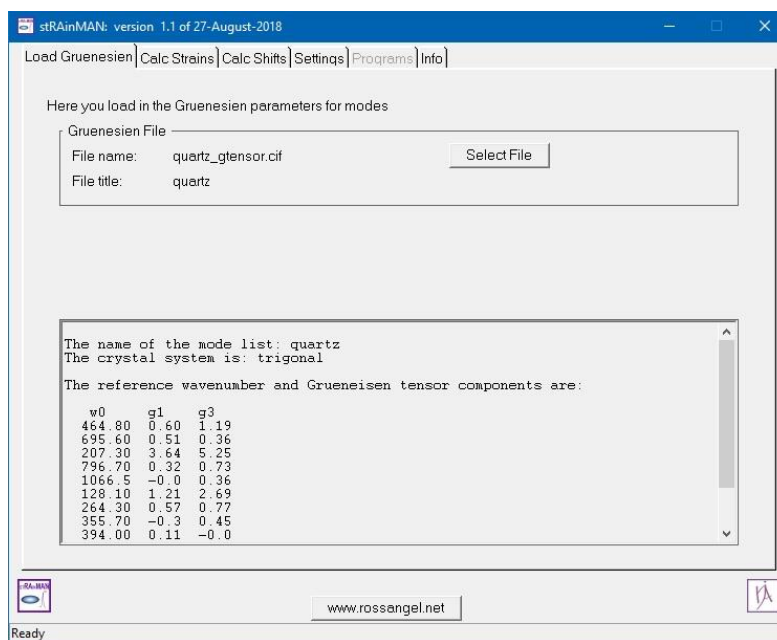
Figure 2. A screen shot of the stRAinMAN GUI showing the *Load Gruenesien* tab after a mode list for quartz has been loaded from the Grüneisen file listed in Table 3. Not all of the mode list is visible, but it can be accessed with the scroll bar on the right-side of the output window.

Table 2. Data names used to describe modes in Grüneisen files for stRAinMAN	
Data name	Definition
_mode_name	Name of mode, text
_mode_w0	Value of ω_0^m, of a mode in cm^{-1}
_mode_gamma_1	Value of γ_1^m of a mode, if not give assumed 0
_mode_gamma_2	γ_2^m
_mode_gamma_3	γ_3^m
_mode_gamma_4	γ_4^m
_mode_gamma_5	γ_5^m
_mode_gamma_6	γ_6^m
_mode_symm	Symmetry label of a mode, e.g. A1g
Note: All of these data names can be used together in a cif loop_ structure as shown in Table 3.	

Table 3. Example of a Grüneisen file for quartz.	
File contents	Explanation
data_quartz_modes	Start of data block (only the first datablock is used by stRAinMAN).
_chemical_name_mineral quartz _space_group_crystal_system trigonal	Optional name for data Crystal system: required
loop_ _mode_w0 _mode_gamma_1 _mode_gamma_3 464 0.60 1.19 700 0.50 0.36 206 3.66 5.28 799 0.32 0.73 1067 -0.02 0.36 128 1.21 2.70 265 0.57 0.77 356 -0.31 0.45 395 0.11 -0.05 451 0.54 0.69 1083 0.02 0.33 1165 -0.05 -0.09	Standard *cif* loop header structure. Data will contain ω_0^m, γ_1^m and γ_3^m for each mode. _mode_symm and _mode_name could also be used. One line for each mode, with ω_0^m, γ_1^m and γ_3^m in the same order as specified in the loop header. Modes can appear in any order

It is not required to list all of the modes of a crystal in the Grüneisen file, nor even all of the Raman-active modes. Only the modes of interest need be listed, but other modes can also be listed even if they are not employed in calculations. Thus, a single file can be kept for each mineral, and used for all subsequent calculations without any need to edit it. When a valid set of Grüneisen tensor components has been loaded into stRAinMAN, the calculation tabs become active (Figure 2). The *Calc Shifts* tab allows mode wavenumber shifts to be calculated from strains input by the user. There is the option to limit the input strains to only those allowed by the symmetry of the crystal (Figure 3). The output window contains the calculated change in wavenumber of each mode (the 'shift') for the input strains, calculated following Equation 5 as:

$$\Delta\omega^m = \omega_0^m \gamma_i^m \varepsilon_i \tag{17}$$

where $\gamma_i^m \varepsilon_i$ follows the Einstein summation convention and means the sum over all components i = 1–6.

It is important in this calculation to use the value of ω_0^m that was used to determine the values of γ_i^m, as their values depend on the value of ω_0^m. If the measured wavenumber of a mode in an

unstrained crystal, say $\omega_{0,exp}^m$, is slightly different from ω_0^m, the calculated change $\Delta\omega^m$ can be added to the measured $\omega_{0,exp}^m$ to obtain the wavenumber $\omega_{exp}^m = \omega_{0,exp}^m + \Delta\omega^m$ expected from an experimental measurement.

The *Calc strains* tab of the stRAinMAN GUI allows the user to calculate the strains in a crystal from the measured changes in wavenumbers of several modes. In order to obtain accurate values of strains it is essential to measure the mode wavenumbers $\omega_{0,exp}^m$ in an unstrained crystal of the same material under the same experimental conditions as the sample of interest, and to input $\omega_{exp}^m = \omega_{exp}^m - \omega_{0,exp}^m$ into the program. The stRAinMAN program checks that the values of $\Delta\omega_{exp}^m$ of a sufficient number of modes are input to allow the calculation of the symmetry-independent strain quantities of the crystal. Thus, a minimum of one mode is required to determine $\varepsilon_1 + \varepsilon_2 + \varepsilon_3$ in cubic crystals, and two modes to determine the quantities $\varepsilon_1 + \varepsilon_2$ and ε_3 in uniaxial crystals, etc. If exactly this number of modes are input, then only the values of the strain quantities can be determined by the program. If more modes are used, the estimated uncertainties of the strain components are also calculated by linear least-squares inversion of Equation (5) with the symmetry constraints applied, along with the value of χ^2 from the least-squares to indicate the consistency of the measured mode wavenumbers. The measured $\Delta\omega_{exp}^m$ can be input directly into the GUI (Figure 4) or, for ease of processing large datasets, they can be read from a data file. The data file format is illustrated in Table 4. It consists of two essential header lines, followed by one line of mode shifts for each measurement. The mode shifts can appear in any order, but they must have the same order in every line. The header line labelled 'w0:' defines the order of the data by labelling the columns with the ω_0^m values. These must match (within 1 cm^{-1}) the values of ω_0^m in the file with the phonon-mode Grüneisen tensor components. For reasons of space, when a file is used to input the mode shifts, the uncertainties of calculated strain quantities are not output to the GUI. They can be obtained by first opening a log file under the *Settings* tab of the GUI, which will then contain the results of all calculations that are performed. This provides a useful method by which results of calculations can then be cut and pasted into graphics or spreadsheet programs for further analysis and display.

The stRAinMAN program is written in Fortran-95 using the CrysFML (Rodriguez-Carvajal and González-Platas 2003) library. The program is free for non-commercial use and does not require any commercial software or libraries other than those provided with the program. It is freely available for download from www.rossangel.net for Windows operating systems, together with phonon-mode Grüneisen parameter files for common minerals, and example input files for

illustrating the calculation of strains from measured Raman shifts. Basic help information is provided within the program, and this paper serves as the full description of how the stRAinMAN program operates.
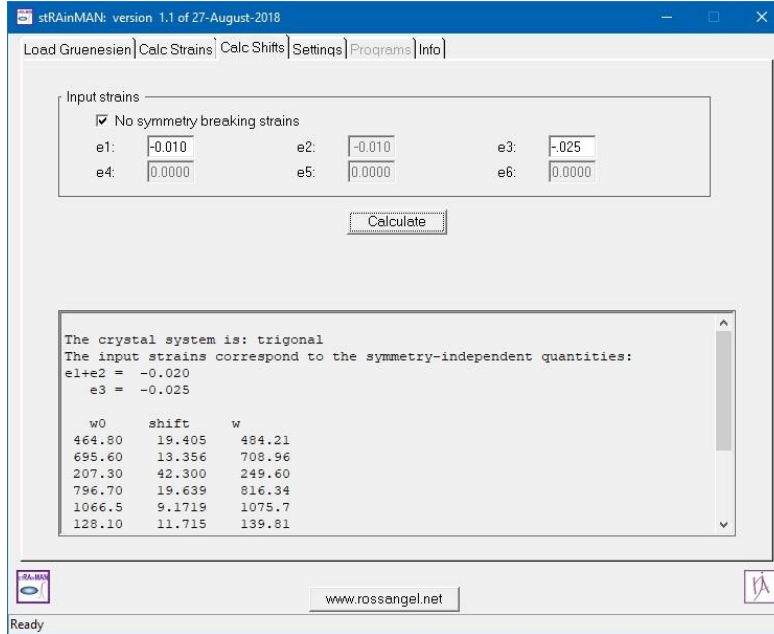
Figure 3. The *Calc Shifts* tab of the stRAinMAN GUI showing the result of a calculation for quartz. By ticking the box labeled 'No symmetry breaking strains' the value of strain ε_2 is set equal to the value input for ε_1, and the input boxes for the shear strains are de-activated. The output window contains the calculated change in wavenumber of each mode $\Delta\omega^m$ (labeled as 'shift') for the input strains as well as the final value of the wavenumber 'w' assuming that the mode in the unstrained crystal has a wavenumber of ω_0^m.

42
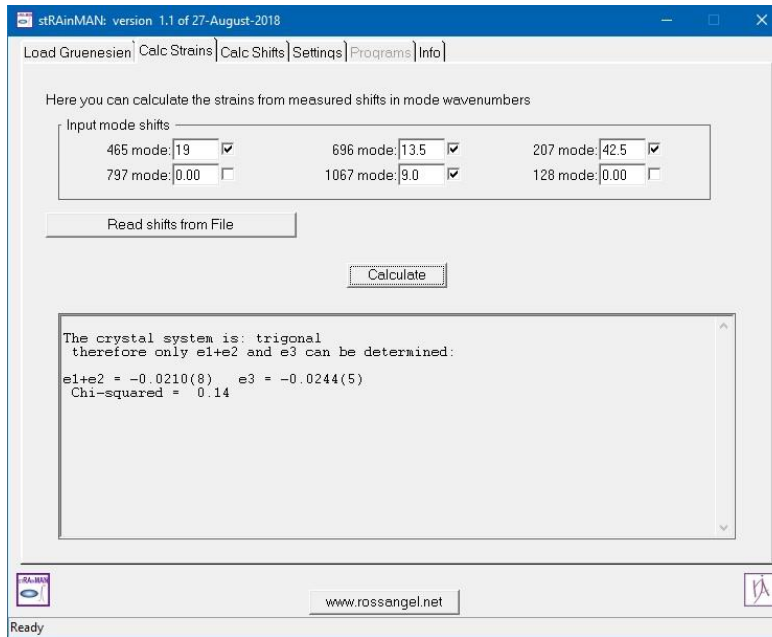
Figure 4. The *Calc Strains* tab of the stRAinMAN GUI showing the strains calculated from the changes in mode wavenumbers input into four of the boxes in the GUI. Because there are only two independent strain quantities that can be calculated for a uniaxial crystal, inputing data for at least three modes (four in the screenshot) allows the program to calculate the uncertainties in the strains, which are shown in parentheses. The *Read Shifts from File* button allows experimental data of changes in wavenumbers to be read from a list in a text file (Table 4).

Table 4. Example of a data file with measured changes in Raman shifts.	
File contents	Explanation
title: Quartz shifts for calculating strains w0: 206 464 700 1067 shifts: 42.3 19.4 13.3 9.2 -43.0 -22.0 -10.0 -15.0 -0.88 2.7 -5.6 8.5 24.1 9.4 10.4 0.6	Title of the file Value of ω_0^m to identify the mode in this file Start of data 1 line per spectrum. Each line contains measured values of $\Delta\omega^m$ in the order specified by the line labelled 'w0:'. The order of the modes in this file does not have to match the order in which they are listed in the Grüneisen file.

Acknowledgements

References

Angel, R.J., Bujak, M., Zhao, J., Gatta, G.D., and Jacobsen, S.D. (2007) Effective hydrostatic limits of pressure media for high-pressure crystallographic studies. Journal of Applied Crystallography, 40(1), 26-32.

Angel, R.J., Mazzucchelli, M.L., Alvaro, M., Nimis, P., and Nestola, F. (2014) Geobarometry from host-inclusion systems: The role of elastic relaxation. American Mineralogist, 99(10), 2146-2149.

Ashley, K.T., Barkoff, D.W., and Steele-MacInnis, M. (2017) Barometric constraints based on apatite inclusions in garnet. American Mineralogist, 102(4), 743-749.

Barron, T.H.K., Collins, J.F., Smith, T.W., and White, G.K. (1982) Thermal expansion, Grüneisen functions and static lattice properties of quartz. Journal of Physics C: Solid State Physics, 15, 4311-4326.

Briggs, R.J., and Ramdas, A.K. (1977) Piezospectroscopy of the Raman spectrum of α-quartz. Physical Review B, 16(8), 3815-3826.

Brown, I.D. (1996) CIF (Crystallographic Information File): A standard for crystallographic data interchange. Journal of Research of the National Institute of Standards and Technology, 101(3), 341-246.

Camara, F., Nestola, F., Angel, R.J., and Ohashi, H. (2009) Spontaneous strain variations through the low temperature displacive phase transition of $LiGaSi_2O_6$ clinopyroxene. European Journal of Mineralogy, 21, 599-614.

Campomenosi, N., Mazzucchelli, M.L., Mihailova, B.D., Scambelluri, M., Angel, R.J, Nestola, F., Reali, A., and Alvaro, M. . (2018) How geometry and anisotropy affect residual strain in host inclusion system: coupling experimental and numerical approaches. American Mineralogist, accepted.

Cantrell, J.H. (1980) Generalized Grüneisen tensor from solid nonlinearity parameters. Physical Review B, 21(10), 4191-4195.

Carpenter, M.A., Salje, E.K.H., and Graeme-Barber, A. (1998) Spontaneous strain as a determinant of thermodynamic properties for phase transitions in minerals. European Journal of Mineralogy, 10(4), 621-691.

Eshelby, J.D. (1957) The determination of the elastic field of an ellipsoidal inclusion, and related problems. Proceedings of the Royal Society of London. Series A. Mathematical and Physical Sciences, 241, 376-396.

Gallivan, S.M., and Gupta, Y.M. (1995) Study of tensile deformation in shocked Z-cut, α−quartz using time resolved Raman spectroscopy. Journal of Applied Physics, 78, 1557-1564.

Grüneisen, E. (1926) Zustand des festen Körpers. Handbuch der Physik, 1, 1-52.

Key, S.W. (1967) Grüneisen tensor for anisotropic materials. Journal of Applied Physics, 38(7), 2923-2928.

Kohn, M.J. (2014) "Thermoba-Raman-try": Calibration of spectroscopic barometers and thermometers for mineral inclusions. Earth and Planetary Science Letters, 388, 187-196.

Kroll, H., Kirfel, A., and Heinemann, R. (2014) Axial thermal expansion and related thermophysical parameters in the Mg,Fe olivine solid-solution series. European Journal of Mineralogy, 26, 607-621.

Levine, L.E., Okoro, C., and Xu, R. (2015) Full elastic strain and stress tensor measurements from individual dislocation cells in copper through-Si vias. IUCrJ, 2, 635-642.

Mazzucchelli, M.L., Burnley, P., Angel, R.J., Morganti, S., Domeneghetti, M.C., Nestola, F., and Alvaro, M. (2018) Elastic geothermobarometry: Corrections for the geometry of the host-inclusion system. Geology, 46(3), 231-234.

Murri, M., Mazzucchelli, M.L., Campomenosi, N., Korsakov, A.V., Prencipe, M., Mihailova, B., Scambelluri, M., Angel, R.J., and Alvaro, M. (2018) Raman elastic geobarometery for anisotropic mineral inclusions. American Mineralogist, 103, 1869-1872.

Nye, J.F. (1957) Physical properties of crystals. 329 p. Oxford University Press, Oxford.

Özkan, H., and Jamieson, J. (1978) Pressure dependence of the elastic constants of non-metamict zircon. Physics and Chemistry of Minerals, 2, 215-224.

Pina-Binvignat, F.A., Malcherek, T., Angel, R.J., Paulmann, C., Schlüter, J., and Mihailova, B. (2018) Effect of radiation-induced structural damage on the structural response of zircon to high pressures. Physics and Chemistry of Minerals, published online.

Prencipe, M. (2012) Simulation of vibrational spectra of crystals by ab initio calculations: an invaluable aid in the assignment and interpretation of the Raman signals. The case of jadeite ($NaAlSi_2O_6$). Journal of Raman Spectroscopy, 43, 1567-1569.

Rodriguez-Carvajal, J., and González-Platas, J. (2003) Crystallographic Fortran 90 Modules Library (CrysFML): a simple toolbox for crystallographic computing programs. Commission on Crystallographic Computing of the IUCr Newsletter, 1.

Schlenker, J.L., Gibbs, G.V., and Boison Jr., M.B. (1978) Strain-Tensor Components Expressed in Terms of Lattice Parameters. Acta Cryst., A34, 52-54.

Schmidt, C., and Ziemann, M.A. (2000) In-situ Raman spectroscopy of quartz: A pressure sensor for hydrothermal diamond-anvil cell experiments at elevated temperatures. American Mineralogist, 85, 1725-1734.

Sørensen, H.O., Schmidt, S., Wright, J.P., Vaughan, G.B.M., Techert, S., Garman, E.F., Oddershede, J., Davaasambu, J., Paithankar, K.S., Gundlach, C., and Poulsen, H.F. (2012) Multigrain crystallography. Zeitschrift für Kristallographie, 227, 63-78.

Stangarone, C., Angel, R. J., Prencipe, M., Campomenosi, N., Mihailova, B., & Alvaro, M. (2019). Measurement of strains in zircon inclusions by Raman spectroscopy. European Journal of Mineralogy. (in press)

Voigt, W. (1910) Lehrbuch der Kristallphysik. Teubner, Leipzig.

Zhang, Y. (1998) Mechanical and phase equilibria in inclusion–host systems. Earth and Planetary Science Letters, 157(3–4), 209-222.

Zhao, J., Angel, R.J., and Ross, N.L. (2010) Effects of deviatoric stresses in the diamond-anvil pressure cell on single crystal samples. Journal of Applied Crystallography, 43, 743-751.

Zhao, J., and Ross, N. (2015) Non-hydrostatic behavior of KBr as a pressure medium in diamond anvil cells up to 5.63GPa. Journal of Physics Condensed Matter, 27, 185402.

Zhukov, V.P., and Korsakov, A.V. (2015) Evolution of host-inclusion systems: a visco-elastic model. Journal of Metamorphic Geology, 33(8), 815-828.

Zicovich-Wilson, C.M., Pascale, F., Roetti, C., Saunders, V.R., Orlando, R., and Dovesi, R. (2004) Calculation of the vibration frequencies of α-quartz: The effect of Hamiltonian and basis set. Journal of Computational Chemistry, 25(15), 1873-1881.

Ziman, J.M. (1960) Electrons and phonons: the theory of transport phenomena in solids. 469 p. Oxford University Press, Oxford.

Zotov, N. (1990) Review of relationships between different strain tensors. Acta Crystallographica A, 46, 627-628.

3. RAMAN ELASTIC GEOBAROMETRY FOR ANISOTROPIC MINERAL INCLUSIONS

Mara Murri[1], Mattia L. Mazzucchelli[1], Nicola Campomenosi[2], Andrey V. Korsakov[3], Mauro Prencipe[4], Boriana D. Mihailova[5], Marco Scambelluri[2], Ross J. Angel[1], Matteo Alvaro[1]

[1]*Department of Earth and Environmental Sciences, University of Pavia, Via A. Ferrata, 1 I-27100 4 Pavia, Italy*
[2]*Department of Earth Science, Environment & Life, University of Genoa, Corso Europa 26, 16132 Genoa, Italy*
[3]*V S Sobolev Institute of Geology and Mineralogy SB RAS, Novosibirsk*
[4]*Earth Sciences Department, University of Torino, Via Valperga Caluso 35 Italy*
[5]*Department of Earth Sciences, University of Hamburg, Grindelallee 48, D-20146 Hamburg, Germany*

ABSTRACT

Elastic geobarometry for host-inclusion systems can provide new constraints to assess the pressure and temperature conditions attained during metamorphism. Current experimental approaches and theory are developed only for crystals immersed in a hydrostatic stress field, whereas inclusions experience deviatoric stress. We have developed a method to determine the strains in quartz inclusions from Raman spectroscopy using the concept of the phonon-mode Grüneisen tensor. We used *ab initio* Hartree-Fock/Density Functional Theory to calculate the wavenumbers of the Raman-active modes as a function of different strain conditions. Least-squares fits of the phonon-wavenumber shifts against strains have been used to obtain the components of the mode Grüneisen tensor of quartz (γ_1^m and γ_3^m) that can be used to calculate the strains in inclusions directly from the measured Raman shifts. The concept is demonstrated with the example of a natural quartz inclusion in eclogitic garnet from Mir kimberlite and has been validated against direct X-ray diffraction measurement of the strains in the same inclusion.

Keywords: deviatoric stress; elastic anisotropy; mineral inclusions; metamorphic rocks; quartz in garnet; elastic barometry

INTRODUCTION

Mineral inclusions entrapped in ultra-high-pressure metamorphic rocks can provide fundamental information about geological processes such as subduction and continental collision. When a host-inclusion pair is exhumed from depth to the Earth's surface non-lithostatic stresses are developed in the inclusion because of the contrast in their elastic properties (Angel et al. 2015

and references therein). The inclusion is under compressive stress if it is more compressible than the host. If correctly interpreted, these stresses on the inclusion allow the stress conditions at entrapment to be estimated. However, the theory for elastic geobarometry for host-inclusion pairs is only developed for crystals immersed in a hydrostatic stress field. This is valid for an isotropic and spherical inclusion entrapped in an isotropic host as it is subject to isotropic strains imposed by the host and will, therefore, exhibit isotropic stresses; that means the inclusion will be under hydrostatic pressure. However, if inclusions of elastically anisotropic minerals such as quartz, coesite, or zircon are entrapped in a cubic host such as garnet the same isotropic strain imposed by the garnet will result in anisotropic (i.e. deviatoric) stresses in the inclusion (see Figure 1). Thus, the stress state of the inclusion will be different from the hydrostatic case, and it cannot be characterized by a single "pressure" value (Anzolini et al. 2018). Furthermore, the shifts of Raman mode frequencies under deviatoric stress are unknown in general. The limited experimental evidence (e.g. Briggs and Ramdas 1977) is that the Raman modes change differently from those measured under hydrostatic pressure. Therefore, the key question remains that posed by Korsakov et al. (2010), can shifts of Raman modes measured in hydrostatic experiments be used to interpret the Raman shifts from an inclusion under non-hydrostatic stress? And what errors does this introduce into estimates of inclusion stress and entrapment conditions?

Since it is challenging to perform experiments under controlled deviatoric stress conditions, we have performed *ab initio* Hartree-Fock/Density Functional Theory (HF/DFT) calculations to determine how the Raman modes of quartz change under both hydrostatic pressure and deviatoric stress conditions. We show how the HF/DFT simulations can be used to determine the strains (and by inference the stresses) within a crystal inclusion via mode Grüneisen tensors and measurement of its Raman shifts.
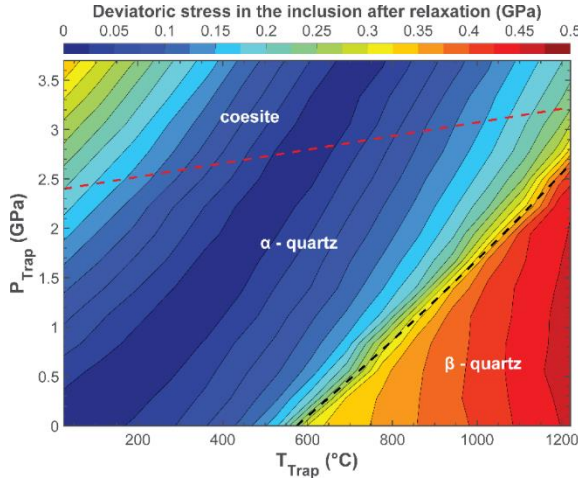
Figure 1. Deviatoric stress $|\sigma_1 - \sigma_3|$ in a quartz inclusion in a pyrope garnet (where σ_1 and σ_3 are parallel to the *a* and *c* axes in quartz, respectively) at room conditions as a function of *P* (GPa) and *T* (°C) of entrapment. The EoS of quartz and pyrope are from Angel et al. (2017) and Milani et al. (2015). The anisotropic relaxation was calculated using the elastic tensors for quartz and pyrope (Sinogeikin and Bass 2002; Lakshtanov et al. 2007).

GRÜNEISEN TENSOR AND STRAINS

It is well known that when stresses are applied to a crystal, for example by changing the pressure, the phonon wavenumbers are shifted. This is most easily seen in the change in Raman peak positions measured under hydrostatic pressure. The shifts of certain modes of materials (e.g. the 464 cm^{-1} mode of quartz) have frequently been used as secondary pressure standards. However, there is a common misconception that the observed wavenumber shifts of the Raman-active modes are directly related to the magnitude of the applied pressure or stress. If that were true, then Raman modes would not show a change in wavenumber when the temperature of a free crystal is changed at ambient pressure. Instead, Raman modes generally exhibit a decrease in wavenumber as temperature is increased. As Figure 2 shows, the shift of the 464 cm^{-1} mode of quartz with both pressure and temperature shows the same dependence upon volume. These observations point to the correct interpretation that the shift $\Delta\omega$ of the wavenumber ω of a vibrational mode is primarily due to the strains of the crystal induced by the applied temperature or pressure. Thus, the Raman peak position of a crystal under a strain $\boldsymbol{\varepsilon}$ (i.e. the full strain tensor) is determined by the second-rank symmetric tensor: the mode Grüneisen tensor $\boldsymbol{\gamma^m}$ (Ziman 1960, Key 1967, Cantrell 1980) characteristic of each phonon mode *m*, which can be written in Voigt (1910) notation as:

$$\frac{-\Delta\omega}{\omega} = \gamma_1^m \varepsilon_1 + \gamma_2^m \varepsilon_2 + \gamma_3^m \varepsilon_3 + \gamma_4^m \varepsilon_4 + \gamma_5^m \varepsilon_5 + \gamma_6^m \varepsilon_6 \tag{(1)}$$

This equation means that the changes in the Raman peak positions in general depend on all the components of the strain tensor (see Supplementary material, Appendix IV), not just on the

relative change in the volume (i.e. $\varepsilon_1 + \varepsilon_2 + \varepsilon_3$). Because the mode Grüneisen tensor is a symmetric second-rank property tensor, it is subject to the same symmetry constraints on its component values as other second-rank property tensors, such as the thermal expansion and compressibility tensors. For the trigonal symmetry of quartz $\gamma_1^m = \gamma_2^m \neq \gamma_3^m$, and $\gamma_4^m = \gamma_5^m = \gamma_6^m = 0$. Garnet is almost elastically isotropic (Sinogeikin and Bass 2002) so the strain imposed by the garnet host does not break the symmetry of the quartz inclusion. Therefore, we are interested specifically in the cases when $\varepsilon_1 = \varepsilon_2$, for which the shift in the phonon wavenumbers should be given by:

$$\frac{-\Delta\omega}{\omega} = 2\gamma_1^m \varepsilon_1 + \gamma_3^m \varepsilon_3 \tag{(2)}$$

To determine the values of γ_1^m and γ_3^m independently of one another it is not sufficient to measure the Raman shifts under hydrostatic pressure, because only a single series of values of ε_1 and ε_3 are measured. We, therefore, use HF/DFT simulations to calculate the Raman modes at different imposed strains on the crystal to determine its structure and properties at those strains.
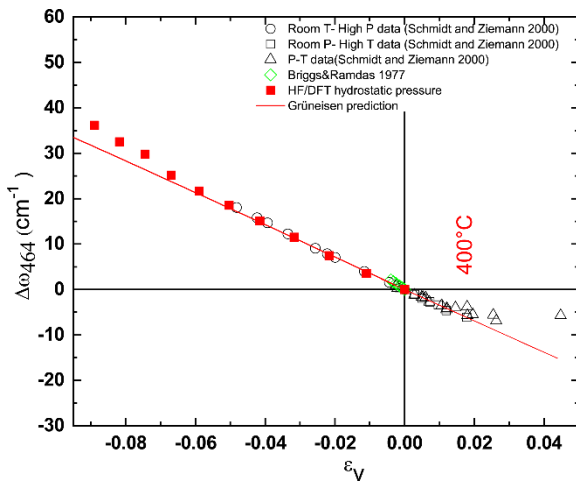
Figure 2. The wavenumber shift ($\Delta\omega$) of the 464 cm^{-1} mode of a free quartz crystal measured under different P, T and stress conditions form a single trend with volume strain ε_V. The deviation at positive strains is caused by the transition from α to β quartz that occurs at 573°C. Away from the transition, the experimental data are reproduced by both the HF/DFT simulations under hydrostatic pressure (red filled squares), and the prediction from the mode Grüneisen parameters (line).

RAMAN SHIFTS AND STRAINS FROM AB INITIO CALCULATIONS

Ab initio HF/DFT simulations have been performed by means of CRYSTAL 14 code (Dovesi et al. 2014) employing the hybrid Hamiltonian WC1LYP (Wu and Cohen 2006) that has been demonstrated to be particularly suitable for the accurate reproduction of the elastic and

vibrational properties (Zicovich-Wilson et al. 2004; Prencipe et al. 2014). Further computational details are reported in the Supplementary material (Appendix IV).

We will only discuss in detail the Raman-active modes near 464 cm^{-1} (non-degenerate A_1 mode) and 696 cm^{-1} (doubly degenerate E mode) because they give peaks in the Raman spectra that are easily resolved from the peaks of the host garnets. Note that all E modes in quartz are polar, and therefore have longitudinal optical (LO) and transverse optical (TO) components that generate two separate Raman peaks, whose intensity ratio varies depending on the scattering geometry. Because of the polarization mixing (Loudon 1964), the wavenumber of the LO component depends on the angle between the triad axis of quartz and the phonon-propagation direction that in the case of backscattering geometry coincides with the direction of the laser beam. For the E mode of interest in this study, the LO-TO splitting is small. At ambient conditions ω_{ETO} = 696 cm^{-1}, while the maximum ω_{ELO} ~ 697.5 cm^{-1} and it corresponds to the case when the **c** axis is perpendicular to the laser beam. The two components are thus very close to each other and in specific experimental geometries may generate peaks of similar intensity. To avoid possible contribution from the LO component that may lead to a subtle artificial shift of the corresponding Raman peak toward higher wavenumbers, one should either rotate the sample about the direction of the laser beam to verify that the peak position does not change, or find the orientation at which the wavenumber of the Raman peak is lowest (which should be when the **c** axis is perpendicular to the polarization of the incident light).

Figure 3a and 3b are contour maps that display the HF/DFT wavenumber shifts of the A1 mode near 464 cm^{-1} and ETO mode near 696 cm^{-1} as a function of the two independent strain components. For small strains (close to the origin) the iso-shift lines are parallel to one another and equally spaced, confirming that the values of γ_1^m and γ_3^m are constants over these strain ranges. The contour lines for the two modes have different slopes (e.g Figure 3a, 3b, and 3c) indicating that the values of their Grüneisen components are different. Further, Figure 3a shows that the iso-shift lines are not parallel to isochors which are represented by lines of equal volume strain [$\varepsilon_V = 2\varepsilon_1 + \varepsilon_3$]. If the wavenumber shifts are plotted against the stress components σ_1 and σ_3 (Fig. S4 Supplemental material) then the iso-shift lines are not parallel to isobars [lines of constant pressure $(2\sigma_1 + \sigma_3)/3 = -P$]. Therefore, in general, Raman shifts do not measure either volume or pressures; for uniaxial crystals like quartz, they indicate the principal normal strain components ε_1 and ε_3. The Grüneisen tensor components for all modes were then determined by fitting Equation 2 by

least-squares to the wavenumber shifts at different strain states simulated by HF/DFT calculations. For the 464 mode, the maximum misfit was $1.76\ \mathrm{cm}^{-1}$ (see Supplemental material for residual plots and full details).

HF/DFT calculations are performed under static stress at absolute-zero temperature. Inclusions are measured at room temperature. To use the mode Grüneisen tensors to determine strains in inclusions, one has to also demonstrate that their values are independent of P and T. This is equivalent to the solid behaving according to the quasi-harmonic approximation (QHA). We achieve this by calculating the strains of a free quartz crystal relative to room conditions from the known unit-cell parameter variation of quartz (Angel et al. 2017) with P and T. We then compare the wavenumber shifts from room-condition values using the Grüneisen components (γ_1^m and γ_3^m) for the two modes at $464\ \mathrm{cm}^{-1}$ and $696\ \mathrm{cm}^{-1}$ (i.e. 0.60 and 1.19; 0.50 and 0.36) determined by HF/DFT and Equation 2 with experimental data. The line in Figure 2 shows that for the mode near $464\ \mathrm{cm}^{-1}$ the experimentally measured wavenumber shifts under high pressure at room T and those up to ~ 400°C at room P are reproduced by the Grüneisen components determined by HF/DFT. At higher temperatures, the predicted shifts differ from the experimental data because of pre-transition effects associated with the α-β quartz transition that cannot be accounted using QHA. Furthermore, the fundamental soft mode near $206\ \mathrm{cm}^{-1}$, which is heavily involved in the temperature α- to β-quartz phase transition (Scott 1968), clearly violates the QHA, and HF/DFT simulations cannot be used to determine the mode Grüneisen components. In order to use this band to determine strains in inclusions, the variation of its position with strain must be determined experimentally.
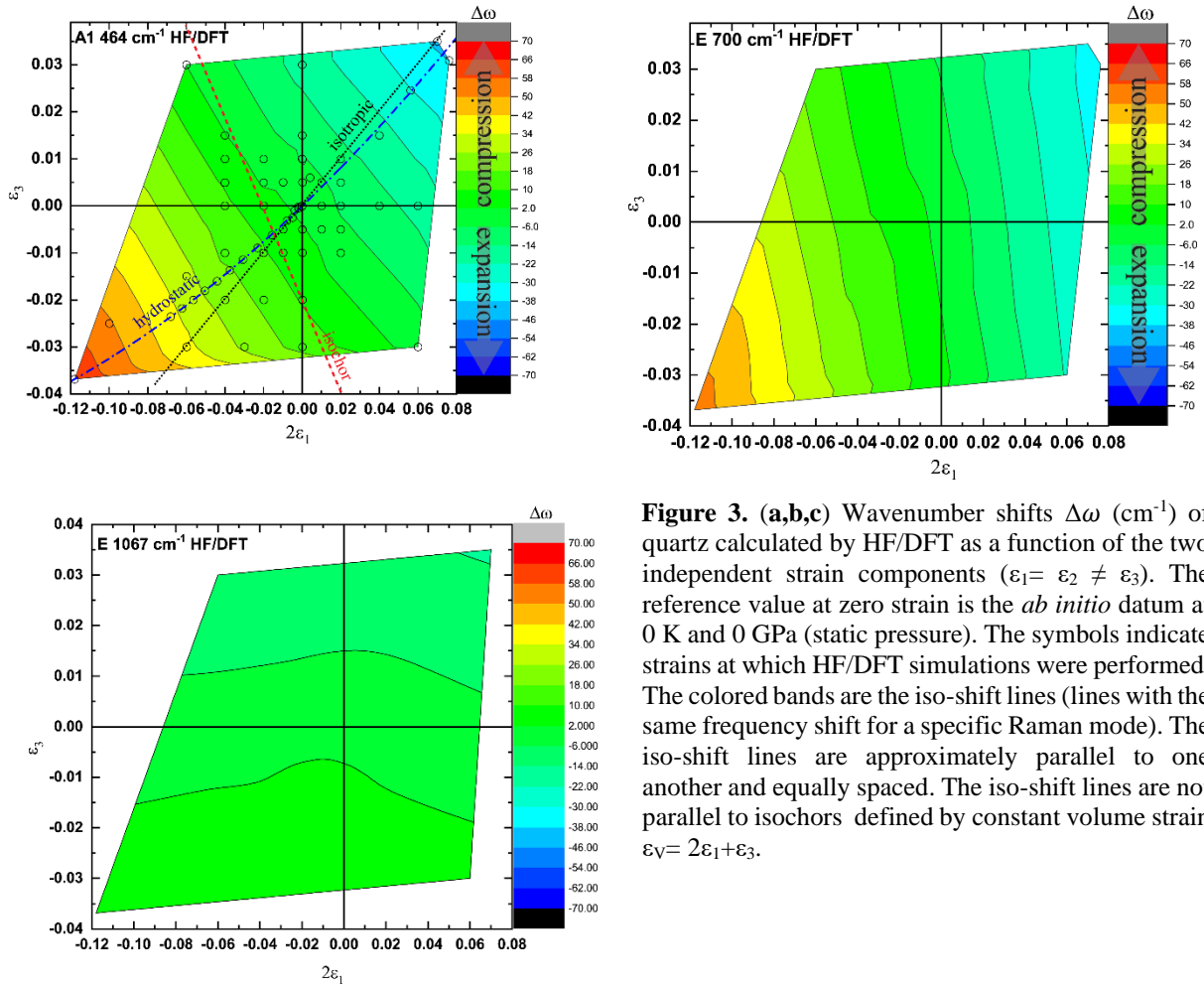
Figure 3. (**a,b,c**) Wavenumber shifts $\Delta\omega$ (cm^{-1}) of quartz calculated by HF/DFT as a function of the two independent strain components ($\varepsilon_1 = \varepsilon_2 \neq \varepsilon_3$). The reference value at zero strain is the *ab initio* datum at 0 K and 0 GPa (static pressure). The symbols indicate strains at which HF/DFT simulations were performed. The colored bands are the iso-shift lines (lines with the same frequency shift for a specific Raman mode). The iso-shift lines are approximately parallel to one another and equally spaced. The iso-shift lines are not parallel to isochors defined by constant volume strain $\varepsilon_V = 2\varepsilon_1 + \varepsilon_3$.

VALIDATION FROM RAMAN SCATTERING AND X-RAY DIFFRACTION

To validate this approach, we performed micro-Raman spectroscopy and X-ray diffraction measurements on quartz inclusion in garnet from a diamond-grade eclogite xenolith (TM90-1) from the Mir kimberlite pipe (Yakutiya). We selected this example as it has the highest Raman shifts reported for quartz inclusions in garnet (Korsakov et al. 2009; Zhukov and Korsakov 2015). Parallel polarized Raman spectra were collected in backscattering geometry with a Horiba Jobin-Yvon T64000 triple-monochromator spectrometer (spectral resolution of ~2 cm^{-1}, instrumental accuracy in peak positions of ~0.35 cm^{-1} and 2μm spot size) following the same protocol reported in Campomenosi et al. (under review). Figure 4 shows that the shift of the 464 cm^{-1} Raman line changes significantly across the crystal as a consequence of edge and corner effects (Campomenosi et al. under review and Mazzucchelli et al. 2018), and is lowest at the center of the inclusion. We

determined the unit-cell parameters of the inclusion by single crystal X-ray diffraction measurements using the 8-position centering method (SINGLE, Angel and Finger 2011) using a newly developed Huber 4-circle Eulerian cradle diffractometer equipped with point detector and microfocus source (120 μm spot size). The difference between the unit cell parameters of the inclusion a = 4.86669(44) Å, c = 5.35408(14) Å and those of a free crystal measured on the same instrument [a = 4.91160(7) Å, c = 5.40325(9) Å] shows that the inclusion is under strains ε_1= -0.00914(9), ε_3= -0.00910(26), and ε_V =-0.02714(30). Relative to room conditions the quartz inclusion is currently under isotropic strain within the experimental uncertainties. From these strains and the Grüneisen-tensor components for the mode near 464 cm^{-1} (i.e. γ_1^{464}= 0.60 and γ_3^{464} =1.19), we calculate an expected wavenumber shift of 10.12 cm^{-1}. This is between the minimum and maximum shifts actually measured on the inclusion (Figure 4) because the unit-cell parameters measured by X-ray diffraction are an average over the entire volume of the inclusion. Conversely, if we take the shifts of the Raman modes near 464 and 696 cm^{-1} measured at the center of the inclusion and the calculated mode Grüneisen components we predict the following strains: ε_1= -0.0093(5) and ε_3= -0.0070(5). In this case the total strain that is lower than that measured by X-ray diffraction, again because this method provides an average over the inclusion.
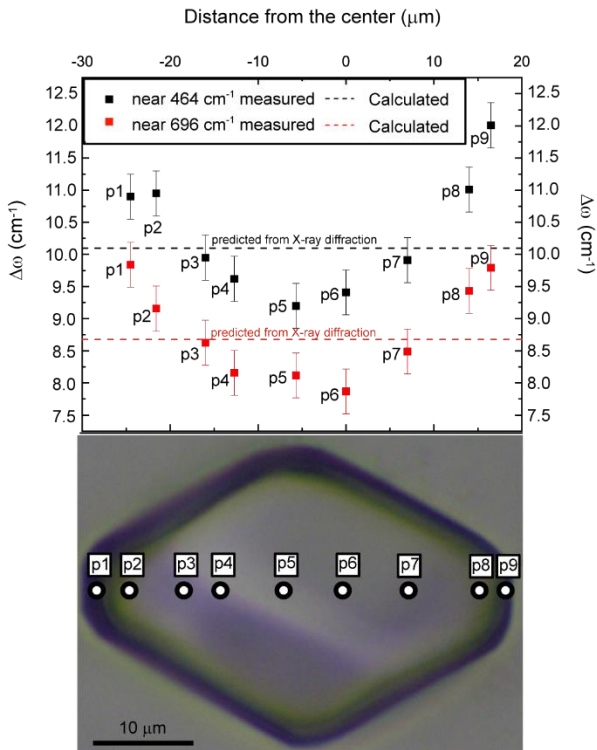
Figure 4. Wavenumber shifts of the 464 cm^{-1} and 696 cm-1 modes measured in a traverse across a quartz inclusion in pyrope from the eclogite xenolith TM90-1 (Korsakov et al.2009). The phonon wavenumber shifts calculated from the strains determined by X-ray diffraction and the mode Grüneisen tensor are in good agreement with the average of the measured shifts.

IMPLICATIONS

We have demonstrated by a combination of HF/DFT simulations and comparison to experimental Raman data that quartz has some Raman-active modes whose wavenumbers are only a function of strain (for small strains) and are not directly dependent on P and T. The HF/DFT simulations show also that in general the shift of a Raman line does not indicate either the volume change (or volume strain) or the mean normal stress but is a more complex function of the linear strains (Figure 3). The linear strains of a quartz inclusion can be determined from the wavenumber shifts of at least two Raman peaks by using the mode Grüneisen components determined by HF/DFT. Conversely, a wavenumber shift for a specific Raman-active mode can be determined from the linear strains measured by X-ray diffraction and by using the mode Grüneisen components determined by HF/DFT. We proved that strains and Raman shifts vary significantly across an inclusion (Figure 4) as a result of the influence of shape combined with elastic anisotropy (Mazzucchelli et al. 2018, Campomenosi et al. under review), and should never be averaged. The Raman shifts measured in the center of inclusions are least affected by the presence of edges and should be the only ones used to infer, after shape corrections (Mazzucchelli et al. 2018), the entrapment conditions. On the other hand, X-ray diffraction measurements give strain components that are averaged over the entire volume of the investigated crystal. For the example discussed, the interpretation of wavenumber shift of the mode near 464 cm^{-1} measured at the center of the quartz inclusion with the hydrostatic calculation (Schmidt and Ziemann 2000) leads to only a small error in the estimation of the mean normal stress (i.e. pressure) of ca. 0.03 GPa. This would lead to an error in the calculated entrapment pressure of 0.06 GPa. However, this is not always the case. When the deviatoric stress (Figure 1) in the inclusion is higher, the error is larger. For example, a quartz inclusion in garnet reset at 1.5 GPa and 1100°C during exhumation will have a wavenumber shift of the Raman mode near 464 cm^{-1} that would yield an entrapment pressure of 0.6 GPa too low when the hydrostatic calibration is used. In anisotropic hosts the discrepancy from the hydrostatic calibration also depends on the relative orientation of the host and inclusion. For example, for quartz in zircon the error in the calculated entrapment pressure can vary from 0.2 to 0.6 GPa for the same entrapment condition (i.e. 0.3 GPa and 800°C) depending on orientation.

Acknowledgments

References

Angel, R.J., and Finger, L.W. (2011). SINGLE: a program to control single-crystal diffractometers. Journal of Applied Crystallography, 44(1), 247-251.

Angel, R.J., Nimis, P., Mazzucchelli, M.L., Alvaro, M., and Nestola, F. (2015). How large are departures from lithostatic pressure? Constraints from host–inclusion elasticity. Journal of Metamorphic Geology, 33(8), 801-813.

Angel, R.J., Alvaro, M., Miletich, R., and Nestola, F. (2017). A simple and generalised P–T–V EoS for continuous phase transitions, implemented in EosFit and applied to quartz. Contributions to Mineralogy and Petrology, 172(5), 29.

Anzolini, C., Prencipe, M., Alvaro, M., Romano, C., Vona, A., Lorenzon, S., Smith, E.M., Brenker F.E., and Nestola, F. (2018). Depth of formation of super-deep diamonds: Raman barometry of $CaSiO_3$-walstromite inclusions. American Mineralogist, 103(1), 69-74.

Briggs, R.J., and Ramdas, A.K. (1977). Piezospectroscopy of the Raman spectrum of α-quartz. Physical Review B, 16(8), 3815.

Cantrell Jr, J.H. (1980). Generalized Grüneisen tensor from solid nonlinearity parameters. Physical review B, 21(10), 4191.

Civalleri, B., D'Arco, P., Orlando, R., Saunders, V., and Dovesi, R. (2001) Hartree–Fock geometry optimisation of periodic systems with the CRYSTAL code. Chemical Physics Letters, 348, 131–138.

Dovesi, R., Orlando, R., Erba, A., Zicovich-Wilson, C.M., Civalleri, B., Casassa, S., Maschio, L., Ferrabone, M., De La Pierre, M., D'Arco, P. and Noël, Y. (2014). CRYSTAL14: A program for the *ab initio* investigation of crystalline solids. International Journal of Quantum Chemistry, 114(19), 1287-1317.

Key, S.W. (1967). Grüneisen tensor for anisotropic materials. Journal of Applied Physics, 38(7), 2923-2928.

Korsakov, A.V., Perraki, M., Zhukov, V.P., De Gussem, K., Vandenabeele, P., and Tomilenko, A.A. (2009). Is quartz a potential indicator of ultrahigh-pressure metamorphism? Laser Raman spectroscopy of quartz inclusions in ultrahigh-pressure garnets. European Journal of Mineralogy, 21(6), 1313-1323.

Korsakov, A.V., Zhukov, V.P., and Vandenabeele, P. (2010). Raman-based geobarometry of ultrahigh-pressure metamorphic rocks: applications, problems, and perspectives. Analytical and bioanalytical chemistry, 397(7), 2739-2752.

Kuzmany, H. (2009) Solid-State Spectroscopy, An Introduction, second edition, cap-9, p. 185–200. Springer. doi: 10.1007/978-3-642-01479-6.

Lakshtanov, D.L., Sinogeikin, S.V., and Bass, J.D. (2007). High-temperature phase transitions and elasticity of silica polymorphs. Physics and Chemistry of Minerals, 34(1), 11-22.

Loudon, R. (1964). The Raman effect in crystals. Advances in Physics, 13(52), 423-482.

Mazzucchelli, M.L., Burnley, P., Angel, R.J., Morganti, S., Domeneghetti, M.C., Nestola, F., and Alvaro, M. (2018). Elastic geothermobarometry: Corrections for the geometry of the host-inclusion system. Geology, 46(3), 231-234.

Milani, S., Nestola, F., Alvaro, M., Pasqual, D., Mazzucchelli, M.L., Domeneghetti, M.C., and Geiger, C.A. (2015). Diamond–garnet geobarometry: The role of garnet compressibility and expansivity. Lithos, 227, 140-147.

Prencipe, M., Maschio, L., Kirtman, B., Salustro, S., Erba, A., and Dovesi, R. (2014). Raman spectrum of NaAlSi2O6 jadeite. A quantum mechanical simulation. Journal of Raman Spectroscopy, 45(8), 703-709.

Schmidt, C., and Ziemann, M.A. (2000). In-situ Raman spectroscopy of quartz: A pressure sensor for hydrothermal diamond-anvil cell experiments at elevated temperatures. American Mineralogist, 85(11-12), 1725-1734.

Scott, J.F. (1968) Evidence of coupling between one- and two-phonon excitations in quartz. Physical Review Letters, 21(13) 907-910.

Sinogeikin, S.V., and Bass, J.D. (2002). Elasticity of majorite and a majorite-pyrope solid solution to high pressure: Implications for the transition zone. Geophysical Research Letters, 29(2).

Voigt W. Lehrbuch der Kristallphysik (B. G. Teubner. Berlin. 1910). p.754.

Wu, Z., and Cohen, R.E. (2006) More accurate generalized gradient approximation for solids. Physical Review B, 73, 235116.

Zhukov, V.P., and Korsakov, A.V. (2015). Evolution of host-inclusion systems: a visco-elastic model. Journal of Metamorphic Geology, 33(8), 815-828.

Zicovich-Wilson, C.M., Pascale, F., Roetti, C., Saunders, V.R., Orlando, R., and Dovesi, R. (2004). Calculation of the vibration frequencies of α-quartz: The effect of Hamiltonian and basis set. Journal of Computational Chemistry, 25(15), 1873-1881.

Ziman, J.M. (1960). Electrons and phonons: the theory of transport phenomena in solids. Oxford University Press. p.469

4. THE EFFECTS OF NON-HYDROSTATIC STRESS ON THE STRUCTURE AND PROPERTIES OF ALPHA-QUARTZ

Mara Murri[1], Matteo Alvaro[1], Ross J. Angel[1], Mauro Prencipe[2], Boriana D. Mihailova[3]

[1]*Department of Earth and Environmental Sciences, University of Pavia, Via A. Ferrata, 1 I-27100 4 Pavia, Italy*
[2]*Earth Sciences Department, University of Torino, Via Valperga Caluso 35 Italy*
[3]*Department of Earth Sciences, University of Hamburg, Grindelallee 48, D-20146 Hamburg, Germany*

ABSTRACT

The study of the effects of non-hydrostatic stresses on rock-forming minerals is fundamental for understanding how minerals respond to tectonic stresses in the Earth's interior. Larger deviatoric stresses of the order of GPa can arise from physical interaction between minerals (e.g. host-inclusion systems, compositional gradients) at the micrometric scale, even if at the large-scale large stresses are annealed by plastic flows. Thus, experimental data under hydrostatic pressure do not provide us access to all the possible modifications and structural changes experienced by minerals subjected to deviatoric stresses.

Therefore, we carried out *ab initio hybrid* Hartree-Fock/Density Functional Theory simulations to determine the properties of alpha quartz, since it is one of the most abundant minerals in the Earth's crust with a very simple chemistry and structure. We calculated its structure, elastic parameters and Raman-active vibrational modes as a function of different applied strains, which allow us to show how phonon frequencies and structural parameters (bond lengths and angles) are affected by deviatoric stress conditions rather than hydrostatic pressure.

Keywords: quartz, deviatoric stress, Grüneisen tensor, Raman spectroscopy, *ab initio* HF/DFT

INTRODUCTION

The majority of in-situ high-pressure experiments in mineral physics attempt to measure mineral properties or structure under stress conditions that are, or approximately are, hydrostatic by immersing the sample in a fluid pressure medium. The motivations are several. Deviatoric stresses are very difficult to characterize because, in contrast to a hydrostatic pressure, they require determination of three principal stress components. Further, it is believed that the temperatures within the Earth below the crust are sufficiently high to allow plastic flow to dissipate deviatoric

stress much quicker than geological or tectonic timescales, so that the stress experienced by minerals in most of the Earth is effectively hydrostatic.

Nonetheless, there are several reasons to characterise the behaviour of crystals under deviatoric stresses. Not least because the question of the free energy of a solid under deviatoric stress is poorly defined (e.g. Gibbs 1875, avoided this issue) and the effects of non-hydrostatic stress on phase equilibria are controversial (e.g. Hobbs and Ord 2016; Wheeler 2014, 2018). There is experimental evidence that the equilibrium boundary of reconstructive phase transitions such as quartz to coesite can be shifted by several kbar by deviatoric stress (e.g. Hirth and Tullis 1994; Richter et al. 2016). The importance of deviatoric stress has certainly long been recognized in the study of phase transitions involving symmetry-breaking strains, where they can shift equilibrium transition temperatures at the rate of thousands of K per kbar (Bismayer et al. 1982). And shear stress has been shown to promote the inversion of orthoenstatite to clinoenstatite (Coe and Kirby 1975; Clément et al. 2018) and transformations in many other minerals (e.g. Kirby and Stern 1993). Such stresses do not have to originate externally from the rock as tectonic forces; sub-GPa levels of deviatoric stress can certainly develop even in monomineralic rocks as a result of grain-grain contacts and space constraints when the P or T of the rock unit is changed. And GPa levels of deviatoric stress can arise within single crystals as a result of compositional gradients and be supported without cracking or plastic flow (e.g. Scheidl et al. 2014).

The simplest example of a system that gives rise to deviatoric stresses is that of an isolated inclusion in a host mineral. An inclusion entrapped in an isotropic host such as garnet will be subject to isotropic strains. If it is elastically isotropic it will therefore exhibit equal stresses in all directions, and it will be under hydrostatic pressure. Thus, the behaviour of the inclusion will be the same as for a crystal in a fluid pressure medium, and the measured pressure in the inclusion can then be used to constrain the conditions of P and T under which it was entrapped (e.g. Rosenfeld and Chase 1961; Zhang 1998; Angel et al. 2014b). In contrast, if the inclusion is elastically anisotropic then it must develop anisotropic (i.e. deviatoric) stresses, and it cannot be characterized by a single "pressure" datum (e.g. Anzolini et al. 2018; Nestola et al. 2018). Further, because the effects of deviatoric stress on the bond lengths and angles of the inclusion mineral are, in general, unknown, the shifts of phonon frequencies under deviatoric stress are also unknown in general. The limited evidence (e.g. Briggs and Ramdas 1977; Gallivan and Gupta 1995; Korsakov et al. 2009) is that the Raman-peak positions change differently from under hydrostatic pressure.

The experimental generation and measurement of controlled deviatoric stress states is challenging. Therefore, we have performed *ab initio hybrid* HF/DFT (Hartree-Fock/Density Functional Theory) calculations to determine how the crystal structure, lattice parameters and phonon frequencies of quartz change under both hydrostatic pressure and deviatoric stress conditions. Quartz is an ideal candidate for exploring the general issues because it is a structurally-simple framework and it is one of the most common inclusion minerals found in metamorphic rocks. Its properties as a function of *P* and *T* have been determined many times with a variety of techniques (Raman spectroscopy; X-ray and neutron diffraction; Brillouin spectroscopy) which can provide a basis for validating our HF/DFT results under hydrostatic conditions. We explore how the structure, properties, and vibrational modes change under deviatoric stress conditions by mapping how they change with the imposed state of strain. While *ab initio* HF/DFT simulations are internally precise to an arbitrary level, the importance of our calculations is not in the attempt to closely reproduce the experimental results under hydrostatic conditions, but to use them as a tool to predict and understand the real behaviour of minerals under conditions of deviatoric stress that are ubiquitous in rocks.

METHODS

Computational methods

Ab initio hybrid HF/DFT simulations have been performed with the CRYSTAL14 code (Dovesi et al. 2014) by employing the WC1LYP functional which is particularly suitable for the correct reproduction of the elastic and vibrational properties of crystals (e.g. Prencipe 2012, 2018; Stangarone et al. 2016). The WC1LYP functional is based on the generalized gradient approximation (GGA) exchange functional WC (Wu and Cohen 2006), mixed with 16% of the exact non-local Hartree–Fock exchange. The functional also includes the LYP correlation contribution (Lee et al. 1988). The grid for the numerical evaluation of the DFT exchange–correlation functionals was chosen by the keyword XLGRID of the CRYSTAL14 user manual (Dovesi et al. 2014) and corresponds to a total of 37,547 points in the unit cell. A measure of the numerical accuracy provided by such a grid is the evaluation of the total number of electrons in the unit cell, by the numerical integration of the electron density over the cell volume. For quartz, we obtained 90.00003 electrons out of 90 for the reference volume at the *static limit* (no zero point and thermal pressures due to vibrational effects included; see Prencipe et al. 2011) and at a pressure of 0 GPa. The localized *contracted* atomic basis sets used were Si 86-311G** (Pascale et al. 2005)

and 8-411G(2d) (Valenzano et al. 2006) for Si and O, respectively, which have been successfully employed to calculate *ab initio* structures and properties of silicates (e.g. Stangarone et al. 2017). Within the CRYSTAL code, the accuracy in evaluating the Coulomb and Hartree-Fock exchange series is controlled by the keyword TOLINTEG, for which we set the five parameters to 8 (T1, T2, T3 and T4) and 18 (T5) (Dovesi et al. 2014). The diagonalization of the Hamiltonian matrix was performed at 7 independent *k* vectors in the reciprocal space (Monkhorst net; Monkhorst and Pack 1976) by setting to 3 the shrinking factor IS (Dovesi et al. 2014). Cell parameters and fractional coordinates were optimized by analytical gradient methods, as implemented in CRYSTAL14 (Civalleri et al. 2001; Dovesi et al. 2014). Geometry optimization was considered converged when each component of the gradient (TOLDEG parameter in CRYSTAL14) was smaller than 0.00003 Hartree/Bohr and displacements (TOLDEX) were smaller than 0.00012 Bohr with respect to the previous step. Lattice parameters and fractional coordinates were optimized at the WC1LYP level (at the static limit), at pressures from 0 to 10 GPa (with step of 0.5 GPa from 0 to 5 GPa and then a simulation at 10 GPa) using the keyword EXTPRESS. For the non-hydrostatic simulations, the cell parameters were fixed at the chosen strain conditions and only the fractional coordinates were optimized with the keyword ATOMONLY (Civalleri et al. 2001; Dovesi et al. 2014).

Vibrational wavenumbers of all of the normal modes were calculated at the Γ point within the limit of the harmonic approximation, by diagonalizing a mass-weighted Hessian matrix, whose elements are the second derivatives of the full potential of the crystal with respect to the mass-weighted atomic displacements (Pascale et al. 2004). Structural and vibrational data at 0 GPa, at the static limit, are reported in the deposited crystallographic information file (*cif*) that contains the results of all of the simulations that we performed.

The space group symmetry of α-quartz, SiO_2, is P3$_2$21with a primitive unit cell containing 9 atoms. This gives rise to 27 crystal normal phonons in α-quartz, three of which are acoustic phonons and have zero wavenumber at the Brillouin-zone centre. Hence, the representation of the remaining 24 optic phonons at the center of the Brillouin zone is:

$$\Gamma_{opt} = 4A_1 + 4A_2 + 8E \qquad\qquad (1)$$

The A_1 modes are non-polar and only Raman-active, A_2 modes are only infrared-active, while the doubly degenerate E ones are polar and both Raman- and infrared-active, and therefore exhibit transverse optic (TO) and longitudinal optic (LO) components.

To calculate the properties of quartz at finite temperatures from the results of the HF/DFT simulations at the static limit, we used the quasi-harmonic approximation (QHA) to calculate both the zero-point and isotropic thermal pressure contributions to the total pressure at P and T (see Prencipe et al. 2011). We use the isotropic mode Grüneisen parameters $\boldsymbol{\gamma^m}$ calculated for every optic phonon mode "m" at every unit cell volume, expressed as:

$$\gamma^m = -\frac{V}{\omega_0^m}\frac{\partial\omega^m}{\partial V} \tag{2}$$

where ω^m is the frequency of a single normal phonon mode m and V is the unit-cell volume. In this calculation we only have access to the mode frequencies at the Brillouin zone centre from the HF/DFT simulations and so we cannot include the effects of frequency dispersion across the Brillouin zone. The total pressure P for the crystal is given within the QHA as a sum of three contributions over all of the phonon modes (e.g. Anderson 1995):

$$P = -(\frac{\partial E_{st}}{\partial V})_T + \frac{1}{2V}\hbar\Sigma\omega^m\gamma^m + \frac{kT}{V}\Sigma\gamma^m\frac{\hbar\omega^m/kT}{e^{\hbar\omega^m/kT}-1} \tag{3}$$

The first term is the static pressure, which is the derivative of the internal static energy E_{st} with respect to volume at 0 K, and the second term is the zero-point pressure, which accounts for vibrations that are active at 0 K. The third term is the thermal pressure. It is zero at 0 K and increases with increasing temperature because amplitudes of atomic vibrations increase as temperature increases, which effectively increase the number of phonons. The assumption of QHA is that phonon frequencies do not change along the isochors, an issue that we explore in this paper. Given that quartz exhibits the α - β transition that involves significant mode softening as well as multi- phonon coupling (Shapiro et al. 1967), it provides a stringent test of the applicability of the QHA.

Raman spectroscopic measurements

The complete Raman spectrum of quartz was measured as a function of temperature from 110 K to 1100 K in order to provide a validation of the Raman frequencies obtained from the HF/DFT simulations. Raman scattering experiments were conducted with a Horiba Jobin–Yvon S.A.S. T64000 triple-monochromator spectrometer (holographic 1800 grooves/mm gratings) equipped with an Olympus BX41 confocal microscope (Olympus LM Plan FLN 50 × objective with a numerical aperture of 0.5) and a Symphony liquid-N_2-cooled charge-coupled device detector on a gem quality crystal of quartz with a thickness of 1mm and properly cut to collect

separately A_1, E(LO) and E(TO) Raman-active modes. Raman spectra were excited by the green line (λ = 514.532 nm) of a Coherent 90C Fred Ar^+ laser to ensure minimal photoluminescence background. The spectrometer was calibrated to the T_{2g} mode at 520.5 cm^{-1} of a Si wafer. The spectral resolution was ~2 cm^{-1} and the instrumental accuracy in determining the peak positions was ~0.35 cm^{-1}.

Polarized Raman spectra were collected in *-x(zz)x*, *x(yz)x* and *-z(yx)z* scattering geometry (Porto's notation; Scott and Porto 1967), with *z* along the crystallographic **c** axis, to collect A_1, E(LO) and E(TO) modes, respectively. Measurements were carried out in the temperature range 110–700 K using a Linkam THMS600 heating/cooling stage and a TMS94 temperature controller. For all experiments, the sample chamber was purged with N_2 gas to avoid freezing of atmospheric water on the sample at low temperatures. In addition, the Raman spectra at temperatures from 300K up to 1100 K were collected in air using a Linkam TS1200 heating stage and a T95 temperature controller. For all measurements, the sample was kept for 5 minutes at the desired experimental temperature before the data collection was started to ensure that there was no thermal gradient across the crystal. The acquisition time was chosen to yield a satisfactory signal-to-noise ratio, and thus the spectra for A_1 and E(LO) modes were collected for 10–30 s averaging over a minimum of 5 accumulations in the wavenumber range 15-1615 cm^{-1}. The spectra of E(TO) modes were collected for 60 s over a minimum of 6 accumulations in the range 15-1215 cm^{-1}.

The OriginPro® 2018 software package was used for data evaluation. The collected spectra were baseline corrected for the continuum luminescence background, and temperature-reduced to account for the Bose–Einstein distribution function: $I_{reduced} = I_{measured}/(n(\omega, T) + 1)$, $n(\omega, T) = 1/(\exp (\hbar\omega/kT) - 1)$ with ω being the phonon wavenumber, $\hbar$ the reduced Planck's constant, k the Boltzmann constant, and *T* the temperature (Kuzmany 2009), and normalized to the acquisition time. Peak positions, full widths at half maximum (FWHMs), and integrated intensities were determined from fits with pseudo-Voigt functions ($PV = (1 - q) * Lorentz + q * Gauss$, q is the weight coefficient). The criterion for the maximum number of fitted peaks was $\Delta I < I/2$ with I and ΔI being the calculated magnitude and uncertainty of each peak intensity. In particular, an asymmetry of the strongest A_1 peak in quartz (wavenumber mode near 464 cm^{-1}) can be just detected even at room temperature but is negligibly small. The asymmetry increases with temperature, suggesting that it is a result of multi-phonon scattering. Therefore, the fitting procedure on this peak was carried out with the introduction of an additional peak near 490 cm^{-1}

with a position fixed to the sum of ω_1 (2nd order peak near 145 cm^{-1}) and ω_3 (1st order peak near 355 cm^{-1}) for the *-y (zz)y* scattering geometry.

The Raman wavenumbers measured at 110 K and 300 K are reported in Table 1 along with an estimate of each phonon wavenumber at 0 K obtained by a simple extrapolation against temperature. The values extrapolated to 0 K are close to those from the HF/DFT simulations performed at the static limit and at 0 GPa of pressure. In particular, the agreement between them is better at higher wavenumbers with the largest difference of about 7 cm^{-1} in the lowest-wavenumber mode (i.e. E(TO) 140.5 against 133.1 cm^{-1} and E(LO) 140.5 vs 132.9 cm^{-1}), 2% in the medium-wavenumber region (i.e. from 200-450 cm^{-1}) and around 1% in the high-wavenumber region. Here we reported E(LO) frequencies from HF/DFT to have a comparison with the experimental ones. However, in general, calculated LO frequencies are not as accurate as the TO ones (Pascale et al. 2004): TO frequencies are derived directly from total energy calculations as a function of the nuclear displacements. In contrast, LO frequencies also rely on a further model that takes into account the coupling of the electric field, which is created as the nuclei move along each normal frequency mode, with the electron density of the crystal (to this end, the *ab initio* dielectric and polarizability tensors must be also calculated) Therefore, hereafter, we will not discuss E(LO) frequency modes from the *ab initio* simulations.

Mode	$\omega_{\text{HF/DFT (0K)}}$	$\omega_{0\,K}$	esds	$\omega_{110\,K}$	esds	$\omega_{300\,K}$	esds
Table 1. Wavenumbers (cm^{-1}) of Raman-active modes							
E (TO)	140.5	133.1	0.2	131.4	0.0	128.1	0.0
E (LO)	140.5	132.9	0.1	131.7	0.0	128.5	0.0
A_1	217.9	221.3	0.4	216.3	0.0	207.3	0.0
E(TO)	269.1	267.2	0.2	266.3	0.2	264.3	0.1
E(LO)	271.6	268.3	0.1	267.4	0.0	265.3	0.0
A_1	346.9	354.5	0.1	355.0	0.0	355.7	0.1
E(TO)	391.8	393.9	0.2	394.1	0.1	394.0	0.0
E(LO)	400.3	403.5	0.1	403.4	0.1	403.3	0.1
E(TO)	446.8	454.4	0.8	452.5	0.8	449.7	0.2
E(LO)	506.7	512.8	0.2	512.0	0.1	510.0	0.0
A_1	471.7	468.3	0.2	467.3	0.0	464.8	0.0
E(TO)	699.9	698.8	0.2	697.7	0.3	695.6	0.1
E(LO)	702.7	700.8	0.5	699.5	0.3	698.0	0.2
E(TO)	803.0	799.1	0.4	799.5	1.1	796.7	0.3
E(LO)	817.6	811.3	0.1	810.7	0.1	809.3	0.0
E(TO)	1071.8	1067.2	0.4	1067.1	1.2	1066.5	0.3
E(LO)	1235.4	1231.1	2.4	1229.3	1.3	1231.7	0.6
A_1	1088.8	1083.0	0.1	1083.0	0.1	1082.1	0.2
E(TO)	1165.1	1158.8	1.2	1160.8	0.2	1161.3	0.0
E(LO)	1162.0	1157.6	0.4	1158.1	0.3	1159.0	0.2

Note: $\omega_{\text{HF/DFT (0K)}}$ is from the HF/DFT simulations at 0 K. The ω_{0K} are values extrapolated to 0 K from experimental measurements, ω_{110K} and ω_{300K} are values measured at 110 K and 300 K.

RESULTS
Structure

The lowest temperature at which the structure of SiO_2 quartz has been determined is 20 K, by neutron powder diffraction (Tucker et al. 2001). The mean Si-O bond distance from the HF/DFT simulation at 0 K (at the static limit and P=0 GPa) is longer than that determined experimentally at 20 K by 0.017 Å, of which approximately 0.002 Å can be attributed to the effects of correlated motion on the refined crystal structure, if calculated by the simple rigid bond method (Downs et al. 1992). The remaining discrepancy of 0.015 Å is typical of this flavour of HF/DFT, amounting to about 1%. The simulated structure at $T = 0$ K and $P_{\text{static}} = 0$ GPa also displays the typical underestimate of polyhedral distortion compared to experiments (see also Fischer and Angel 2017) and the combined effect is that the tetrahedral volume in the simulation is 2.3% larger than the experimental measurement at 20 K. This is responsible for the simulated cell volume at $P_{\text{static}} = 0$ GPa also being 2.3% too big. However, because all of the volume error arises from the

overestimation of the SiO_4 volume, the value of Si-O-Si bond angle at low T and its variation with volume under compression (Figure 1) is well-reproduced by the simulations. The difference between the simulations and the bond angles from diffraction measurements at room pressure (red symbols in Figure 1) is the result of the effects of thermal motion in the real structure.
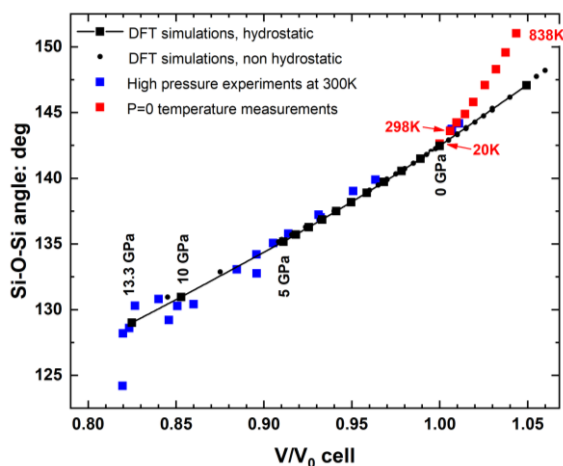
Figure 1. The variation of Si-O-Si bond angle from HF/DFT simulations and experiments (Levien et al. 1980; Hazen et al. 1989; Kihara 1990; Glinnemann et al. 1992; Kim-Zajonz et al. 1999; Tucker et al. 2001). Experimental values of volume are scaled by the experimental value at 20 K (Tucker et al. 2001), and the HF/DFT volumes by the value from the simulation at P_{static} = 0GPa.

The large correlated motions of the atoms in the real structure (the rigid-unit modes) increase with temperature (Dove et al. 1999; Tucker et al. 2001). As a consequence, conventional structure refinements to Bragg diffraction data underestimate the true local bond length and overestimate the true Si-O-Si angle due to a 'swinging -arm' effect (Busing and Levy 1964; Downs et al. 1992; Kihara 2001). This is particularly clear for quartz where the Si-O distances and thus the SiO_4 volumes from traditional structure refinements (Kihara 1990) actually decrease with increasing temperature (Figure 2). By contrast, the simulations at 0 K and $V/V_0 > 1$, which contain no dynamical effects, and the true local bond lengths (Figure 11 in Tucker et al. 2001) determined from total scattering measurements, exhibit no such shortening. This discrepancy of conventional refinement results increases strongly as the α - β phase transition is approached (Figure 2, also Tucker et al. 2001) as a consequence of the increased magnitude of the dynamic displacements of the atoms. Even the behaviour of Si-O bond lengths on compression is very different in the

HF/DFT from the experiments performed at room *T* (Figure 2). While the HF/DFT show a smooth compression with decreasing cell volume, corresponding to a zero-pressure bulk modulus of about 490 GPa, the experiments show much less compression and much more scatter. It may be that this difference, apart from indicating the limited precision of the structure refinements based on experimental diffraction data, is due to the competing effects of direct compression (which would shorten Si-O distances) and the suppression of the rigid unit modes (RUMs) which would lead to an apparent increase of Si-O distances.
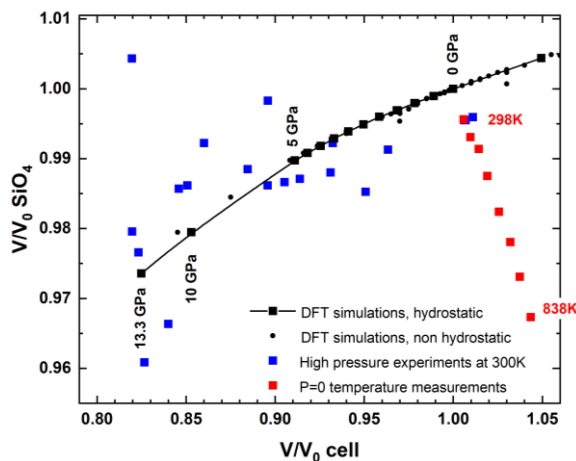
Figure 2. The variation of volume of the SiO$_4$ tetrahedra from HF/DFT simulations and experiments (Levien et al. 1980; Hazen et al. 1989; Kihara 1990; Glinnemann et al. 1992; Kim-Zajonz et al. 1999; Tucker et al. 2001). Experimental values are scaled by the experimental value at 20 K (Tucker et al. 2001), and the HF/DFT volumes by the value from the simulation at $P_{static} = 0$GPa. Note the apparent contraction of the SiO$_4$ tetrahedra with increasing temperature when data are taken from conventional structure refinements.

The precision of the HF/DFT thus allows one to show that the volumes of the tetrahedra are an order-of-magnitude stiffer than the structure as a whole, and that tetrahedral compression only contributes to about 13% of the volume change of the unit cell induced by increasing hydrostatic pressure. As in most framework materials, the majority of the volume compression is accommodated by the changes in the angles at the bridging atoms shared between the relatively rigid polyhedra (Figure 1). The resulting change in the Si-Si distances (Figure 3) provides 87% of the total volume change of quartz. The agreement of Si-Si distances between the high-temperature

experiments and simulations confirms that the differences in SiO_4 volumes and Si-O-Si angles between the HF/DFT simulations and experimental data are the consequence of the librational motion of the O atoms around the Si atoms. Structure refinements return accurate positions for the Si atoms because their thermally induced vibrational motion is much more isotropic and more Gaussian than the O atoms.
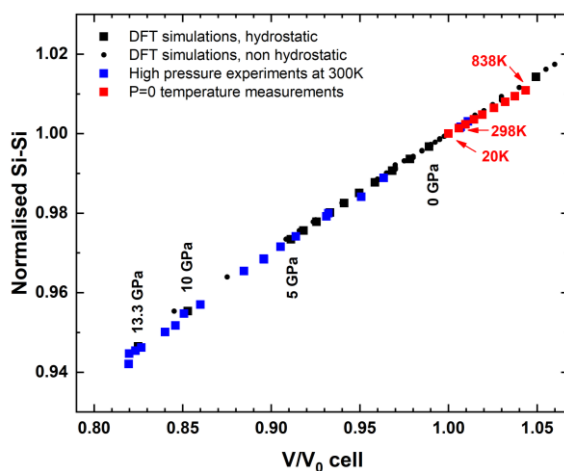
Figure 3. The variation of the Si-Si distance across their common bridging oxygen from HF/DFT simulations and experiments (Levien et al. 1980; Hazen et al. 1989; Kihara 1990; Glinnemann et al. 1992; Kim-Zajonz et al. 1999; Tucker et al. 2001). Experimental values are scaled by the experimental value at 20 K (Tucker et al. 2001), and the HF/DFT volumes by the value from the simulation at $P_{static} = 0 GPa$.

What is remarkable in these figures is that they show that deviatoric stress has little effect on the tilts (Figure 1 and 3) and volume of the tetrahedra (Figure 2); the deviatoric strains only have a secondary effect on these structural parameters as demonstrated by the small scatter in these plots against volume. This can also be clearly seen in Figure 4a and 4b which are contoured plots of the Si-O-Si angle and the tetrahedral volumes as a function of the inifinitesimal Lagrangian strains $\varepsilon_1 = a/a_0 - 1$ and $\varepsilon_3 = c/c_0 - 1$. The reference state of no strain (at the origin) is the unstrained simulation at 0 K and 0 GPa static pressure. In these plots the top-right quadrant represents volume expansion, the bottom-left quadrant volume compression. The other two quadrants represent conditions of large shears where the top-left quadrant is a condition of $\varepsilon_1 = \varepsilon_2 < 0$, or compression in the (001) plane and expansion along the **c**-axis ($\varepsilon_3 > 0$), and the bottom-right quadrant has the reversed sense of strains. The α - β quartz transition occurs experimentally with increasing

temperature and thus increasing volume and should therefore be found in the top right-hand corner of these contour plots. Analysis of the structural parameters show that the simulated structures approach the symmetry of β quartz at positive strains, but do not reach it exactly. This is because the transition involves multi-phonon dynamics (e.g. Shapiro et al. 1967; Kihara 2001) that are not included in the static HF/DFT simulations.

For the Si-O-Si angle (Figure 4a) and the SiO_4 volume (Figure 4b), and for the inter-tetrahedral Si-Si and the mean Si-O bond distances within the tetrahedra (not shown), the contours are quasi-parallel to isochors, which are lines of constant volume and thus volume strain $\varepsilon_V = 2\varepsilon_1 + \varepsilon_3$. By contrast, the contours of the plots of O-Si-O angles (Figure 4c, d, e) show a very different dependence on the strains. The angles 1-2 and 3-4 (Figure 4d) which involve the O-O edges of the SiO_4 tetrahedron perpendicular to the **c**-axis have contours almost perpendicular to the isochors, meaning that this angle hardly changes under hydrostatic compression but is very sensitive to deviatoric stress. The angles 1-4 and 2-3 (a pair of symmetrically equivalent angles, Figure 4c) show a similar pattern, but with lower sensitivity to the shear strains and in the opposite sense, while angle 2-4 (Figure 4e) shows almost no dependence on changes in the **c**-axis length (i.e. ε_3). The angular distortion of the SiO_4 groups from an ideal tetrahedron can be represented by the angle variance (AV) (Robinson et al. 1971), which exhibits a much stronger variation with deviatoric stress or strains than with isotropic stress or strains (Figure 4f). For example, the AV for isotropic strains $\varepsilon_1 = -0.03$ and $\varepsilon_3 = -0.03$ is only around 2.6, whereas for the same ε_1, and $\varepsilon_3 = +0.03$, the AV is 12.0. These results therefore demonstrate that non-symmetry-breaking deviatoric stress and strain is accommodated in the quartz structure mostly by internal angular deformation of the SiO_4 tetrahedra.
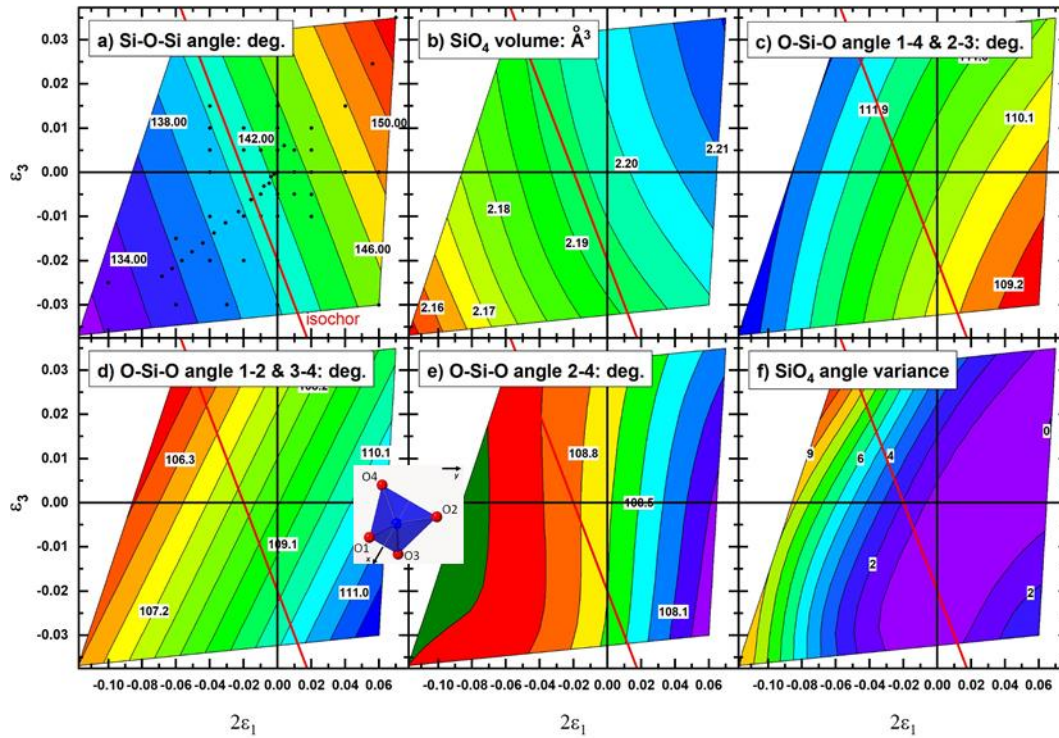
Figure 4. Contoured plots of structural parameters calculated by HF/DFT as a function of strains. The dots in (a) are the strains at which HF/ DFT simulations were performed. The reference state plotted at the origin is at 0 K and 0 GPa static pressure. The red line is the isochor passing through the origin, and contour values are given on the plots. The contours for tetrahedral tilt and volume are quasi-parallel to isochors indicating that tetrahedral tilting and compression are the major mechanisms for accommodating volume change in quartz. The inset shows the SiO_4 tetrahedron at approximately x,y,z = 0.47,0,0 in the reference structure at zero pressure viewed down the z-axis, with the oxygen atoms numbered to identify the O-Si-O angles contoured in parts c, d, and e. The contours for O-Si-O bond angles and the angle variance (part f) are transversal to the isochors, showing that deviatoric stress and strain is mostly accommodated by tetrahedral shear.

Thermoelastic properties

Despite the unit cell volumes of the HF/DFT simulation being 2.3% too large compared to low *T* measurements, the HF/DFT structure is about 10% too stiff. The bulk modulus determined by fitting the volumes from the hydrostatic simulations against the static pressures with a fourth order Birch-Murnaghan equation of state (BM4 EoS, Angel et al. 2014a) is 43.0 GPa, whereas the experimental determination of the full elastic tensor at 5 K (Tarumi et al. 2007) yields 38.8 GPa for the Reuss bulk modulus. The overestimation of the stiffness of the structure by HF/DFT is not isotropic; the **a**-axis is predicted to be 12% too stiff, whereas the **c**-axis is only 5% too stiff. This may indicate that even at 5 K the elastic moduli of the quartz structure are still affected by the

dynamics, as at higher temperatures (e.g. Demuth et al. 1999; Figure 2 in Kimizuka et al. 2003; Belmonte 2017).

The volume thermal expansion obtained from the HF/DFT simulations with the thermal contribution calculated from the phonon mode frequencies via QHA is significantly lower than the experimental thermal expansion above 100 K (Figure 5). This is mainly because the calculations do not include the contributions of the acoustic phonons. Moreover, the calculations do not also include any phonon dispersion across the entire Brillouin zone, nor any intrinsic anharmonicity of the vibrational modes, nor do they account for phonon-phonon interactions. The agreement with experiments becomes significantly worse with increasing temperature due to the presence of two very anharmonic modes (the two-phonon excitation near 147 cm^{-1} and the fundamental soft mode near 207 cm^{-1}) which probably couple to drive the α-β quartz transition (Shapiro et al. 1967). Such multi-phonon coupling is not included in QHA. A further consequence is that the slopes of the isochors calculated by QHA are not correct, and the softening of the bulk modulus due to the phase transition is not modelled; while the bulk modulus from QHA is ca. 3.4 GPa too stiff at 300 K and it is 20 GPa too stiff at 800 K, just 48 K below the transition.
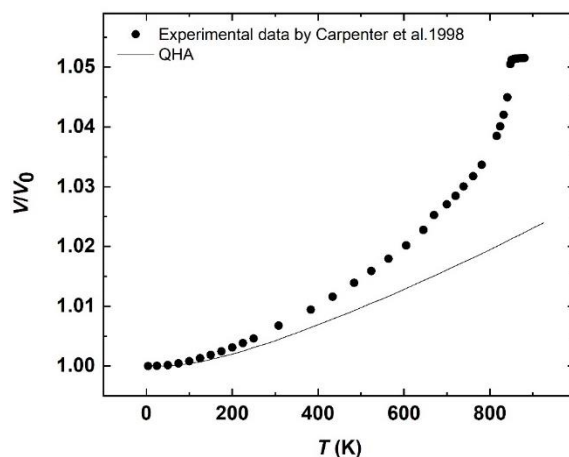
Figure 5. Comparison between measured volume variation of quartz with temperature (symbols) and that predicted by the QHA (line).

The total energy of most of the simulated structures under various strain conditions fall approximately on a parabolic curve when plotted against volume (Figure 6), with the minimum at the reference geometry (0 K and 0 GPa static). This variation agrees well with the elastic energy calculated using the experimentally determined elastic moduli of quartz (e.g. Tarumi et al. 2007;

70

Lakshtanov et al. 2007). The biggest deviatoric strains (highlighted in red colour) that correspond to the two opposite extreme conditions of deviatoric strains ($\varepsilon_3 = -\varepsilon_1$, with $\varepsilon_{1} = \pm 0.03$) generate an elastic energy that is larger than the hydrostatic compression at the same volume that is equivalent to approximately an additional 3% of volume compression (Figure 6).
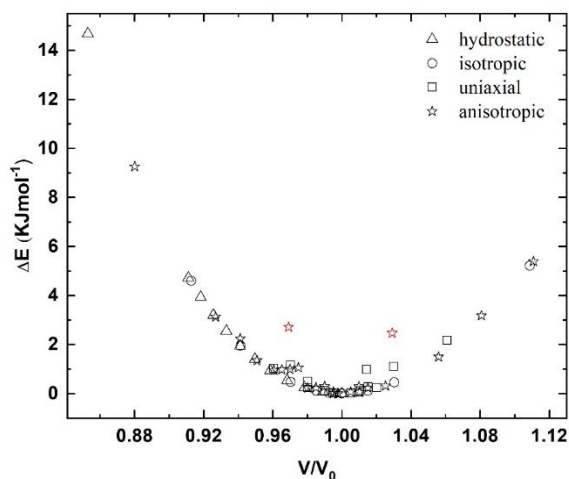
Figure 6. Total energies in kJmol[-1] as a function of volume for all of the calculated structures of quartz. The reported energy differences are calculated with respect to the energy at 0 K and 0GPa static pressure (reference geometry).

Atomic dynamics

Figure 7 shows the calculated change in phonon wavenumbers of three Raman-active peaks (207, 796 and 1161 cm^{-1}) as a function of the two symmetry-independent strain components ($\varepsilon_1 = \varepsilon_2 \neq \varepsilon_3$). The contours in these plots are the iso-shift lines, along which the frequency shift for a specific Raman mode does not change with strain. Analysis of the atomic motions associated with each Raman peak shows that the low wavenumber modes (100-450 cm^{-1}) seem to be dominated by quasi-rigid motions (i.e. external modes) that affect the Si-O-Si distances and angles and thus, as a static deformation, would change the volume of the unit cell. As might be expected, such modes tend to have iso-shift lines that are quasi-parallel to the contours of the Si-O-Si angle and SiO$_4$ volume (Figure 4a, b) under static strains. The high wavenumber region (>450 cm^{-1}) involves significant internal deformation of the SiO$_4$ tetrahedra but one can hardly ascribe the crystal phonon modes in quartz as pure internal or external SiO$_4$ vibrations, because quartz is a fully connected framework of tetrahedra. Most of the Raman-active phonon modes in quartz (with the

71

only exceptions being the two near 355 and 394 cm^{-1} and that near 1067 cm^{-1} that show positive slopes and a near-zero slope, respectively) show similar iso-shift line trends with negative slopes (Figure 7 and also Figure 3 in Murri et al. 2018), indicative of a contribution of volume-changing motions. Thus, there is no obvious correlation between the trends of structural parameters with strain and the vibrational mode wavenumbers with imposed strain. This is because the equilibrium structural parameters are determined by the configuration of lowest internal energy, whereas the vibrational frequencies are determined by the curvature of the energy surface.
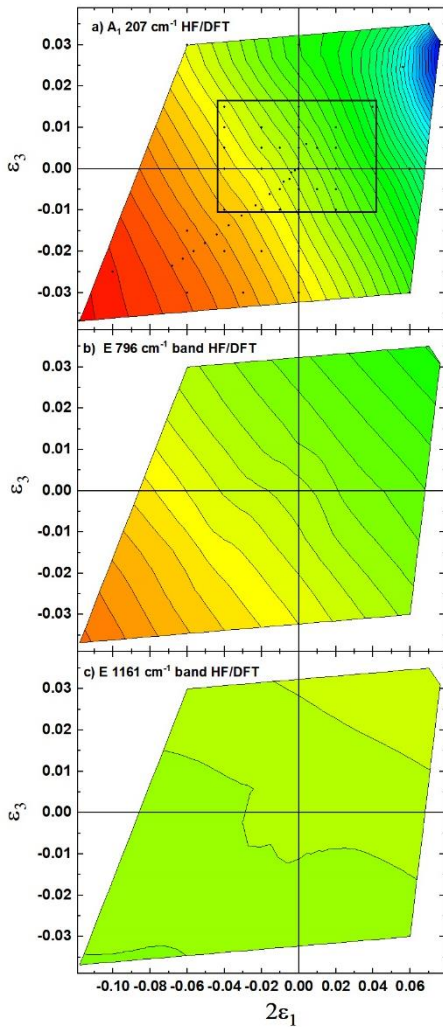
Figure 7. Contour map of the quartz Raman peaks near 207, 796 and 1161 cm^{-1}. The dots in (a) are the strains at which HF/ DFT simulations were performed. The reference state plotted at the origin is at 0 K and 0 GPa static pressure. Contour intervals are 6 cm^{-1} in all three plots.

The QHA, expressed in Eq. (2), states that the frequencies of vibrational modes within an isotropic or cubic solid are only dependent upon the volume (Grüneisen 1926). The shift $\partial\omega$ of the

wavenumber ω^m of a vibrational mode is due to the strains of the crystal induced by the applied temperature or pressure. The wavenumber under a strain $\boldsymbol{\varepsilon}$ is determined by the second-rank symmetric mode Grüneisen tensor $\boldsymbol{\gamma^m}$ (Ziman 1960; Key 1967; Cantrell 1980; Angel et al. 2018) for each phonon mode:

$$\frac{-\Delta\omega^m}{\omega_0^m} = \boldsymbol{\gamma^m}:\boldsymbol{\varepsilon} \tag{4}$$

The ":" in Eq. (4) is a double-scalar product between the two tensors. Because strain is a second-rank symmetric tensor and the fractional shift $\frac{-\Delta\omega^m}{\omega_0^m}$ must be independent of coordinate transformations, it follows that the phonon-mode Grüneisen tensor is a second-rank symmetric property tensor that links the change in the static lattice (strain) and lattice dynamics (phonon wavenumbers) in a crystal (Barron et al. 1980). Eq. (4) can be written out in Voigt notation (Voigt 1910) as:

$$\frac{-\Delta\omega^m}{\omega_0^m} = \gamma_1^m\varepsilon_1 + \gamma_2^m\varepsilon_2 + \gamma_3^m\varepsilon_3 + \gamma_4^m\varepsilon_4 + \gamma_5^m\varepsilon_5 + \gamma_6^m\varepsilon_6 \tag{5}$$

Note that under the Voigt convention used here for strains, the values of the shear strains $\varepsilon_4, \varepsilon_5, \varepsilon_6$ are one-half of the values of the corresponding tensor components $\varepsilon_{23}, \varepsilon_{13}, \varepsilon_{12}$. This equation means that the changes in the Raman peak positions in general depend on all of the strains in three dimensions experienced by the crystal, not just the volume. In principle, the values of the six components, γ_i^m with $i = 1$ to 6, of a mode Grüneisen tensor may change with pressure and temperature, and with the magnitude of the strains. The values of γ_i^m are different for different modes.

Because the mode Grüneisen tensor is a symmetric second-rank property tensor, it is subject to the same symmetry constraints on its component values as other second-rank property tensors, such as the thermal expansion and compressibility tensors (Barron et al. 1980; Angel et al. 2018). Therefore, for the trigonal symmetry of quartz $\gamma_1^m = \gamma_2^m$ and, $\gamma_4^m = \gamma_5^m = \gamma_6^m = 0$.

Further, our HF/DFT simulations are performed while maintaining the trigonal symmetry of the quartz, so that $\varepsilon_1 = \varepsilon_2$, and the shift in the wavenumbers of modes should be given by:

$$\frac{-\partial\omega^m}{\omega_0^m} = 2\gamma_1^m\varepsilon_1 + \gamma_3^m\varepsilon_3 \tag{6}$$

Eq. (6) describes a planar surface where shifts are related to strains relative to a reference state. This is what is seen in the majority of plots of the phonon wavenumber shifts in Figure 7: the contours are approximately parallel and equally-spaced for each mode. It is then more convenient to determine first the best-fit surfaces in terms of two coefficients (a_1 and a_3):

$$-\partial\omega^m = a_1\varepsilon_1 + a_3\varepsilon_3 \tag{7}$$

The Grüneisen tensor components γ_1^m and γ_3^m of each mode then follow as:

$$\gamma_1^m = \frac{a_1}{2\omega_0^m} \quad \text{and} \quad \gamma_3^m = \frac{a_3}{\omega_0^m} \tag{8}$$

Some phonon modes exhibit non-planar surfaces in the contour maps as indicated by contour lines being unequally spaced or strongly curved, the strongest non-planarity being exhibited by the soft mode at 207 cm^{-1} (Figure 7a), although other modes also show softening as the transition is approached (towards the upper-right corner of the contour plots). This behaviour is equivalent to saying that the mode Grüneisen tensor components are not constants. Since some modes exhibit such non-linear behaviour, we restricted the fit to determine the mode Grüneisen tensor components to small values of strains, as indicated by the box in Figure 7a. We determined the values of a_1 and a_3 by minimising the sum of the squared difference between calculated and observed wavenumber shifts, and then used Eq. (8) to obtain the values of the γ_1^m and γ_3^m . Grüneisen tensor components obtained by using different reference wavenumbers (ω_0 measured in experiments at 300 K and those calculated at 0 K by HF/DFT simulations) are reported in Table 2. Differences between the two sets of Grüneisen components were also calculated (Δ $\gamma_{1\ (300K-0K)}$ and Δ $\gamma_{3\ (300K-0K)}$) and they decrease with increasing wavenumbers (see Table 2). For the reasons given above, the comparison of computational and experimental wavenumbers for the E modes is given only for the E (TO) components. In order to properly measure the E (TO) components without the contribution from the LO ones, one should collect polarized Raman spectra on an oriented sample with the **c** axis perpendicular with respect to the polarization of the incident light (Murri et al. 2018).

Table 2 Grüneisen components determined by using experimental and computational ω_0 at 300 K and 0 K, respectively. The differences between them due to the different ω_0 are also reported.

Mode	$\omega_{0\ 300K}$	$\gamma_1 300K$	$\gamma_3 300\ K$	$\omega_{0\ HF/DFT\ (0K)}$	$\gamma_1 0\ K$	$\gamma_3 0\ K$	$\Delta\gamma_1$ (300K-0K)	$\Delta\gamma_3$ (300K-0K)
E (TO)	128.1	1.21	2.69	140.5	1.10	2.46	0.11	0.24
A$_1$	207.3	3.64	5.25	217.9	3.46	4.99	0.18	0.26
E(TO)	264.3	0.57	0.77	269.1	0.56	0.76	0.01	0.01
A$_1$	355.7	-0.31	0.45	346.9	-0.31	0.46	0.01	-0.01
E(TO)	394	0.11	-0.05	391.8	0.11	-0.05	0.00	0.00
E(TO)	449.7	0.55	0.69	446.8	0.55	0.70	0.00	0.00
A$_1$	464.8	0.60	1.19	471.7	0.59	1.17	0.01	0.02
E(TO)	695.6	0.51	0.36	699.9	0.50	0.36	0.00	0.00
E(TO)	796.7	0.32	0.73	803	0.32	0.73	0.00	0.01
E(TO)	1066.5	-0.02	0.36	1071.8	-0.02	0.36	0.00	0.00
A$_1$	1082.1	0.02	0.33	1088.8	0.02	0.33	0.00	0.00
E(TO)	1161.3	-0.05	-0.09	1165.1	-0.05	-0.09	0.00	0.00

The resulting Grüneisen tensor components (see Table 2) are in the range from 0 to 2.5 in agreement with those reported by Briggs and Ramdas (1977), with the only exception being for the mode near 207 cm^{-1}. The resulting mode Grüneisen tensor components can also be tested against the experimentally-measured wavenumber shifts against temperature by using the measured unit-cell parameters (Carpenter et al. 1998) to determine the strains at each temperature. The predicted wavenumber shifts with temperature of the Raman modes calculated in this way from the mode Grüneisen tensors are shown for three typical examples in Figure 8. There is very good agreement between the predicted trends and the experimental data for most Raman peaks, similar to the peak near 796 cm^{-1} (Figure 8). Most of the Raman-active modes in the medium and high wavenumber region, (e.g. the 464 and 696 cm^{-1} peaks) have this behaviour and have mode Grüneisen components generally greater than 0.5 (Table 2). The second group shows a slightly worse agreement, similar to that displayed by the 1161 cm^{-1} peak having much smaller mode Grüneisen components, around 0.05. The third group consists of the modes involved in driving the phase transition such as the 207 cm^{-1} peak, which have large mode Grüneisen components (>1) and low frequencies, where the fit is poor even at room *T*. Overall for the medium and high frequency region the predicted trends show a good agreement for the Raman peaks like those near 796 and 1161cm^{-1} at least up to 400 K above which the influence of the α - β phase transition clearly becomes significant. Nonetheless, the shifts predicted by the mode Grüneisen tensors are in generally better agreement with experimental data than those predicted by QHA (dashed lines

in Figure 8) by starting from the same results from the HF/DFT simulations at 0 K and using the property that the Raman shifts do not change along the isochors under the QHA. The same approach was adopted to also predict the trends in pressure from the mode Grüneisen tensor components, by using the experimental lattice parameters from Scheidl et al. (2016) to calculate the pressure-induced strains (Figure 9). The agreement with the experimental data at pressure (Schmidt and Ziemann 2000) for both the 207 and 464 cm^{-1} peaks is good (see Figure 9), and in fact better than the agreement with the high-temperature data.
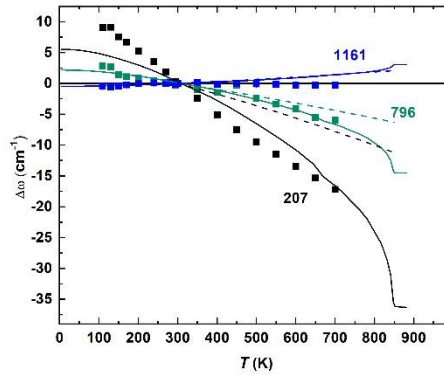
Figure 8. Experimental wavenumber changes of the Raman peaks near 207, 796 and 1161 cm^{-1} as a function of temperature are reported together with the predictions of the mode Grüneisen tensors (solid lines) and QHA (dashed lines) from HF/DFT calculations.
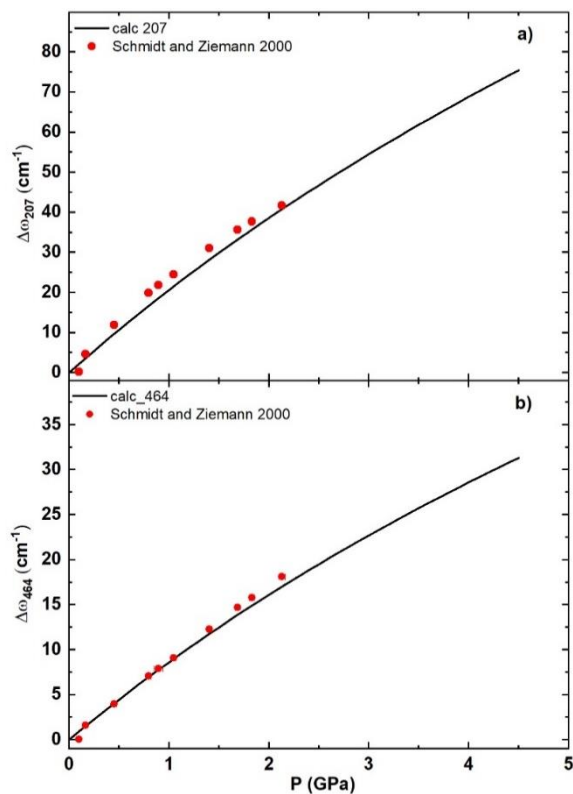
Figure 9. Experimental wavenumber changes of the Raman peaks near (a) 207 cm^{-1} and (b) 464 cm^{-1} as a function of pressure are reported together with predictions from HF/DFT- based calculations.

CONCLUSIONS

HF/DFT allows us to explore the effects of non-hydrostatic stresses on the structure and properties of minerals without the difficulties inherent in experiments. The stresses and strains can be chosen by the user, the symmetry-breaking (or not) is clear, and the stresses and strains are homogeneous. In contrast, deviatoric stresses in experiments can only be supported with a stress gradient which means that the stress state in the sample is inhomogeneous, which creates problems in interpretation; for example, a diffraction experiment on a significant volume of a stressed sample yields cell parameters that are an average across the probed volume, which often encompasses the entire sample volume (e.g. Murri et al. 2018; Campomenosi et al. 2018). Further, stress gradients in experimental apparatus often decay with time, providing a further challenge in measurement and interpretation, as does the stress distribution in any experimental sample that is a mixture of phases of different properties (e.g. Cionoiu et al. 2018).

For quartz we have shown by HF/DFT simulations that the strains induced by deviatoric stress away from hydrostatic conditions are mostly accommodated by shearing deformation of the SiO_4 tetrahedra, and not by significant changes in Si-O distances or Si-O-Si angles. This is because the shear deformations have small changes in volume of the unit-cell, whereas changes in the sizes and tilts of the SiO_4 tetrahedra have a direct effect on the volume of the unit-cell. This is consistent with the idea that the SiO_4 tilts and rotations are the major structural change associated with the α - β transition, and thus reflect the behaviour of the primary order parameter; at the macroscopic thermodynamic level the α - β phase transition involves no deformation of the unit cell because the symmetry change is from trigonal to hexagonal, and thus should be insensitive to deviatoric stresses and strains. A further consequence is that the changes in internal energy induced by deviatoric stress and strain are of the same magnitude as the changes induced by overall volume change.

The determination by HF/DFT of the Raman shifts and how they change with imposed strains allows the phonon-mode Grüneisen tensor to be calculated for each mode. A general implication of our results (Table 2) is that the phonon modes that may drive displacive phase transitions will generally have large absolute values of the Grüneisen tensor components. The phonon-mode Grüneisen tensor provides a quite accurate prediction of the changes in Raman mode wavenumbers induced by high pressure (Fig. 9), even for the 207 cm^{-1} wavenumber mode that is the fundamental soft mode driving the α - β phase transition. This suggests that the mode Grüneisen tensors could be used to determine the strains in crystals from the measured Raman shifts (Murri et al. 2018) even for modes whose behaviour with temperature is not predicted well.

References

Anderson, O.L. (1995) Equations of state of solids for geophysics and ceramic science,Oxford, UK.

Angel, R.J., Gonzalez-Platas, J., and Alvaro, M. (2014a) EosFit7c and a Fortran module (library) for equation of state calculations. Zeitschrift für Kristallographie-Crystalline Materials, 229, 405-419.

Angel, R.J., Mazzucchelli, M.L., Alvaro, M., Nimis, P., and Nestola, F. (2014b) Geobarometry from host-inclusion systems: The role of elastic relaxation. American Mineralogist, 99, 2146-2149.

Angel, R.J., Murri, M., Mihailova, B., and Alvaro, M. (2018) Stress, Strain and Raman Shifts. Zeitschrift für Kristallographie-Crystalline Materials, 234 (2), 129-140.

Anzolini, C., Prenicipe, M., Alvaro, M., Romano, C., Vona, A., Lorenzon, S., Smith, E.M., Brenker, F.E., and Nestola, F. (2018) Depth of formation of super-deep diamonds: Raman barometry of $CaSiO_3$-walstromite inclusions. American Mineralogist, 103, 69-74.

Barron, T.H.K., Collins, J.G., and White, G.K. (1980) Thermal expansion of solids at low temperatures. Advances in Physics, 29, 609-730.

Belmonte, D., 2017. First principles thermodynamics of minerals at HP–HT conditions: MgO as a prototypical material. Minerals, 7(10), p.183.

Bismayer, U., Salje, E.K.H., and Joffrin, C. (1982) Reinvestigation of the stepwise character of the ferroelastic transition in lead phosphate-arsenate, $Pb_3(PO_4)_2$-$Pb_3(AsO_4)_2$. Journal de Physique, 43, 1379-1388.

Briggs, R.J., and Ramdas, A.K. (1977) Piezospectroscopy of the Raman spectrum of α-quartz. Physical Review B, 16, 3815-3826.

Busing, W.L., and Levy, H.A. (1964) The effect of thermal motion on the estimation of bond lengths from diffraction measurements. Acta Crystallographica, 17, 142-146.

Campomenosi, N., Mazzucchelli, M.L., Mihailova, B.D., Scambelluri, M., Angel, R.J, Nestola, F., Reali, A., and Alvaro, M. (2018) How geometry and anisotropy affect residual strain in host inclusion system: coupling experimental and numerical approaches. American Mineralogist, 103(12), 2032-2035.

Cantrell, J.H. (1980) Generalized Grüneisen tensor from solid nonlinearity parameters. Physical Review B, 21, 4191-4195.

Carpenter, M.A., Salje, E.K.H., Graeme-Barber, A., Wruck, B., Dove, M.T., and Knight, K.S. (1998) Calibration of excess thermodynamic properties and elastic constant variations associated with the alpha-beta phase transition in quartz. American Mineralogist, 83, 2-22.

Cionoiu, S., Tajcmanova, L., Moulas, E., and Stünitz, H. (2018) Phase transitions under differential stress: Deviatoric stresses or pressure? Geophysical Research Abstract, 20,18504.

Civalleri, B., D'Arco, P., Orlando, R., Saunders, V., and Dovesi, R. (2001) Hartree–Fock geometry optimisation of periodic systems with the CRYSTAL code. Chemical Physics Letters, 348,131–138.

Clément, M., Padrón-Navarta, J.A., Tommasi, A., and Mainprice, D. (2018) Non-hydrostatic stress field orientation inferred from orthopyroxene (Pbca) to low-clinoenstatite ($P2_1/c$) inversion in partially dehydrated serpentinites. American Mineralogist, 103, 993-1001.

Coe, R.S., and Kirby, S.H. (1975) The orthoenstatite to clinoenstatite transformation by shearing and reversion by annealing: mechanism and potential applications. Contributions to Mineralogy and Petrology, 52(1), 29-55.

Demuth, T., Jeanvoine, Y., Hafner, J., and Angyan, J. (1999) Polymorphism in silica studied in the local density and generalized-gradient approximations. Journal of Physics: Condensed Matter, 11, 3833-3874.

Dove, M.T., Gamghir, M., and Heine, V. (1999) Anatomy of a structural phase transition: theoretical analysis of the displacive phase transition in quartz and other silicates. Physics and chemistry of minerals, 26, 344-353.

Dovesi, R., Orlando, R., Erba, A., Zicovich-Wilson, C.M., Civalleri, B., Casassa, S., Maschio, L., Ferrabone, M., De La Pierre, M., D'Arco, P., Noël, Y., Causà, M., Rérat, M., and Kirtman, B (2014) CRYSTAL14: A program for the ab initio investigation of crystalline solids. International Journal of Quantum Chemistry,114, 1287-1317.

Downs, R.T., Gibbs, G., Bartelmehs, K.L., and Boisen, M.B. (1992) Variations of bond lengths and volumes of silicate tetrahedra with temperature. American Mineralogist, 77, 751-757.

Fischer, M., and Angel, R.J. (2017) Accurate structures and energetics of neutral-framework zeotypes from dispersion-corrected DFT calculations. The Journal of Chemical Physics, 146, 174111.

Gallivan, S.M., and Gupta, Y.M. (1995) Study of tensile deformation in shocked Z-cut, α−quartz using time resolved Raman spectroscopy. Journal of Applied Physics, 78, 1557-1564.

Gibbs, J.W. (1875) On the equilibrium of heterogeneous substances. First part. Transactions of the Connecticut Academy of Arts and Sciences, 3, 108-248.

Glinnemann, J., King, H.E., Schulz, H., Hahn, T., La Placa, S.J., and Dacol, F. (1992) Crystal structures of the low-temperature quartz-type phases of SiO_2 and GeO_2 at elevated pressure. Zeitschrift für Kristallographie-Crystalline Materials, 198, 177-212.

Grüneisen, E. (1926) Zustand des festen Körpers. Handbuch der Physik

Hazen, R.M., Finger, L.W., Hemley, R., and Mao, H. (1989) High-pressure crystal chemistry and amorphisation of alpha-quartz. Solid State Communications, 72, 507-511.

Hirth, G., and Tullis, J. (1994) The brittle-plastic transition in experimentally deformed quartz aggregates. Journal of Geophysical Research: Solid Earth, 99, 11731–11747.

Hobbs, B.E., and Ord, A. (2016) Does non-hydrostatic stress influence the equilibrium of metamorphic reactions? Earth-Science Reviews, 163, 190-233.

Key, S.W. (1967) Grüneisen tensor for anisotropic materials. Journal of Applied Physics, 38, 2923-2928.

Kihara, K. (1990) A X-ray study of the temperature dependence of the quartz structure. European Journal of Mineralogy, 2, 63-77.

Kihara, K. (2001) Molecular dynamics interpretation of structural changes in quartz. Physics and Chemistry of Minerals, 28, 365-376.

Kimizuka, H., Kaburaki, H., and Kogure, Y. (2003) Molecular-dynamics study of the high-temperature elasticity of quartz above the α-β phase transition. Physical Review B, 67, 024105.

Kim-Zajonz, J., Werner, S., and Schulz, H. (1999) High pressure single crystal X-ray diffraction study on ruby up to 31 GPa. Zeitschrift für Kristallographie-Crystalline Materials, 214, 331-336.

Kirby, S.H., and Stern, L.A. (1993) Experimental dynamic metamorphism of mineral single crystals. Journal of Structural Geology, 15, 1223-1240.

Korsakov, A.V., Perraki, M., Zhukov, V.P., De Gussem, K., Vandenabeele, P., and Tomilenko, A.A. (2009) Is quartz a potential indicator of ultrahigh-pressure metamorphism? Laser Raman spectroscopy of quartz inclusions in ultrahigh-pressure garnets. European Journal of Mineralogy, 21, 1313-1323.

Kuzmany, H. (2009) Solid-state spectroscopy: an introduction. Springer Science & Business Media

Lakshtanov, D.L., Sinogeikin, S.V., and Bass, J.D. (2007) High-temperature phase transitions and elasticity of silica polymorphs. Physics and Chemistry of Minerals, 34, 11-22.

Lee, C., Yang, W., and Parr, R.G. (1988) Development of the Colle-Salvetti correlation-energy formula into a functional of the electron density. Physical Review B, 37, 785-789.

Levien, L., Prewitt, C.T., and Weidner, D.J. (1980) Structure and elastic properties of quartz at pressure. American Mineralogist, 65, 920-930.

Monkhorst, H.J., and Pack, J.D. (1976) Special points for Brillouin-zone integrations. Physical Review B, 12, 5188-5193.

Murri, M., Mazzucchelli, M.L., Campomenosi, N., Korsakov, A.V., Prencipe, M., Mihailova, B., Scambelluri, M., Angel, R.J., and Alvaro, M. (2018) Raman elastic geobarometery for anisotropic mineral inclusions. American Mineralogist, 103, 1869-1872.

Nestola, F., Prencipe, M., Nimis, P., Sgreva, N., Perritt, S.H., Chinn, I.L., and Zaffiro, G. (2018) Toward a robust elastic geobarometry of kyanite inclusions in eclogitic diamonds. Journal of Geophysical Research: Solid Earth, 123, 6411-6423.

Pascale, F., Zicovich-Wilson, C.M., Lopez Gejo, F., Civalleri, B., Orlando, R., and Dovesi, R. (2004) The calculation of the vibrational frequencies of crystalline compounds and its implementation in the CRYSTAL code. Journal of Computational Chemistry, 25, 888–897.

Pascale, F., Zicovich-Wilson, C. M., Orlando, R., Roetti, C., Ugliengo, P., and Dovesi, R. (2005) Vibration frequencies of $Mg_3Al_2Si_3O_{12}$ pyrope. An ab initio study with the CRYSTAL code. The Journal of Physical Chemistry B, 109, 6146-6152.

Prencipe, M. (2012) Simulation of vibrational spectra of crystals by ab initio calculations: an invaluable aid in the assignment and interpretation of the Raman signals. The case of jadeite ($NaAlSi_2O_6$). Journal of Raman Spectroscopy, 43, 1567–1569.

Prencipe, M. (2018) Quantum mechanics in earth sciences: a one-century-old story. Rendiconti Lincei. Scienze Fisiche e Naturali, 1-21.

Prencipe, M., Scanavino, I., Nestola, F., Merlini, M., Civalleri, B., Bruno, M., and Dovesi, R. (2011) High-pressure thermo-elastic properties of beryl ($Al_4Be_6Si_{12}O_{36}$) from ab initio calculations, and observations about the source of thermal expansion. Physics and Chemistry of Minerals, 38, 223-239.

Richter, B., Stunitz, H., and Heilbronner, R. (2016) Stresses and pressures at the quartz-to-coesite phase transformation in shear deformation experiments. Journal of Geophysical Research: Solid Earth, 121, 8015-8033.

Robinson, K., Gibbs, G., and Ribbe, P.H. (1971) Quadratic elongation: a quantitative measure of distortion in coordination polyhedra. Science, 172, 567-570.

Rosenfeld, J.L., and Chase, A.B. (1961) Pressure and temperature of crystallization from elastic effects around solid inclusion minerals? American Journal of Science, 259, 519-541.

Scheidl, K.S., Kurnosov, A., Trots, D.M., Boffa Ballaran, T., Angel, R.J., and Miletich, R. (2016) Extending the single-crystal quartz pressure gauge up to hydrostatic pressure of 19 GPa. Journal of Applied Crystallography, 49, 2129-2137.

Scheidl, K.S., Schaeffer, A.K., Petrishcheva, E, Habler, G., Fischer, F.D., Schreuer, J., and Abart, R. (2014) Chemically induced fracturing in alkali feldspar. Physics and Chemistry of Minerals, 41, 1-16.

Schmidt, C., and Ziemann, M.A. (2000) In-situ Raman spectroscopy of quartz: A pressure sensor for hydrothermal diamond-anvil cell experiments at elevated temperatures. American Mineralogist, 85, 1725-1734.

Scott, J.F., and Porto, S.P.S. (1967) Longitudinal and transverse optical lattice vibrations in quartz. Physical Review, 161, 903-910.

Shapiro, S.M., O'Shea, D.C., and Cummins, H.Z. (1967) Raman scattering study of the alpha-beta phase transition in quartz. Physical Review Letters, 19, 361-364.

Stangarone, C., Tribaudino, M., Prencipe, M., and Lottici, P.P (2016) Raman modes in Pbca enstatite ($Mg_2Si_2O_6$): an assignment by quantum mechanical calculation to interpret experimental results. Journal of Raman Spectroscopy, 47, 1247-1258.

Stangarone, C., Böttger, U., Bersani, D., Tribaudino, M., and Prencipe, M. (2017) Ab initio simulations and experimental Raman spectra of Mg_2SiO_4 forsterite to simulate Mars surface environmental conditions. Journal of Raman Spectroscopy, 48, 1528-1535.

Tarumi, R., Nakamura, K., Ogi, H., and Hirao, M. (2007) Complete set of elastic and piezoelectric coefficients of α-quartz at low temperatures. Journal of Applied Physics, 102, 113508.

Tucker, M.G., Keen, D.A., and Dove, M.T. (2001) A detailed structural characterization of quartz on heating through the α-β phase transition. Mineralogical Magazine, 65, 489-507.

Valenzano, L., Torres, F.J., Doll, K., Pascale, F., Zicovich-Wilson, C.M., and Dovesi, R. (2006) Ab initio study of the vibrational spectrum and related properties of crystalline compounds; the case of $CaCO_3$ calcite. Zeitschrift für Physikalische Chemie, 220, 893-912.

Voigt, W. (1910) Lehrbuch der Kristallphysik. Teubner,Leipzig.

Wheeler, J. (2014) Dramatic effects of stress on metamorphic reactions. Geology, 42, 647-650.

Wheeler, J. (2018) The effects of stress on reactions in the Earth: Sometimes rather mean, usually normal, always important. Journal of Metamorphic Geology, 36, 439-461.

Wu, Z., and Cohen, R.E. (2006) More accurate generalized gradient approximation for solids. Physical Review B, 73, 235116

Zhang, Y. (1998) Mechanical and phase equilibria in inclusion–host systems. Earth and Planetary Science Letters, 157,209-222.

Ziman, J.M. (1960) Electrons and phonons: the theory of transport phenomena in solids. Oxford University Press,Oxford.

5. QUANTIFYING HEXAGONAL STACKING IN DIAMOND

Mara Murri,[1] Rachael L. Smith,[2] Kit McColl,[2] Martin Hart,[2] Matteo Alvaro,[1] Adrian P. Jones,[3] Péter Németh,[4] Christoph G. Salzmann,[2] Furio Corà,[2] Maria C. Domeneghetti,[1] Fabrizio Nestola,[5] Nikolay V. Sobolev,[6] Sergey A. Vishnevsky,[6] Alla M. Logvinova,[6] Paul F. McMillan[2]

[1]*Department of Earth and Environmental Sciences, University of Pavia, Via A. Ferrata, 1 27100 Pavia, Italy*
[2]*Department of Chemistry, University College London, 20 Gordon Street, London WC1H 0AJ, UK*
[3]*Department of Earth Sciences, University College London, WC1E 6BT, UK*
[4]*Institute of Materials and Environmental Chemistry, Research Centre for Natural Sciences-HAS, Magyar tudósok körútja 2, 1117 Budapest, Hungary*
[5]*Department of Geosciences, University of Padova, Via G. Gradenigo 6, I-35131 Padova, Italy*
[6]*V.S. Sobolev Institute of Geology and Mineralogy, Siberian Branch of Russian Academy of Sciences, Koptyug Ave., 3, Novosibirsk 90, 630090, Russia*

ABSTRACT

Diamond is a material of immense technological importance and an ancient signifier for wealth and societal status. In geology, diamond forms as part of the deep carbon cycle and typically displays a highly ordered cubic crystal structure. Impact diamonds, however, often exhibit structural disorder in the form of complex combinations of cubic and hexagonal stacking motifs. The structural characterization of such diamonds remains a challenge. Here, impact diamonds from the Popigai crater were characterized with a range of techniques. Using the MCDIFFaX approach for analysing X-ray diffraction data, hexagonality indices up to 40% were found. The effects of increasing amounts of hexagonal stacking on the Raman spectra of diamond were investigated computationally and found to be in excellent agreement with trends in the experimental spectra. Electron microscopy revealed nanoscale twinning within the cubic diamond structure. Our analyses lead us to propose a systematic protocol for assigning specific hexagonality attributes to the mineral designated as lonsdaleite among natural and synthetic samples.

INTRODUCTION

Impact cratering is one of the most common geological processes resulting in accretion and remodelling of planetary surfaces and contributing to development of their atmosphere and even biological evolution. Assessing the frequency of impacts on a tectonically inactive body, such as the Moon, is relatively straightforward through inspection of the planetary surface. However, on Earth, impact structures are typically obscured or have been obliterated by tectonic activity and volcanic resurfacing, erosion and burial processes, and surface vegetation. In order to deduce the presence of a terrestrial impact site it is often necessary to be guided by markers present in the mineral record that provide evidence of shock metamorphism within the country rock or among remnants derived from the impactor (Stoffler and Grieve 2007). When a sufficiently large projectile (e.g., >50 m for stony and >20 m for iron meteorites) passes through the atmosphere without significant deceleration or disruption, it impacts the surface at velocities typically >11 km s^{-1}. This causes shock waves that radiate into the target at velocities on the order of several km s^{-1} producing pressures (P), temperatures (T) and strain fields that are orders of magnitude greater than those achieved by endogenic metamorphism. The extreme P-T conditions generated can cause melting and even vaporization of refractory phases, and result in structural and phase transformations among minerals of the impacted rocks. One such mineralogical marker is the presence of features indicating hexagonal symmetry in the X-ray diffraction patterns of diamonds recovered from the impact site (Frondel and Marvin 1967; Hanneman et al. 1967). Such features have been associated with the presence of lonsdaleite, a metastable form of diamond that has also been reported to be formed in static as well as dynamic shock high pressure-high temperature (HPHT) laboratory experiments (e.g. Bundy and Kasper 1967; Erskine and Nellis 1991; Utsumi and Yagi 1991; Utsumi et al. 1994; Bundy et al. 1996; Yoshiasa et al. 2003; Isobe et al. 2013; Németh et al. 2014; Kraus et al. 2016; Turneaure et al. 2017).

Lonsdaleite-bearing diamonds have been reported to occur in samples collected from large impact craters such as Popigai in Siberia (e.g. Koeberl et al. 1997; Vishnevsky et al. 1997; Masaitis 1998; Vishnevsky and Montanari 1999Jones et al. 2016; Yellisseyev et al. 2016) in addition to the type mineral phase described from Canyon Diablo (Barringer Meteor Crater, Arizona) (Foote 1891; Barringer 1905; Hanneman et al. 1967, Bundy and Kasper 1967). The cubic structure of diamond is based on tetrahedrally bonded carbon atoms linked into a 4-connected net, with all C-C bonds and C-C-C angles identical at 1.54 Å and 109.47°, respectively. The structure is usefully

described in terms of layers of corrugated six-membered ring units with a cyclohexane "chair" conformation that are stacked with identical orientation perpendicular to the cubic (111) axis, accompanied by a shift half-way across the diagonal of the six-membered rings (Salzmann et al. 2015). This constitutes the thermodynamically stable form of carbon over a very wide range of pressures and temperatures (Oganov et al. 2013). An alternative motif is achieved by successively stacking mirror images of the layers on top of each other resulting in hexagonal symmetry when propagated in three dimensions along the stacking direction. The two structures correspond to 3C and 2H motifs, respectively, using Ramsdell symbols to designate the layered stacking polytypes.

A form of diamond exhibiting hexagonal features in its X-ray diffraction pattern was described by Bundy and Kasper for a phase produced by H*PHT* treatment of graphite (Bundy and Kasper 1967). The powder X-ray diffraction data could be associated with a hexagonal phase having unit cell parameters a = b = 2.51 Å and c = 4.12 Å, and a density similar that of cubic diamond (3.51 g cm^{-3}). An analogous material was also reported from shock compression studies (Crowan et al. 1968). Diamonds containing similar hexagonal X-ray signatures were then reported within samples from the Canyon Diablo and Goalpara (Assam, India) meteorite impact sites (Hanneman et al. 1967). The hexagonal diamond form was associated with the 2H stacking polytype of elemental carbon by analogy with wurtzite vs sphalerite structures of tetrahedrally bonded compounds such as SiC and ZnS. It was assigned the mineral name lonsdaleite in recognition of the contributions of Kathleen Lonsdale to crystallography (Frondel and Marvin 1967). Other layered arrangements are also found among SiC and other tetrahedrally bonded materials, with different repeat sequences of the cubic (c) and hexagonal (h) stacking motifs occurring along the stacking direction giving rise to various 4H, 6H, 8H and other polytypes. These have been reported to occur among diamond materials prepared by vapor deposition techniques (Sanjay Bhargava et al. 1995; Fayette et al. 1995; Chiem et al. 2003).

Because of its importance as a mineralogical marker for shock impact events as well as possibly leading to a useful class of technological materials, it is essential to fully understand and describe the nature of the lonsdaleite structure, how it is formed and can be controlled. Questions have arisen concerning the identification of the mineral lonsdaleite with a purely hexagonally crystalline structure (Németh et al. 2014; Salzmann et al. 2015; Németh et al. 2015). In addition, the interpretation of lonsdaleite as evidence for shock metamorphism has been questioned recently (Daulton et al. 2017). The presence of hexagonal features in natural impact diamonds is typically

interpreted as the result of shock transformation from graphite present in country rocks, although shock compression of diamond and graphite present within the impactor is also considered (e.g. Frondel and Marvin 1967; Bundy and Kasper 1967; Lonsdale 1971; Garvie and Németh 2009; Garvie et al. 2014). In most samples, the hexagonal phase has been reported to occur in close association with cubic diamond and graphite, often as inclusions within the shocked crystals. Although monocrystalline lonsdaleite was reported to occur (Shumilova et al. 2011), the electron diffraction data, used as evidence, can also be interpreted as twinned cubic diamond following the description presented by Németh et al. (2014). In a transmission electron microscopy (TEM) study of materials recovered from a static compression experiment, Shiell et al. (2016) claimed to have produced nearly pure (90%) hexagonal diamond. However, the diffraction data exhibited only amorphous rings that were more consistent with the signatures of quenchable amorphous diamond as reported by Zeng et al. (2017). Kraus et al. (2016) likewise claimed the synthesis of pure hexagonal diamond by shock compression of a pyrolytic graphite sample. However, that description was based on observation of a doubled feature in the X-ray diffraction pattern that could equally well be interpreted as two peaks of coexisting cubic diamond structures formed within different strain regimes that can occur during shock processes. Although Turneaure et al. (2017) reported the finding of pure hexagonal diamond from highly oriented pyrolytic graphite, the orientational relationship deduced from the X-ray reflections contradict the direct High Resolution Transmission Electron Microscopy (HRTEM) observations of the graphite to diamond transition reported by Garvie et al. (2014). Furthermore, the reflections attributed to hexagonal diamond are in fact consistent with nanotwinned cubic diamond reported by Németh et al. (2014).

Németh et al. (2014) conducted a detailed analysis of HRTEM images and diffraction data to show that the characteristic features for even the type lonsdaleite material are best interpreted in terms of the cubic diamond structure containing multiple stacking faults and twinning defects, rather than as an sp^3-bonded layered phase with hexagonal symmetry (Németh et al. 2014, 2015). Salzmann et al. (2015) and later Jones et al. (2016) applied the MCDIFFaX technique (Treacy et al. 1991) to analyse the X-ray diffraction data of natural and laboratory-produced diamonds in order to determine their average hexagonality Φ_h, i.e., the fraction of hexagonal stacking, and differentiate between ordered vs disordered stacking sequences. This approach allows fitting the diffuse scattering features that arise from stacking disorder. The MCDIFFaX results led to construction of a "stackogram" with poles extending along a line containing a random sequence

of stacking between fully cubic and fully hexagonal end-members, with two other extrema extending towards a physical mixture of locally ordered domains (i.e., $(ccc)_n$ coexisting with $(hh)_n$) vs a fully ordered polytype structure $(chch)_n$ (Salzmann et al. 2015; Jones et al. 2016). The results were reported along lines of constant Φ_h in terms of Φ_{cc} (i.e., the probability of cubic stacking occurring after a previous cubic event) and Φ_{hc} (i.e., probability of cubic stacking consecutive to a previous hexagonal event). The hexagonality Φ_h is calculated from the switching probabilities according to $\Phi_h = \Phi_{ch} / (\Phi_{hc}+\Phi_{ch})$. Those analyses of the X-ray diffraction data revealed that the impact diamond samples contain multiple intermediate stacking sequences that occupy a range of average hexagonality indices with a distribution of Φ_{cc} vs Φ_{hc} values. It was concluded that lonsdaleite should best be described as stacking disordered diamond.

Microbeam Raman spectroscopy has also been used to detect the presence of hexagonal lonsdaleite vs cubic diamond structures in natural and laboratory samples (Le Guillou et al. 2010; Ross et al. 2011; Goryainov et al. 2014). The 3C diamond phase exhibits a single Raman peak (T_{2g} symmetry) at 1332 cm^{-1}. Subtle shifts in the peak position along with peak broadening can reveal the presence of non-isotropic strains, associated with impurities or structural defects within the samples. However, characteristic broadening and development of asymmetry in the main Raman band extending to lower wavenumber is also used to diagnose the appearance of "lonsdaleite"-like structures. Ab initio calculations predict that the 2H structure with $P6_3/mmc$ space group and Z=4 atoms in its primitive unit cell should exhibit three Raman peaks with A_{1g}, E_{1g} and E_{2g} symmetry at the Brillouin zone centre (Spear et al. 1990; Wu 2007; Denisov et al. 2011; Ivanova and Mavrin 2014; Jones et al. 2016). Deconvolution of the Raman spectra of natural diamonds produced by shock events, including samples from the Popigai impact crater, have been used to deduce the presence of coexisting 3C and 2H diamonds (Goryainov et al. 2014; Ovsyuk et al. 2018). However, that interpretation does not agree with the MCDIFFaX analysis of the X-ray data for similar suites of samples that indicate the presence of complex interlaced hexagonal / cubic stacking regimes (Salzmann et al. 2015; Jones et al. 2016), or with HRTEM data indicating that the hexagonal diffraction features arise from nanoscale twinning and layer stacking defects within the cubic 3C diamond structure (Németh et al. 2014, 2015).

Here we present a systematic analysis of a suite of diamond samples (Figure 1) from the Popigai impact crater using a combination of X-ray diffraction with MCDIFFaX analysis of the results, followed by Raman spectroscopy accompanied by a series of Density Functional Theory

(DFT) calculations for different hexagonal/cubic stacking sequences, and HRTEM studies of the shocked phases. Our results allow us to suggest a new systematic protocol to be used to describe hexagonal diamond and lonsdaleite structures found in nature or created in the laboratory.
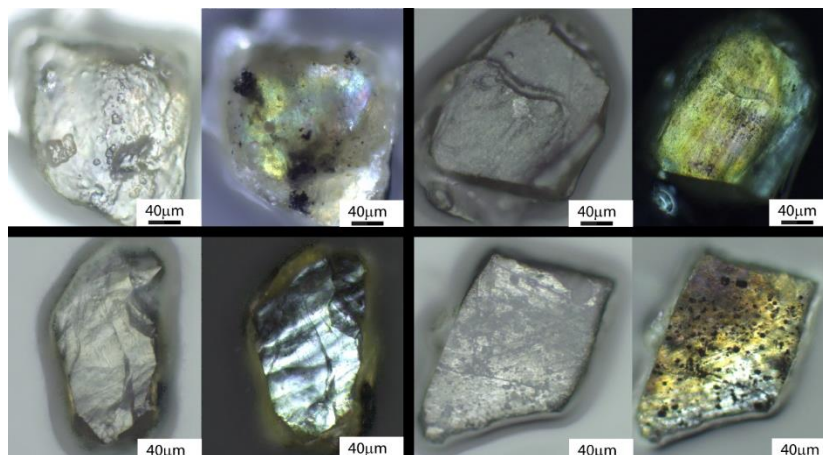
Figure 1. Optical images of representative Popigai impact diamonds collected using reflected and transmitted light.

HEXAGONALITY INDICES FROM X-RAY DIFFRACTION ANALYSIS

We obtained powder X-ray diffraction patterns of 23 Popigai impact diamond samples and analysed the data using the MCDIFFaX approach which is based on a general recursive algorithm coupled with a Monte-Carlo type parameter that allows calculating diffraction patterns of minerals with stacking defects and preventing also the refinement convergence in false minima (for details see Treacy et al 1991 and Salzmann et al. 2015). A typical diffraction pattern displaying the diffuse diffraction features arising from the stacking disorder is shown in Figure 2a. The results from the fits allowed us to plot their Φ_h, Φ_{cc} and Φ_{hc} values on a stackogram, where they are compared with previous data obtained from Canyon Diablo and laboratory shocked samples (Figure 2b). As mentioned previously, the leading diagonal extends between the cubic 3C and hexagonal 2H diamond structures. The other two poles indicate the clustering of cubic vs hexagonal stacking sequences, ranging between a physical mixture of extended $(ccc)_n$ and $(hh)_n$ stacking sequences to fully ordered $(chch)_n$ polytypes. The hexagonality of sample, Φ_h, can be read off from their position with respect to the dashed lines of constant Φ_h. The data for the Popigai samples all lie near the top right corner with Φ_h ranging from almost zero to 0.4 and a large number of samples located close to $\Phi_h = 0.2$. These are distinct from the Canyon Diablo sample (Salzmann et al. 2015) with

Φ_h ~0.45 which is located towards the physical mixture pole of the stackogram. This observation is certainly related to the fact that formation of the two impact craters involved very different shock conditions (Heymann et al. 1966; Masaitis 1998).

Our results indicate that using MCDIFFaX to analyse X-ray diffraction data and to plot the findings on a stackogram is a very powerful method to obtain detailed insights into the overall hexagonality of a diamond sample as well as the degree of clustering of the hexagonal vs cubic layer sequences. In addition to this observation, Figure S1 demonstrates a useful relationship between the crystallographic c/a ratio and the hexagonality of a diamond sample.
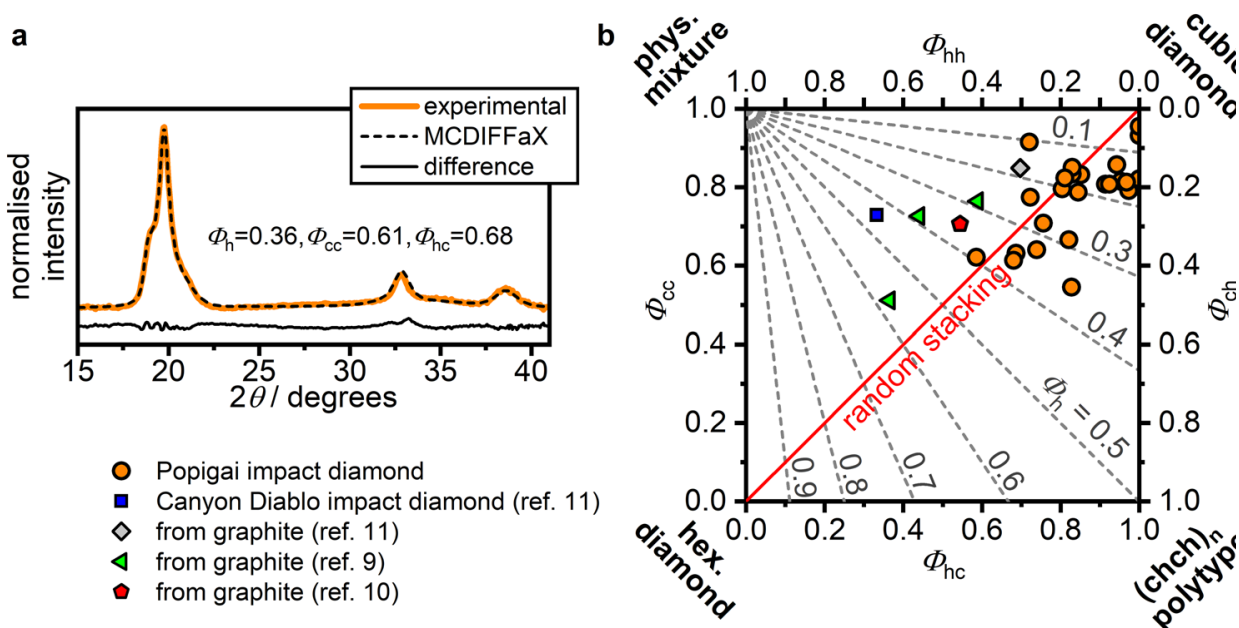
Figure 2. Characteristics of cubic-hexagonal stacking disorder in Popigai diamonds. A) X-ray diffraction pattern of a Popigai diamond sample fitted using MCDIFFaX (Treacy et al. 1991). B) First-order stacking probabilities of all Popigai samples shown on a 'stackogram' (Treacy et al. 1991. Lines of constant hexagonality are shown as grey dashed lines whereas the solid red line indicates random stacking.

EFFECT OF STACKING DISORDER ON THE RAMAN SPECTRA

Further information can be gained from interpretation of Raman spectra of diamond samples produced during shock events (Goryainov et al. 2014; Ovsyuk et al. 2018). However, here we advise caution in applying simple interpretations based on physical mixtures of 3C/2H diamonds to the observed spectra. Because our X-ray data analysis showed that the Popigai samples studied

contained a range of nanoscale layer stacking structures, we carried out DFT calculations to predict the Raman signatures for various 48-layer model structures with ordered vs disordered stacking regimes, corresponding to specific positions on the stackogram along the random stacking line ($\Phi_{hc} = \Phi cc$) and the 50% isohexagonality line ($\Phi_h = 0.5$). Simulated Raman spectra from these model structures are presented in Figure 3a ($\Phi_{hc} = \Phi cc$) and 3b ($\Phi_h = 0.5$). Moving along the random stacking line starting from the 3C polytype, as an increasing fraction of hexagonal stacking is introduced to the models, the spectra develop Raman intensity in the ~1290-1305 cm^{-1} region, which ultimately becomes the strongest feature for $\Phi_h > 0.75$. Weaker features emerge at 1210 cm^{-1}, that also grow in intensity as Φh increases. The full range of experimental and calculated spectra is presented in the Supporting Information (Appendix IV).
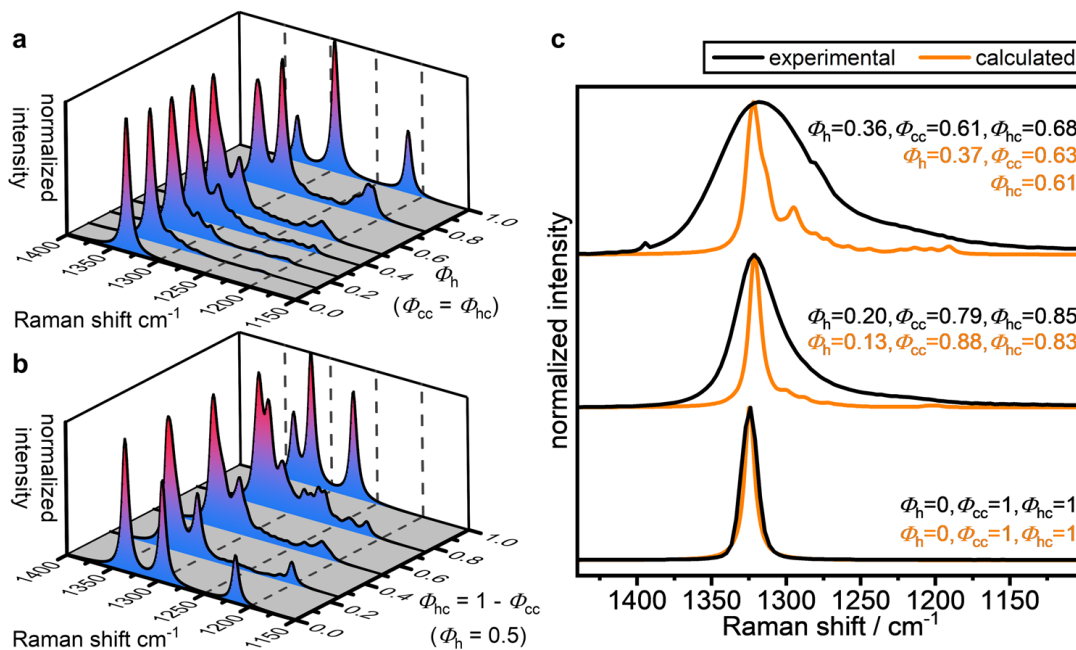
Figure 3. Effect of stacking disorder on the Raman spectra of diamond exhibiting cubic-hexagonal features in their stacking pattern. A) Calculated Raman spectra along the random stacking line and B) along the line of constant 50% hexagonality. C) Comparison of experimental Raman spectra of Popigai and cubic diamonds with corresponding calculated spectra of similar hexagonalities. The calculated spectra in part c were downshifted by 10 cm^{-1} to allow for better comparison with experimental data.

Considering structures along the 50% isohexagonality line, starting at $\Phi_{hc} = 0$, the spectrum of the physical mixture exhibits three peaks, and clearly demonstrates the overlap of the T_{1g} cubic diamond peak with the E_{1g} peak of the 2H polytype, which give rise to a single feature at ~1335 cm^{-1}. As Φ_{hc} increases, this band decreases in intensity and a new peak at ~1320 cm^{-1} emerges on the shoulder of the main peak at $\Phi_{hc} > 0.75$ and ultimately becomes the most intense feature for

the $(chch)_n$ polytype. The peak at ~1210 cm^{-1}, present in the physical mixture, decreases in intensity along the $\Phi_h = 0.5$ line as Φ_{hc} increases, and is not present in the $(chch)_n$ polytype. A comparison of the peak intensity in the ~1210 cm^{-1} region against the ~1270 cm^{-1} region may therefore give information on the local domains present for samples with a given degree of hexagonality. Intensity at ~1210 cm^{-1} can be considered diagnostic of (hh) stacking elements, whereas intensity at ~1270 cm^{-1} indicates ordered (ch) stacking. Stacking disorder generally manifests itself by weak Raman features at around 1250 cm^{-1}, whereas zero intensity is observed in this region for all the ordered polytypes.

Experimental Raman spectra of two Popigai and a cubic diamond are shown in Figure 3c together with calculated spectra for modelled structures with similar stacking characteristics. The peak positions matched well after application of a 10 cm^{-1} downshift to the calculated spectra. The assumed broadening of the calculated 3C spectrum closely matches the experimentally observed broadening. The experimental samples displaying hexagonalities of 0.20 and 0.36, respectively, all show significantly increased broadening compared to the 3C spectrum, becoming more prominent for the samples with higher hexagonality. Furthermore, the Popigai samples display a notably asymmetric envelope, with a longer 'tail' extending to lower wavenumber, where features from (hh) and (ch) stacking are expected to be appear. This indicates that the broadening is not solely a result of the small (5–20 nm) grain size, dislocations or strain, but can be attributed to peaks resulting from multiple different types of stacking disorder present within the sample, that cannot be resolved experimentally.

In general, our DFT results indicate that as soon as hexagonal stacking elements are introduced into the diamond structure, the Raman spectra develop additional intensity at around 1300 cm^{-1}, with weaker peaks observed down to approximately 1200 cm^{-1}. The presence of a significant degree of cubic stacking is revealed by the maintenance of intensity in the 1330-1350 cm^{-1} region, although peaks for purely hexagonal stacking also occur within this range. Our conclusion is that although the appearance of the Raman spectra in the 1200-1350 cm^{-1} range can give an indication that hexagonal layer stacking structures are present, they cannot be used as a primary diagnostic of the detailed structures that are present.

HRTEM ANALYSIS

An atomic scale interpretation of the structures present within diamond samples is only possible using HRTEM imaging combined with electron diffraction data analysis. We performed HRTEM

analysis for the impact-produced Popigai diamonds. The samples studied consisted of ~5-30 nm-size aggregated grains consistent with previous findings (Ohfuji et al. 2015). The grains contained abundant 111 stacking faults and subnano-sized twins (Figure 4), that gave rise to the complexity of stacking disordered diamond previously described for the Canyon Diablo sample (Németh et al. 2014). Extensive defects divided the grains into nanosize domains and resulted in streaking of the 3C diamond reflections in the diffraction profiles. The HRTEM data confirmed the highly defective nature of the structures examined at the nanoscale, that gave rise to the globally averaged cubic / hexagonal stacking sequences deduced from analysis of the X-ray diffraction and Raman spectroscopic data.
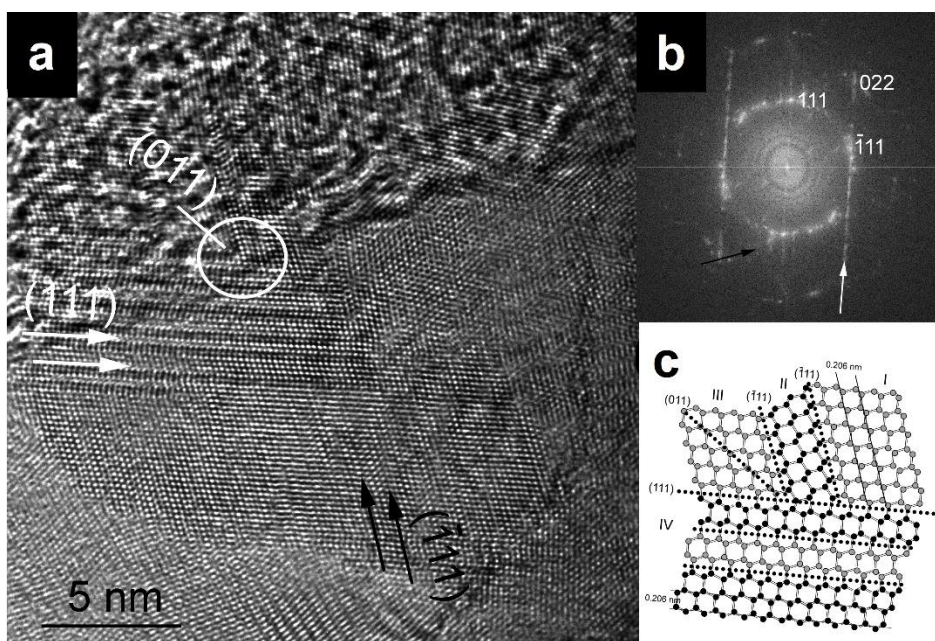
Figure 4. Abundant stacking faults and twins from a Popigai diamond (Φ_h=0.20, Φ_{cc}=0.79, Φ_{hc}=0.85). A) Multiple (111) and (-111) twins (indicated by shaded overlays) give rise to (011) intergrowth. (111) and (-111) stacking faults are marked by white and black arrows. Structure model of the white circled area is shown in C). B) Fast-Fourier transform calculated from A) shows streaking of reflections (indicated by arrows) as a result of stacking disorder. C) Idealized structure model of multiple (111) and (-111) twins. Twin modules (individuals) are represented by Roman numerals. The relationship between modules I and IV is (011).

DISCUSSION

Our combined results lead to the following suggestions for a new protocol to be used for analysing and describing lonsdaleite and various stacking disordered diamond materials recovered from meteor impact sites or produced in laboratory experiments. The first step of characterisation should be carried out using Raman spectroscopy. In absence of broadening of the main feature at ~1320

cm^{-1} accompanied by a tail towards lower wavenumbers, a diamond sample is unlikely to contain hexagonal stacking. However, analysing the spectra of materials that exhibit such bands simply in terms of physical mixtures of 3C and 2H diamond phases or domains is too simplistic. Instead, the experimental spectra should be benchmarked against the library of calculated Raman spectra presented here across the stackogram (detailed information is presented in Supporting Information, Appendix IV). More robust structural insights can then be gained using powder X-ray diffraction. We suggest that the data should be obtained with high enough quality to then be examined using the MCDIFFaX approach, and the results plotted on a stackogram to ascertain the average hexagonality and the degree of clustering of cubic vs hexagonally stacked layer sequences. This procedure can then readily distinguish among samples that have experienced different degrees of shock, which implies different *P-T* conditions for the formation of the impact structure, or samples prepared in the laboratory (Heymann et al. 1966; Masaitis 1998) (Figure 2). Finally, we suggest that a final stage of the analysis should involve use of HRTEM techniques to observe the actual nature of the layer stacking and local structural defects that give rise to the nanoscale structures, that may not be visible to the X-ray diffraction or Raman spectroscopic examinations.

CONCLUSIONS

We obtained X-ray diffraction data for a suite of diamond samples from the Popigai impact site, and analysed the results using the MCDIFFaX approach. That allowed us to plot the samples on a stackogram that indicated the overall degree of hexagonality and provided an indication of the clustering of cubic vs hexagonal layering within the sp^3 bonded structures. DFT calculations of predicted Raman signatures for different cubic/hexagonal stacking sequences permitted a detailed interpretation of the different features occurring in the experimentally observed Raman spectra. Finally, HRTEM studies demonstrated the existence of multiple stacking faults along twin planes within the 3C cubic diamond structure giving rise to the overall observed hexagonal symmetry of selected Popigai samples. The results clearly indicate that these classic examples of lonsdaleite-containing impact diamonds are best described as materials containing intergrowths of cubic and hexagonally stacked layers at the nanoscale. Our suggested protocol for examining and cataloguing samples derived from previous and future studies will lead to a better standardised and more universally accepted description of what diamonds containing features indicating hexagonal

stacking actually correspond to, and will aid in the geological interpretation of diamond-related materials recovered from impact sites.

Methods

Samples

A general description of the Popigai astrobleme, including its structure, geology, petrology of impactites, etc. is presented by Vishnevsky and Montanari (1999). The Popigai diamondiferous impactites (tagamites and suevites) are usually strong glass-bearing hard rocks made up of impact melt glass with various additions of target rock fragments, mainly Archean gneisses. The extraction of the impact diamonds was accomplished by crushing the rocks to a powder, heating in molten NaOH at 550°C for 1 hour, then dissolving in aqueous HCl followed by washing in water. Most of the sample dissolves, and the remainder consists of a small number of mineral grains, including the impact diamonds. These diamond grains were hand separated under optical microscopic examination. The Popigai impact diamonds are small (grain size usually 0.1 to 0.5 mm) and exhibit a range of colors: colorless, white, yellow, gray, dark-gray to black; yellow and dark grains are the most common (Figure 1) (Vishnevsky et al. 1997). Two main morphologies are observed: flattened and more bulky volume-xenomorphic grains. The carbon isotopic composition, $\delta^{13}C_{PDB}$, ‰, of the Popigai diamonds was between -12.30 to -18.67, within the range of the target rock graphite (Vishnevsky and Palchik 1975; Koeberl et al. 1997). X-ray examination shows the Popigai diamonds are polycrystalline fine-grained aggregates showing evidence for preferred orientation. The crystallites vary between ~1 μm down to several nm in size. Although the cubic phase dominates, the diamonds exhibit varying degrees of hexagonality as described in this work.

Experimental

X-ray diffraction experiments were carried using a prototype instrument in the Department of Geosciences at the University of Padova (Angel and Nestola 2016). The instrument consists of a Rigaku-Oxford Diffraction Supernova kappa-geometry goniometer equipped with an X-ray micro-source assembled with a Pilatus 200 K Dectris detector. The micro-X-ray source, MoK_{α} ($\lambda = 0.71073$ Å) operates at 50 kV and 0.8 mA (power = 40 W). Data collections were set up in in a phi scan mode over $360°$, since the samples are polycrystalline aggregates and the experiments were carried out. The diffraction data were fit using the MCDIFFaX approach (full details are given in Supplementary Information, see Appendix IV)[37]. For measuring Raman spectra and recording HRTEM images, Popigai and cubic diamond samples were crushed using WC cubes. The Raman spectra are shown as they recorded. They were collected by directly measuring the diamond samples on the WC supports using a Renishaw inVia spectrometer with 325 nm laser excitation in order to detect both sp^2 and sp^3 vibrations (e.g. Ferrari 2007; Ferrari and Robertson 2000, 2001 and references therein). For HRTEM analysis, a drop of isopropyl alcohol was dropped onto the crushed diamond sample on the WC mount and a lacey carbon grid was swiped across to pick up sample. HRTEM imaging was conducted using a FEI Titan 80/300 STEM/TEM instrument equipped with a Cs (image) corrector, a windowless Bruker XFlash EDS detector and operated at 200 kV. Samples were placed on a single tilt holder and HRTEM images were analysed using the Gatan Digital Micrograph 3.6.1 software.

Computational

Model structures with 48 layers and a range of different first-order stacking probabilities were prepared using our *Stacky* program (Playford et al. 2018). First-principles calculations were then performed using the periodic DFT code CRYSTAL17 (Dovesi et al. 2018). Electronic exchange and correlation were described using the hybrid-exchange functional B3LYP. An all-electron atom-centred Gaussian basis set was used to describe the C atom, available from the CRYSTAL online database (www.crystal.unito.it),

with the online label (C_6-21_G*_dovesi_1990). Reciprocal space was sampled using an 8×8×1 k-point mesh. The self-consistent field (SCF) procedure was performed up to a convergence threshold of $\Delta E = 10^{-9}$ Hartree (Ha) per unit cell. The Coulomb and exchange series were truncated with thresholds of 10^{-7}, 10^{-7}, 10^{-7}, 10^{-7} and 10^{-14}. Full geometry optimizations (lattice parameters and atomic positions) were performed using tight convergence criteria. The thresholds for the maximum and root mean square (rms) of the forces were set to 0.00015 Ha and 0.0001 Ha, respectively, and the maximum and rms of the displacements were set to 0.00045 Ha and 0.0003 Ha, respectively. Raman intensities were calculated using the coupled perturbed Kohn-Sham (CPKS) method (Maschio et al. 2012). The data are presented as orientationally and polarization averaged powder spectra.

References

Angel, R. J., and Nestola, F. (2016) A century of mineral structures: How well do we know them?. American Mineralogist, 101(5), 1036-1045.

Barringer, D. M. (1905) Coon Mountain and its crater. Proceedings of the Academy of Natural Sciences of Philadelphia, 861-886.

Bhargava, S., Bist, H. D., Sahli, S., Aslam, M., & Tripathi, H. B. (1995) Diamond polytypes in the chemical vapor deposited diamond films. Applied physics letters, 67(12), 1706-1708.

Bundy, F. P., and Kasper, J. S. (1967) Hexagonal diamond—a new form of carbon. The Journal of Chemical Physics, 46(9), 3437-3446.

Bundy, F. P., Bassett, W. A., Weathers, M. S., Hemley, R. J., Mao, H. U., & Goncharov, A. F. (1996) The pressure-temperature phase and transformation diagram for carbon; updated through 1994. Carbon, 34(2), 141-153.

Chiem, C. V., Seo, H. K., Ansari, S. G., Kim, G. S., Seo, J. M., and Shin, H. S. (2003) Lonsdaleite diamond growth on reconstructed Si (100) by hot-filament chemical vapour deposition (HFCVD). Korean Journal of Chemical Engineering, 20(6), 1154-1157.

Crowan, G. R., Dunnington, B. W. and Holtzman, A. H. (1968) Process for synthesizing diamond. E. I. du Pont de Nemours and Co., Netherlands Patent Release No. 6506395 (1965); US Patent No. 3,401,019, September 10.

Daulton, T. L., Amari, S., Scott, A. C., Hardiman, M., Pinter, N., and Anderson, R. S. (2017) Comprehensive analysis of nanodiamond evidence relating to the Younger Dryas Impact Hypothesis. Journal of Quaternary Science, 32(1), 7-34.

Denisov, V.N., Mavrin, B.N., Serebryanaya, N.R., Dubitsky, G.A., Aksenenkov, V.V., Kirichenko, A.N., Kuzmin, N.V., Kulnitskiy, B.A., Perezhogin, I.A. and Blank, V.D. (2011) First-principles, UV Raman, X-ray

diffraction and TEM study of the structure and lattice dynamics of the diamond–lonsdaleite system. Diamond and Related Materials, 20(7), 951-953.

Dovesi, R., Erba, A., Orlando, R., Zicovich-Wilson, C.M., Civalleri, B., Maschio, L., Rérat, M., Casassa, S., Baima, J., Salustro, S. and Kirtman, B. (2018) Quantum-mechanical condensed matter simulations with CRYSTAL. Wiley Interdisciplinary Reviews: Computational Molecular Science, 8(4), p.e1360.

Erskine, D. J., and Nellis, W. J. (1991) Shock-induced martensitic phase transformation of oriented graphite to diamond. Nature, 349(6307), 317.

Fayette, L., Mermoux, M., Marcus, B., Brunet, F., Germi, P., Pernet, M., Abello, L., Lucazeau, G. and Garden, J., (1995) Analysis of the fine structure of the Raman line and of X-ray reflection profiles for textured CVD diamond films. Diamond and Related Materials, 4(11), 1243-1250.

Ferrari, A.C. and Robertson, J., 2000. Interpretation of Raman spectra of disordered and amorphous carbon. Physical review B, 61(20), p.14095.

Ferrari, A.C. and Robertson, J., 2001. Resonant Raman spectroscopy of disordered, amorphous, and diamondlike carbon. Physical review B, 64(7), p.075414.

Ferrari, A.C., 2007. Raman spectroscopy of graphene and graphite: disorder, electron–phonon coupling, doping and nonadiabatic effects. Solid state communications, 143(1-2), pp.47-57.

Foote, A. E. (1891) ART. XLIV.--A New Locality for Meteoric Iron with a Preliminary Notice of the Discovery of Diamonds in the Iron. American Journal of Science (1880-1910), 42(251), 413.

Frondel, C., and Marvin, U. B. (1967) Lonsdaleite, a hexagonal polymorph of diamond. Nature, 214(5088), 587.

Garvie, L. A. J., and Németh, P. (2009) The Structure of Canyon Diablo" Diamonds". In Lunar and Planetary Science Conference (Vol. 40).

Goryainov, S. V., Likhacheva, A. Y., Rashchenko, S. V., Shubin, A. S., Afanas' ev, V. P., and Pokhilenko, N. P. (2014) Raman identification of lonsdaleite in Popigai impactites. Journal of Raman Spectroscopy, 45(4), 305-313.

Hanneman, R. E., Strong, H. M., and Bundy, F. P. (1967) Hexagonal diamonds in meteorites: implications. Science, 155(3765), 995-997.

Heymann, D., Lipschutz, M. E., Nielsen, B., and Anders, E. (1966) Canyon Diablo meteorite: metallographic and mass spectrometric study of 56 fragments. Journal of geophysical research, 71(2), 619-641.

Isobe, F., Ohfuji, H., Sumiya, H., and Irifune, T. (2013) Nanolayered diamond sintered compact obtained by direct conversion from highly oriented graphite under high pressure and high temperature. Journal of Nanomaterials, 2013, 15.

Ivanova, T. A., and Mavrin, B. N. (2013) Ab initio temperature dependence of the thermal expansion of diamond and the frequency shift of optical phonons. Physics of the Solid State, 55(1), 160-163.

Jones, A.P., McMillan, P.F., Salzmann, C.G., Alvaro, M., Nestola, F., Prencipe, M., Dobson, D., Hazael, R. and Moore, M. (2016) Structural characterization of natural diamond shocked to 60 GPa; implications for Earth and planetary systems. Lithos, 265, 214-221.

Koeberl, C., Masaitis, V. L., Shafranovsky, G. I., Gilmour, I., Langenhorst, F., and Schrauder, M. (1997) Diamonds from the Popigai impact structure, Russia. Geology, 25(11), 967-970.

Kraus, D., Ravasio, A., Gauthier, M., Gericke, D.O., Vorberger, J., Frydrych, S., Helfrich, J., Fletcher, L.B., Schaumann, G., Nagler, B. and Barbrel, B. (2016) Nanosecond formation of diamond and lonsdaleite by shock compression of graphite. Nature communications, 7, 10970.

Le Guillou, C., Rouzaud, J. N., Remusat, L., Jambon, A., and Bourot-Denise, M. (2010) Structures, origin and evolution of various carbon phases in the ureilite Northwest Africa 4742 compared with laboratory-shocked graphite. Geochimica et Cosmochimica Acta, 74(14), 4167-4185.

Lonsdale, K. (1971) Formation of lonsdaleite from single-crystal graphite. American Mineralogist: Journal of Earth and Planetary Materials, 56(1-2), 333-336.

Masaitis, V. L. (1998) Popigai crater: Origin and distribution of diamond-bearing impactites. Meteoritics & Planetary Science, 33(2), 349-359.

Maschio, L., Kirtman, B., Orlando, R., and Rèrat, M. (2012) Ab initio analytical infrared intensities for periodic systems through a coupled perturbed Hartree-Fock/Kohn-Sham method. The Journal of Chemical Physics, 137(20), 204113.

Németh, P., Garvie, L. A., Aoki, T., Dubrovinskaia, N., Dubrovinsky, L., and Buseck, P. R. (2014) Lonsdaleite is faulted and twinned cubic diamond and does not exist as a discrete material. Nature communications, 5, 5447.

Németh, P., Garvie, L. A., and Buseck, P. R. (2015) Twinning of cubic diamond explains reported nanodiamond polymorphs. Scientific reports, 5, 18381.

Oganov, A. R., Hemley, R. J., Hazen, R. M., and Jones, A. P. (2013) Structure, bonding, and mineralogy of carbon at extreme conditions. Reviews in Mineralogy and Geochemistry, 75(1), 47-77.

Ohfuji, H., Irifune, T., Litasov, K. D., Yamashita, T., Isobe, F., Afanasiev, V. P., and Pokhilenko, N. P. (2015) Natural occurrence of pure nano-polycrystalline diamond from impact crater. Scientific reports, 5, 14702.

Ovsyuk, N. N., Goryainov, S. V., and Likhacheva, A. Y. (2018) Raman Scattering in Hexagonal Diamond. Bulletin of the Russian Academy of Sciences: Physics, 82(7), 778-780.

Playford, H. Y., Whale, T. F., Murray, B., Tucker, M. G., and Salzmann, C. G. (2018) Analysis of stacking disorder in ice I using pair distribution functions. Journal of Applied Crystallography, 51(4).

Ross, A.J., Steele, A., Fries, M.D., Kater, L., Downes, H., Jones, A.P., Smith, C.L., Jenniskens, P.M., Zolensky, M.E. and Shaddad, M.H. (2011) MicroRaman spectroscopy of diamond and graphite in Almahata Sitta and comparison with other ureilites. Meteoritics & Planetary Science, 46(3), pp.364-378.

Salzmann, C. G., Murray, B. J. and Shephard, J. J. (2015) Extent of stacking disorder in diamond. Diamond and Related Materials, 59, 69-72.

Sharp, T.G. and DeCarli, P.S. (2006) Shock effects in meteorites. Meteorites and the Early Solar System II, Ed. Lauretta, D.S. & McSween, H.Y. Jr., pp. 653-677 (University of Arizona Press, Arizona, USA, 2006).

Shiell, T. B., McCulloch, D. G., Bradby, J. E., Haberl, B., Boehler, R., and McKenzie, D. R. (2016) Nanocrystalline hexagonal diamond formed from glassy carbon. Scientific Reports, 6, 37232.

Shumilova, T. G., Mayer, E., and Isaenko, S. I. (2011) Natural monocrystalline lonsdaleite. In Doklady Earth Sciences (Vol. 441, No. 1, pp. 1552-1554). SP MAIK Nauka/Interperiodica.

Spear, K. E., Phelps, A. W., and White, W. B. (1990) Diamond polytypes and their vibrational spectra. Journal of Materials Research, 5(11), 2277-2285.

Stöffler, D., Grieve, R. A. F., Fettes, D., and Desmons, J. (2007) Impactites. Metamorphic rocks: A classification and glossary of terms, recommendations of the International Union of Geological Sciences, 82-92.

Treacy, M. M. J., Newsam, J. M., and Deem, M. W. (1991) A general recursion method for calculating diffracted intensities from crystals containing planar faults. Proceedings of the Royal Society of London. Series A: Mathematical and Physical Sciences, 433(1889), 499-520.

Turneaure, S. J., Sharma, S. M., Volz, T. J., Winey, J. M., and Gupta, Y. M. (2017) Transformation of shock-compressed graphite to hexagonal diamond in nanoseconds. Science advances, 3(10), eaao3561.

Utsumi, W., and Yagi, T. (1991) Formation of hexagonal diamond by room temperature compression of graphite. Proceedings of the Japan Academy, Series B, 67(9), 159-164.

Utsumi, W., Yamakata, M., Yagi, T., and Shimomura, O. (1994) In situ X-ray diffraction study of the phase transition from graphite to hexagonal diamond under high pressures and high temperatures. In AIP Conference Proceedings (Vol. 309, No. 1, pp. 535-538). AIP.

Vishnevsky, S., Afanasiev, V. P., Argunov, K. P. and Palchik, N. A. (1997) Impact diamonds: their features, origin and significance. Siberian Branch of Russian Academy Scientific Press (Novosibirsk) (available in Russian and English).

Vishnevsky, S., and Montanari, A. (1999) Popigai impact structure (Arctic Siberia, Russia): Geology, petrology, geochemistry, and geochronology of glass-bearing impactites. Special Papers-Geological Society Of America, 19-60.

Yelisseyev, A. P., Afanasiev, V. P., Panchenko, A. V., Gromilov, S. A., Kaichev, V. V., and Saraev, A. A. (2016) Yakutites: Are they impact diamonds from the Popigai crater?. Lithos, 265, 278-291.

Yoshiasa, A., Murai, Y., Ohtaka, O., and Katsura, T. (2003) Detailed structures of hexagonal diamond (lonsdaleite) and wurtzite-type BN. Japanese journal of applied physics, 42(4R), 1694.

Wu, B. R. (2007) Structural and vibrational properties of the 6H diamond: First-principles study. Diamond and Related Materials, 16(1), 21-28.

Zeng, Z., Yang, L., Zeng, Q., Lou, H., Sheng, H., Wen, J., Miller, D.J., Meng, Y., Yang, W., Mao, W.L. and Mao, H.K. (2017) Synthesis of quenchable amorphous diamond. Nature communications, 8(1), 322.

6. CONCLUSIONS AND FUTURE WORK

The study of minerals behavior under oriented stress fields is of fundamental importance to understand geological processes such as subduction, exhumation and impact shock events. Furthermore, the investigation of the elastic properties and traces of deformation of minerals allows the determination not only of their formation conditions (i.e. P-T of entrapment), but also of the most accurate procedure to characterize them.

The investigation of oriented stresses in the host-inclusion systems from UHPM rocks (Chapter **2**, **3** and **4**) allowed me to:

- Demonstrate that Raman spectroscopy measures strains and not stresses or pressures, thus showing that Raman hydrostatic pressure calibrations should not be used to interpret measurements of host-inclusion systems.

- Prove that strains and Raman shifts vary significantly across an inclusion as a result of the influence of shape combined with elastic anisotropy (Mazzucchelli et al. 2018; Campomenosi et al. 2018), and therefore that the Raman shifts measured in the center of inclusions are the least affected by the presence of edges and should be the only ones used to infer entrapment conditions.

- Determine the strains still acting on a quartz inclusion from the Raman wavenumber shifts and vice-versa by means of the phonon-mode Grüneisen tensor.

- Explore the effects of non-hydrostatic stresses on the structure and properties of alpha-quartz without the difficulties inherent in experiments, showing that the strains induced by deviatoric stress are mostly accommodated by shearing deformation of the SiO_4 tetrahedra, and not by significant changes in Si–O distances or Si–O–Si angles that is consistent with the observation that the SiO_4 tilts and rotations are the major structural change associated with the α–β transition.

In addition to the deviatoric stresses that can develop at the host-inclusion interface (e.g. birefringent haloes, see Chapter 1.2 and introduction of Chapter 2, 3 and 4), non-hydrostatic conditions could also occur even at the moment of entrapment as suggested by some geodynamical models (e.g. Mancktelow 1995; Mancktelow 2008 and Raimbourg and Kimura 2008). The presence of deviatoric stresses breaks the direct association of pressure with depth (i.e. 30 km depth = 1 GPa) and could make coesite or diamond, for example, stable at shallower

depths (e.g. 3GPa=50 km) from which they can be brought to the Earth's surface with different exhumation rates with respect to those calculated for lithostatic conditions (e.g. Massonne et al. 2007).

Therefore, a further development in the current theory for elastic geobarometry is needed to account for elastically anisotropic properties of the mineral phases in order to be able to detect possible deviatoric stresses at the time of entrapment. This requires further development beyond the concept of the entrapment isomeke which is a line in P-T space where the fractional volume changes of the host and inclusion are the same, see Chapter 1.2 and references therein. To account for the anisotropic elastic behavior of minerals (e.g. minerals with different elastic properties in different directions as for example quartz that is stiffer along c and softer along a-axis) the concept of axial isomekes is required. An axial isomeke is a line in P-T space along which a direction in the inclusion crystal expands and contracts by the same fractional amount as the parallel direction in the host crystal. This actually was the original concept of Rosendfeld and Chase (1961). The basic idea (see Figure 1) as detailed in some recent manuscripts (e.g. Alvaro et al 2020; Mazzucchelli et al 2019) is that if the entrapment occurred under hydrostatic conditions all of the axial isomekes should cross in one single point providing a unique P and T point of entrapment (Alvaro et al. 2020 and Mazzucchelli et al. 2019). In principle, if we can determine independent strain components in the inclusions with low correlations (see Bonazzi et al 2019) and with small uncertainties (i.e. uncertainty on a single strain smaller than its deviation from the hydrostatic stress or isotropic strain lines, see Bonazzi et al 2019) then, the axial isomekes not crossing at one single point could be interpreted in two ways. One option is the occurrence of non-elastic deformations processes occurring after the entrapment, the other option is that possible local deviatoric stresses have been recorded at the entrapment. Of course, validation of the latter will require a considerable amount of work including the development of methods to analyse inclusions with symmetry lower than uniaxial and to model correctly the effects of deviatoric stresses at entrapment.
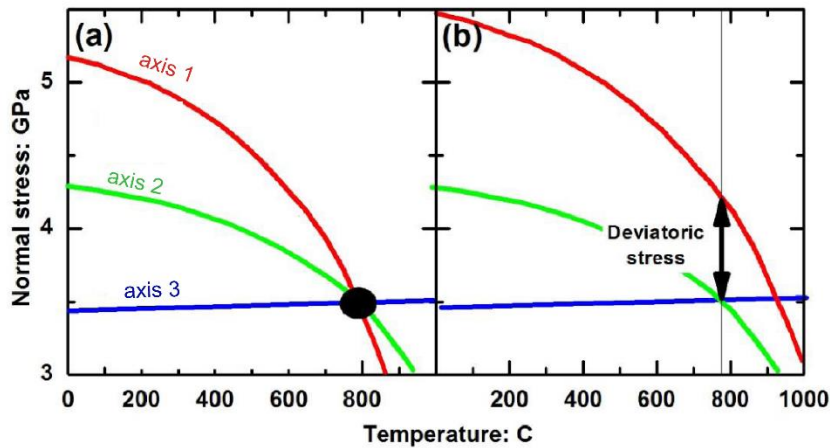
Figure 1. Sketches (not calculated) of linear isomekes for three perpendicular directions in a triaxial inclusion (e.g. olivine or coesite) trapped in a garnet. If the three lines cross at one point (a) then that uniquely identifies the entrapment conditions. If they do not cross at one point (b) then an independent determination of the entrapment temperature or pressure yields the deviatoric stress field at entrapment (courtesy of Matteo Alvaro).

On the other hand, the analysis of shock features due to the occurrence of highly oriented stress fields in Popigai impact diamonds (Chapter 5) led to a complete re-thinking on how these shocked materials, in particular diamonds, have to be investigated. In collaboration with colleagues from London, Budapest and Novosibirsk, we realized that more than one analysis is required on such samples to be able to understand their deformation features. Therefore, the major outcome from this work is that only a multi-technique approach can shed light on the nature of the preserved shock features in diamonds, whereas one technique is not enough and could lead to erroneous interpretations.

 It is now clear that the study of the effects of oriented stresses on mineral phases is still far from complete. Therefore, my next steps will be related to the investigation of shocked minerals found in impactites in order to first test if it is possible to detect the anisotropic (e.g. uniaxial) strain fields experienced by crystal structures during shock events and constrain the orientation of the imposed stresses.

During my PhD, besides the investigation of quartz, I took part in studies of other phases including diamond, zircon and rutile (e.g. Jones et al. 2016; Stangarone et al. 2019a; Murri et al. 2019b and Musiyachenko et al. in prep). Also, I am currently carrying out simulations on olivine to obtain its Grüneisen tensor that will allow us to determine strains from the measured Raman wavenumber shifts following the same procedure that works for quartz, zircon and rutile.

Deviatoric stresses in the most common silicate mineral inclusions found in garnet hosts (i.e. quartz, zircon and rutile) are mostly accommodated by distortion and deformation of the SiO_4 tetrahedra and ZrO_8 polyhedra (see Murri et al. 2019a; Stangarone et al. 2019a and Musiyachenko et al. in prep). These studies show that the dominant structural response of crystal structures to deviatoric stress is shear deformation of the strongly-bonded cation-oxygen polyhedra and, where this is allowed by the topology of the structure, the tilting of the polyhedra with respect to one another. Changes in bond distances are generally small because the stress that we measured on natural inclusions sitting in their host is less than 2 GPa and as a consequence small Raman wavenumber shifts are detected. This means that for infinitesimal strains the frequencies behave linearly and therefore the estimated Grüneisen components are constant in that range and they can be used to predict the strains as a function of the measured frequencies or viceversa for several minerals (i.e. quartz, zircon, rutile).

All of these mineral phases are also found in shock-impact environments as well as being common inclusion/host minerals in UHPM rocks. In particular, quartz is found in impactites and in meteorite fragments where it is full of planar deformation features (PDFs) (e.g. Stöffler and Langenhorst 1994; Grieve et al. 1996 and Fazio et al. 2018), zircon is found to convert to reidite under impact (e.g. Glass and Liu 2001; Gucsik et al. 2004; Wittmann and Reimold 2009; Chen et al. 2013; Reddy et al. 2015; Cavosie et al. 2018; Stangarone et al. 2019b) and diamond is found with intergrowths of cubic and hexagonally stacked layers at the nanoscale (e.g. Koeberl 1997; Masaitis 1998; Salzmann et al. 2015; Jones et al. 2016 and Murri et al. 2019b). Therefore, one could investigate whether the changes in Raman spectra found in shocked minerals are in part or in whole caused by residual strains. If so, this would enable Raman spectroscopy to be used to characterize shocked materials, far faster than the present methods of high-resolution TEM.

However, one of the challenges to applying these methods to more complex materials such as impactite is that the work I have already described is based on *ab initio* calculations of elastically deformed minerals but with their original symmetry. This is appropriate for inclusions hosted in cubic garnets provided they were trapped under hydrostatic conditions because the symmetry of the inclusion is not broken by the isotropic strain imposed by the garnet host mineral. However, in minerals subject to strain gradients the symmetry is broken. The simplest example to consider is the breaking of the symmetry of cubic host crystals, such as garnet and diamond, around

inclusions due to the mutual elastic relaxation, which can be seen optically by the appearance of birefringent haloes (e.g. Howell et al. 2010, Howell 2012). The effect of symmetry-breaking by strains on the frequencies of phonon modes is not known and is completely different from the structural phase transitions involving soft modes. This is an additional complication, but there is a direct relation between the stress-induced birefringence and the Raman scattering generated by the fully symmetrical phonon modes (Campomenosi et al. under revision). Indeed, Campomenosi et al. under revision show that the ratio between measured Raman peak intensities collected in cross and parallel polarized scattering geometry of totally symmetrical modes, represents a useful tool to constrain the radial stress decay from the host-inclusion boundary. Further, the authors demonstrate how group-theory considerations and tensor analysis of the morphic effect on the phonons and optical properties of the host can help to derive useful information on the symmetry of the acting stress. Moreover, *ab initio* simulations could be performed based on the experimental evidence from optical microscopy analyses (e.g. birefringent haloes as markers of local deformation, Campomenosi et al under revision), micro Raman spectroscopy (strain gradients across the crystal, Murri et al. 2018 on American Mineralogist, Campomenosi et al under revision) and X-ray diffraction (overall deformation Murri et al. 2018 in American Mineralogist) in order to build up a series of calculations resembling the natural samples. Of course, this will require simulations to be performed that account for symmetry breaking strains that so far, I have not needed to address in the context of interpreting spectra from inclusions. Establishing the boundary conditions above which the symmetry would collapse (i.e. symmetry breaking strains) will already provide key constraints for interpretation of several geologically-relevant processes.

References

Alvaro, M., Mazzucchelli, M.L., Angel, R.J., Murri, M., Campomenosi, N., Scambelluri, M., Nestola, F., Korsakov, A., Tomilenko, A.A., Marone, F., Morana, M. (2020) Fossil subduction recorded by quartz from the coesite stability field, Geology, in press.

Bonazzi, M., Tumiati, S., Thomas, J.B., Angel, R.J. and Alvaro, M., 2019. Assessment of the reliability of elastic geobarometry with quartz inclusions. Lithos, 350, p.105201.

Campomenosi, N., Mazzucchelli, M.L., Mihailova, B.D., Scambelluri, M., Angel, R.J, Nestola, F., Reali, A., and Alvaro, M. (2018) How geometry and anisotropy affect residual strain in host inclusion system: coupling experimental and numerical approaches. American Mineralogist, 103(12), 2032-2035.

Campomenosi, N., Mazzucchelli, M.L., Mihailova, B.D., Angel, R.J., and Alvaro, M. (under revision). Using polarized Raman spectroscopy to study the stress gradient in mineral systems with anomalous birefringence.

Cavosie, A.J., Timms, N.E., Erickson, T.M., and Koeberl, C. (2018) New clues from Earth's most elusive impact crater: evidence of reidite in Australasian tektites from Thailand. Geology, 46, 203–206.

Chen, M., Yin, F., Li, X., Xie, X., Xiao, W., and Tan, D. (2013) Natural occurrence of reidite in the Xiuyan crater of China. Meteoritics & Planetary Science, 48, 796–805.

Fazio, A., Pollok, K., and Langenhorst, F. (2018) Experimental evidence for mechanical Brazil twins as an indicator of low-pressure shock metamorphism (< 17.5 GPa). Geology, 46(9), pp.787-790.

Glass, B.P., and Liu, S., (2001). Discovery of high-pressure ZrSiO4 polymorph in naturally occurring shock-metamorphosed zircons. Geology, 29(4), pp.371-373.

Grieve, R.A., Langenhorst, F., and Stöffler, D. (1996) Shock metamorphism of quartz in nature and experiment: II. Significance in geoscience. Meteoritics & Planetary Science, 31(1), pp.6-35.

Gucsik, A., Zhang, M., Koeberl, C., Salje, E.K., Redfern, S.A., and Pruneda, J.M. (2004). Infrared and Raman spectra of ZrSiO4 experimentally shocked at high pressures. Mineralogical Magazine, 68(5), pp.801-811.

Howell, D., Wood, I. G., Dobson, D. P., Jones, A. P., Nasdala, L., and Harris, J. W. (2010) Quantifying strain birefringence halos around inclusions in diamond. Contributions to Mineralogy and Petrology, 160, 705-717

Howell, D. (2012) Strain-Induced Birefringence in Natural Diamonds. European Journal of Mineralogy, 24, 575-585.

Jones, A.P., McMillan, P.F., Salzmann, C.G., Alvaro, M., Nestola, F., Prencipe, M., Dobson, D., Hazael, R., and Moore, M. (2016) Structural characterization of natural diamond shocked to 60 GPa; implications for Earth and planetary systems. Lithos, 265, 214-221.

Koeberl, C., Masaitis, V. L., Shafranovsky, G. I., Gilmour, I., Langenhorst, F., and Schrauder, M. (1997). Diamonds from the Popigai impact structure, Russia. Geology, 25(11), 967-970.

Mancktelow, N. S. (1995) Non-lithostatic pressure during sediment subduction and the development and exhumation of high pressure metamorphic rocks. Journal of Geophysical Research: Solid Earth, 100(B1), 571-583.

Mancktelow, N. S. (2008) Tectonic pressure: Theoretical concepts and modelled examples. Lithos, 103(1-2), 149-177.

Masaitis, V. L. (1998). Popigai crater: Origin and distribution of diamond-bearing impactites. Meteoritics & Planetary Science, 33(2), 349-359.

Massonne, H., Kennedy, A., and Nasdala, L.N. (2007) Dating of zircon and monazite from diamondiferous quartzofeldspathic rocks of the Saxonian Erzgebirge - hints at burial and exhumation velocities. Mineralogical Magazine, 71, 407–425.

Mazzucchelli, M.L., Burnley, P., Angel, R.J., Morganti, S., Domeneghetti, M.C., Nestola, F., and Alvaro, M. (2018). Elastic geothermobarometry: Corrections for the geometry of the host-inclusion system. Geology, 46(3), 231-234.

Mazzucchelli, M.L., Reali, A., Morganti, S., Angel, R.J. and Alvaro, M., 2019. Elastic geobarometry for anisotropic inclusions in cubic hosts. Lithos, 350, p.105218.

Murri M., Alvaro M., Angel R.J., Prencipe M., Mihailova B.D. (2019a) Physics and Chemistry of Minerals, 46(5), 487-499

Murri, M., Smith, R.L., McColl, K., Hart, M., Alvaro, M., Jones, A.P., Németh, P., Salzmann, C.G., Corà, F., Domeneghetti, M.C. Nestola, F., Sobolev, N,V., Vishnevsky, S.A, Logvinova, A.M., and McMillan, P.F. (2019b). Quantifying hexagonal stacking in diamond. Scientific Reports, 9(1), p.10334.

Musiyachenko, K.A., Murri, M., Prencipe M., Angel R.J., Alvaro, M. (in preparation) A new Grüneisen tensor for rutile and its application in host inclusion systems.

Raimbourg, H., and Kimura, G. (2008) Non-lithostatic pressure in subduction zones. Earth and Planetary Science Letters, 274(3-4), 414-422.

Reddy, S.M., Johnson, T.E., Fischer, S., Rickard, W.D.A., and Taylor, R.J.M. (2015). Precambrian reidite discovered in shocked zircon from the Stac Fada impactite, Scotland. Geology, 43, 899–902.

Salzmann, C. G., Murray, B. J. and Shephard, J. J. (2015). Extent of stacking disorder in diamond. Diamond and Related Materials, 59, 69-72.

Stangarone, C., Angel, R. J., Prencipe, M., Campomenosi, N., Mihailova, B., and Alvaro, M. (2019a) Measurement of strains in zircon inclusions by Raman spectroscopy. European Journal of Mineralogy.

Stangarone, C., Angel, R. J., Prencipe, M., Mihailova, B., and Alvaro, M. (2019b) New insights into the zircon-reidite phase transition. American Mineralogist 104 (6), 830-837

Stöffler, D., and Langenhorst, F. (1994). Shock metamorphism of quartz in nature and experiment: I. Basic observation and theory. Meteoritics, 29(2), pp.155-181.

Wittmann, A., and Reimold, W. (2009). The record of ground zero in the Chesapeake Bay impact crater—Suevites and related rocks. GSA Special Paper, 458, 349–376.

APPENDIX I. INTRACRYSTALLINE "GEOTHERMOMETRY" ASSESSED ON CLINO AND ORTHOPYROXENE BEARING SYNTHETIC ROCKS

Mara Murri[1], Fernando Cámara[2], John Adam[3], Maria C. Domeneghetti[1], Matteo Alvaro[1]

[1]*Department of Earth and Environmental Sciences, University of Pavia, Via A. Ferrata, 1 I-27100* 4 *Pavia, Italy*
[2]*Dipartimento di Scienze della Terra, Università degli Studi di Milano, Italy*
[3]*Department of Earth and Planetary Sciences, Macquarie University, Sydney, 2109, Australia*

ABSTRACT

Recent discussion on the application of intracrystalline "geothermometers" based on the Fe-Mg order-disorder reaction in pyroxene in natural rocks, indicates that the available calibration equations for clino and orthopyroxenes (cpx and opx), which express the equilibrium intracrystalline Fe-Mg distribution coefficient k_D (Fe-Mg) as a function of temperature, require independent validation.

In this paper, we tested the available experimental calibrations for clino and orthopyroxenes by determining the site occupancies of these minerals in synthetic samples grown from a hydrous nepheline basanite in a piston-cylinder apparatus at 1050°C at 2.0 GPa to 1170 °C at 3.0 GPa and quenched very rapidly by shutting off the power. The site occupancies were determined by single crystal X-ray diffraction (SC-XRD) and used to calculate the closure temperature, T_C, of cation ordering using available calibrations of k_D (Fe-Mg) vs. T. The calculated T_C values of both clino and orthopyroxenes were found to be close to the temperatures at which they were quenched, in line with expected kinetic behaviour, when calibrations for cpx (Murri et al. 2016) and opx (Stimpfl et al. 2005) based on SC-XRD structure refinements were used. In particular, the smallest discrepancy between calculated and actual temperature is of the order of a few degrees (12 °C for cpx and 4 °C for opx), and the largest is of the order of tens of degrees (22 °C for cpx and 55 °C for opx). On the other hand, much lower T_Cs were obtained when calibrations based on Mössbauer determination of site occupancies were used.

These results confirm that the two methods (i.e. SC-XRD and Mössbauer) give inherently different site occupancy data and that the same methodology should thus be used for both calibration and natural samples in the determination of cooling rate of host rocks.

Keywords: pyroxenes, intracrystalline thermometry, synthetic samples, closure temperature.

INTRODUCTION

Studies of both intra- and intercrystalline cation ordering are commonly used to infer the thermal history of crystals and their host rocks. The two approaches make use of cation partitioning but have different response rates to temperature change. Intercrystalline exchange thermometry is normally used for systems with many mineral phases. At initial temperature, these minerals must be in mutual equilibrium and have comparatively slow responses to changes in temperature (due to long diffusion paths). Thus, the method of intercrystalline exchange thermometry is commonly used to retrieve the maximum temperature experienced by the host rock. On the other hand, the intracrystalline approach is based on cation exchange between crystallographic sites within a single crystal, and its sensitivity to temperature change thus tends to be much greater, leading to a closure temperature (T_C) of cation ordering that is significantly lower for slow cooled rocks than the inferred peak temperature from intercrystalline exchange thermometry. Using Mueller's (1967) kinetic formulation of Fe-Mg order-disorder in orthopyroxene, Ganguly (1982) developed a numerical method for retrieving the cooling rates of rocks on the basis of the quenched ordering states of pyroxenes. As Ganguly himself notes, for slowly cooled rocks, the retrieved cooling rates are only applicable to a limited temperature range around the T_C for the specific samples, which are typically much lower than the temperatures determined by intercrystalline thermometry (e.g. Ganguly et al. 1994).

In earlier studies, the intracrystalline cation exchange reaction in pyroxenes - Mg($M1$) + Fe($M2$) = Mg($M2$) + Fe ($M1$) - was used to define a distribution coefficient, k_D(Fe-Mg), as (Fe/Mg)^{M1}/(Fe/Mg)^{M2}, and calibrated as a function of temperature yielding a linear relation between lnk_D and $1/T$(K). The site occupancies were determined either by single crystal X-ray diffraction or by Mössbauer spectroscopy. Over the past 45 years, intracrystalline thermometry based on Fe^{2+}-Mg ordering measured by SC-XRD has been extensively applied to opx, pigeonite (Virgo and Hafner 1969; Saxena and Ghose 1971; Smyth 1973; Sueno et al. 1976; Ganguly 1982; Ghose and Ganguly 1982; Ganguly and Saxena 1987; Molin and Zanazzi 1991; Sykes-Nord and Molin, 1993; Ganguly and Domeneghetti 1996; Stimpfl et al. 1999; Pasqual et al. 2000; Fioretti et al. 2007; Alvaro et al. 2011; Scandolo et al. 2015) and cpx bearing rocks (McCallister et al. 1976; Dal Negro et al. 1982; Ghose and Ganguly 1982; Molin and Zanazzi 1991; Brizi et al. 2000;

Nestola et al. 2016) of extraterrestrial (Alvaro et al. 2011, 2015) and terrestrial origin (Murri et al. 2016).

As stated by Ganguly (1982) and shown in his Figure 19 (redrawn here as Figure 1 for the purpose of discussion), the temperature that can be retrieved from k_D is, in general, neither (i) the crystallization temperature (T_0) of the mineral as, after this event, cooling starts inducing the ordering process; nor (ii) the quenching temperature (T_Q) at which the ordering process is ultimately blocked. The temperature retrieved from k_D, referred to as the closure temperature of cation ordering, T_C, is in fact the apparent equilibration temperature (Dodson 1976) corresponding to the quenched ordering state, as illustrated in Figure 1, and is intermediate between T_0 and T_Q; the difference between T_0 and T_C decreases as the cooling rate increases.
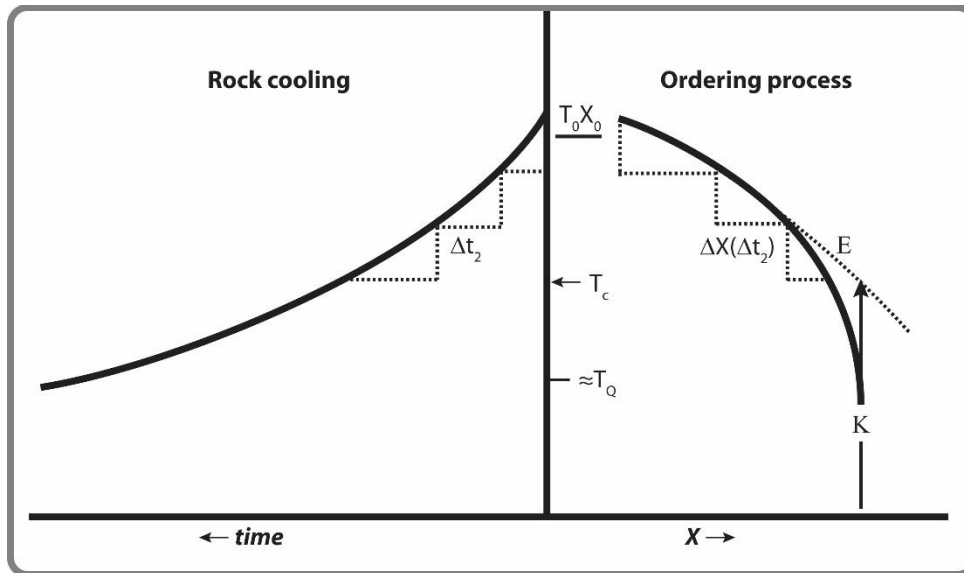
Figure 1. Redrawn from *Figure 19* by Ganguly, (1982). Ordering in a continuously cooling system. X_0 is the ordering state at the temperature T_0. E is the equilibrium ordering path, whereas K is the actual ordering path which is controlled by the kinetics of intracrystalline exchange and cooling rate. T_C is the closure temperature or temperature of apparent equilibration corresponding to the quenched ordering state. T_Q is the temperature from which the observed ordering state has been effectively quenched.

It follows that the closure temperature of the exchange depends upon the kinetics of the Fe^{2+}-Mg order-disorder reaction combined with the cooling rate. How well Fe^{2+} - Mg order – disorder is preserved in natural rocks is affected by the "speed" at which the reaction occurs (and thus by the cooling rate of the crystal). This "speed" can be determined experimentally (see Domeneghetti et al. 1999, 2005, 2007; Alvaro et al. 2011, 2015). It is dependent on temperature

and is thus linked to the cooling rate of the mineral phase (see Ganguly 1982). It can be interpreted as the capacity of the cation exchange reaction to proceed in response to the cooling path of the host rock. For minerals subject to fast cooling rates (typically in the order of 1°C/day or more, calculated around the corresponding T_C, Takeda 1987; Tribaudino et al. 1997, Domeneghetti et al. 1999; Zema et al. 1999; Alvaro et al. 2011; Di Rocco et al. 2016), and where there is no re-heating or any reopening of the system at temperatures above the T_C, one could reasonably expect the calculated closure temperatures to be close to peak temperatures, where peak is meant as the maximum temperature achieved by the whole system (as during eruptions of submarine volcanoes or submarine lava flows). In contrast, for minerals in rocks with slow cooling rates (e.g. 1 °C/Ma at the T_C = 250 °C for opx from mesosiderites, Ganguly et al. 1994), the cooling path can be followed down to temperatures of the order of very few hundreds of degrees (e.g. for blanketing processes).

With a number of calibrated "geothermometers" available, intracrystalline exchange thermometry has demonstrated wide applicability in the field of earth and planetary sciences, especially in the determination of cooling rates. This includes exploration of the cooling paths of volcanic rocks in a wide range of thermal environments from slow cooling martian nakhlites (e.g. Righter et al. 2014; Giesting et al. 2015; Righter et al. 2016; Giesting et al. 2016 and Filiberto 2016) to fast cooling terrestrial submarine lavas (e.g. Malgarotto et al. 1993).

To assess the quality of calibration of k_D (Fe-Mg) vs. T, we carried out a series of X-ray diffraction experiments followed by structural refinements to determine the closure temperature of rapidly quenched synthetic samples, and compared the retrieved T_C values with their synthesis temperatures (T_0). At the rate at which the samples were quenched, T_C could be expected to be very similar to T_0 if calibrations were correct and site occupancy determination was not affected by methodology (X-ray diffraction vs. Mössbauer spectroscopy).

EXPERIMENTAL METHODS
Synthesis and sample selection for X-ray diffraction

Our study was performed on pyroxenes crystallized experimentally from a natural nepheline basanite (UT-70489) by Adam and Green (2006). These synthesis experiments were originally conducted to determine mineral/melt partition coefficients for conditions of garnet lherzolite melting. Details of the experimental techniques used are contained in Adam and Green

(2006). In brief, experiments were performed in end-loaded piston-cylinder apparatus at Macquarie University. Furnace assemblies were of diameter 12.7 mm with talc/Pyrex® sleeves and boron nitride inserts. A cold-piston-in technique was employed together with a -10 % correction for the effects of friction on measured pressures. Temperatures were measured with $Pt-Pt_{90}Rd_{10}$ thermocouples and controlled by means of a Leeds and Northrup Electromax V single-loop controller. The starting materials were mixtures of trace element-doped glass and H_2O (5-10 wt. %) contained in graphite-lined Pt capsules. Run conditions varied from 3.5 to 1.0 GPa and from 1020 to 1190 °C. Total duration of each run was 48 hours. To encourage the growth of large crystals, runs were maintained at 110 °C above target temperatures for the first 30 minutes and then gradually cooled over the next 30 minutes to final run temperature. Oxygen fugacities were not buffered, but in the capsule type used are believed to be relatively low and between those of magnetite-wustite and Ni-NiO (see discussion of Green 1976). This assessment is confirmed by application of the results of Mallmann and O'Neill (2009) to the relative partitioning of (redox sensitive) V and (non redox-sensitive) Ga and Sc in the same experiments.

At the end of each run experiments were quenched by shutting power to the apparatus. This resulted in initial temperature decreases of several hundreds of °C within 2-3 seconds. After each experiment, capsules were sectioned and polished, and the concentrations of major, minor and trace elements in run products were determined by electron microprobe and LAM-ICP-MS (see Adam and Green 2006). Crystals used in the present study were selected from three experiments. Individual crystals were extracted from different portions of each capsule so as to avoid the possibility of past contact with one another.

The distances between selected crystals and the absence of other interacting phases allowed us to assume that no intercrystalline exchange had taken place after quenching in these experiments. This is further corroborated by the results of intercrystalline geothermometry in Adam and Green (2006). Three experiments were selected for study - runs R80, 1948 and 1950 - as those provided suitable crystals of both cpx and opx with radius larger than 60μm. The synthesis conditions of the individual experiments were as follows: run R80, 1170 °C and 3.0 GPa; run 1948, 1160 °C and 2.5 GPa; run 1950, 1050 °C and 2.0 GPa. A total of six crystals were extracted from the glass at the polished surface of the half-recovered capsules with the aid of a sharp needle, and their quality was checked by optical microscopy (for absence of twinning) and then by X-ray diffraction (for sharp peak profile).

Single-crystal X-ray diffraction and structure refinement

Single crystal X-ray data collections were performed with a three-circle Bruker/AXS SMART-Apex diffractometer equipped with a CCD detector, using graphite monochromatized Mo *K*α X-ray radiation (λ = 0.71073 Å, 55 kV, 30 mA), for R80 (opx), 1948 (cpx and opx), 1950 (cpx and opx) samples. For the cpx R80, the intensity data collection was performed with a Philips PW1100 4-circle point-detector, using graphite monochromatized Mo *K*α X-ray radiation (λ = 0.71073 Å, 55 kV, 30 mA). Data collections and reductions were performed following the same procedure as in Adam et al. (2007). Table 1a and 1b show the unit cell parameters, the discrepancy indices R_{merge}, R_{all}, R_w on all the F_o^2 and the goodness of fit (*S*) of the structure refinements with chemical constraints for the six crystals.

Table 1a. Unit cell parameters for clinopyroxenes R80, 1948 and 1950 and information on data collection and structural refinement.

	CPX R80 N.1	CPX 1948 N.1	CPX 1950
Size (mm) of the crystal	$0.198 \times 0.165 \times 0.165$	$0.1 \times 0.075 \times 0.05$	$0.085 \times 0.075 \times 0.05$
P (Gpa)	3	2.5	2
T_Q (°C)	1170	1160	1050
a (Å)	9.6860 (3)	9.6962 (5)	9.7217 (6)
b (Å)	8.8447 (2)	8.8587 (5)	8.8945 (6)
c (Å)	5.2639 (2)	5.2623 (3)	5.2599 (3)
β(°)	107.007 (3)	106.885 (1)	106.548 (2)
V (Å³)	431.24 (2)	432.52 (4)	435.98 (5)
θ_{max} - θ_{min} (°)	35-3.2	38.6-3.2	35-3.2
Refl.no.	957	1202	969
R_{merg} (%)	2.5	1.6	2.2
R_{all}	0.02	0.021	0.025
R_w	0.046	0.052	0.06
S	1.06	1.13	1.07
m.a.n.* M1	13.25 (2)	13.57 (2)	13.99 (3)
m.a.n.* (M2+M21)	17.99 (5)	18.65 (5)	19.49 (5)
m.a.n.* (M1+M2+M21)	31.24 (5)	32.23 (5)	33.48 (6)

Standard deviations are given in parentheses. *Refl.no.* is the number of measured reflections; $R_{int} = \Sigma \mid F_o^2 - F_o^2 \text{(mean)} \mid / \Sigma [F_o^2]$ where F_o and F_c are the observed and calculated structure factors; $R_{all} = \Sigma \mid\mid F_o^2 \mid - \mid F_c^2 \mid\mid / \Sigma [F_o^2]$; $R_w = \{\Sigma [w(F_o^2 - F_c^2)^2] / \Sigma [w(F_o^2)^2]\}^{1/2}$; $S = [\Sigma [w(F_o^2 - F_c^2)^2] / (n\text{-}p)]^{0.5}$, where *n* is the number of reflections and *p* is the total number of parameters refined. * m.a.n. is the mean atomic number (in electrons per formula unit) before introducing the chemical constraints. Crystal system monoclinic *C*2/*c*; radiation type Mo *K*α.

Table 1b. Unit cell parameters for orthopyroxenes R80, 1948 and 1950 and information on data collection and structural refinement.

	OPX R80 N.1	OPX 1948 N.1	OPX 1950
Size (mm) of the crystal	$0.06 \times 0.035 \times 0.035$	$0.09 \times 0.05 \times 0.04$	$0.150 \times 0.055 \times 0.045$
P (Gpa)	3	2.5	2
T_Q (°C)	1170	1160	1050
a (Å)	18.2624 (9)	18.2836 (10)	18.2815 (7)
b (Å)	8.8220 (4)	8.8328 (5)	8.8466 (3)
c (Å)	5.2036 (3)	5.2067 (3)	5.2075 (2)
$\alpha=\beta=\gamma$ (°)	90	90	90
V (Å3)	838.36 (7)	840.86 (8)	842.20 (5)
$\theta_{max} - \theta_{min}$ (°)	38.7-2.2	35.1-2.2	38.7-3.2
$Refl.no.$	2353	1854	2363
R_{merg} (%)	3.6	4.8	3.8
R_{all} (%)	0.036	0.037	0.032
R_w (%)	0.08	0.087	0.073
S	1.13	1.15	1.11
m.a.n.* M1	13.06 (3)	13.07 (4)	13.31 (3)
m.a.n.* M2	15.34 (4)	15.44 (5)	16.38 (4)
m.a.n.* (M1+M2)	28.40 (5)	28.52(6)	29.68(5)

Standard deviations are given in parentheses. *Refl.no.* is the number of measured reflections; $R_{int} = \Sigma \left| F_o^2 - F_o^2 (\text{mean}) \right| / \Sigma [F_o^2]$ where F_o and F_c are the observed and calculated structure factors; $R_{all} = \Sigma \left| \left| F_o^2 \right| - \left| F_c^2 \right| \right| / \Sigma [F_o^2]$; $R_w = \{ \Sigma [w(F_o^2 - F_c^2)^2] / \Sigma [w(F_o^2)^2] \}^{1/2}$; $S = [\Sigma [w(F_o^2 - F_c^2)^2] / (n-p)]^{0.5}$, where n is the number of reflections and p is the total number of parameters refined. * m.a.n. is the mean atomic number (in electrons per formula unit) before introducing the chemical constraints. Crystal system orthorhombic *Pbca*; radiation type Mo $K\alpha$.

The observed F_o^2 values were treated with a full-matrix least-squares refinement in the *C*2/*c* space group for cpx and *Pbca* for opx using SHELX-97 (Sheldrick 2008). For cpx we started from the atomic coordinates for sample TS7 N.1 (Domeneghetti et al. 2013) and followed the same refinement procedure as Rossi et al. (1987), taking into account the *M*21 and O2B1 split sites, refined with isotropic displacement parameters. For opx we followed the structural refinement procedure of Domeneghetti et al. (2007). The extinction correction was applied with the procedures of the SHELX-97 program. The atomic scattering curves were taken from the *International Tables for X-ray Crystallography* (Ibers and Hamilton 1970, 1974). Neutral versus ionized scattering factors were refined for all sites not involved in chemical substitutions

(Hawthorne et al. 1995). For cpx, complete ionization of Mg and Fe in the $M1$ site, of Ca and Mg in the $M2$ site, and of Fe in the $M21$ site was assumed, whereas for opx complete ionization of Mg and Fe in $M1$ and $M2$ sites was assumed. Individual weights and the weighting scheme suggested by the program were used. Tables 1a and 1b respectively show the mean atomic numbers (m.a.n.) in electrons per formula unit (e.p.f.u.) at the crystallographic sites - $M1$, $M2$ and $M21$ for cpx; and $M1$ and $M2$ for opx - obtained when the structure refinement, without chemical constraints, reached convergence.

Electron Microprobe Analysis (EMPA)

Major and minor elements, including halogens, were analyzed with a JEOL 8200 Super Probe operating in X-ray wavelength-dispersive mode (WDS-EMPA) at the Department of Earth Sciences, University of Milan. Operating conditions included an accelerating voltage of 15 kV, a specimen current of 5 nA, and a beam diameter of 1 μm. Corrections to the raw data were made with the ϕρZ procedure. The following standard and spectral lines were used for calibration: omphacite (NaKα), K-feldspar (KKα), grossular (CaKα, SiKα), olivine (MgKα), NiAs (NiKα), rhodonite (MnKα), fayalite (FeKα), almandine (AlKα), Cr (CrKα), V (VKα), ilmenite (TiKα), and graftonite (PKα).

The results of EMPA performed on cpx and opx single crystals reported in Tables 2a and 2b are in good agreement with those reported by Adam and Green (2006) and Adam et al. (2007). Moreover, for both cpx and opx samples, the values of electrons per formula unit calculated from the EMPA (see Table 2a and 2b) agree within less than 1 standard deviation with the calculated mean atomic numbers from the unconstrained refinements (see Table 1a and 1b).

Table 2a. Electron microprobe analysis for clinopyroxenes R80, 1948 and 1950 and formula in atoms per formula unit (a.p.f.u.) based on six oxygen atoms.

	CPX R80		CPX 1948		CPX 1950	
	(averaged 10 spots)		(averaged 10 spots)		(averaged 10 spots)	
wt%						
SiO_2	52.71	(33)	51.77	(23)	51.90	(70)
Al_2O_3	7.20	(15)	6.62	(31)	4.32	(87)
TiO_2	0.54	(5)	0.62	(4)	0.81	(24)
Cr_2O_3	0.29	(3)	0.14	(3)	0.17	(6)
FeO	5.31	(12)	6.33	(12)	7.07	(47)
MnO	0.16	(3)	0.15	(4)	0.16	(3)
NiO	0.01	(2)	0.06	(3)	0.02	(2)
MgO	16.04	(23)	16.52	(30)	16.25	(31)
CaO	14.94	(9)	15.71	(31)	17.68	(86)
Na_2O	2.19	(6)	1.57	(7)	1.11	(12)
K_2O	0.01	(1)	0.01	(1)	0.00	(0)
P_2O_5	0.03	(3)	0.03	(5)	0.03	(3)
Total	99.42	(49)	99.43	(29)	99.40	(32)
a.p.f.u.						
Si	1.905	(5)	1.880	(7)	1.903	(25)
AlIV	0.094	(5)	0.119	(6)	0.096	(25)
P	0.001	(1)	0.001	(2)	0.001	(1)
Al	0.213	(5)	0.164	(9)	0.091	(13)
Ti	0.015	(1)	0.017	(1)	0.022	(7)
Cr	0.008	(1)	0.004	(1)	0.005	(2)
Fe^{2+}	0.161	(4)	0.190	(4)	0.213	(14)
Ni	0.001	(2)	0.005	(3)	0.002	(2)
Mn^{2+}	0.005	(1)	0.005	(1)	0.005	(1)
Mg	0.864	(9)	0.894	(15)	0.888	(17)
Ca	0.579	(5)	0.611	(13)	0.695	(34)
Na	0.153	(5)	0.110	(5)	0.079	(9)
Total	3.998	(4)	4.000	(4)	4.000	(5)
m.a.n.*	30.93	(28)	32.08	(25)	33.44	(56)

m.a.n.*: calculated total mean atomic number for *M*1 *M*2 and *M*21 sites, in electrons per formula unit. Standard deviations are given in parentheses.

Table 2b. Electron microprobe analysis for orthopyroxenes R80, 1948 and 1950 and formula in atoms per formula unit (a.p.f.u.) based on six oxygen atoms.

	OPX R80		OPX 1948		OPX 1950	
	(averaged 5 spots)		(averaged 10 spots)		(averaged 10 spots)	
wt%						
SiO_2	54.94	(19)	55.07	(44)	54.13	(42)
Al_2O_3	3.51	(7)	2.96	(45)	3.10	(61)
TiO_2	0.17	(2)	0.19	(4)	0.31	(5)
Cr_2O_3	0.13	(3)	0.17	(4)	0.17	(5)
FeO	9.27	(22)	9.3	(11)	12.42	(30)
MnO	0.17	(3)	0.15	(5)	0.18	(4)
NiO	0.03	(4)	0.01	(2)	0.07	(3)
MgO	30.13	(25)	30.49	(35)	27.87	(51)
CaO	1.28	(3)	1.40	(6)	1.84	(37)
Na_2O	0.31	(4)	0.20	(3)	0.17	(4)
K_2O	0.01	(1)	0.00	(1)	0.00	(1)
P_2O_5	0.04	(2)	0.02	(3)	0.02	(2)
Total	99.95	(17)	99.93	(30)	100.22	(25)
a.p.f.u.						
Si	1.925	(6)	1.931	(12)	1.922	(14)
AlIV	0.074	(7)	0.069	(12)	0.077	(14)
P	0.001	(1)	0.001	(1)	0.001	(1)
Al	0.071	(6)	0.054	(9)	0.052	(13)
Ti	0.005	(1)	0.005	(1)	0.008	(1)
Cr	0.004	(1)	0.005	(1)	0.005	(2)
Fe^{2+}	0.270	(7)	0.271	(3)	0.367	(9)
Ni	0.002	(3)	0.001	(2)	0.006	(3)
Mn^{2+}	0.005	(1)	0.005	(1)	0.006	(1)
Mg	1.573	(12)	1.593	(15)	1.475	(26)
Ca	0.048	(1)	0.053	(2)	0.070	(14)
Na	0.021	(3)	0.014	(2)	0.011	(3)
Total	4.000	(6)	4.000	(4)	4.000	(4)
m.a.n.*	28.77	(42)	28.76	(34)	30.00	(12)

m.a.n.*: calculated total mean atomic number for $M1$ and $M2$ sites, in electrons per formula unit. Standard deviations are given in parentheses.

RESULTS

Site populations and Fe^{2+}-Mg ordering degree

To determine the pyroxene site population, we performed full-matrix least-squares refinements using the results from the EMPA analysis as chemical constraints, and the same refinement strategy and constraints as in Domeneghetti et al. (2013) for the cpx and in Domeneghetti et al. (2007) for the opx (in both cases assuming 1 standard deviation as the error). In particular, for cpx, Mn was partitioned in the same way as Fe^{2+} (Hawthorne and Ito 1978). Otherwise, for the opx, $M1$ and $M2$ site distribution was obtained by considering Mn fully ordered in the $M2$ site in accordance with the stronger preference of Mn compared to Fe^{2+} for the $M2$ site observed by Stimpfl (2005a, 2005b) in a donpeacorite sample.

The Fe^{2+}-Mg ordering state was obtained from the site population as distribution coefficient (k_D), considering as negligible the influence of pressure (as shown by the refinement results reported in Pandolfo et al. 2012).

The site populations obtained from the structural refinements with chemical constraints; and the distribution coefficients (k_D) with relative propagated errors, are reported in Table 3a and Table 3b for cpx and opx respectively. In Table 4 the tetrahedral and octahedral mean bond distances for opx, obtained from the structure refinement, are reported. The positional and atomic displacement parameters for cpx and for opx are shown in Tables S1 and S2 (deposited as supplementary material, see Appendix IV).

Table 3a. Site population for clinopyroxenes R80, 1948 and 1950 obtained from structure refinements using chemical constraints.								
		CPX R80		**CPX 1948**		**CPX 1950**	
Site							
T	Si	1.905		1.887		1.923	
	Al	0.095		0.114		0.077	
M1	Mg	0.694	(3)	0.712	(3)	0.764	(4)
	Fe	0.068	(2)	0.086	(2)	0.109	(3)
	Al	0.213		0.177		0.093	
	Cr	0.008		0.004		0.005	
	Ti	0.015		0.018		0.026	
	Mn	0.002		0.002		0.003	
M2	Mg	0.174	(4)	0.166	(4)	0.112	(7)
	Fe	0.090	(2)	0.105	(2)	0.106	(3)
	Ca	0.578		0.622		0.706	
	Mn	0.003		0.003		0.002	
	Na	0.156		0.104		0.074	
	XFe	0.15		0.18		0.20	
	Fs	10		12		12	
	k_D	0.191	(5)	0.191	(4)	0.150	(10)
T_C(°C)		1182	(13)	1182	(12)	1066	(28)

Note: $k_D = [(Fe^{2+}_{M1})(Mg_{M2})/(Fe^{2+}_{M2})(Mg_{M1})]$. The site occupancy values represent atoms per six oxygen atoms. Chemical constraints introduced are based on the chemical analysis (see Table 2a).

Table 3b. Site population for orthopyroxenes R80, 1948 and 1950 obtained from structure refinements using chemical constraints.

Site		OPX R80		OPX 1948		OPX 1950	
T	Si	1.930		1.939		1.934	
	Al	0.070		0.061		0.066	
M1	Mg	0.851	(3)	0.869	(3)	0.849	(3)
	Fe	0.064	(2)	0.062	(2)	0.082	(2)
	Al	0.076		0.058		0.056	
	Cr	0.004		0.006		0.005	
	Ti	0.005		0.005		0.008	
M2	Mg	0.715	(3)	0.715	(3)	0.636	(3)
	Fe	0.211	(2)	0.212	(2)	0.276	(4)
	Ca	0.048		0.054		0.071	
	Mn	0.005		0.006		0.006	
	Na	0.020		0.014		0.011	
	XFe	0.15		0.15		0.19	
	Fs	15		15		19	
	k_D	0.255	(8)	0.242	(8)	0.223	(5)
$T_C(°C)$		1138	(21)	1105	(20)	1054	(13)

Note: $k_D = X_{FeM1} (1-X_{FeM2})/X_{FeM2} (1-X_{FeM1})$. The site occupancy values represent atoms per six oxygen atoms. Chemical constraints introduced are based on the chemical analysis (see Table 2b).

Table 4. Bond lengths (Å) for orthopyroxenes

	R80	1948	1950
<SiA-O>	1.628 (2)	1.629 (2)	1.628 (2)
<SiB-O>	1.644 (2)	1.644 (2)	1.643 (2)
<M1-O>	2.073 (2)	2.076 (2)	2.079 (2)
<M1-O> calc *	2.071	2.073	2.075
<M2-O>	2.175 (2)	2.178 (2)	2.179 (2)

Notes: standard deviations are given in parentheses.
*: <M1-O>cal= 2.078 $XMgM1$+ 2.129 XFe^{2+}_{M1} + 2.030 XFe^{3+}_{M1} + 1.929 $XAl_{(6)M1}$ + 1.990 XTi_{M1} + 2.010 XCr_{M1} + 2.173 XMn_{M1} + 0.006 XFe^{2+}_{M2}.(Equation 18 from Domeneghetti et al., 1995)

Closure temperatures of quenched samples

For cpx and opx the relationship between the distribution coefficient (k_D) and the closure temperature of the Fe-Mg exchange reaction (T_C) is usually defined using calibration equations that express lnk_D as a function of $1/T$(K). For both systems (cpx and opx), recent calibration equations obtained from X-ray single-crystal diffraction data are available (Brizi et al. 2000; Stimpfl et al. 2005; Alvaro et al. 2011, 2015; Murri et al. 2016). In our study we only considered those determined for samples with compositions close to those of our own samples (i.e. with Fs_{12} and Fs_{10} for cpx, while for opx with Fs ranging between Fs_{15} and Fs_{19}). In particular, for cpx we relied on the calibration of Murri et al. (2016) because it produces reliable results on samples in the compositional range between Fs_9 and Fs_{24} [with $Fs=100*\Sigma Fe/(\Sigma Fe+Mg+Ca)$ where $\Sigma Fe=Fe^{2+}+Fe^{3+}+Mn$]. It is expressed by the relationship:

$$lnk_D = -4040 \ (\pm 180)/ \ T(K) + 1.12 \ (\pm 0.17) \ (R^2=0.988) \tag{1}$$

For opx, we used the calibration of Stimpfl et al. (2005) because it is valid for compositions close to Fs_{16}. It is given by:

$$lnk_D = -2984 \ (\pm 69)/T(K) + 0.747(\pm 0.078) \ (R^2=0.99) \tag{2}$$

As shown in Table 5, the calculated T_C values are in extremely good agreement with the quenching/synthesis temperatures within less than 1 e.s.d. for most of the samples. The largest discrepancy (i.e. 17°C for cpx 1950 and 55°C for opx 1948) does not exceed 3 e.s.d.s.

Table 5. The calculated T_C temperatures for both clinopyroxenes and orthopyroxenes.			
	R80	**1948**	**1950**
P (GPa)	3	2.5	2
T_Q (°C)	1170	1160	1050
T_C Cpx(°C)[*]	1182 (13)	1182 (12)	1066 (28)
T_C Opx(°C)[†]	1138 (21)	1105 (20)	1054 (13)
Notes: P and T are pressure and temperature at which the synthesis experiments performed by Adam and Green (2006) have been performed. [*]For the equation used see the text (equation 1 by Murri et al. 2016) [†]For the equation used see the text (equation 2 by Stimpfl et al. 2005)			

DISCUSSION

Estimation of closure temperature relies on accurate and precise determination of the Fe^{2+}-Mg ordering state expressed as the distribution coefficient (k_D). For this purpose, it is important that the influence of Fe^{3+} on site populations be accurately determined. In this respect, it is important to note that in cpx and opx crystals with low total iron, such as those in this study (from 0.16 (0.04) to 0.36 (0.05) a.p.f.u.), even a very small variation in Fe^{3+} content strongly affects calculated k_D values. This in turn affects calculated T_Cs. For example, if we presume a presence of Fe^{3+} of 0 to 0.036 a.p.f.u., applying the procedure of Papike et al. (1974) (^{VI}Al+ Fe^{3+} + Cr + 2Ti = ^{VI}Al + Na) in both cpx and opx, leads to T_C values that are lower by about 150°C in cpx (except for cpx R80 where Fe^{3+} occupancy remains zero) and by 66 to 242°C in opx. However, the relatively reduced synthesis conditions in which the crystals were grown, along with data from the EMPA analyses reported by Adam and Green (2006), and those performed on the single crystals from this study, do not support the presence of Fe^{3+} (see following paragraph for discussion on Fe^{3+}). Furthermore, at least for the opx samples, crystal-chemical evidence can be used to constrain R^{3+} cations. From equation (18), as in Domeneghetti et al. (1995), which allows the fraction of ^{IV}Al to be retrieved from the <SiB-O> with a good level of approximation (± 0.01), we obtained ^{IV}Al contents ranging from 0.052 to 0.061, thus constraining the total amount of R^{3+} cations that can enter the *M*1 site.

Moreover, when the *M*1 site populations (reported in Table 3b) of our opx were checked by comparing mean M1-O bond distances (see values of <M1-O> in Table 4 for opx) obtained from structure refinements with values calculated by equation (21) from Domeneghetti et al. (1995) the calculated <M1-O> were found to be shorter than the observed values suggesting that no Fe^{3+} is located in the *M*1 sites. Otherwise, there would have been a further decrease in the calculated <M1-O>. Regardless, we note that where the presence of Fe_{tot} consents a Mössbauer analysis, it must be carried out on both cpx and opx samples in order to yield a correct evaluation of Fe^{3+}/Fe^{total}. Unfortunately, in addition to their low Fe_{tot} content, the small size of our crystals did not allow the application of Mössbauer analysis. Thus, we carried out the present study without accounting for possible Fe^{3+}.

Estimates of T_C are strongly dependent on the choice of calibration equation. While for opx our choice was limited to one equation (i.e. Stimpfl et al. 2005), for cpx there are various options. These include the calibrations of Brizi et al. (2000) which are based on samples compositionally

similar to our own. Thus, we calculated closure temperatures for our cpx samples using Brizi et al.s' (2000) Eq. (3), based on an augite crystal from Vulcano basalt dike (PD30, $En_{42}Fs_{12}Wo_{46}$). We also used Brizi et al.s' (2000), Eq. (4), which accounts for the influence of Ca+Na and R^{3+} contents, to model the T_C for all of our samples. As a further comparison, we calculated T_C using Alvaro et al.s' (2015) calibration, obtained on a Martian augite crystal from Miller Range nakhlite (MIL 03346,13). This had a composition of about $En_{36}Fs_{24}Wo_4$, (see Table 6).

Table 6. The calculated T_C temperatures for clinopyroxenes			
	R80	**1948**	**1950**
P (GPa)	3	2.5	2
T_Q (°C)	1170	1160	1050
T_C (°C)[*]	1026 (9)	1026 (7)	953 (18)
T_C (°C)[¥]	1041 (12)	1045 (10)	943 (25)
T_C (°C)[†]	1146 (13)	1146 (10)	1044 (24)
Notes: P and T are pressure and temperature at which the synthesis experiments from Adam and Green (2006) have been performed. [*] $-lnk_D = 5305\ (\pm351)/T(K) - 2.428\ (\pm0.289)$; ($R = 0.98$) (Brizi et al., 2000) [¥] $T(K) = [12100\ (750) - 27700\ (1700)(Ca + Na + R^{3+}) + 20400\ (1000)(Ca + Na + R^{3+})^2]/[-lnk_D + 7.1\ (0.6) - 20.3\ (1.4)(Ca + Na + R^{3+}) + 15.2\ (0.8)(Ca + Na + R^{3+})^2]$ (Brizi et al., 2000) [†] $lnk_D = -4421\ (\pm561) / T(K) + 1.46\ (\pm0.52)$ ($R^2=0.988$) (Alvaro et al., 2015)			

From Tables 5 and 6 it can be seen that the smallest discrepancies between T_C (from XRD) and T_Q (or T_0) for cpx (6-24°C) were obtained using the calibrations of Murri et al. (2016) and Alvaro et al. (2015). Much larger deviations (97-144 °C) were obtained with the calibrations of Brizi et al. (2000), confirming that their calibrations underestimate T_C, as previously observed by Alvaro et al. (2015) for nakhlite pyroxenes.

For this reason, we suggest that the older calibrations for cpx, such as those of Brizi et al. (2000), should be treated with caution (see also the comment in Alvaro et al. 2015).

For opx the calibration of Stimpfl et al. (2005) gives discrepancies between closure temperatures (T_C) and quenching/synthesis temperatures T_Q (or T_0), that range from 4°C to 55°C. These are less than 2 e.s.d.s in all cases (see Table 5).

For purposes of comparison, we applied the calibration obtained by Wang et al. (2005) to our opx samples using a high-sensitivity Mössbauer spectrometer on two single-crystals of opx with X_{Fs} of 0.11 and 0.16. Site population was determined by these authors and by us according to Stimpfl et al. (2005), assuming Mn and Ca to be totally ordered in the *M2* site. From the results

reported in Table 7 it is evident that the three T_C data are much lower than the T_Q (or T_0) of the synthesis/quenching, with discrepancies of 190, 214 and 158°C for opx R80, 1948 and 1950 respectively. Similarly, much lower temperatures (984, 948 and 892°C for opx R80, 1948 and 1950) were calculated by applying Anovitz et al.s' (1988) Eq.(17) on sample M32b with XFe = 0.39 obtained by Mössbauer spectroscopy on powder material. This systematic underestimation of T_C inclines us to agree with Wang et al.'s (2005) judgment that "one cannot mix results from the two methods".

Table 7. The calculated T_C temperatures for orthopyroxenes.			
	R80	**1948**	**1950**
P (GPa)	3	2.5	2
T_Q (°C)	1170	1160	1050
T_C Opx(°C)[*]	1138 (21)	1105(20)	1054 (13)
T_C Opx(°C)[†]	980 (22)	946 (22)	892 (14)
Notes: P and T are pressure and temperature at which the synthesis experiments by Adam and Green (2006) have been performed. [*]For the equation used see the text (equation 2 by Stimpfl et al., 2005) [†]lnk_D = 0.391(±0.131) -2205(±141) /T (K) (Wang et al., 2005) obtained by Mössbauer spectroscopy.			

Overall, the T_C values obtained with Murri et al.s' (2016) and Stimpfl et al.s' (2005) calibrations for both phases (cpx and opx) of each experiment mutually agree within less than 2 e.s.d.s (see Table 5), thus providing cross-validation of the results between the two phases. Further, T_Cs calculated for all the samples using both opx and cpx agree within less than 2 e.s.d.s with the quenching/synthesis temperatures. Such good agreement confirms the reliability of the method and shows its potential use in a very broad range of formation temperatures (in our case quenching/synthesis) and cooling rates.

Acknowledgments

References

Adam, J., and Green, T. H., (2006) Trace element partitioning between mica-and amphibole-bearing garnet lherzolite and hydrous basanitic melt: 1. Experimental results and the investigation of controls on partitioning behaviour. Contributions to Mineralogy and Petrology, 152, 1–17.

Adam, J., Oberti, R., Cámara, F., and Green, T. H. (2007) An electron microprobe, LAM-ICP-MS and single-crystal X-ray structure refinement study of the effects of pressure, melt-H_2O concentration and fO_2 on experimentally produced basaltic amphiboles. European Journal of Mineralogy, 19, 641–655.

Alvaro, M., Cámara, F., Domeneghetti, M.C., Nestola, F., and Tazzoli, V. (2011) HT $P2_1/c$–$C2/c$ phase transition and kinetics of Fe^{2+}–Mg order–disorder of an Fe-poor pigeonite: implications for the cooling history of ureilites. Contributions to Mineralogy and Petrology, 162, 599–613.

Alvaro, M., Domeneghetti, M.C., Fioretti, A.M., Cámara, F., and Marinangeli, L. (2015) A new calibration to determine the closure temperatures of Fe-Mg ordering in augite from nakhlites. Meteoritics and Planetary Science, 50, 499–507.

Anovitz, L. M., Essene, E. J., and Dunham, W. R. (1988) Order-disorder experiments on opx; implications for the opx geospeedometer. American Mineralogist, 73(9-10), 1060-1073.

Brizi, E., Molin, G., and Zanazzi, P.F. (2000) Experimental study of intracrystalline Fe^{2+}-Mg exchange in three augite crystals: Effect of composition on geothermometric calibration. American Mineralogist, 85, 1375–1382.

Dal Negro, A., Carbonin, S., Molin, G.M., Cundari, A., and Piccirillo, E.M. (1982) Intracrystalline cation distribution in natural clinopyroxenes of tholeiitic, transitional, and alkaline basaltic rocks. In Advances in Physical Geochemistry pp. 117–150. Springer.

Di Rocco, T., Nava, J., Gemelli, M., D'Orazio, M., Domeneghetti, M. C., Alvaro, M., Pack, A., and Folco, L. (2016) Allan Hills 12073: A Metal-Rich Eucrite. 79th Annual Meeting of the Meteoritical Society, Berlin 7-12 August, LPI Contributions no. 1921.

Dodson, M.H. (1976) Kinetic processes and thermal history of slowly cooling solids. Nature, 259, 551-553.

Domeneghetti, M. C., Molin, G.M., and Tazzoli, V. (1995) A crystal-chemical model for Pbca orthopyroxene. American Mineralogist, 80(3-4), 253-267.

Domeneghetti, M.C., Molin, G.M., Zema, M., and Tazzoli, V. (1999) Thermal History of Howardites: The Orthopyroxene as a Geospeedometer. Meteoritics and Planetary Science Supplement, 34, A33.

Domeneghetti, M. C., Zema, M., and Tazzoli, V. (2005) Kinetics of Fe^{2+}-Mg order-disorder in $P2_1/c$ pigeonite. American Mineralogist, 90, 1816–1823.

Domeneghetti, M. C., Fioretti, A. M., Cámara, F., Molin, G., and Tazzoli, V. (2007) Thermal history of ALH 84001 meteorite by Fe^{2+}-Mg ordering in orthopyroxene. Meteoritics and Planetary Science, 42, 1703–1710.

Domeneghetti, M.C., Fioretti, A.M., Cámara, F., McCammon, C., and Alvaro, M. (2013) Thermal history of nakhlites: A comparison between MIL 03346 and its terrestrial analogue Theo's flow. Geochimica et Cosmochimica Acta, 121, 571–581.

Fioretti, A. M., Domeneghetti, M. C., Molin, G., Cámara, F., Alvaro, M., and Agostini, L. (2007) Reclassification and thermal history of Trenzano chondrite. Meteoritics and Planetary Science, 42, 2055–2066.

Ganguly, J. (1982) Mg-Fe order-disorder in ferromagnesian silicates: II. Thermodynamics, kinetics and geological applications. In S. Saxena, Ed., Advances in Physical Geochemistry, Vol. 2, pp. 58–99. Springer-Verlag.

Ganguly, J., and Saxena, S.K. (1987) Exchange equilibrium and Intercrystalline Fractionation. In Mixtures and mineral reactions. pp. 131-165. Springer-Verlag. New York.

Ganguly, J., Yang, H., and Ghose, S. (1994) Thermal history of mesosiderites: Quantitative constraints from compositional zoning and Fe-Mg ordering in orthopyroxenes. Geochimica et Cosmochimica Acta, 58, 2711–2723.

Ganguly, J., and Domeneghetti, M.C. (1996) Cation ordering of orthopyroxenes from the Skaergaard Intrusion: Implications for the subsolidus cooling rates and permeabilities. Contributions to Mineralogy and Petrology, 122, 359–367.

Ghose, S., and Ganguly, J. (1982) Mg-Fe Order-Disorder in Ferromagnesian Silicates. In S. Saxena, Ed., Advances in Physical Geochemistry Vol. 2, pp. 3–99. Springer New York.

Giesting, P. A., Schwenzer, S. P., Filiberto, J., Starkey, N. A., Franchi, I. A., Treiman, A. H., Tindle, A. G., and Grady, M.M. (2015) Igneous and shock processes affecting chassignite amphibole evaluated using chlorine/water partitioning and hydrogen isotopes. Meteoritics and Planetary Science, **50**, 433–460.

Giesting, P. A., and Filiberto, J. (2016) The formation environment of potassic-chloro-hastingsite in the nakhlites MIL 03346 and pairs and NWA 5790: Insights from terrestrial chloro-amphibole. Meteoritics and Planetary Science, 51(11), 2127–2153.

Green, D.H. (1976) Experimental testing of "equilibrium" partial melting of peridotite under water-saturated, high-pressure conditions. The Canadian Mineralogist, 14, 255–268.

Hawthorne, F. C., and Ito, J. (1978) Refinement of the crystal structures of $(Mg_{0.776}Co_{0.224})SiO_3$ and $(Mg_{0.925}Mn_{0.075})SiO_3$. Acta Crystallographica B, 34, 891–893.

Hawthorne, F.C., Ungaretti, L., and Oberti, R. (1995) Site populations in minerals; terminology and presentation of results of crystal-structure refinement. The Canadian Mineralogist, 33, 907–911.

Ibers, J.A., and Hamilton, W.C. (1970) International Tables for X-ray Crystallography, pp. 99-101 Journal of Chemical Physics, Vol. 4. Kynoch Press, Birmingham, UK.

Ibers, J. A., and Hamilton, W.C. (1974) International Tables for X-ray Crystallography, vol. 3. Birmingham: Kynoch Press.(Present distributor Kluwer Academic Publishers, Dordrecht.), 278 p.

Malgarotto, C., Molin, G., and Zanazzi, P.F. (1993) Cooling history of a dyke on Alicudi (Aeolian Islands) from intracrystalline Fe2+–Mg exchange reaction in clinopyroxene. European Journal of Mineralogy, 5, 755–762.

Mallman, G., and O'Neill, H.S.C. (2009) The crystal/melt partitioning of V during mantle melting as a function of oxygen fugacity compared with some other elements (Al, P, Ca, Sc, Ti, Cr, Fe, Ga, Y, Zr and Nb). Journal of Petrology, 50, 1765–1794.

McCallister, R. H., Finger, L. W., and Ohashi, Y. (1976) Intracrystalline Fe^{2+}-Mg equilibria in three natural Ca-rich clinopyroxenes. American Mineralogist, 61, 671–676.

Molin, G., and Zanazzi, P.F. (1991) Intracrystalline Fe^{2+}-Mg ordering in augite: experimental study and geothermometric applications. European Journal of Mineralogy, 3, 863–875.

Mueller, R. F. (1967) Model for order-disorder kinetics in certain quasi-binary crystals of continuously variable composition. Journal of Physics and Chemistry of Solids, 28(11), 2239-2243.

Murri, M., Scandolo, L., Fioretti, A. M., Nestola, F., Domeneghetti, C. M., and Alvaro, M. (2016) The role of Fe content on the Fe-Mg exchange reaction in augite. American Mineralogist, 101, 2747–2750.

Nestola, F., Alvaro, M., Casati, M. N., Wilhelm, H., Kleppe, A. K., Jephcoat, A. P., Domeneghetti, M. C., and Harris, J. W. (2016) Source assemblage types for cratonic diamonds from X-ray synchrotron diffraction. Lithos, 265, 334–338.

Pandolfo, F., Nestola, F., Cámara, F., and Domeneghetti, M. C. (2012) High-pressure behavior of space group *P*2/*n* omphacite. American Mineralogist, 97, 407–414.

Pasqual, D., Molin, G., and Tribaudino, M. (2000) Single-crystal thermometric calibration of Fe-Mg order-disorder in pigeonites. American Mineralogist, 85, 953–962.

Papike, J. J., Cameron, K. L., and Baldwin, K. (1974) Amphiboles and pyroxenes: characterisation of other than

quadrilateral components and estimates of ferric iron from microprobe data. Geological Society of America, 6, 1053-1054.

Righter, K., Keller, L. P., Rahman, Z., and Christoffersen, R. (2014) Redox-driven exsolution of iron-titanium oxides in magnetite in Miller Range (MIL) 03346 nakhlite: Evidence for post crystallization oxidation in the nakhlite cumulate pile? American Mineralogist, 99, 2313–2319.

Righter, K., Danielson, L. R., Pando, K. M., Shofner, G. A., Sutton, S. R., Newville, M., and Lee, C. T. (2016) Valence and metal/silicate partitioning of Mo: Implications for conditions of Earth accretion and core formation. Earth and Planetary Science Letters, 437, 89–100.

Rossi, G., Oberti, R., Dal Negro, A., Molin, G.M., and Mellin, M. (1987) Residual electron density at the M2 site in $C2/c$ clinopyroxenes: Relationships with bulk chemistry and sub-solidus evolution. Physics and Chemistry of Minerals, **14**, 514–520.

Saxena, S. K., and Ghose, S. (1971) Mg^{2+}-Fe^{2+} order-disorder and the thermodynamics of the orthopyroxene crystalline solution. American Mineralogist, 56, 532–559.

Scandolo, L., Mazzucchelli, M. L., Alvaro, M., Nestola, F., Pandolfo, F. and Domeneghetti, M. C. (2015) Thermal expansion behaviour of orthopyroxenes: the role of the Fe-Mn substitution. Mineralogical Magazine, 79(1), 71–87.

Sheldrick, G.M. (2008) A short history of SHELX. Acta Crystallographica A, 64, 112–122.

Smyth, J. (1973) Orthopyroxene structure up to 850°C. American Mineralogist, 58, 636–648.

Stimpfl, M., Ganguly, J., and Molin, G. (1999) Fe^{2+}-Mg order- disorder in orthopyroxene: equilibrium fractionation between the octahedral sites and thermodynamic analysis. Contributions to Mineralogy and Petrology, 136, 297–309.

Stimpfl, M. (2005a) The Mn, Mg-intracrystalline exchange reaction in donpeacorite $(Mn_{0.54}Ca_{0.03}Mg_{1.43}Si_2O_6)$ and its relation to the fractionation behaviour of Mn in Fe, Mg-opx. American Mineralogist, 90,155–161.

Stimpfl, M. (2005b) The Mn, Mg-intracrystalline exchange reaction in donpeacorite $(Mn_{0.54}Ca_{0.03}Mg_{1.43}Si_2O_6)$ and its relation to the fractionation behaviour of Mn in Fe, Mg-orthopyroxene, vol 90, p 155. American Mineralogist, 90,776 (Erratum).

Stimpfl, M., Ganguly, J., and Molin, G. (2005) Kinetics of Fe^{2+}–Mg order disorder in orthopyroxene: experimental studies and applications to cooling rates of rocks. Contributions to Mineralogy and Petrology, 150, 319– 334.

Sueno, S., Cameron, M., and Prewitt, C. (1976) Orthoferrosilite: High-temperature crystal chemistry. American Mineralogist, 61, 38–53.

Sykes-Nord, J. A., and Molin, G. (1993) Mg-Fe order-disorder reaction in Fe-rich orthopyroxene; structural variations and kinetics. American Mineralogist, 78, 921–931.

Takeda, H. (1987) Mineralogy of Antarctic ureilites and a working hypothesis for their origin and evolution. Earth and Planetary Science Letters, 81, 358–370.

Tribaudino, M., Fioretti, A. M., Martignagoc, F. and Molin, G. (1997) TEM texture and crystal chemistry of co-existing ortho-and clinopyroxene in the Antarctic ureilite FRO90054: implications for thermal history. Meteoritics, 32, 671–678.

Virgo, D. and Hafner, S. (1969) Fe^{2+}, Mg order-disorder in heated orthopyroxenes. Mineralogical Society of America Special Paper, 2, 67–81.

Wang, L., Moon, N., Zhang, Y., Dunham, W. R., and Essene, E. J. (2005) Fe-Mg order-disorder in orthopyroxenes. Geochimica et Cosmochimica Acta, 69 (24), 5777-5788.

Zema, M., Domeneghetti, M. C. and Tazzoli, V. (1999). Order-disorder kinetics in orthopyroxene with exsolution products. American Mineralogist, 84, 1895-1901.

APPENDIX II. COOLING HISTORY AND EMPLACEMENT OF A PYROXENITIC LAVA AS PROXY FOR UNDERSTANDING MARTIAN LAVA FLOWS

Mara Murri[1], Maria C. Domeneghetti[1], Anna M. Fioretti[2], Fabrizio Nestola[3], Francesco Vetere[4,5], Diego Perugini[4], Alessandro Pisello[4], Manuele Faccenda[3], Matteo Alvaro[1*]

[1]*Department of Earth and Environmental Sciences, University of Pavia, Via A. Ferrata, 1 27100 Pavia, Italy*
[2]*Istituto di Geoscienze e Georisorse CNR, Padova, Italy*
[3]*Department of Geosciences, University of Padova, Via G. Gradenigo 6, 35131 Padova, Italy*
[4]*Department of Physics and Geology, University of Perugia, piazza Università 1, 06123 Perugia, Italy.*
[5]*Institute of Mineralogy, Leibnitz Universität Hannover, Callinstr. 3, D-30167, Hannover, Germany.*

ABSTRACT

Terrestrial analogues are often investigated to get insights into the geological processes occurring on other planetary bodies. Due to its thickness and petrological similarities, the pyroxenitic layer of the 120m-thick magmatic pile Theo's Flow (Archean Abitibi greenstone belt Ontario, Canada), has always been regarded as the terrestrial analogue for Martian nakhlites. However, its origin and cooling history and, as a consequence those of nakhlites, have always been a matter of vigorous debate. Did this lava flow originate from a single magmatic event similar to those supposed to occur on Mars or do the different units derive from multiple eruptions? We demonstrate, by a combination of geothermometric constraints on augite single crystals and numerical simulations, that Theo's Flow has been formed by multiple magma emplacements that occurred at different times. This discovery supports the idea that the enormous lava flows with similar compositions observed on Mars could be the result of a process where low viscosity lavas are emplaced during multiple eruptions. This has profound implications for understanding the multiscale mechanisms of lava flow emplacement on Earth and other planetary bodies.

TERRESTRIAL LAVA FLOWS AS ANALOGUE FOR MARTIAN LAVAS: THE CASE OF THEO'S FLOW

Investigation of ancient lava flows provides unprecedented insights for the understanding of eruptive activity occurring on both the Earth's surface and on other planetary bodies. An ancient lava flow such as Theo's Flow, due to its thickness and lithology of the stratigraphic layers, represents the perfect candidate that has been used in the past 20 years as a terrestrial analogue for thick lava flows erupted on Mars.

Theo's Flow is a 120m-thick magmatic pile located in the mafic and ultramafic region of the Archean Abitibi greenstone belt (Munro Township, Ontario) (Pyke and Eckstrand 1973) that was affected by metamorphic alteration under greenschist facies conditions (e.g. < 500°C). However, the well-preserved textural relationships and absence of evidence of alteration of the augites within the flow suggest that they did not suffer either a resetting of their chemical signatures or metamorphic alteration (Lentz et al. 2011). The entire magmatic pile contains the following lithologies (bottom to top): peridotite (~9m), pyroxenite (~60m), gabbro together with a pegmatitic pyroxenite (~40m) and hyaloclastite (~10 m thick). The top quenched margin of the hyaloclastite is a breccia (Arndt 1975) that together with pillow basalts and pyroclastites (Condie 1981) suggests that subaerial setting followed by a submarine environment characterized the origin and evolution of Theo's Flow. In particular, based on detailed petrography and geochemistry, the pyroxenite layer has always been regarded as the best terrestrial analogue of nakhlites (Lentz et al. 1999, 2011). This lava flow dates to ~ 2.7Ga, based on ages determined on nearby komatiites (Shirey 1977). The best outcrop of Theo's Flow is in the direction of the flow (Arndt 1977) and, as showed in Lentz *et al*. 2011, it is comprised of a magmatic pile of different lithologic units.

Based on detailed petrological and stratigraphic analyses Lentz *et al.* (1999,2011) concluded that the lithologic diversity observed in Theo's Flow was the result of a differentiation process of a single, thick magma pulse, rather than being generated by the eruption of multiple magmatic batches with distinct composition. This conclusion was based on the absence of sharp boundaries between adjacent units and on the progressive compositional changes observed in mineral and bulk-rock compositions. According to these authors (Lentz et al. 2011), even if this hypothesis was further supported by the matching between the average composition of the whole magmatic pile with that of the quenched hyaloclastite breccia at the top, the latter being considered

as having the composition of the primary magma, "the exact nature of the differentiation process remains uncertain". Therefore, the origin of Theo's Flow and its cooling history have been extensively debated (e.g. Lentz et al. 1999,2011; Alvaro et al. 2015 and Richter et al. 2016) mostly because the original assumption of Lentz *et al.* (201)1 that the 120 m of lava have been emplaced as a consequence of one single eruptive event. This would be a rather unusual phenomenon on planet Earth but is commonly accepted for Mars because, considering measurements made on imagery of actual Martian flows (e.g. Schaber et al. 1978; Yoshioka 1995; Mouginis-Mark and Yoshioka 1998; Head et al. 1998 and Glaze et al. 2003), thicknesses of the order of 120 m seem reasonable.

However, several authors (e.g. Treiman 2005; Hammer 2009 and Domeneghetti et al. 2013) raised concerns about some inconsistencies between the cooling rate and temperature estimates obtained from petrographic/textural evidence (fast cooling rates 3-6°C/h) against those from geothermometric data (slow cooling rates 0.1°C/h). Because of these contrasting results Domeneghetti *et al.* (2013) and then Alvaro *et al.* (2015) proposed for nakhlites and Theo's Flow, respectively, a mechanism of emplacement with subsequent injections blanketing one another, but this hypothesis has never been tested. Given the analogy with Martian lava flows, the mechanism and timing of differentiation of Theo's Flow deserves further investigation to shed light on these geological processes on Mars.

THE EMPLACEMENT OF THEO'S FLOW: A MULTI-ERUPTION SCENARIO

If we follow the idea that Theo's Flow was emplaced into a pre-existing V shape topography (valley), a possible scenario for the emplacement mechanism could be related to effusive submarine eruptions as suggested in the literature (Lentz et al. 2011). Magma–water interactions can occur deep within the Earth or near the surface as possibly happened for the Theo's Flow. In such a case, convective cooling by water should be considered as the dominant cooling mechanism because it is more efficient than convective, radiative, and conductive cooling observed on the Earth surface (Griffiths and Fink 1992; Gregg 2013). Fink and Griffiths (1990) and more recently Gregg (2013) proposed that the convective heat flux from the surface of a submarine lava flow leads to an almost immediate cooling of magma. As an example, after 1s, a basalt erupting at 1423 K passes through the solidus and glass transition temperature at a depth of

2 mm and 0.5 mm, respectively. The rupture of crust is a reasonable process during surface eruption (Deschamps et al. 2014) where the new and fast-formed crust can incur in rupture from which new blob of magma will come out. Active pillow lava lobe inflating on transverse and radial cracks with high-effusion-rate are plausible events for flows moving down to a steep slope. As an example, inflated Pahoehoe flows can display large inflation structures such as plateaus and cover several hundreds of square meters as observed in Iceland, and the inflation height can reach a maximum of 20 m in the case of submarine or subaqueous flows (Deschamps et al. 2014). Since Theo's Flow is described as a 120 m thick lava flow this would require superimposed flows each of the order of 10-50 m thick closely emplaced in time. Finally, the study of lava flows in submarine environments requires that the effective gravity force acting on the flow is considered. Due to the lower density difference between the lava and the water it is smaller in water than on Earth surface (Fink and Griffiths 1990). The reduced gravity (g') is given by:

$$g' = \frac{g \, (\rho - \rho w)}{\rho} \qquad (1)$$

and it takes into account ρ (the lava density) and density of the surrounding seawater ρw. With a lava density of 2600 kg m^{-3}, if we consider a shallow subaqueous environment where density of water is close to 1000 kg m^{-3} and ambient water temperature ranges from 273 to 283 K, the effective gravity is 6.03 ms^{-2}. Whereas, with the same lava density, at 1000 m deep and a temperature of 273 K where seawater has a density of 1046 kg m^{-3}, the effective gravity is 5.85 ms^{-2}. This implies that the buoyancy force countering the effect of the gravity is significantly higher in water and this greatly increases the ability of lava to inflate and also increases the thickness of the lava flow by about 30% (Deschamps et al. 2014; Gregg and Fornari 1998). Considering that in subaqueous environments the height of flows is on the order of 10 m we should therefore explore the possible scenario already proposed (Alvaro et al. 2015; Domeneghetti et al. 2013) of superimposed lava flows rather than one single-flow unit.

Thermal constraints on slowly cooled paleo lava flows cannot rely upon conventional chemical geothermometry based on intercrystalline cation exchange because at low temperature (below 600-700°C) long-range diffusion is kinetically hindered. Conversely, the short range of intracrystalline exchange reaction can proceed to much lower temperatures (i.e. about 500°C, see Ganguly 1982 and Murri et al. 2018 for further details) thus allowing it to be used to estimate the cooling history for complex magma bodies that may have interacted with one another.

EXPERIMENTAL CLOSURE TEMPERATURE AND COOLING RATES

To understand the magmatic evolution and the cooling history of the whole of Theo's Flow we applied a newly-determined geothermometric calibration (Murri et al. 2016) of the Fe^{2+}-Mg intracrystalline exchange reaction between $M1$ and $M2$ sites in augite crystals (Alvaro et al. 2015; Ganguly 1982; Murri et al. 2016, 2018; McCallister et al. 1976; Dal Negro et al. 1982; Ghose and Ganguly 1982; Molin and Zanazzi 1991; Brizi et al. 2000 and Alvaro et al. 2011) to determine the closure temperature (T_C) and cooling rates for each lithological layer in the Theo's Flow pile.

We selected 6 augite single crystals from 4 small chips (5 to 10 grams) sampled at four different stratigraphic depths below the cooling surface of Theo's Flow (red dots in Figure 1). One crystal has been selected from the peridotite (TSC 3.9) and five from the pyroxenite layers (TSC 3.12_1 TSC 3.12_2; TSC 3.22; TSC 3.31_1; TSC 3.31_2) sampled at different depths (see Figure 1). These results have been combined with those obtained by Domeneghetti et al. (2013) on two more crystals from the pyroxenite layer at an intermediate depth (see blue open circles in Figure 1). All of the selected clinopyroxenes have Fs contents [with Fs=100*ΣFe/(ΣFe+Mg+Ca) where ΣFe=Fe^{2+}+Fe^{3+}+Mn] within the compositional range of Fs_9 to Fs_{24} previously reported by Murri *et al.* (2016). High-resolution microfocus (beam size 120μm) single-crystal X-ray diffraction measurements [MoKα ($\lambda = 0.71073$ Å) operating at 50 kV and 0.8 mA (power = 40 W)] have been carried out on each crystal. The collected intensity data (Table S1) have been used for structure refinements to determine the cation site occupancies (Table S2) adopting the results from electron microprobe analyses (i.e. EMPA) to constrain the composition (Domeneghetti et al. 2013). Full compositional data of the selected six augite crystals obtained by electron microprobe are reported in the supplementary material (Table S3, see Appendix IV).

The Fe^{2+}-Mg ordering state was obtained from the site populations in order to calculate the closure temperature by means of the intracrystalline distribution coefficient (k_D), using the expression (Brizi et al. 2000) $k_D = [(Fe^{2+}_{M1}) (Mg_{M2})/(Fe^{2+}_{M2})(Mg_{M1})]$. The relationship between the distribution coefficient (k_D) and T_C is usually expressed using calibration equations of the lnk_D as a function of $1/T$(K).

For our augite samples the calibration equation (Murri et al. 2016), reported in equation 2, was used because it produces reliable results on samples with compositions ranging between Fs_9 and Fs_{24} as demonstrated from the investigation of synthetic samples (Murri et al. 2018). In particular,

the equation was obtained using data from Murri et al. (2016) Theo's Flow augite (TS7 N.16, Fs$_9$) together with those from Alvaro et al. (2015) on augites from the Miller Range nakhlite sample (MIL 03346, Fs$_{24}$).

$$lnk_D = -4040 \ (\pm180)/ \ T(K) + 1.12 \ (\pm0.17) \ (R^2=0.988) \tag{2}$$

The resulting T_C are reported in Table 1 and in Figure1 (where an average T_C is reported for levels where two crystals were sampled). They show a thermal gradient of about 170°C across the pyroxenite unit. Furthermore, the maximum recorded T_C value is 791(15) °C at 65m depth and towards the top of the flow the closure temperatures drop to values of 734 (19) °C and 764 (20) °C. In particular, the closure temperature of 791°C (top of the pyroxenite unit) indicates a relative fast cooling rate with respect to all the other measured temperatures suggesting that, at the time of its eruption, no material was present above the pyroxenite and it was cooled down at the contact with the atmosphere (subaerial, submarine environment). Therefore, this evidence coupled with the observed thermal gradients and measured closure temperatures seems to point towards a multiple-eruption scenario rather than to support the hypothesis of one single magma emplacement differentiated in-situ (Lentz et al. 2011). In this new scenario the different composition of the lithologic units could be therefore be simply ascribed to an initial differentiation process in the magma chamber prior to eruption.
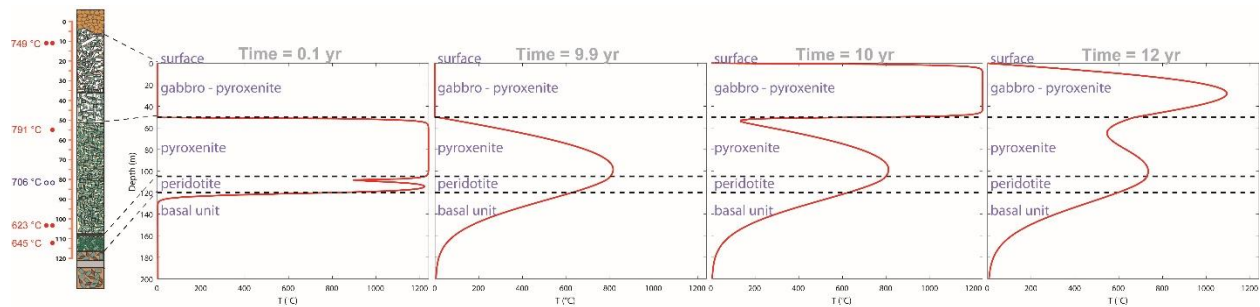
Figure 1. Lithostratigraphic column for the lava pile on the left with closure temperatures determined for all the samples in this study (red dots) and previously (Domeneghetti et al. 2013, blue open circles). Thermal evolution over time for each layer of the Theo's Flow lava pile. The peridotite and pyroxenite emplacements are approximately coeval and they are followed by the gabbro – pyroxenite emplacement 10 years later.

RECONSTRUCTED THERMAL HISTORY FOR THEO'S FLOW

To further test this new hypothesis, we carried out numerical simulations to assess the possibility of different magma emplacements blanketed by subsequent events of different durations as previously suggested (Alvaro et al. 2015; Domeneghetti et al. 2013). This model couples the closure temperature with the cooling rate determined on each single crystal, providing the timing for each subsequent lava flow emplacement.

We solved the 1D heat diffusion equation with the finite difference method in a 300 m thick vertical profile considering the variation of physical properties due to the different lithologic units (see Table S4 and Figure 2). We imposed a surface temperature (T_{surf} =0°C) in the uppermost 120m of the profile to simulate the initial presence of air/water, whereas we have computed the temperature according to a steady state geotherm for the basement (120-300m). The emplacement of a single lava flow is modelled by increasing the temperature instantaneously from T_{surf} to T_{magma} (T_{magma}=1240°C see Lentz et al. 2011 and Vetere et al. 2019). In order to study the influence of the timing of the eruption on the cooling rates we performed several simulations by varying the eruption time sequence. Average cooling rates have been estimated as:

$$CR \ (°C/h) = (T_{magma} - T_{closure}) \ / \ (t_{closure} - t_{emplacement}) \qquad (3)$$

where T is the temperature in °C and t is the time in hours. Figure 2 and Table 1 compare the cooling rates calculated using the model from Ganguly (1982) (see Alvaro *et al*. 2015 for further details) with those determined from the modeled scenarios.

In summary, the scenario which best reproduces the cooling rates inferred from the intra-crystalline distributions that we measured in augites is that for which the pyroxenite lava flow occurs immediately after the peridotite (i.e. 0.1 year later). This time span is sufficient for the pyroxenite to blanket the peridotite and slow its cooling rate according to the measured closure temperature. The gabbro-pyroxenite lava flow occurs in a later stage with a minimum interval of 10 years after the emplacement of the pyroxenite.

The late stage-emplacement of the gabbro-pyroxenite unit allows the pyroxenite beneath to cool down sufficiently fast in agreement with our closure temperature (791°C) estimate without invoking any reset of the Fe-Mg ordering degree (i.e. no chemical re-opening of the system) as we would have considered for the hypothesis of a single stage emplacement differentiated in-situ.

The latter hypothesis can be excluded even more considering the low viscosity of the pyroxenite measured by Vetere *et al*. (2019) that undergoing fast cooling would not have had time to differentiate after emplacement but could be consistent with differentiation in a magma chamber. Furthermore, the closure temperatures determined in this work coupled with the low viscosity data by Vetere *et al.* (2019) on the same composition, also explain the high (120m) thickness for these lavas on Earth (e.g. Ontario lava flows). The only contrasting evidence that poses against the multistage event could be the absence of the hyaloclastite at the top of each layer and the gradational contacts between the subsequent lithologic unit.

However, even in the multiple stage emplacement scenario, we could expect gradational contacts between the peridotite and the pyroxenite since they are almost coeval. Also between the pyroxenite and the gabbro a gradational contact can be expected because of the blanketing process in which the gabbro above the pyroxenite unit reheated its topmost part (up to 500-600°C) without re-opening the Fe-Mg system in the augites that would require much higher T (T_C= 791°C, see Figure 1). The absence of the hyaloclastite can simply be explained by its mechanical erosion (Jaeger et al. 2010; Hurwitz et al. 2010).
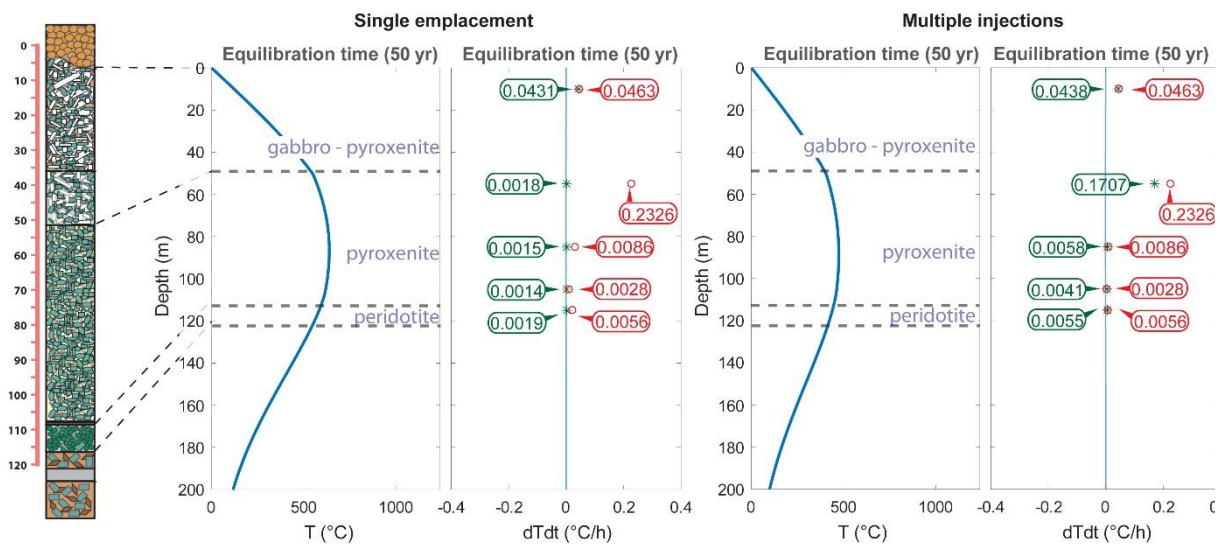
Figure 2. Comparison between the cooling rates determined on our samples following the approach by Ganguly (1982) (red labels) and those calculated from our 1D model (green labels) comparing the single emplacement vs multiple subsequent emplacements.

Units	Gabbro-Pyrox.	Top Pyrox.	Middle Pyrox.	Low Pyrox.	Peridotite
T_C (°C)	749	791	706.5	622	645
CR (°C/h)*	0.0463	0.2326	0.0086	0.0028	0.0056
CR (°C/h)[†]	0.0438	0.1707	0.0058	0.0041	0.0055
CR (°C/h)[‡]	0.0431	0.0018	0.0015	0.0014	0.0019

Table 1. * Cooling rates estimated by using the model from Ganguly (1982), [†] cooling rates from the modeled scenario with multiple injections and those from a unique magma emplacement [‡]

CONCLUSIONS

Because of its similarity with Martian lava flows Theo's Flow has always been regarded as the analogue to be used for interpreting magmatic processes on Mars. The 120m-thick Theo's lava pile has always been considered the result of one single eruptive event, a rather unusual phenomenon on Earth but commonly accepted for Mars. However, the inconsistencies between cooling rate and temperature estimates from petrographic/textural evidence (fast cooling rates 3-6°C/h) and from geothermometric data (slow cooling rates 0.1°C/h) led several authors (Treiman 2005; Hammer 2009; Domeneghetti et al. 2013) to question the one-stage emplacement process in search for alternative scenarios.

To unravel this extensive debate, we used a combination of temperature constraints on single augite crystals and numerical simulations to demonstrate that Theo's Flow has been formed by multiple magma emplacements at different times. We can therefore summarize this new hypothesis for the thermal history of Theo's Flow as follows: in the Archean age, the erupted differentiated lavas flowed at very high temperatures in a turbulent regime (Vetere et al. 2019). Because of their low viscosity, these lavas flowed for considerable distances until they were trapped by topography. The first emplacements, almost coeval, were those of the peridotite and pyroxenite in a subaerial or subaqueous environment and then the gabbro flow mechanically-eroded (Vetere et al. 2019; Jaeger et al. 2010; Hurwitz et al. 2010) the hyaloclastite at the top of the pyroxenite, thus leaving as the only preserved hyaloclastite quenched breccia the one on the top of the whole pile.

This discovery supports the idea that the enormous lava flows with similar composition found on Mars could be the result of a process where low viscosity lavas (Vetere et al. 2019) are

emplaced during multiple eruptions. Moreover, Udry and Day (2018) recently hypothesized a similar scenario for nakhlites and chassignites demonstrating that these lithologies were emplaced close or onto the surface of Mars as multiple flows. The proposed process explains at the same time the fast cooling rates recorded by the textures of the rock and the low closure temperatures recorded by the single minerals (e.g. intracrystalline exchange in pyroxenes) for which the subsequent magma emplacement would then re-equilibrate the system at much lower temperatures similar to those expected for high thicknesses single lava pile, at least for the peridotite-pyroxenite transition. This has profound implications for our understanding of multiscale mechanisms for lava flow emplacements on Earth and other planetary bodies.

Methods

Single-crystal X-ray diffraction and data reduction

X-ray diffraction experiments were carried out on each crystal using a diffractometer in the Department of Geosciences at the University of Padova (Angel and Nestola 2016). The instrument consists of a Rigaku-Oxford Diffraction Supernova kappa-geometry goniometer equipped with an X-ray micro-source assembled with a Pilatus 200 K Dectris detector. The micro-X-ray source, MoKα ($\lambda = 0.71073$ Å) operates at 50 kV and 0.8 mA (power = 40 W). The micro source ensures a brilliance at least ten times higher than conventional sealed X-ray tubes and a beam spot of ~0.120 mm. At the same time, the Pilatus 200 K detector ensures a very high sensitivity and negligible noise. Data collections have been performed using the Crysalis software (Rigaku-Oxford-Diffraction©) package. Data reduction, including intensity integration together with background and Lorentz-polarization corrections, have been carried out within the Crysalis package. The unit-cell parameters, the discrepancy indices R_{int} , R_{all}, R_w on all the F_o^2 and the goodness of fit (S) of the structure refinements with chemical constraints for the six crystals are reported in Table S1.

Electron Microprobe analyses (EMPA)

Major and minor elements were analyzed with a Cameca-SX50 electron microprobe with a fine-focused beam (1 μm diameter) operating in wavelength-dispersive (WDS) mode. Operating conditions were 15 kV accelerating voltage and 15 nA beam current; counting times were 20 s on the peaks and 20 s on the background. The following synthetic endmember mineral standards were used: diopside for Mg, ferrosilite for Fe, wollastonite for Si and Ca, chromite for Cr, corundum for Al, $MnTiO_3$ for Mn and Ti, and a natural albite (Amelia albite) for Na. X-ray counts were converted into oxide weight percentages using the PAP correction program (as in Fioretti *et al.* 2007). Analyses are precise to within 1% for major elements and 3–5% for minor elements. The results of the chemical analysis are reported in Table S2. The crystal chemical formula was calculated on the basis of six oxygen atoms (Papike 1969). Only those spot analyses with total cation contents of 4.000 ± 0.005 atoms on the basis of six oxygen atoms and charge balance $3^{[4]}$ Al + Na − $3^{[6]}$Al − 4Ti − 3Cr − $3Fe^{3+} \leq |0.005|$ were selected and averaged. The Fe^{3+} content was calculated by stoichiometry (Droop 1987).

Structure refinements

The observed $F_o{}^2$ values were then treated with a full-matrix least-squares refinement in the *C*2/*c* space group by using the SHELX-97 program (Sheldrick 2008), starting from the atomic coordinates of sample TS7 N.2 (Domeneghetti et al. 2013) and taking into account the *M*21 and O2B1 split sites (Rossi et al. 1987), that were refined with isotropic displacement parameters. The atomic scattering curves were taken from *the International Tables for X-ray Crystallography* (Ibers and Hamilton 1970). Neutral versus ionized scattering factors were refined for all sites not involved in chemical substitutions to ensure charge neutrality (Hawtorne et al. 1995; Redhammer et al. 2010; Nestola et al. 2008). Complete ionization was assumed for Mg and Fe in the *M*1 site, for Ca and Mg in the *M*2 site and for Fe in the *M*21 site. Individual weights and the weighting scheme suggested by the program were used. The extinction correction was applied with the procedures of the SHELX-97 program. Table S1 reports the mean atomic numbers (m.a.n.) in electrons per formula unit (e.p.f.u.) at the crystallographic sites (*M*1, *M*2, *M*21) obtained when the structure refinement reached convergence, before introducing the chemical constraints. For all samples the calculated mean atomic numbers from the refinements unconstrained agree within less than 1 standard deviation with the values of electrons per formula unit (e.p.f.u.) calculated from the EMPA (Table S2). Therefore, this enabled us to use the results from the EMPA as chemical constraints for the structural refinements, following the procedure and taking into account the same constraints as in [16] assuming 1 standard deviation as the error, in order to determine the clinopyroxene site distribution. The site populations obtained from the structural refinements with chemical constraints and the distribution coefficients (k_D) with relative propagated errors are reported in Table S3.

References

Alvaro, M., Cámara, F., Domeneghetti, M., Nestola, F.and Tazzoli, V. HT P21/c–C2/c phase transition and kinetics of Fe^{2+}–Mg order–disorder of an Fe-poor pigeonite: implications for the cooling history of ureilites. Contributions to Mineralogy and Petrology 162, 599-613 (2011).

Alvaro, M., Domeneghetti, M. C., Fioretti, A. M., Cámara, F.and Marinangeli, L. A new calibration to determine the closure temperatures of Fe-Mg ordering in augite from nakhlites. Meteoritics and Planetary Science 50, 499-507 (2015).

Angel, R. J., & Nestola, F. A century of mineral structures: How well do we know them? American Mineralogist 101(5), 1036-1045 (2016).

Arndt, N. T. Ultramafic rocks of Munro Township and their volcanic setting. [Ph.D. dissertation]: Toronto, University of Toronto, (1975).Pyke, D. R., Naldrett, A. J.& Eckstrand, O. R. Archean ultramafic flows in Munro Township, Ontario. Geological Society American Bullettin 84, 995-978 (1973).

Brizi, E., Molin, G.and Zanazzi, P. F. Experimental study of intracrystalline Fe^{2+}-Mg exchange in three augite crystals: Effect of composition on geothermometric calibration. American Mineralogist 85, 1375-1382 (2000).

Condie, K.C. Archean greenstone belts, in Condie K.C., ed., Developments in Precambrian Geology. Amsterdam, Netherlands, Elsevier, 434 p. (1981).

Dal Negro, A., Carbonin, S., Molin, G. M., Cundari, A. and Piccirillo, E. M. Intracrystalline cation distribution in natural clinopyroxenes of tholeiitic, transitional, and alkaline basaltic rocks. in Advances in Physical Geochemistry (eds. Saxena, S. K.) 117-150 (Springer, New York, 1982).

Deschamps, A., Grigné, C., Le Saout, M., Soule, S.A., Allemand, P., Van Vliet-Lanoe, B. and Floc'h, F. Morphology and dynamics of inflated subaqueous basaltic lava flows. Geochemistry, Geophysics, Geosystems 15, 2128-2150 (2014).

Domeneghetti, M.C., Fioretti, A., Cámara, F., McCammon, C. and Alvaro M. Thermal history of nakhlites: A comparison between MIL 03346 and its terrestrial analogue Theo's Flow. Geochimica et Cosmochimica Acta 121, 571-581 (2013).

Droop, G. A general equation for estimating Fe^{3+} concentrations in ferromagnesian silicates and oxides from microprobe analyses, using stoichiometric criteria. Mineralogical Magazine 51, 431-435 (1987).

Fink, J. H.and Griffiths, R. W. Radial spreading of viscous-gravity currents with solidifying crust. Journal of Fluid Mechanics 221, 485-509 (1990).

Fioretti, A.M., Domeneghetti, M.C., Molin, G., Cámara, F., Alvaro, M. and Agostini, L. Reclassification and thermal history of Trenzano chondrite. Meteoritics and Planetary Science 42, 2055-2066 (2007).

Ganguly, J. Mg-Fe order-disorder in ferromagnesian silicates: II. Thermodynamics, kinetics, and geological applications. in Advances in Physical Geochemistry 2 (eds. Saxena, S.K.) 58-99 (Springer- Verlag, 1982).

Ghose, S.and Ganguly, J. Mg-Fe order-disorder in ferromagnesian silicates. in Advances in Physical Geochemistry 2, (eds. Saxena, S. K.) 3-99 (1982).

Glaze, L. S., Baloga, S. M., & Stofan, E. R. A methodology for constraining lava flow rheologies with MOLA. Icarus, 165(1), 26-33 (2003).

Gregg, T. K. P. and Fornari, D. J. Long submarine lava flows: Observations and results from numerical modeling. Journal of Geophysical Research: Solid Earth 103, 27517-27531 (1998).

Gregg, T. K. Deep-sea eruptions. in Modeling Volcanic Processes: The Physics and Mathematics of Volcanism (eds. Fagents, S. A., Gregg, T. K. P., & Lopes R. M. C.) 258-274 (Cambridge University Press New York, 2013).

Griffiths, R. W.and Fink, J. H. Solidification and morphology of submarine lavas: A dependence on extrusion rate Journal of Geophysical Research: Solid Earth 97, 19729-19737 (1992).

Hammer, J. E. Application of a textural geospeedometer to the late-stage magmatic history of MIL 03346. Meteoritics and Planetary Science 44, 141-154 (2009).

Hawthorne, F. C., Ungaretti, L.and Oberti, R. Site populations in minerals; terminology and presentation of results of crystal-structure refinement. The Canadian Mineralogist 33, 907-911 (1995).

Head, J.W., Kreslavsky, M., Hiesinger, H., Ivanov, M., Pratt, S., Seibert, N., Smith, D.E. and Zuber, M.T.Oceans in the past history of Mars: Tests for their presence using Mars Orbiter Laser Altimeter (MOLA) data. Geophysical Research Letters, 25, 4401-4404 (1998).

Hurwitz, D.M., Fassett, C.I., Head, J.W. and Wilson, L. Formation of an eroded lava channel within an Elysium Planitia impact crater: Distinguishing between a mechanical and thermal origin. Icarus, 210, 626-634 (2010)

Ibers,J. A. and Hamilton,W. C. International tables for X-ray crystallography. Journal of Chemical Physics 99-101 (Kynoch Press,Birmingham, UK, 1970).

Jaeger, W.L., Keszthelyi, L.P., Skinner Jr, J.A., Milazzo, M.P., McEwen, A.S., Titus, T.N., Rosiek, M.R., Galuszka, D.M., Howington-Kraus, E. and Kirk, R.L.Emplacement of the youngest flood lava on Mars: A short, turbulent story. Icarus, 205, .230-243 (2010).

Lentz, R. C. F., Taylor, G. J.and Treiman, A. H. F. Formation of a Martian pyroxenite: A comparative study of the nakhlite meteorites and Theo's Flow. Meteoritics and Planetary Science 34, 919-932 (1999).

Lentz, R. C. F., McCoy, T. J., Collins, L. E., Corrigan, C. M., Benedix, G. K., Taylor, G. J., and Harvey, R. P. Theo's Flow, Ontario, Canada: A terrestrial analog for the Martian nakhlite meteorites. Geological Society of America Special Papers 483, 263-277 (2011).

McCallister, R. H., Finger, L. W. and Ohashi, Y. Intracrystalline Fe (super 2+) -Mg equilibria in three natural Ca-rich clinopyroxenes. American Mineralogist 61, 671-676 (1976).

Molin, G.and Zanazzi, P. F. Intracrystalline Fe^{2+}-Mg ordering in augite: experimental study and geothermometric applications. European Journal of Mineralogy 3, 863-875 (1991).

Mouginis-Mark, P., and Yoshioka, M. T. The long lava flows of Elysium Planita, Mars. ournal of Geophysical Research: Planets, 103, 19389-19400 (1998).

Murri, M., Scandolo, L., Fioretti, A.M., Nestola, F., Domeneghetti, C.M. and Alvaro, M. The role of Fe content on the Fe-Mg exchange reaction in augite. American Mineralogist 101, 2747-2750 (2016).

Murri, M., Cámara, F., Adam, J., Domeneghetti, M. C.and Alvaro, M. Intracrystalline "geothermometry" assessed on clino and orthopyroxene bearing synthetic rocks. Geochimica et Cosmochimica Acta 227, 133-142 (2018).

Nestola, F., Boffa Ballaran, T., Liebske, C., Thompson, R.and Downs, R.T. The effect of the hedenbergitic substitution on the compressibility of jadeite. American Mineralogist 93, 1005-1013 (2008).

Papike, J. J. Pyroxenes and Amphiboles: crystal chemistry and phase petrology Mineralogical Society of America 2, Special Paper N.2 (eds. Papike, J.J.) (1969).

Pyke, D. R., Naldrett, A. J. and Eckstrand, O. R. Archean ultramafic flows in Munro Township, Ontario. Geological Society of America Bulletin 84, 995–978 (1973)

Redhammer, G.J., Cámara, F., Alvaro, M., Nestola, F., Tippelt, G., Prinz, S., Simons, J., Roth, G. and Amthauer, G. Thermal expansion and high-temperature P21/c-C2/c phase transition in clinopyroxene-type $LiFeGe_2O_6$ and comparison to $NaFe(Si,Ge)_2O_6$. Physics and Chemistry of Minerals 37, 685-704 (2010).

Richter, F., Chaussidon, M., Mendybaev, R. and Edwin, K. Reassessing the cooling rate and geologic setting of Martian meteorites MIL 03346 and NWA 817. Geochimica et Cosmochimica Acta 182, 1-23 (2016).

Rossi, G., Oberti, R., Dal Negro, A., Molin, G. M., and Mellini, M. Residual electron density at the M2 site in C2/c clinopyroxenes:Relationships with bulk chemistry and sub-solidus evolution. Physics and Chemistry of Minerals 14, 514-520 (1987).

Schaber, G. G., Horstman, K. C., and Dial Jr, A. L. Lava flow materials in the Tharsis region of Mars. In Lunar and Planetary Science Conference Proceedings 9, 3433-3458 (1978).

Sheldrick, G. M. A short history of SHELX. Acta Crystallographica Section A: Foundations of Crystallography A64, 112-122 (2008).

Shirey, S. B. Initial Os isotopic compositions of Munro Township, Ontario, komatiites revisited: Additional evidence for near-chondritic, late-Archean convecting mantle beneath the Superior Province. Abstracts of the 7th Goldschmidt Conference: LPI Contribution 921, Abstract 2375, (1977).

Treiman, A. H. The nakhlite meteorites: Augite-rich igneous rocks from Mars. Chemie der Erde-Geochemistry 65, 203-270 (2005).

Udry, A., and Day, J.M.D. 1.34 billion-year-old magmatism on Mars evaluated from the co-genetic nakhlite and chassignite meteorites. Geochimica et Cosmochimica Acta, 238, 292-315 (2018).

Vetere, F., Murri, M., Alvaro, M., Domeneghetti, M.C., Rossi, S., Pisello, A., Perugini, D. and Holtz, F. Viscosity of pyroxenite melt and its evolution during cooling. Journal of Geophysical Research: Planets 124, 1451-1469 (2019).

Yoshioka, M. J. T. Volcano and lava flow morphology of Elysium Mons. Mars and implications for eruption character. Univ. Hawaii unpub (Doctoral dissertation, M. Sc. Thesis) (1995).

APPENDIX III. VISCOSITY OF PYROXENITE MELT AND ITS EVOLUTION DURING COOLING

F. Vetere[1,2], M. Murri[3], M. Alvaro[3], M. C. Domeneghetti[3], S. Rossi[1], A. Pisello[1],
D. Perugini[1], and F. Holtz[2]

[1]*Department of Physics and Geology, University of Perugia, Perugia, Italy*
[2]*Institute of Mineralogy, Leibniz Universität Hannover, Hannover, Germany*
[3]*Department of Earth and Environmental Sciences, University of Pavia, Pavia, Italy*

ABSTRACT

New viscosity experiments at superliquidus temperatures and during cooling at a rate of 10 K/hr
have been performed at different shear rates on a synthetic pyroxenite melt. Results revealed that
this melt is extremely fluid at temperature between 1646 and 1530 K and measured viscosities are
between 2.2 and 7.8 Pa·s. Such very low viscosities allow the lava to flow in turbulent regime as
confirmed by the high Reynolds numbers, which are always >2,000. As a consequence, very long
distance could be covered by the lava flow. If we consider this studied composition as proxy for
Mars lava flows coupled with very high effusion rates, our results might explain the presence of
extraordinary large volcanic channels, as recently hypothesized for the Kasei Valles on Mars, even
considering that the gravity is approximately one third that of Earth. Few literature data tracking
viscosity during cooling are available, and they reported shear thinning effect on different
compositions. Our experiments performed at 0.1 and 1 s^{-1} have shown complex variation in the
apparent viscosity, confirming that nonequilibrium rheology represents a still unexplored field of
investigation useful to better understand the real geological scenarios occurring in magmatic and
volcanic systems.

PLAIN LANGUAGE SUMMARY

The study of the flow of matter (rheology) is the key factor to understand dynamic processes and
behavior of magma rising through volcanic conduit and lava emplacement on Earth or other
terrestrial planets. Today we can monitor the evolution of magma and volcanic mixtures by
measuring their viscosity and its variation as temperature, composition, and fluid regimes vary.
The available data are mainly derived from isothermal experimental approaches, and very few
studies focused on monitoring viscosity behavior while changing both the cooling rate and the
shear stress. In this study we have monitored in detail the viscosity variation of an analog

composition prepared to reproduce Theo's Flow lava (Ontario, CA), considered as a terrestrial analog of Martian nakhlites. Measurements were performed using the concentric cylinder technique. Results show a very high fluidity of the melt in the temperature range between 1643 and 1530 K (2.2 to 7.8 Pa·s). As temperature drops into the subliquidus temperature (i.e., below 1530 K), apparent viscosity continuously increases to 6×104 Pa·s, where a brittle failure was observed. These results can provide indications on how extraordinary long lava flows might have developed on the Martian surface.

INTRODUCTION

Recently, experiments under constant temperature were performed in order to study the behavior of lavas in different geological settings on both Earth and other Earth-like planets (Chevrel et al., 2013; Rossi et al., 2017; Sehlke & Whittington, 2015; Vona et al., 2011, and references therein). Indeed, volcanic eruptive styles are governed by magma rheology, and rheology governs lava emplacement mechanisms. Most of the published experimental approaches aim to track the viscosity variation as a function of temperature, volatile content, and crystallinity. Moreover, experimental study on crystallization induced by variable decompression rates allowed scientists to shed new light on processes governing magma ascent dynamics (Fiege et al., 2015, and references therein). Following the pioneering work of Carmichael (1974), reporting the rheological

importance of the coexistence of crystals and liquid material melt solidification processes have been investigated via experiments under different applied cooling rates (see Hammer, 2008, for a general summary). Diverse studies at crystal-melt disequilibrium conditions have been performed (e.g., Lofgren, 1980; Cashman, 1993; Lange et al., 1994; Arzilli & Carroll, 2013; Vetere et al., 2015, and reference therein), but only recently has even the deformation acting on lavas been taken into account with both laboratory approaches (Kolzenburg et al., 2018; Kolzenburg et al., 2018; Kolzenburg et al., 2019) and direct measurements in the field (Chevrel et al., 2018). These are extremely important mechanisms that deserve further investigation as most of the magmatic and volcanic environment are controlled by nonequilibrium processes. Magma or lava rheology changes over time, even if imposed variables such as composition and temperature remain the same.

In this contribution, we present new results about the role of shear rates on the viscosity of partly crystallized silicate melts and an attempt to link different shear rates to nucleation and growth timescales (Kolzenburg et al., 2016) collecting viscosity data under a controlled cooling rate.

As stated in the review provided by Wilson and Head (1994), the "full range of volcanic eruption styles observed on Earth is to be expected" on Mars as well. "Due to the lower gravity, fluid convective motions and crystal settling processes will be slower on Mars than on Earth, and this fact guarantees larger diapirs to ascend to shallower depths. Thus, it is plausible that the dike widths increase on Mars by a factor of 2 and this results on higher effusion rates estimated by a factor of 5. The lower gravity causes cooling-limited flows to be longer, implying that we might expect compositionally similar cooling-limited lava flows to be about 6 times longer on Mars than on Earth." As a consequence, as reported in Wilson and Head (1994), Icelandic Laki lava flows (30–60 km in length) would have 200–350 km of length on Mars.

In this context, caution must be taken on the effect of gravity and cooling on Mars compared to Earth, by considering identical volume and topography. Thus, this would provide a potential explanation for the several hundreds of kilometers of flows that have been documented on the Martian surface (Kasei Valles or the more recently debated Hrad Vallis; Hopper & Leverington, 2014; Leverington, 2018). In particular, Kasei Valles is considered to be the largest outflow system on Mars with a length of more than 2,000 km and a width of up to several hundred kilometers. The total volume of magma erupted is estimated to be ~5×106 km^3 and, in magnitude, is comparable to some of the large igneous provinces on Earth like the Deccan Traps with an area of 0.5–1.5 $\times$ 106 km^2 and a volume estimate of >1.5×106 km^3 (Coffin & Eldholm, 1994).

On the other hand, we can only refer to lava rheology estimates derived from remote sensing data, which are actually one of the most applied methods, to retrieve lava flow velocity (e.g., Hulme, 1974; Moore et al., 1978; Hiesinger et al., 2007; Chevrel, Giordano, et al., 2013). This methodology considers morphologic similarities between terrains on terrestrial planets and those observed on Earth. In fact, the emplacement of lava flows can be modeled using a single rheological parameter (apparent viscosity or apparent yield strength) calculated from

morphological dimensions by using Jeffreys' and Hulme's equations (Jeffreys, 1925; Hulme, 1974).

Nonetheless, given the nonlinear dynamics of lava flows and domes, which may determine remarkable thermal effects, significant limitations may be observed and should be carefully considered before applying this method to any natural context (Giordano, 2019, and reference therein).

Being aware that there are only few studies that tried to quantify the lava rheology of Martian volcanism (Chevrel et al., 2013; Chevrel et al., 2014; Sehlke & Whittington, 2016; Vaucher et al., 2009; Wilson et al., 2009; Wilson & Head, 1994) and considering that the composition investigated in this study is similar to Martian nakhlites (see Table 1), we used our new viscosity data to estimate the lava flowing ability of one of the potential volcanic compositions erupted on Mars.

Sehlke and Whittington (2016) provided new methods for the estimation of the viscosity of planetary tholeiitic melts, pointing to model various volcanic processes, while Dundas and Keszthelyi (2014) calculated emplacement and (thermal) erosive effects of lava in south Kasei Valles on Mars. In both approaches, temperature and melt composition are required in order to calculate viscosity and estimate the lava flow velocity and lava flux. To our knowledge, only very few experimental data sets on planetary magma/lava viscosity introduce cooling rate and shear rates as potential parameters affecting magma mobility (e.g., Kolzenburg et al., 2019; Kolzenburg, Giordano, et al., 2018). Presently, only a few general models and combined equations (e.g., Mader et al., 2013; Vona et al., 2011) are able to track viscosity variation taking into account the crystalline phases in terms of their volume, aspect ratio, and applied shear stress. However, most existing viscosity models are not very accurate when applied to compositions that are different from those used in the experiments. The aim of this work is to better understand the rheology of multiphase silicate melt systems with the hope that such data could be incorporated into a general model able to track magma/lava rise and flow before emplacement. Up to now, such experiments have been performed under isothermal conditions and, in some cases, at variable shear rates (Sato, 2005; Ishibashi & Sato, 2007; Caricchi et al., 2007; Ishibashi, 2009; Vona et al., 2011, Vona & Romano, 2013; Pistone et al., 2012; Mader et al., 2013, and reference therein; Sehlke &

Whittington, 2015; Campagnola et al., 2016; Vetere et al., 2017). Recently, Kolzenburg et al. (2017), following the work of Giordano et al. (2007), highlighted the importance of monitoring the viscosity during cooling, suggesting that it is an important influence also of the applied shear rates. Data from Kolzenburg et al. (2017) and Kolzenburg, Di Genova, et al., 2018, Kolzenburg, Giordano, et al., 2018, Kolzenburg et al., 2019) show that the effective viscosity of the lava can drastically increase, as a function of temperature and time, until reaching a specific subliquidus temperature that, revising the concept first introduced by Giordano et al. (2007), they named Tcutoff, suggesting that the viscosity increase is a consequence of the onset of crystallization, which is mainly controlled by the cooling rate. In such a context these authors also highlighted a second-order shear rate effect on the rheological departure. In this contribution, we present new experimental results complementing the data set of viscosity measurements under controlled cooling and shear rates conditions to investigate the change in viscosity induced by crystal nucleation and growth. We use a pyroxenite melt as a starting material that is representative of the composition of Theo's Flow (Ontario, Canada), already extremely well characterized by Lentz et al. (1999, 2011) and considered a terrestrial analog of Martian nakhlites. The most salient compositional and textural features are reported in Table 1. Furthermore, constraints on mineral cooling rates and closure temperatures for the system of Theo's Flow were already available in Alvaro et al. (2015) and in Murri et al. (2016) where the authors estimated a cooling rate of about 0.091 K/hr for a lava flow of 50 m in thickness and a TC value around 973 K for clinopyroxenes (augites). The intracrystalline geothermometry was then validated against synthetic augite crystals in Murri et al. (2018) where the authors measured closure temperatures nearly identical with respect to the quenching temperatures of the experiments. These constraints on the natural samples provide background

parameters to be used for our controlled laboratory experiments.

Table 1. Compositions of Residual Glasses of the Crystal-Bearing Run Products and of the Starting Material.

	SiO$_2$	TiO$_2$	Al$_2$O$_3$	FeO	MgO	CaO	Na$_2$O	K$_2$O	Fe^{2+}/Fe$_{tot}$	r (Kg/m^3)	NBO/T F	F tot vol-area%	F Cpx vol-area%	F Ol vol-area%	F Ox vol-area%
SM	51.97	0.79	5.82	10.63	14.41	15.16	1.11	0.12	0.22	2.774[a]	1.14[c]	0	0	0	0
std	0.30	0.03	0.15	0.23	0.36	0.22	0.04	0.02	0.02	2.698[b]	0.73[d]				
TF01-1	55.78	1.63	11.48	11.00	7.00	10.26	2.46	0.23	0.16	2.670[a]	0.48[c]	62.6[f]			
std	0.73	0.06	0.44	0.81	0.31	0.39	0.21	0.02	0.02	2.605[b]	0.58[e]	65.4±7.3[g]	60.5±7.1[g]	2.9±0.8[g]	1.8±0.5[g]
TF01-2	51.52	1.18	9.01	14.51	10.02	11.58	1.90	0.20	0.20	2762[a]	0.73[c]	51.2 f			
std	0.29	0.02	0.15	0.16	0.16	0.20	0.06	0.02	0.01	2.689[b]	0.64[e]	50.5±6.3[g]	47.2±5.8[g]	1.8±0.7[g]	1.5±0.5[g]
TF1-1	53.66	1.25	9.77	12.50	8.87	11.59	2.00	0.22	0.18	2.719[a]	0.65[c]	53.1[f]			
std	0.56	0.04	0.13	0.58	0.20	0.23	0.06	0.01	0.02	2.650[b]	0.63[e]	49.3±5.7[g]	47.4±5.0[g]	0[g]	1.9±0.8[g]
Nakhla*	48.84	0.34	1.61	19.69	12.93	14.85	0.46	0.14							
Th top 120	49.74	1.04	8.57	15.93	11.92	11.41	1.11	0.05							
Th per 6.9	44.11	0.50	4.03	15.83	32.96	2.46	0.03	0.01							
Th per 10.1	44.52	0.46	3.73	15.85	30.93	4.26	0.02	0.02							
Th pxite 32.4	52.53	0.71	5.46	11.16	13.97	15.47	0.29	nd							
Th pxite 51.9	52.40	0.79	6.09	11.54	13.21	14.93	0.78	nd							

Note. The starting composition (SM) as well as experimental residual glass compositions (TF0.1-1, TF0.1-2, and TF1-1) represent an average of 20 measurements. Results are reported in wt %. std refers to 1 standard deviation. Determination of ferrous-ferric ratios was achieved by a wet chemical microcolorimetric method (Schuessler et al., 2008; Vetere et al., 2014). Comparison with natural compositions from Nakhla and Theo's Flow (see Lentz et al., 1999) is also reported. nd = no data. aGlass density was estimated using the model of Klöß (2000) adding 0.02 wt % H2O. bMelt density was calculated using the Ochs and Lange (1999) model at 1573 K and adding water content equal to 0.02 wt %. cThe nonbridging oxygen per tetrahedron (NBO/T) values as reported in Mysen and Richet (2005) and Mysen et al. (1982) were calculated by considering the reported Fe2+/FeTot ratios. dSM fragility is calculated by using Vogel-Fulcher-Tammann parameters (see equation 3 and related parameters) following Angell (1985), $F = B/(Tg \times (1 - T0/Tg)2$. eFor experimental compositions TF0.1-1, TF0.1-2, and TF1-1,Vogel-Fulcher-Tammann parameters were estimated according to the Giordano et al. (2008) general model. fMass balance calculation. gImage analyses data.

143

STARTING MATERIAL

A synthetic composition derived from a pyroxenite from Theo's Flow is used to test shear rate effects on crystal nucleation and growth during cooling. Theo's Flow lava, located in the Munro Township, eastern Ontario, is described as a differentiated, 120-m-thick lava flow containing peridotite, clinopyroxenite, and gabbro layers covered by hyaloclastite at the top (Lentz et al., 1999, 2011). This lava flow dates to the Archean age (approximately 2.7 Ga) on the basis of the age determined at nearby komatiites (Shirey, 1997). Its name was attributed by Arndt (1977), who first identified and described it. Hyaloclastite at the top quenched margin is a breccia that probably suggests, together with pillow basalts and pyroclastics that occur in this area, a subaerial and/or shallow submarine origin for Theo's Flow (Condie, 1981). Details on the geological setting are reported in Lentz et al. (2011, and references therein). Due to its compositional similarity to nakhlites, one of the most known Martian meteorite groups, this flow is of potential relevant scientific interest also for the study of volcanism on other terrestrial bodies (Friedman, 1998).

The starting material was prepared by melting a mixture of oxides and carbonates. Melting was performed in a Nabertherm HT 04/17 $MoSi_2$-heated box furnace (Nabertherm GmbH, Lilienthal, Germany) at 1673 K, in air. Then, the melt was rapidly quenched to glass by pouring it on a brass plate. As proved by subsequent Raman spectroscopy analysis on quenched glass (see supporting information Figure S1, Appendix IV), the adopted quenching rate allows us to get homogeneous glass, avoiding the occurrence of quench crystals (Vetere et al., 2015, 2017). Qualitatively, the synthetic composition of Theo's Flow shows very high fluidity during quenching, suggesting a high ability to flow.

ANALYTICAL AND EXPERIMENTAL METHODS

Chemical compositions for the starting material and run products were determined by using the electron probe microanalyses (EPMA) installed at the Department of Mineralogy at the University of Hannover (DE), following the procedure reported in Rossi et al. (2017) for glasses and in Vetere et al. (2017) for crystalline phases. Table 1 shows the starting compositions presented in this study plus densities calculated according to Ochs and Lange (1999) for melts and Klöß (2000) for glasses. Nonbridging oxygen per tetrahedron was calculated following the method described in Mysen et al. (1982), considering Fe_2O_3 as a network former and FeO as a network modifier (Table 1). The determination of ferrous-ferric ratios was achieved by a wet chemical microcolorimetric method as proposed in Schuessler et al. (2008) and Vetere et al. (2014).

A rotational Anton Paar RheolabQC viscometer head, equipped with a Gero HTRV 70-250/18 high temperature tube furnace, was used to measure viscosity. This apparatus is installed at the Petro-Volcanology Research Group labs at the University of Perugia and can operate up to 2073 K at room pressure. A Pt_{80}-Rh_{20} crucible with an inner radius of 18.5 mm, an outer radius of 20 mm, and a height of 70 mm was used to host the silicate melt. The spindle is made of Al_2O_3 (with a diameter of 12.2 mm and a length of 60 cm) and is fixed to the head of the viscometer by a standard collet chuck. In order to avoid any contamination of the silicate melts during the experimental runs, the spindle's lower end is covered by a tight-fitting 0.2-mm-thick Pt_{80}-Rh_{20} foil. An Al_2O_3 cylindrical pin (2 mm in diameter and 15 mm in length) is inserted in the previously drilled spindle stabilizing the Pt_{80}-Rh_{20} cover. The rotational viscometer allows measurements under controlled shear rate ($\dot{\gamma}$) and can be used to investigate possible shear effects on the viscosity of melts or partly crystallized systems. Methods and procedures described by Ishibashi (2009) were applied in order to determine melt viscosity. For viscosities of assemblages composed of melt + crystals we followed the same procedure as in Kolzenburg et al. (2016). Briefly, principles of the concentric cylinder rotational viscometer consider that the molten sample is standing in the gap separating the fixed outer cylinder from the rotating inner cylinder run at constant angular velocity (Ω). Krieger and Elrod (1953) and Spera et al. (1988) have shown that Ω is related to the shear stress (σ) by the following relation:
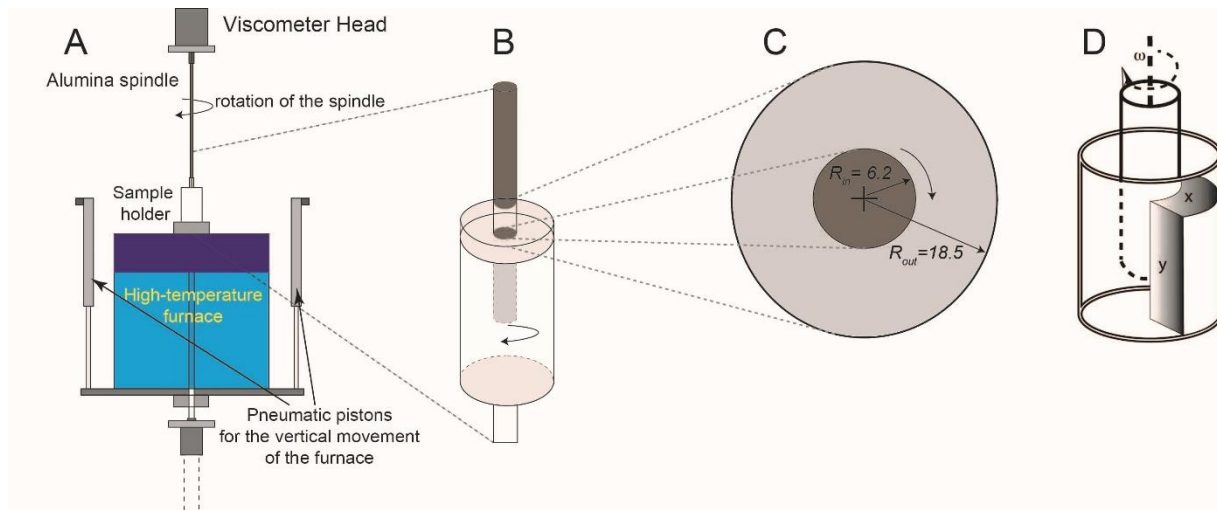
Figure 1. Details of the furnace, viscometer, and sample holder used in this work. Note (a) the movable furnace, (b) the Al spindle covered with Pt cup, and (c) the size of the spindle and the crucible. (d) Details of the sample sections used for the analytical and textural analyses (see text). *x* and *y* are, respectively, perpendicular and parallel cut sections of the sample relative to the spindle.

$$\Omega = \frac{1}{2} \int_{\sigma_c}^{\sigma_i} \frac{\dot{\gamma}}{\sigma} d\sigma \qquad (1)$$

where σ_i and σ_c are the shear stresses at the surfaces of the inner and outer cylinder, respectively. In addition, the relation between the rotational torque (τ) and σ at a distance r from the rotational axis can be described as follows:

$$\tau = 2\pi h r 2\sigma \qquad (2)$$

where h is the length of the inner cylinder immersed in a molten sample.

For the instruments used in this study, the maximum torque is quantified to be between 0.2 and 75 mNm. This would correspond to a viscosity range varying between 0.1 and 108 Pa·s. Consequently, data collected at the low torque end have larger relative uncertainties.

In our case, to measure melt viscosity, we performed measurements at shear rates up to 20 s^{-1} (see section 4), while for the subliquidus measurements shear rates were 1 and 0.1 s^{-1} (details of the measurements are reported also in the supporting information, Appendix IV).

As reported above, Theo's Flow was expected to have a high ability to flow at high temperature. Thus, before running experiments, we calibrated the viscometer using a Wacker silicone standard having a viscosity of 10 Pa·s (Spina et al., 2016). One hundred measurements were performed at 298 K, and the results showed good reproducibility, with average values of 9.8 ± 0.3 Pa·s. Moreover, a second calibration was performed by using NIST 717a standard glass, for which the temperature-viscosity relationship is accurately known (https://www.nist.gov). Reproducibility of measurements on the standard glass is on the order of ±0.03 log unit.

The furnace can move vertically using two pneumatic cylinders (details are reported in Figure 1). For further details on the experimental setup please refer to Morgavi et al. (2015). Temperature was monitored using an in-house built S-type thermocouples (Pt$_{10}$Rh$_{90}$ versus Pt) within an Al2O3 sheath, placed inside the spindle and at the bottom of the crucible. As the rotation of the viscometer prevents the use of thermocouples directly wired to a controller, OMEGA wireless thermocouple transmitters UWTC-Series were employed (OMEGA Engineering, Inc., Stamford, CT, USA). Uncertainty on temperature measurements is on the order of 1 K. Following the calibration proposed by Kolzenburg et al. (2016), one or several wireless thermocouples were positioned inside the spindle, and the

accuracy of the temperature reading was ±1 K. We also find a stable thermal gradient, but since our experiments are run at a relatively high temperature (1673–1473 K), this thermal gradient is <2 K, in agreement with Kolzenburg et al. (2016).

Prior to viscosity measurements, approximately 70 g of melt was stirred at 1673 K for 2 hr at strain rates of 5–20 s^{-1}. This procedure causes the complete removal of gas bubbles and the attainment of a compositionally homogeneous melt (Iezzi et al., 2011; Vetere et al., 2013, 2015). Each melt viscosity experiment has to be considered as a single experiment since after collecting viscosity data, we quenched it and the next experiment was restarted at superliquidus conditions.

Samples used in the subliquidus temperature experiments were first melted at superliquidus conditions. At the end of the experiments, samples were quenched by moving the spindle + crucible into the cooled head of the furnace. The initial quench rate was of the order of approximately 7000 K/hr, which was sufficient to avoid the formation of quench crystals. After quenching, run products were drilled out from the crucible using a diamond core drill and then were mounted in epoxy, ground flat and polished for textural and chemical analyses. The phase compositions, that is, starting melts, glass matrix, and crystalline phases, of all run products were carried out by using EPMA. The analytical conditions of EPMA were the same as those reported in Vetere et al. (2017).

Backscattered electron (hereafter BSE) images were collected by field emission scanning electron microscopy (FE-SEM; FEG LEO 1525, Zeiss Company, Germany) at the Department of Physics and Geology of the University of Perugia (Italy). The energy dispersion X-ray spectroscopy analysis (Quantax 200 with an Xflash 400 detector, Bruker Company, Germany), coupled with the scanning electron microscopy, was used to detect phases.

The textural features were analyzed with FE-SEM using BSE. Images were collected at different magnifications to accurately characterize the textures and the distribution of phases (150X, 400X, 800X, and 1,500X). About 100 FE-SEM images were collected and used for the determination of phase content, abundance, and distribution by image analysis. Image analysis was performed using the Image-ProPlus 6.0 software by applying the same analytical protocol as reported in Iezzi et al. (2011) and Vetere et al. (2013, 2015). For each run product the identification of phases was determined by linking their gray-level ranges with the compositions.

RESULTS

Liquidus Temperature and Composition of Residual Glasses

The liquidus temperature (TL) of the investigated composition was estimated using the alphaMELTS software package (Asimow et al., 2004; Smith & Asimow, 2005), providing a value for TL = 1539 K. Experimental data are in good agreement with this estimate since the experiment performed at T = 1530 K did not show the presence of crystals, whereas experiments performed at 1516 K showed an increase in viscosity, confirming a possible rearrangement of the melt structure and/or nucleation and growth processes. The compositions of residual glasses of the crystal-bearing run products are reported in Table 1 in comparison with the starting material. The residual melt evolution resulted to be dependent on the applied shear rate, cooling temperature, and related run time. The faster the shear rate, the higher the SiO_2 content (please compare experiments TF0.1-2 and TF1-1) of the residual glass. The apparent anomaly for sample TF0.1-1 compared to TF0.1-2 is due to the longer duration (approximately 36,700 s) of the TF0.1 experiment as explained below.

Crystal chemistry

Experiments at subliquidus condition were performed at a cooling rate of 10 K/hr from superliquidus temperature (1623 K) down to 1468 K. Two shear rates of 0.1 and 1 s^{-1} were applied. BSE images were collected on samples cut perpendicular and parallel to the spindle axis (Figure 1d). Selected BSE images are shown in Figures 2 and 3. Figures 2a, 2b, 3a, and 3b report BSE images from the experiment performed at 0.1 s^{-1}; Figures 2c, 2d, 3c, and 3d represent the quench product after viscosity measurement at 1 s^{-1}. Both shear rate experiments were carried out under the previously defined cooling rate (10 K/hr).

Since samples were drilled out and recovered cylinders have a diameter of 6mm and a length of ~10 mm, the total area investigated is approximately 340 mm^2 for each experiment.

At experimental conditions, clinopyroxene (hereafter Cpx) crystals are the dominant phase with only a minor amount of Fe-Ti oxide. Low fraction of olivine is also present only in experiments performed at low shear rate.
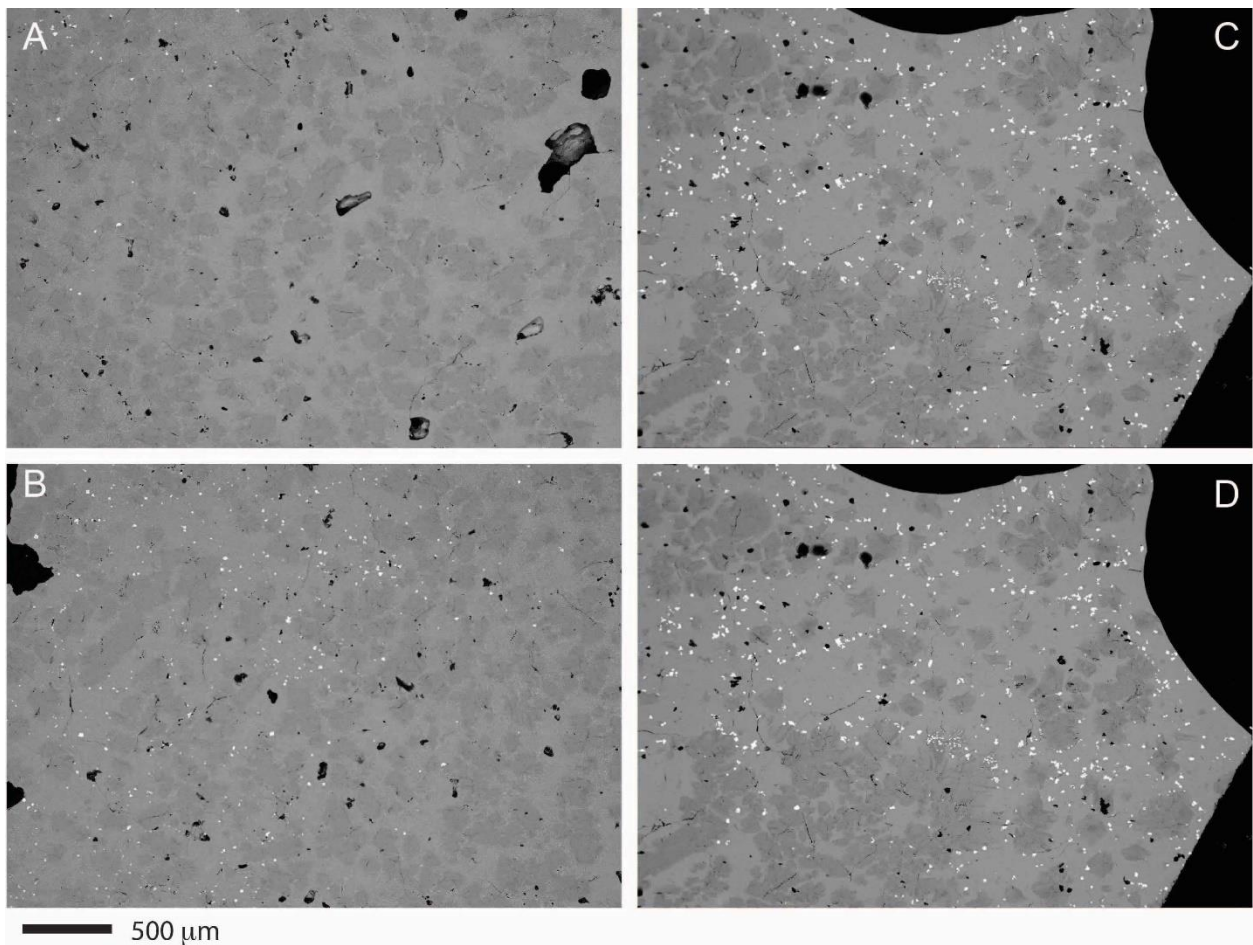
Figure 2. Selected backscattered electron images obtained after the experiments performed at shear rates of 0.1 and 1 s⁻¹. (a, b) $\dot{\gamma}$ =0.1 s−1. (c, d) Quench products after viscosity measurement at $\dot{\gamma}$ =1 s⁻¹.

The crystal fraction distribution as a whole shows no important deviations in volume between the experiments performed at different shear rates (i.e., 0.1 and 1 s⁻¹) and is calculated to be of approximately 50.5 ± 6.3 and 49.3 ± 5.7 vol %, respectively. Mass balance calculations give for the slow dynamic experiments (at shear rate = 0.1 s⁻¹) 51.2 vol % whereas for the 1 s⁻¹ experiment 53.1 vol % of crystalline phases.
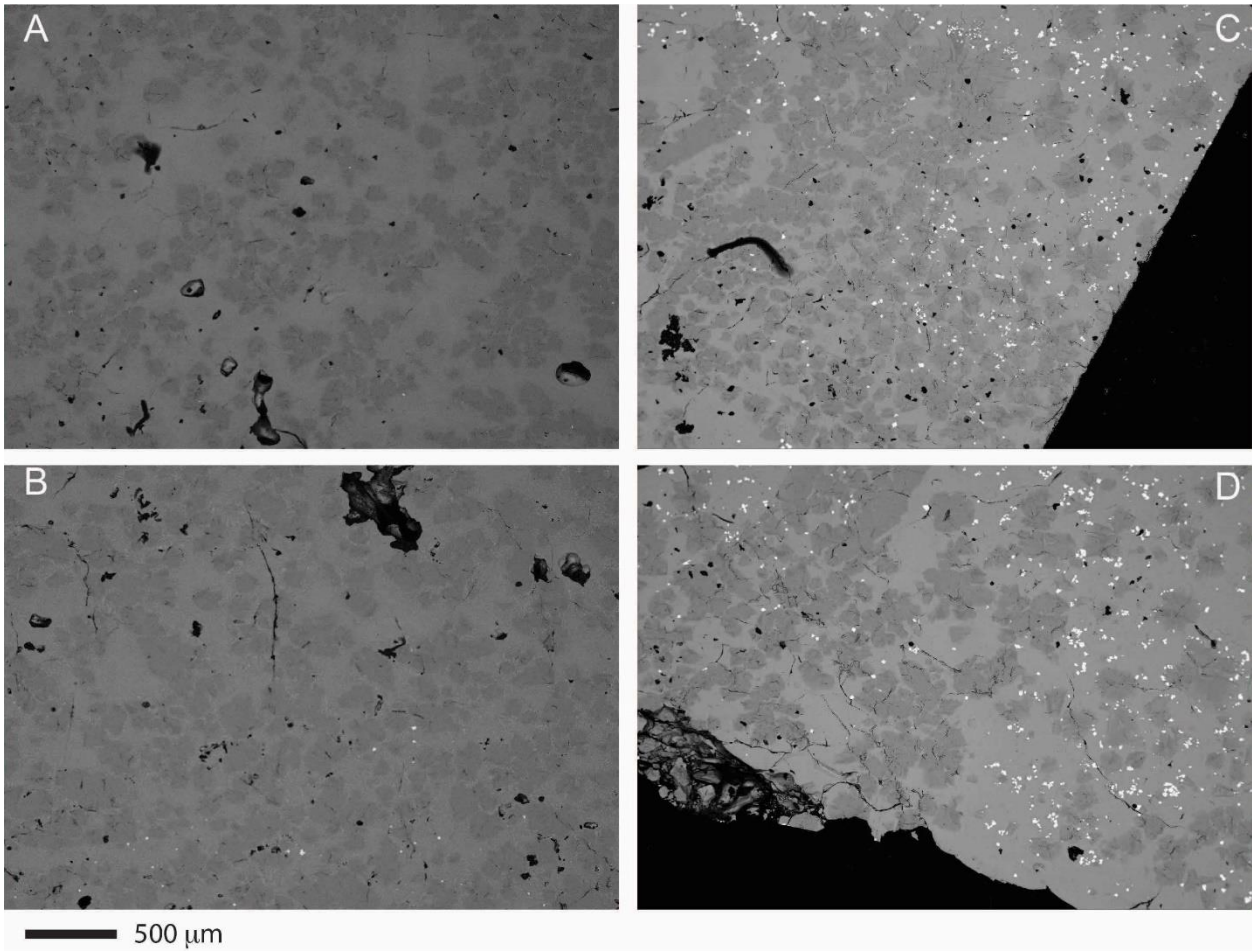
Figure 3. Additional backscattered electron details as in Figure 2 for shear rates of 0.1 and 1 s^{-1}. (a, b) $\dot{\gamma}$ = 0.1 s−1. (c, d) Quench product after viscosity measurement at $\dot{\gamma}$ = 1 s^{-1}.
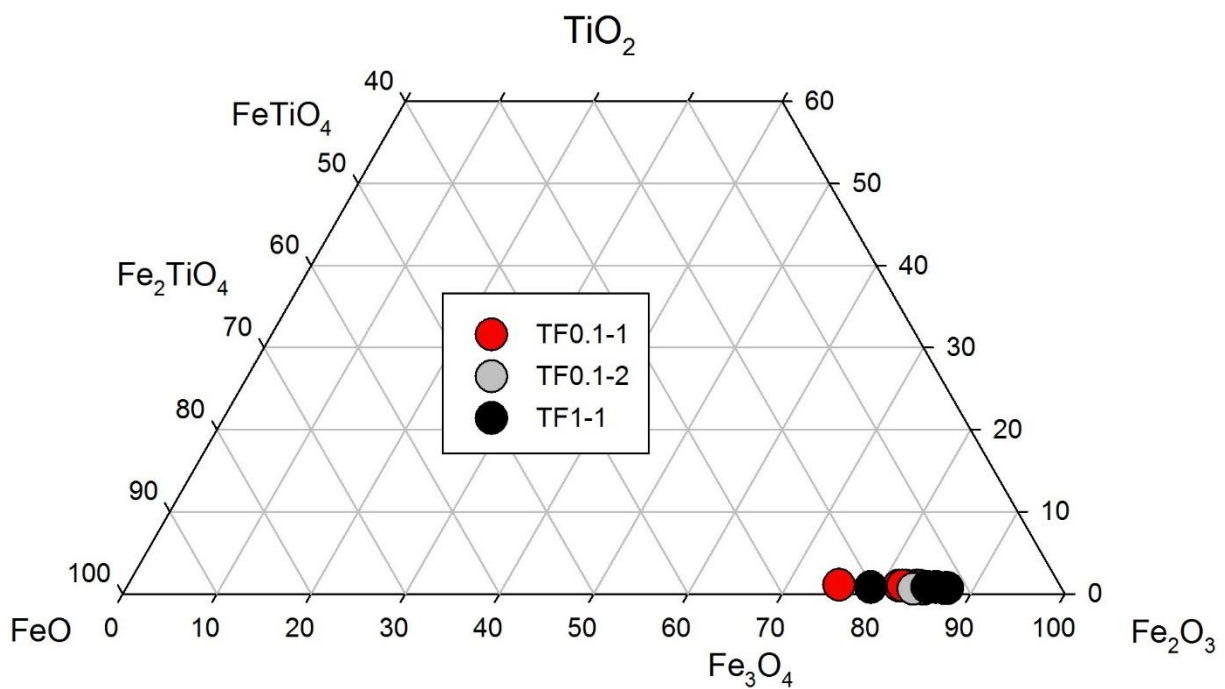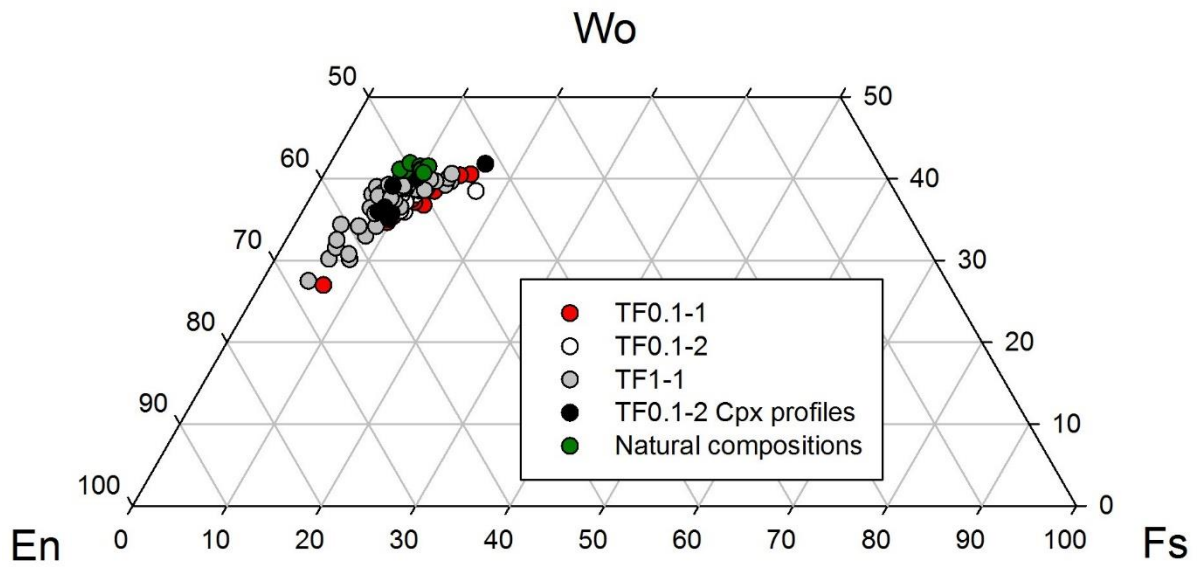
Figure 4. (a) Clinopyroxene (Cpx) and (b) Fe-Ti oxide crystal chemistry after experiments TF0.1-1, TF0.1-2, and TF1-1 (Table S3). Natural Cpx analyses are also reported for Cpx from the analyses by Lentz et al. (1999).

Moreover, PhasePlot simulation (based on Ghiorso & Sack, 1995; Gualda et al., 2012; Ghiorso et al., 2002; Stixrude & Lithgow-Bertelloni, 2011) on Theo's Flow bulk compositions shows, at 1473 K, an amount of crystals of 48.6 vol %, very close to what has been measured above with a composition matching that obtained experimentally (Wo37En51Fs11; see below).

Both experiments exhibit similar amount of pyroxene, although there is a tendency to form more concentrated clusters in experiments performed at higher shear rates (Figures 3a–3c). Also, as shown in Figures 2c, 2d, 3c, and 3d, Fe-Ti oxides crystallize in all experiments (Figure 2 and 3) although they are quantified to be <2 area %. Pyroxenes frequently show complex clusters and a rounded habit and sometimes present slightly elongated shapes on the order of a few hundreds of micrometers. Also, some of them show complex growth history and clear chemical zonation corresponding, for the lighter part, to higher Fe and Ca contents, whereas the dark part is more enriched in Mg content (see below and Figure 4a).

Cpx compositional variation (from Wo27En68Fs4 to Wo42En41Fs17) shows a similar trend for all the three experiments, almost matching the natural Cpx composition from Theo's Flow (Lentz et al., 2011; Figure 4 a and Tables S1 and S2 in the supporting information, Appendix iV). Moreover, at the beginning of the crystallization process, as recently highlighted by Mollo et al. (2018), melt compositional gradient produces Cpx growth layers as a response. This will produce a progressive enrichment in Al, Ti, and Na and depletion in Fe^{2+}, Ca, and Mg while increasing the degree of undercooling (Mollo et al., 2010, 2011, 2012). In particular, the surrounding melts will be depleted in Al and Fe and the feeding available ingredients will cause an overgrowth of Mg-rich Cpx. We are confident that what has been shown in Figures 5a and 5b corresponds exactly to the abovedescription as also demonstrated by EPMA data provided in Table S1 (core-to-rim CPx analyses).

Fe-Ti oxide crystals are much smaller (approximately 10 μm or less) and in some cases more spherical. Composition is close to magnetite with slight chemical variation when considering all the three experiments (Figures 4b, 5a, and 5b and Tables S1 and S2). Furthermore, only in experiments performed at lower shear rate ($\dot{\gamma} = 0.1$ s^{-1}) were few olivine crystals found with a composition close to pure forsterite (Fo96-97, Figure 5a). The reported data are the results of chemical analyses of about 130 crystals analyzed by means of electron microprobe (Tables S1 and S2).
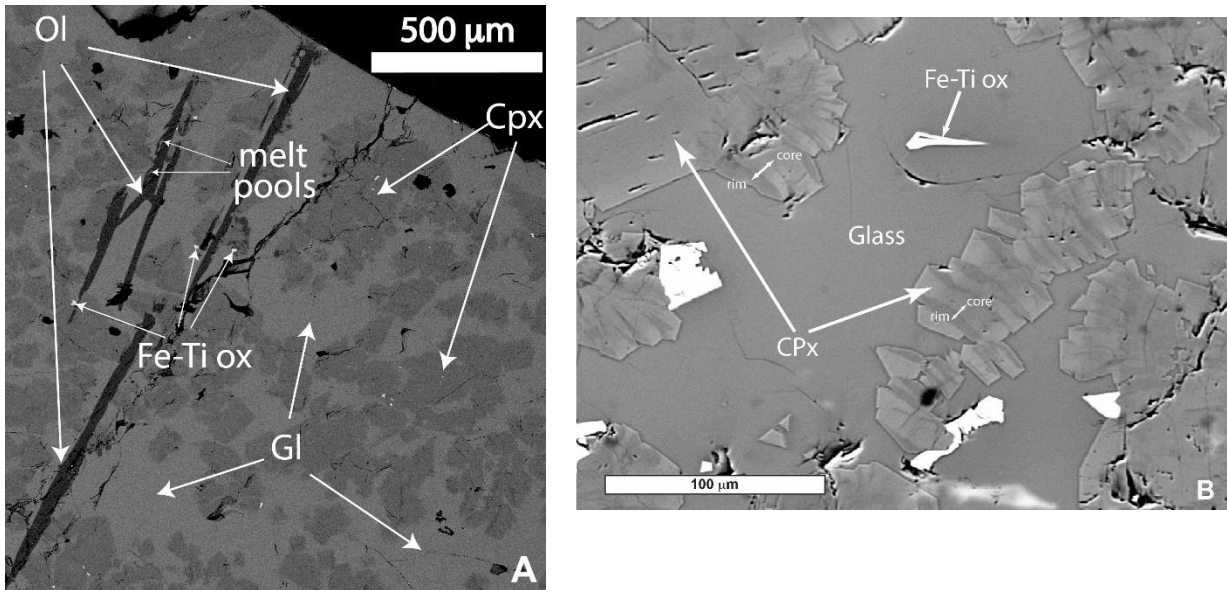
Figure 5. (a) Insight on the low-shear-rate experiment TF0.1-1 with high-aspect-ratio olivine (Ol), darker gray clinopyroxenes (Cpx), and light gray glass (Gl). Bright spots refer to iron and titanium oxides (Fe-Ti ox). (b) Texture features of the Cpx showing bright and dark areas possibly related to a second generation of Cpx (please refers to Table S1 for chemical composition details).

Melt viscosity

Melt viscosity was measured at different shear rates always equal to or higher than 13 s^{-1}. Such a relatively high shear rate was necessary due to the high fluidity of melt, as previously mentioned. Sixteen independent superliquidus experiments were performed in the temperature range between 1646 and 1530 K to determine the dependence of melt viscosity on temperature (Table 2 and Figure 6). In the investigated temperature range, viscosity varies from 2.2 to 7.8 Pa·s. Each viscosity value presented in Table 2 is an average between 100 and 500 readings, collected on timescales from 60 to 120 min, with torque values recorded every 5 to 30 s. The majority of the measurements were performed at a shear rate of 13 s^{-1}.

Table 2. Viscosity Measurements as a Function of Temperature and Shear Rate				
Experiment	Temp	h	std	Shear rate
	(K)	(Pa s)		s^{-1}
TF-1	1646	2.2	0.35	13
TF-2	1618	2.9	0.23	13
TF-3	1586	4.3	0.03	13
TF-4	1583	4.1	0.02	13
TF-5	1578	4.8	0.03	13
TF-6	1569	5.3	0.03	13
TF-7	1558	5.9	0.06	13
TF-8	1545	6.5	0.03	13
TF-9	1545	6.6	0.02	13
TF-10	1543	6.2	0.1	13
TF-11	1535	7.3	0.03	13
TF-12	1530	7.8	0.05	13
TF-13	1545	6.4	0.02	20
TF-14	1543	6.5	0.1	20
TF-15	1535	7.2	0.03	15
TF-16	1530	7.7	0.05	15

Note. Experimental conditions and results of viscosity measurements (η) using the concentric cylinder apparatus. Note that the value for each measurement is a single measurement on a pure-liquid system. $\dot{\gamma}$ refers to the applied shear stress. No differences were found pointing to a Newtonian behavior of this system at the investigated shear rates; std refers to standard deviation of viscosity measurements.

To check for possible dependence of viscosity upon shear rate ($\dot{\gamma}$), we repeated four experiments at 1545, 1543, 1535, and 1530 K with $\dot{\gamma}$ ranging from 15 to 20 s−1 (samples TF-13 to TF-16 in Table 2). As it is evident in Figure 6 and Table 2, data are in very good agreement and no measurable effect of shear rate on viscosity was detected at superliquidus temperature.

An empirical model of viscosity as a function of temperature was developed by using the obtained viscosity data set. The model is based on the Vogel-Fulcher-Tammann (VFT) equation (Vogel, 1921), as follows:

$$\log \eta \ (Pa \ s) = A + B/(T - T_0) \tag{3}$$

where T is the temperature in kelvin, while A, B, and $T0$ are fitting parameters, representing the preexponential term, the pseudo-activation energy (related to the barrier of potential energy obstructing the structural rearrangement of the liquid), and the VFT temperature, respectively. The

VFT approach accounts for the non-Arrhenian temperature dependence of melt viscosity. Data were fitted using a nonlinear least squares regression providing the following parameters: $A = -4.22$ (Pa·s), $B = 4982.0$ (K), and $T0 = 556.1$ (K). This relationship reproduces our experimental data with a root mean square deviation of 0.016 (Figure 6). Note that the fitting parameters reported above are only valid for high-temperature (superliquidus) viscosity data.
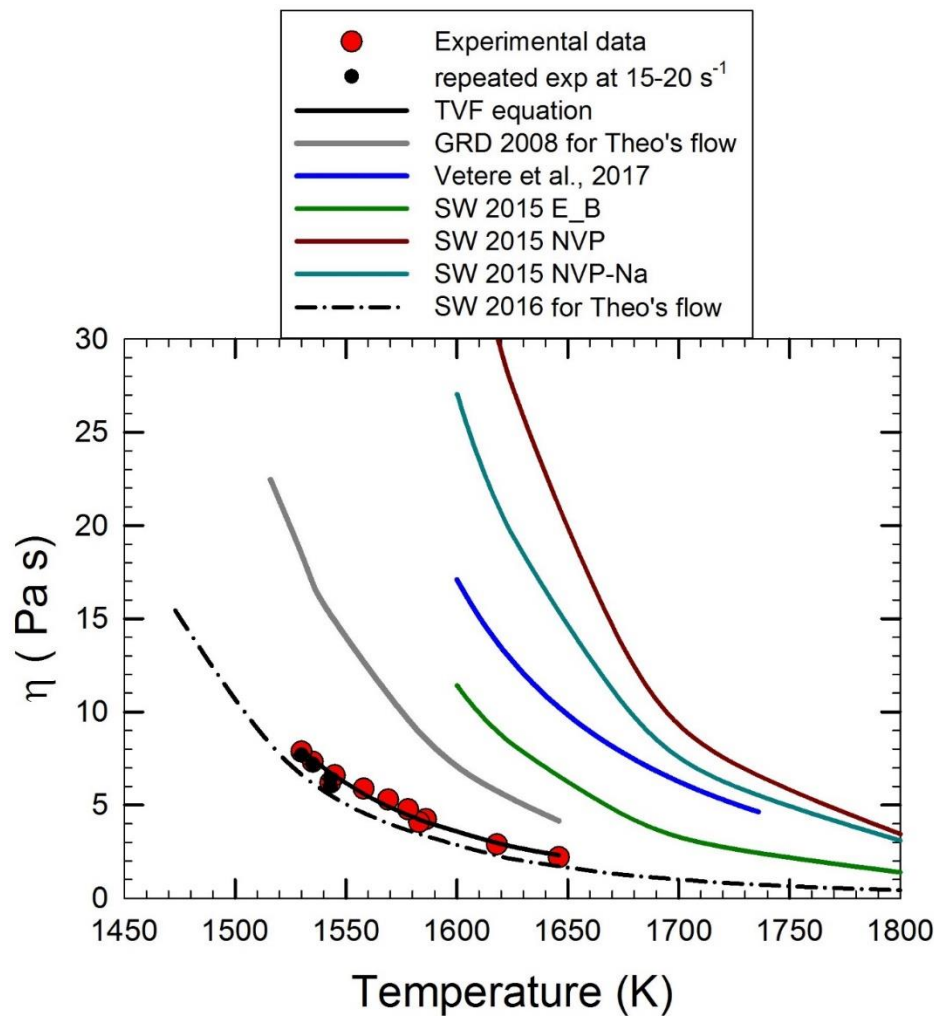
Figure 6. Viscosity data for melts at superliquidus conditions. The black line represents the predictive model given in equation (1). Red circles refer to experimental data performed at $\dot{\gamma} = 13$ s^{-1}, while black circles refer to the repeated experiment performed at higher shear rates of 15 and 20 s^{-1}. No viscosity differences are noticed between 13 and 20 s^{-1}, suggesting a Newtonian behavior of such melts at the experimental high temperatures. The gray line refers to viscosity data derived from Giordano et al. (2008) by using our starting material composition. Colored lines, from top to bottom, refer to literature data of high fluid "mercurian" melts reported by Vetere et al. (2017) and Sehlke and Whittington (2015), respectively. The black dashed line (SW 2016) refers to the Sehlke and Whittington (2016) model for tholeiitic liquids.

An important feature of our composition is the relatively low SiO_2 and the low Al_2O_3 (5.65 wt %) contents. The high-MgO contents are responsible for the low viscosity of our silicate melt. Previous experimental data (e.g., Vetere et al., 2017) are in agreement with the lower melt viscosity described here. The comparison of the experimental viscosity data with those derived by the general model

proposed by Giordano et al. (2008) shows a maximum difference of 10.0 Pa·s at 1530 K (Figure 6). Moreover, Sehlke and Whittington (2016) provided a model based on the Adam-Gibbs theory to relate viscosity (η) to absolute temperature (T) and the configurational entropy of the system (S_{conf}). The modeled data are in excellent agreement with our experimental data for the composition of Theo's Flow as shown in Figure 6. Finally, Liebske et al. (2005) and Dingwell et al. (2004) investigated the viscosity of peridotite melts from room pressure to approximately 13 GPa. Their results show low viscosities (approximately 0.1 Pa·s at 1850 K at 1 atm) that agree with the values obtained by using equation (3) (approximately 0.4 Pa·s at 1850 K).

Partly Crystallized Rheology Under Cooling

Viscosity evolutions during cooling at shear rates of 0.1 and 1 s−1 are shown in Figures 7a and 7b. Viscosity trends show typical S-type curve evolution through time. Experiments were conducted for about 25,000 s applying identical cooling rates (10 K/hr). As shown in different literature studies (e.g., Mader et al., 2013, and reference therein), viscosity increase is primarily due to nucleation and crystal-growth processes under cooling, although the compositional evolution of the melts during crystallization needs to be considered.
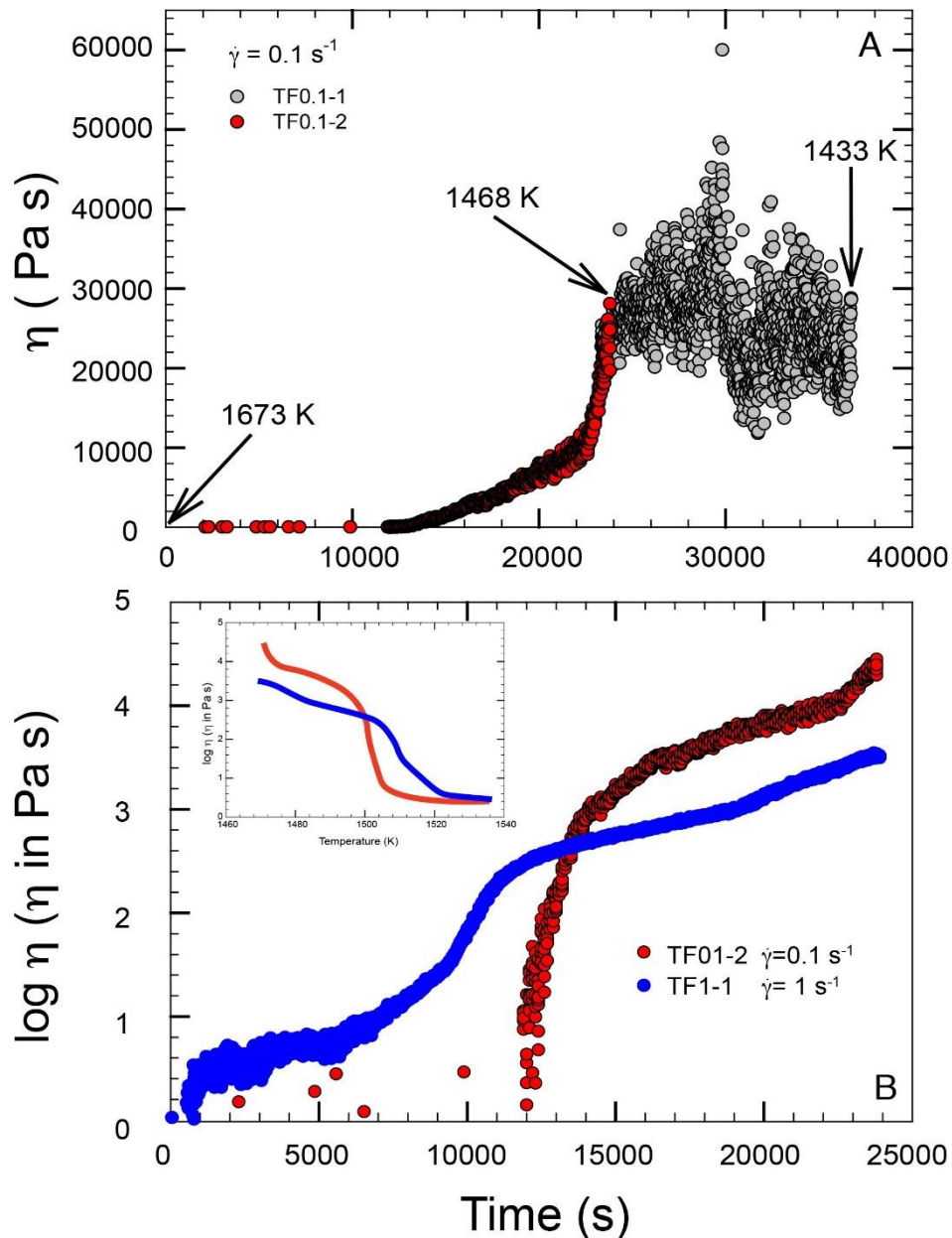
Figure 7. (a) Apparent viscosity versus time path at a rate of 10 K/hr for TF0.1-1 and TF0.1-2 experiments. Note the anomalous viscosity data reading for TF0.1-1 caused by a circular fracture of the melt + crystal system. The detachment points to a brittle failure of the system when viscosity reached the value of approximately 4.77 log (Pa·s) at 1468 K. In particular, the highest viscosity measured (approximately 6.0×10^4 Pa·s) at a shear stress of 5960 Pa possibly corresponds to the brittle failure in this system (see text for further details). (b) Apparent viscosity versus time path and a related cooling rate of 10 K/hr. Note the continuum increase in viscosity and change in the viscosity versus time slopes as cooling proceeds. Difference of about 1 log units in effective viscosity points to evident shear thinning at the imposed shear rates. The symbol covers ±0.2 log units of viscosity. The inset represents log viscosity versus temperature path for the TF0.1-2 and TF1-1 experiments.

The experiment performed at 0.1 s−1 was repeated twice. The first experiment was run for a longer time (approximately 36,700 s; Figure 7a) and, after approximately 24,000 s we recorded anomalous and scattered viscosity values when temperature was below 1468 K (e.g., spikes in viscosity-versus-time plot; Figure 7a). After quenching ($T = 1433$ K), it was clear that the anomalous viscosity was caused by a circular fracture of the melt + crystal system located approximately at 0.7 cm from the

157

spindle wall. A detachment between a part of the sample stacked on the spindle and all the rest of the sample into the crucible was clearly visible, pointing to a brittle failure of the system when viscosity reached the value of approximately 4.77 log (Pa·s) at 1468 K. In particular, the highest viscosity measured (approximately 6.0×10^4 Pa·s) at a shear stress of 5960 Pa possibly corresponds to the brittle failure in our system. For such a reason, to have a reasonable comparison between experiments, the subsequent runs were stopped soon after the temperature reached 1470 K. As expected, in both TF0.1-2 and TF1-1-1 experiments no brittle

behavior was observed. Considering experiments performed at the lowest shear rate (0.1 s^{-1}), a sudden increase in viscosity after 12,000 s during continuous cooling was observed (Figure 7b). Viscosity data collected before 12,000 s are scattered and not useful since the relatively low applied shear rate does not allow the instrument to provide reliable data (i.e., the lower torque limit is reached due to the high fluidity/low viscosity); the experiments conducted at a higher shear rate show the beginning of the increase in viscosity much earlier, at around 5,000 s. The two viscosity curves cross each other after approximately 13,000 s (Figure 7b), where viscosity has a value of approximately 400 Pa·s and the temperature is close to 1500 K. Evolution of the viscosity curves, after 13,000 s, clearly points to a decrease in the apparent viscosity (i.e., the shear rate-versus-shear stress curve does not show linearity) as shear rate increases, with final viscosities of 4,000 and 32,000 Pa·s for TF1-1 and TF0.1-2, respectively (Figure 7b) also considering the fact that the amount of solid phases in TF0.1-2 and TF1-1 is almost identical at the quenching temperature (as shown above).

DISCUSSION
Rheological Evolution

Our results show that the shear rate affects the composition of crystalline phases and the temperature at which they appear. In particular, the few olivine crystals that are present only in the experiment performed at low shear rate are almost pure forsterite in composition. These crystals exhibit large grain sizes (>1 mm) and typical habits due to a nonequilibrium crystallization (i.e., smoothed and with melt pools; see Figure 5a). These olivines represent the high-temperature phase starting their nucleation and growth soon after TL is crossed. Thus, the growth rate of olivine, although based on a limited number of crystals, at a cooling rate of 10 K/hr results to be relatively large and on the order of approximately 5.34×10^{-8} m/s. Cpx have similar chemical composition (Figure 4a) showing similar volume content in both experiments TF0.1-2 and TF1-1-1 (see section 4.2 and Figures 2 and 3), while in TF0.1-1 (the longest experiments) Cpx show relatively higher

crystallinity as confirmed by image analysis (65.4 ± 7.3 area %) and mass balance calculation (62.6 vol %). This is due to the longer run time (up to approximately 36,700 s) that allows reaching a lower temperature (1433 K) before quenching.

The non-Newtonian behavior of suspensions whose viscosity decreases under shear strain (change in apparent viscosity) has been already observed in isothermal experiments (e.g., Ishibashi, 2009; Ryerson et al., 1988; Soldati et al., 2016; Vetere et al., 2017; Vona et al., 2011). Contrary to the classical isothermal viscosity experiments (Campagnola et al., 2016; Vetere et al., 2017; Vona et al., 2011; Vona & Romano, 2013), as expected, during cooling, viscosity never reached a steady value because no equilibrium conditions of the liquid + crystal suspensions were achieved. This is due to the progressive increase of crystallinity with time (Figure 7). In fact, before quenching, the low-shear-rate experiment ends up with a viscosity value of 24,800 Pa·s, following an almost constant increase of the time-viscosity curve, except in the last segment where it gets steeper. As for the high-shear-rate experiment, viscosity reaches the value of 3,150 Pa·s, again following essentially two trajectories, first less steep and then steeper. The kinks in the viscosity time path,
for the TF1-1 and TF0.1-2 experiments (Figure 7b), possibly suggest important changes in crystallinity occurring after 19,000 and 22,500 s, respectively. Such a change in slopes could reflect a second generation of Cpx (see lighter/darker Cpx in Figure 5b) and/or crystal aggregation processes as shown by Campagnola et al. (2016).

The viscosity ratio between TF1-1 and TF0.1-2 is nearly 10 (3.6 and 4.5 in log units), whereas Cpx aspect ratios in both TF0.1-2 and TF1-1 experiments are quite similar, ranging in average between 1 and 3. However, careful examination of Figure 7 points out the following considerations:

a) The apparent viscosity data set derived from TF0.1 experiments shows relatively low and scattered values until a temperature of 1505 K. During this time range (up to approximately 12,000 s), values are not reliable although a qualitative analysis indicates that the apparent viscosity remains relatively low for longer time compared to experiments performed at higher shear rate. The Theo's Flow system represented by the TF0.1 experiment needs to cool from a superliquidus temperature to 1505 K and for about 3.3 hr before viscosity values become measurable (Figure 7 and Table S3). Then, once the temperature of 1505 K is reached, the apparent viscosity requires only approximately 24 min to increase up to approximately 400 Pa·s, while temperature decrease is only 5 K.

b) The TF1-1 viscosity data set shows an apparent viscosity increase, which occurs much earlier than for TF0.1. This is related to the fact, as stressed above, that at lower shear rates, measurements are not feasible due to the instrument's torque limit. Here the viscosity curve shows the classical S-shape curve (Vetere et al., 2017, and reference therein) that allows us to infer nucleation and crystal-growth rate (Vona et al., 2011; Vona & Romano, 2013). As an example, considering (1) an experimental time of 24,800 s (2) a cooling rate of 10 K/hr, (3) a typical Cpx crystal size of 200 μm (as common experimental products, as shown in Figures 2 and 3), and (4) a temperature range from TL (1525 K) to 1473 K, this will correspond to an average growth rate of approximately 8.06×10^{-7} cm/s, which is about 1 log unit lower than the olivine growth rate, as reported above.

Our experimental viscosity data under cooling confirm that higher shear rates result in earlier and more important crystallization compared to low shear rates as reported in Kolzenburg et al. (2017). It is now widely accepted that the more rapid change in rheological behavior at higher strain rates results from increased crystallization rates. Two possible mechanisms could be involved in dynamic crystallization process: (a) a continuous "fresh ingredient" on individual crystal's surface that could facilitate the crystal growth as shown, for example, in simulation for magmatic conditions (Petrelli et al., 2016); and (b) the increased stirring that could efficiently create crystal nuclei, as suggested in literature (Cashman et al., 1999; Emerson, 1926; Vona & Romano, 2013).

Finally, the mentioned Tcutoff (or the temperature at which the system reaches its rheological death) and relative modeling were successfully tested for basaltic systems by Kolzenburg et al. (2019). Applying our cooling rate, it provides a value of approximately 1510 K where viscosity for TF1-1 and TF0.1-2 will be on the order of 10^2 Pa·s (far off from a possible rheological death of Theo's lava flow). This relatively low viscosity value possibly reflects the very different chemistry of our samples and those of Kolzenburg et al. (2019), preventing to derive a general model.

Possible Implications For Terrestrial And Martian Lava Flows

Literature data point to a wide range of possible compositions for magma that erupted on Mars with relatively low viscosity (e.g., augite basalt, NWA 8159 meteorite belonging to the Nakhlite suite or Shergottite with similar composition to the Bounce Rock interior; Sehlke & Whittington, 2016). Moreover, Udry and Day (2018) allow us to compare the bulk rock analyses of nakhlites and chassignites Martian meteorite with our starting composition. Considering that our experiments were performed at relatively oxidized condition and that ferrous iron in the natural composition can be substituted by Ca and Mg and ferric iron can be replaced by Al (Vetere et al., 2006, and reference

therein), we are confident that our starting material can be considered as a possible Martian composition.

In terms of lava flowing ability, it is clear, from the experimental data, that magma and lava flow velocities are highly influenced by the dynamics to which the system is subjected. As we concentrated our study on the pyroxenite unit, we can use experimental viscosity data to investigate the magma velocities and relative possible emplacement mechanisms.

Theo's Flow is chemically similar to the composition of nakhlites, a suite of medium-grained pyroxenite meteorites that may have been erupted as lava flows on Mars and may therefore be a suitable proxy for such lavas. Martian surface gravity is about 3.71 m/s2 (i.e., about 38% that of the Earth) and shows also variations with latitude. This fact will reduce the lava flow speed on Mars surface. As previously reported, at any given scale, processes such as fluid convection and consequent convective heat transfer, crystal settling due to positive or negative buoyancy will be slower on Mars compared to that on Earth due to lower gravity. For identical reason, magma ascent rates on Mars will be slower compared to those on Earth (Wilson & Head, 1994).

It has been demonstrated recently that very wide and extended lava flows on Mars possibly occurred during its volcanic history due to high effusion rates (Hopper & Leverington, 2014; Leverington, 2018). In such a context, the rheology of Martian magma has been poorly quantified essentially because magma compositions are difficult to be constrained from Martian flow morphologies (Bandfield et al., 2000; Mouginis- Mark et al., 1984). Considering the pyroxenite of Theo's Flow as one of the possible compositions erupted on Mars and considering that (1) Fe-rich lunar mare basalt seems to exhibit only a small increase in crystal fraction over the first ~125 K of cooling (Morrison et al., 2019), allowing an extended period of flow at a relatively low viscosity and that (2) very low viscosities are necessary to build very wide and long magma flow units (Hopper & Leverington, 2014; Leverington, 2018), we can infer relatively high eruption temperature. Following this hypothesis and inferring a relatively high ascent rate (although Martian gravity may reduce the ascent velocity), we measured a viscosity of approximately 2 and 8 Pa·s in a temperature range of 1646–1530 K, respectively. Using the experimental viscosity data to infer velocity evolution considering terrain slopes values between 0.1° and 10° and lava flow thicknesses from 1 to 10 m, a magma velocity can be calculated using the approach proposed by Williams et al. (2001), assuming a turbulent lave flow due to its very high fluidity. Lava flow velocity u (m/s), is calculated considering

(1) the ground slope (θ) and (2) the lava friction coefficient λ that is related to the Reynolds number (Re). λ is defined as the ratio between the shear stress at the solid surface and the kinetic energy of the fluid elements. The friction coefficient, being dimensionless, depends on the velocity (u), the thickness of the conduit or channel, the density (ρ), and the viscosity (η). The surface roughness also has to be taken into account. These quantities can be rearranged as ρuh/η, which is the Re. In case of a laminar flow, a simple mathematical treatment gives f = 16/Re for Re < 2,000. More complex is the case for turbulent flows, for which the roughness of a hypothetical conduit must also be considered. The solution proposed here is given by Kakaç et al. (1987) and used in Williams et al. (2001) and also in Byrne et al. (2013).

The following equations (4)–(6) (Williams et al., 2001) are valid only in the case of high Re ≫ 2000:

$$u = \sqrt{\frac{4gh\sin(\theta)}{\lambda}} \tag{4}$$

where g (m/s2) is the acceleration due to gravity and h (m) the lava flow thickness. λ can be calculated as follows:

$$\lambda = \frac{1}{[0.79\ln(Re)-1.64]^2} \tag{5}$$

where Re is the Reynolds numbers defined as:

$$Re = \frac{2\rho uh}{\eta} \tag{6}$$

where ρ is the bulk lava density (2,698 kg/m3) for the melt considered here, as calculated in Table 1, and η is the lava viscosity (Pa·s).

Figure 8 shows velocities versus slope (°) calculated after solving iteratively equations (4)–(6) by changing the lava flow thickness from 1 to 10 m and viscosity from 2 to 8 Pa·s for both Earth and Mars environments (Table S4). Results provide relatively high velocities ranging from 0.9–14.7 and 0.5 to 8.3 m/s for lava flows on Earth and Mars even if gravity on Mars is almost one third that of Earth (e.g., 9.81 and 3.71 m/s2, respectively; calculation is based on 1-m-thick lava having a viscosity of 8 Pa·s flowing on slopes from 0.1° to 10°). These assumptions are valid only when considering a geological scenario in which magma eruption temperature is above TL, although possible delay in

crystallization could happen (e.g., if the dynamics of the system slow down as shown in Kolzenburg et al., 2019), allowing a long-lasting low viscosity.

If eruption temperature is lower than TL, processes such crystal nucleation and growth will take place and drastically affect viscosity. The evolution of viscosity and velocity during cooling is thus related to the amount of crystalline phases and their evolution during cooling, as for the experiments presented here. Although we are aware that a direct control on the evolution of solid phases during cooling is not accessible in our experiments, we do have a direct control on the viscosity-time progress so that we can track velocity change during cooling. In fact, as a first approximation, we can adopt Jeffrey's equation as proposed also in Parfitt and Wilson (2008), keeping in mind that the following equation is applicable to Newtonian fluids:

$$u = \frac{d^2 \cdot \rho \cdot g}{3 \cdot \eta} \cdot sin\theta \qquad (7)$$

where u (m/s) is velocity, d (m) is the channel depth, g (m/s2) is the acceleration due to gravity, and h (m) is the lava flow thickness, and ρ is the bulk lava density. From equation (7), it is evident that the steeper the slope or the lower the viscosity, the higher the velocity. Also, it must be pointed out that viscosity data represent the evolution of the ability to flow under a defined cooling rate of 10 K/hr. Following observations by Vetere et al. (2015), we can possibly assess that this cooling rate applies at approximately 20-cm depth (note, however, that experiments by Vetere et al., 2015, were conducted at static conditions with different cooling rates and different compositions along a basaltic to rhyolitic join).
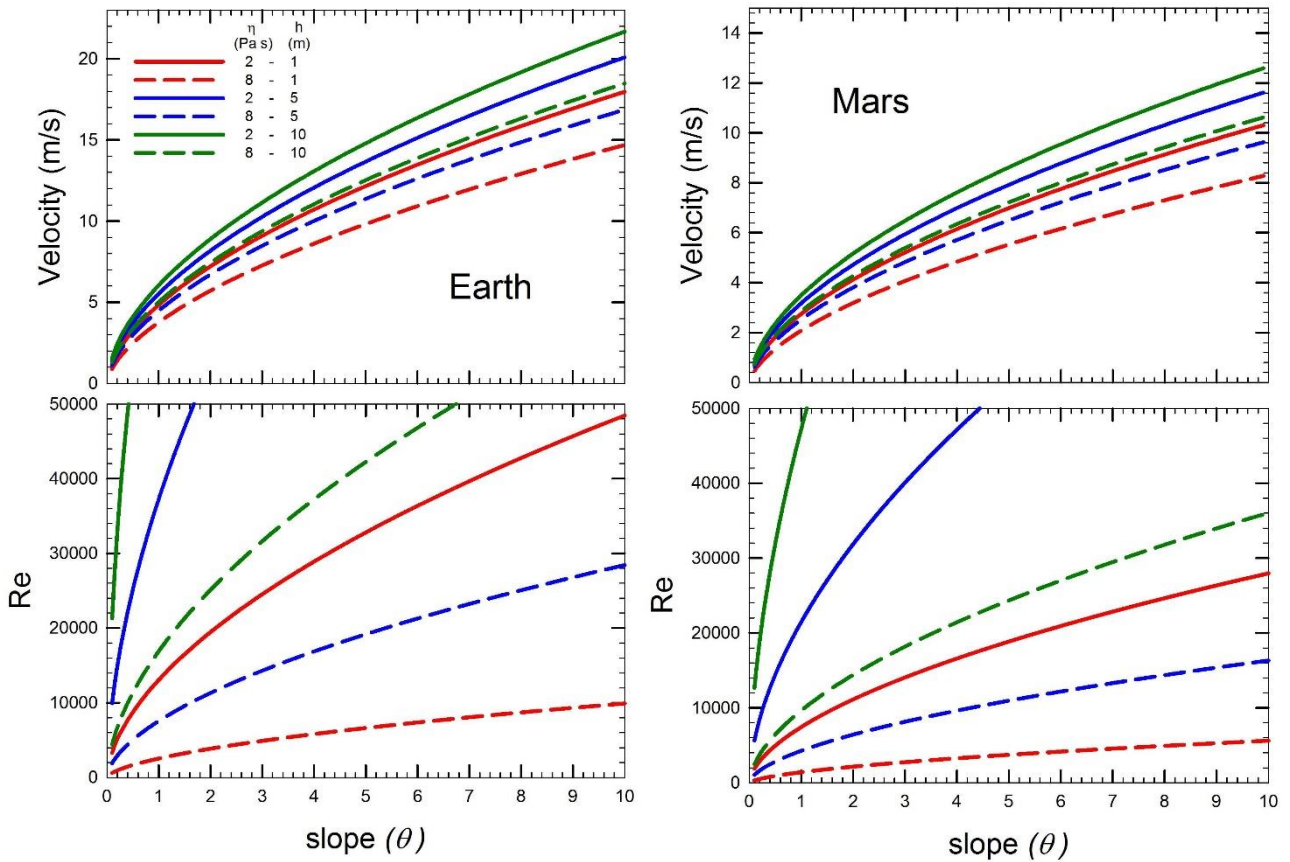
Figure 8. Velocity profiles for terrestrial and Martian environments and relative Reynolds number calculated from equations (4)–(6) by using the experimental viscosity data (η) and a lava flow at 1, 5, and 10 m in depth (hr).

In order to track the velocity evolution of a cooling lava flow with different slopes and flow depths, we used data presented in Figure 8. Calculated velocities for Mars and Earth (Figures S1 and S2 and Table S4 in the supporting information, Appendix IV) environments are provided according to equation (7). As an example, considering a lava flow depth of 5 m, and three different slopes (0.1°, 1°, and 10°), lava flows with a higher shear rate (Figure S2, TF1-1 Mars; and Figure S3, TF1-1 Earth) on very gentle slopes have still the power to continue (although at a relatively low velocity, approximately 0.05 m/s) to flow, while lava flows having a lower shear rate (Figure S2, TF0.1-2 Mars; and Figure S3, TF0.1-2 Earth) will be subjected to a drop in velocity (below 0.01 m.s–1) much earlier. On the other hand, final velocities related to our highest measured viscosities, considering a terrain slope of 1°, vary between 0.05 (Mars) and 0.1 m/s (Earth) if the shear rate is 0.1 s^{-1}, while velocity values increase to approximately 0.4 (Mars) and 1 m/s (Earth) when the shear rate is 1 s^{-1}.

Identical calculations are provided for different terrain slopes and lava flow depths for slopes of 0.1°, 1°, and 10° and for 1, 5, and 10 m of thicknesses, confirming that shear stress plays an important role on velocities, allowing hypothetical lava to flow at a relatively high speed in case of a higher applied shear rate (Figure S2 and S3).

Finally, by considering the eruption temperature close to the liquidus temperature (1525 K), we can estimate the maximum flow length versus time by using our experimental viscosity data provided in Figure 7 and equation (1). Wilson et al. (2009) provided (other than equation (7) for laminar flow) a solution in case of turbulent flow occurrence, thus for Re exceeding the value of 2,000. In this case, the velocity of lava flowing in a turbulent regime (u_t) can be related, as in equation (5), to the flow depth, d; the acceleration due to gravity, g; the terrain slope of the preexisting topography, θ; and the friction factor f, as follows:

$$u_t = [(2g\, d \sin \theta)/f\,]1/2 \qquad (8)$$

where f, in fully turbulent flow is:

$$f = 0.32/Re\, 0.25 \qquad (9)$$

Our viscosity data and related Re calculations (Table S5) suggest turbulent flows for terrain slopes close to or greater than 1°. Results are provided in Figure 9 for terrain slopes of 1° and 5°. Although these calculations are made on the unlikely assumption of constant slopes, we can, at least, have an idea about the possible travel distance for very fluid magmas. As an example, with 1° terrain slope and d equal to 1 m, on Mars, lavas are able to flow approximately for 375 and 296 km if viscosity data obtained at shear rates of 0.1 and 1 s^{-1} are used, respectively. Identical consideration gives magma travel distances of approximately 75 and 60 km if the terrain slope is 1°. It should be noted that the time required for these travel distances are only approximately 7 hr. Figure 9 proves that in order to travel very long distances, Martian magmas must have very high eruption temperatures and low viscosity, implying very low crystal cargo.
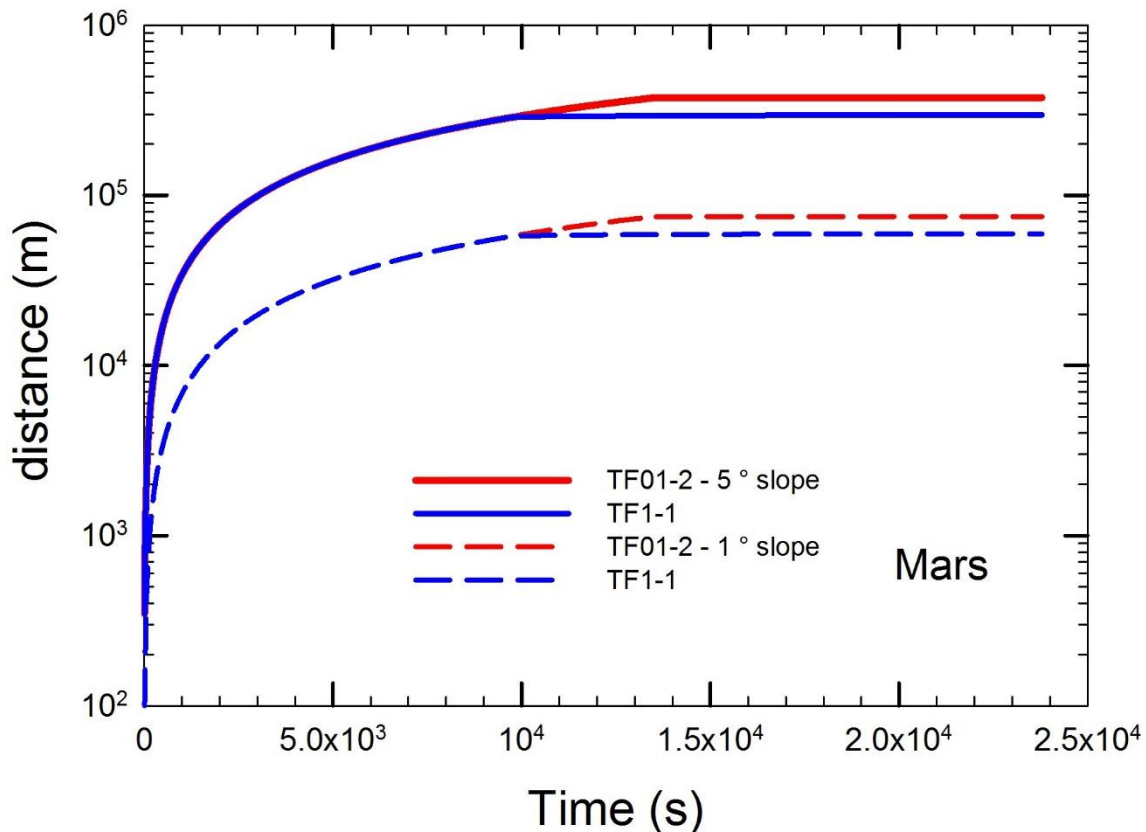
Figure 9. Distance versus time profiles for the Martian environments calculated from equations (8) and (9) by using the experimental viscosity data (η) as in Figure 7 and Tables 3 and S3.

CONCLUSIONS

New viscosity experiments performed at superliquidus and during cooling of 10 K/hr have been performed at different shear rates on a pyroxenite composition derived from the Theo's Flow. Results revealed that this composition is extremely fluid at temperatures between 1643 and 1530 K, and measured viscosities are between 2.2 and 7.8 Pa·s. Such very low viscosities allow the lava to flow in a turbulent regime as confirmed by the high Re numbers, which are usually >2,000 for likely values of lava flow thickness and ground slope. As a consequence, very long distances (up to 375 km) could be covered by the lava flows if the effusion rate is high, preventing dramatic heat loss due to turbulence (Vetere et al., 2017). If we assume that the studied composition is a good proxy for Mars lava flows and with very high effusion rates, our results might explain the presence of extraordinary large volcanic channels, as recently hypothesized for the Kasei Valles on Mars, even considering that the gravity is approximately one third that of Earth (Leverington, 2018). Few literature data tracking viscosity during cooling are available, most of which are performed at isothermal conditions, and they reported shear thinning effect on different compositions (e.g., Ishibashi, 2009; Kolzenburg et al., 2016, 2017; Kolzenburg, Giordano, et al., 2018; Ryerson et al., 1988; Vetere et al., 2017; Vona et al.,

2011). Our experiments have shown an apparent viscosity change behavior during cooling as a result of the applied shear rates (0.1 and 1 s^{-1}), confirming that the rheology of lava flows needs to be studied under dynamic (i.e., nonequilibrium) conditions to better understand the real geological scenarios occurring in magmatic and volcanic systems.

Acknowledgments

References

Alvaro, M., Domeneghetti, M. C., Fioretti, A. M., Cámara, F., and Marinangeli, L. (2015) A new calibration to determine the closure temperatures of Fe-Mg ordering in augite from nakhlites. Meteoritics & Planetary Science, 50(3), 499–507.

Angell, C. A. (1985) Strong and fragile liquids. In K. Ngai, & G. Wright (Eds.), Relaxation in complex systems, (pp. 3–11). Virginia: National Technical Information Service, U.S. Department of Commerce, Springfield.

Arndt, N. T. (1977) Thick, layered peridotite–gabbro lava flows in Munro Township, Ontario. Canadian Journal of Earth Sciences, *14*(11), 2620–2637.

Arzilli, F., and Carroll, M. R. (2013) Crystallization kinetics of alkali feldspars in cooling and decompression- induced crystallization experiments in trachytic melt. Contributions to Mineralogy and Petrology, 166(4), 1011–1027.

Asimow, P. D., Dixon, J. E., and Langmuir, C. H. (2004) A hydrous melting and fractionation model for mid-ocean ridge basalts: Application to the mid-Atlantic ridge near the Azores. Geochemistry, Geophysics, Geosystems, 5, Q01E16.

Bandfield, J. L., Hamilton, V. E., and Christensen, P. R. (2000). A Global view of Martian surface compositions from MGS-TES. Science, 287(5458), 1626–1630.

Byrne, P. K., Holohan, E. P., Kervyn, M., van Wyk de Vries, B., Troll, V. R., and Murray, J. B. (2013) A sagging-spreading continuum of large volcano structure. Geology, 41(3), 339–342.

Campagnola, S., Vona, A., Romano, C., and Giordano, G. (2016) Crystallization kinetics and rheology of leucite-bearing tephriphonolite magmas from the Colli Albani volcano (Italy). Chemical Geology, 424, 12–29.

Caricchi, L., Burlini, L., Ulmer, P., Gerya, T., Vassalli, M., and Papale, P. (2007) Non-Newtonian rheology of crystal-bearing magmas and implications for magma ascent dynamics. Earth and Planetary Science Letters, 264(3-4), 402–419.

Carmichael, R. S. (1974) Igneous Petrology, (p. 793). New York: McGraw-Hill.

Cashman, K. V. (1993) Relationship between plagioclase crystallization and cooling rate in basaltic melts. Contributions to Mineralogy and Petrology, 113(1), 126–142.

Cashman, K. V., Thornber, C., and Kauahikaua, J. P. (1999) Cooling and crystallization of lava in open channels, and the transition of pāhoehoe lava to 'a'ā. Bulletin of Volcanology, 61(5), 306–323.

Chevrel, M. O., Baratoux, D., Hess, K.-U., and Dingwell, D. B. (2014) Viscous flow behavior of tholeiitic and alkaline Fe-rich Martian basalts. Geochimica et Cosmochimica Acta, 124, 348–365.

Chevrel, M. O., Giordano, D., Potuzak, M., Courtial, P., and Dingwell, D. B. (2013) Physical properties of $CaAl_2Si_2O_8$-$CaMgSi_2O_6$-FeO-Fe_2O_3 melts: Analogues for extra-terrestrial basalt. Chemical Geology, 346, 93–105.

Chevrel, M. O., Harris, A. J. L., James, M. R., Calabrò, L., Gurioli, L., and Pinkerton, H. (2018) The viscosity of pāhoehoe lava: In situ syneruptive measurements from Kilauea, Hawaii. Earth and Planetary Science Letters, 493, 161–171.

Chevrel, M. O., Platz, T.b., Hauber, E.c., Baratoux, D., Lavallée, Y., and Dingwell, D. B. (2013) Lava flow rheology: A comparison of morphological and petrological methods. Earth and Planetary Science Letters, 384, 109–120.

Coffin, M. F., and Eldholm, O. (1994) Large igneous provinces: Crustal structure, dimensions, and external consequences. Reviews of Geophysics, 32(1), 1–36.

Condie, K. C. (1981). Archean greenstone belts. Elsevier.

Dingwell, D. B., Courtial, P., Giordano, D., and Nichols, A. R. L. (2004) Viscosity of peridotite liquid. Earth and Planetary Science Letters, 226(1-2), 127–138.

Dundas, C. M., & Keszthelyi, L. P. (2014) Emplacement and erosive effects of lava in south Kasei Valles, Mars. Journal of Volcanology and Geothermal Research, 282, 92–102.

Emerson, O. H. (1926) The formation of aa and pahoehoe. American Journal of Science, s5-12(68), 109–114.

Fiege, A., Vetere, F., Iezzi, G., Simon, A., and Holtz, F. (2015) The roles of decompression rate and volatiles (H_2O + Cl $\pm$ CO_2 $\pm$ S) on crystallization in (trachy-) basaltic magma. Chemical Geology, 411, 310–322.

Friedman, R.C., (1998) Petrologic clues to lava flow emplacement and post-emplacement processes [Ph.D. dissertation]: Honolulu, University of Hawaii at Manoa, 260 p.

Ghiorso, M. S., Hirschmann, M. M., Reiners, P. W., and Kress, V. C. III (2002) The pMELTS: A revision of MELTS for improved calculation of phase relations and major element partitioning related to partial melting of the mantle to 3 GPa. Geochemistry, Geophysics, Geosystems, 3(5), 1030.

Ghiorso, M. S., and Sack, R. O. (1995) Chemical mass transfer in magmatic processes IV. A revised and internally consistent thermodynamic model for the interpolation and extrapolation of liquid-solid equilibria in magmatic systems at elevated temperatures and pressures. Contributions to Mineralogy and Petrology, 119(2-3), 197–212.

Giordano, D. (2019) Advances in the rheology of natural multiphase silicate melts: Import for magma transport and lava flow emplacement. Annals of Geophysics, 61.

Giordano, D., Polacci, M., Longo, A., Papale, P., Dingwell, D. B., Boschi, E., and Kasereka, M. (2007) Thermo-rheological magma control on the impact of highly fluid lava flows at Mt Nyiragongo. Geophysical Research Letters, 34, L06301.

Giordano, D., Russell, J. K., and Dingwell, D. B. (2008) Viscosity of magmatic liquids: a model. Earth and Planetary Science Letters, 271(1-4), 123–134.

Gualda, G. A. R., Ghiorso, M. S., Lemons, R. V., and Carley, T. L. (2012) Rhyolite-MELTS: A modified calibration of MELTS optimized for silica-rich, fluid-bearing magmatic systems. Journal of Petrology, 53(5), 875–890.

Hammer, J. E. (2008) Experimental studies of the kinetics and energetics of magma crystallization. Reviews in Mineralogy and Geochemistry, 69(1), 9–59.

Hiesinger, H., Head, J. W., and Neukum, G. (2007) Young lava flows on the eastern flank of Ascraeus Mons: Rheological properties derived from High Resolution Stereo Camera (HRSC) images and Mars Orbiter Laser Altimeter (MOLA) data. Journal of Geophysical Research, 112, E05011.

Hopper, J. P., and Leverington, D. W. (2014) Formation of Hrad Vallis (Mars) by low viscosity lava flows. Geomorphology, 207, 96–113.

Hulme, G. (1974) The interpretation of lava flow morphology. Geophysical Journal International, 39(2), 361–383.

Iezzi, G., Mollo, S., Torresi, G., Ventura, G., Cavallo, A., and Scarlato, P. (2011) Experimental solidification of an andesitic melt by cooling. Chemical Geology, 283(3-4), 261–273.

Ishibashi, H. (2009) Non-Newtonian behavior of plagioclase-bearing basaltic magma: Subliquidus viscosity measurement of the 1707 basalt of Fuji volcano, Japan. Journal of Volcanology and Geothermal Research, 181(1-2), 78–88.

Ishibashi, H., and Sato, H. (2007) Viscosity measurements of subliquidus magmas: Alkali olivine basalt from the Higashi-Matsuura district, Southwest Japan. Journal of Volcanology and Geothermal Research, 160(3-4), 223–238.

Jeffreys, H. (1925) The flow of water in an inclined channel of rectangular section. The London, Edinburgh, and Dublin Philosophical Magazine and Journal of Science, 6(293), 793–807.

Kakaç, S., Shah, R. K., and Aung, W. (1987) Handbook of single-phase convective heat transfer, (p. 900). New York, NY (USA): John Wiley and Sons Inc.

Klöß, G.H., (2000) Dichtefluktuationen natürlicher Gläser (Dissertation) University of Jena.

Kolzenburg, S., Di Genova, D., Giordano, D., Hess, K. U., and Dingwell, D. B. (2018) The effect of oxygen fugacity on the rheological evolution of crystallizing basaltic melts. Earth and Planetary Science Letters, 487, 21–32.

Kolzenburg, S., Giordano, D., Cimarelli, C., and Dingwell, D. B. (2016) In situ thermal characterization of cooling/crystallizing lavas during rheology measurements and implications for lava flow emplacement. Geochimica et Cosmochimica Acta, 195, 244–258.

Kolzenburg, S., Giordano, D., Hess, K. U., and Dingwell, D. B. (2018) Shear rate-dependent disequilibrium rheology and dynamics of basalt solidification. Geophysical Research Letters, 45, 6466–6475.

Kolzenburg, S., Giordano, D., di Muro, A., and Dingwell, D. B. (2019) Equilibrium viscosity and disequilibrium rheology of a high magnesium basalt from Piton de la Fournaise volcano, La Reunion, Indian Ocean, France. Annals of Geophysics, 61(Vol 61 (2018)), 18.

Kolzenburg, S., Giordano, D., Thordarson, T., Höskuldsson, A., and Dingwell, D. B. (2017) The rheological evolution of the 2014/2015 eruption at Holuhraun, central Iceland. Bulletin of Volcanology, 79(6), 45.

Krieger, I. M., and Elrod, H. (1953) Direct determination of flow curves of non-Newtonian fluid. II. Shearing rate in the concentric cylinder viscometer. Journal of Applied Physics, 24(2), 134–136.

Lange, R. A., Cashman, K. V., and Navrotsky, A. (1994) Direct measurements of latent heat during crystallization and melting of a ugandite and an olivine basalt. Contributions to Mineralogy and Petrology, 118(2), 169–181.

Lentz, R. C. F., McCoy, T. J., Collins, L. E., Corrigan, C. M., Benedix, G. K., Taylor, G. J., and Harvey, R. P. (2011) Theo's Flow, Ontario, Canada: A terrestrial analog for the Martian nakhlite meteorites. The Geological Society of America Special Papers, 483, 263–277.

Lentz, R. C. F., Taylor, G. J., and Treiman, A. H. (1999) Formation of a Martian pyroxenite: A comparative study of the nakhlite meteorite and Theo's Flow. Meteoritics & Planetary Sciences, 34(6), 919–932.

Leverington, D. W. (2018) Is Kasei Valles (Mars) the largest volcanic channel in the solar system? Icarus, 301, 37–57.

Liebske, C., Schmickler, B., Terasaki, H., Poe, B.T., Suzuki, A., Funakoshi, K.I., Ando, R. and Rubie, D.C., (2005) Viscosity of peridotite liquid up to 13 GPa: Implications for magma ocean viscosities. Earth and Planetary Science Letters, 240(3-4), 589–604.

Lofgren, G. (1980) Experimental studies on the dynamic crystallization of silicate melts. In R. B. Hargraves (Ed.), Physics of magmatic processes, (pp. 487–551). Princeton, NJ: Princeton University.

Mader, H. M., Llewellin, E. W., and Mueller, S. P. (2013). The rheology of two-phase magmas: A review and analysis. Journal of Volcanology and Geothermal Research, 257, 135–158.

Mollo, S., Blundy, J., Scarlato, P., De Cristofaro, S.P., Tecchiato, V., Di Stefano, F., Vetere, F., Holtz, F. and Bachmann, O., (2018) An integrated P-T-H_2O-lattice strain model to quantify the role of clinopyroxene fractionation on REE+ Y and HFSE patterns of mafic alkaline magmas: Application to eruptions at Mt. Etna. Earth-Science Reviews, 185, 32–56.

Mollo, S., Del Gaudio, P., Ventura, G., Iezzi, G., and Scarlato, P. (2010) Dependence of clinopyroxene composition on cooling rate in basaltic magmas: Implications for thermobarometry. Lithos, 118(3-4), 302–312.

Mollo, S., Iezzi, G., Ventura, G., Cavallo, A., and Scarlato, P. (2012) Heterogeneous nucleation mechanisms and formation of metastable phase assemblages induced by different crystalline seeds in a rapidly cooled andesitic melt. Journal of non-crystalline solids, 358(12-13), 1624–1628.

Mollo, S., Lanzafame, G., Masotta, M., Iezzi, G., Ferlito, C., and Scarlato, P. (2011) Cooling history of a dike as revealed by mineral chemistry: A case study from Mt. Etna volcano. Chemical Geology, 288(1-2), 39–52.

Moore, H. J., Arthur, D. W. G., and Schaber, G. G. (1978) Yield strengths of flows on the Earth, Mars, and Moon. In Lunar and Planetary Science Conference Proceedings, (Vol. 9, pp. 3351–3378).

Morgavi, D., Petrelli, M., Vetere, F. P., González-García, D., and Perugini, D. (2015) High-temperature apparatus for chaotic mixing of natural silicate melts. Review of Scientific Instruments, 86(10), 105108.

Morrison, A. A., Zanetti, M., Hamilton, C. W., Lev, E., Neish, C. D., and Whittington, A. G. (2019) Rheological investigation of lunar highland and mare impact melt simulants. Icarus, 317, 307–323.

Mouginis-Mark, P. J., Wilson, L., Head, J. W., Brown, S. H., Hall, J. L., and Sullivan, K. D. (1984) Elysium Planitia, Mars: Regional geology, volcanology, and evidence for volcano-ground ice interactions. Earth, Moon, and Planets, 30(2), 149–173.

Murri, M., Cámara, F., Adam, J., Domeneghetti, M. C., and Alvaro, M. (2018) Intracrystalline "geothermometry" assessed on clino and orthopyroxene bearing synthetic rocks. Geochimica et Cosmochimica Acta, 227, 133–142.

Murri, M., Scandolo, L., Fioretti, A. M., Nestola, F., Domeneghetti, C. M., and Alvaro, M. (2016) The role of Fe content on the Fe-Mg exchange reaction in augite. American Mineralogist, 101(12), 2747–2750.

Mysen, B., and Richet, P. (2005) Iron-bearing melts. In Silicate glasses and melt, chap. 10, (pp. 291–327). Amsterdam, Netherlands: Elsevier Sci.

Mysen, B. O., Virgo, D., and Seifert, F. A. (1982) The structure of silicate melts: Implications for chemical and physical properties of natural magma. Reviews of Geophysics, 20(3), 353–383.

Ochs, F. A., and Lange, R. A. (1999) The density of hydrous magmatic liquids. Science, 283(5406), 1314–1317.

Parfitt, E. A., and Wilson, L. (2008) The role of volatiles. Fundamentals of physical volcanology, (pp. 64–76).

Petrelli, M., El Omari, K., Le Guer, Y., and Perugini, D. (2016) Effects of chaotic advection on the timescales of cooling and crystallization of magma bodies at mid crustal levels. Geochemistry, Geophysics, Geosystems, 17, 425–441.

Pistone, M., Caricchi, L., Ulmer, P., Burlini, L., Ardia, P., Reusser, E., Marone, F. and Arbaret, L., (2012) Deformation experiments of bubble-and crystal-bearing magmas: Rheological and microstructural analysis. Journal of Geophysical Research, 117, B05208.

Rossi, S., Petrelli, M., Morgavi, D., González-García, D., Fischer, L. A., Vetere, F., and Perugini, D. (2017) Exponential decay of concentration variance during magma mixing: Robustness of a volcanic chronometer and implications for the homogenization of chemical heterogeneities in magmatic systems. Lithos, 286-287, 396–407.

Ryerson, F. J., Weed, H. C., and Piwinskii, A. J. (1988) Rheology of subliquidus magmas: 1. Picritic compositions. Journal of Geophysical Research, 93(B4), 3421–3436.

Sato, H. (2005) Viscosity measurement of subliquidus magmas: 1707 basalt of Fuji volcano. Journal of Mineralogical and Petrological Sciences, 100(4), 133–142.

Schuessler, J. A., Botcharnikov, R. E., Behrens, H., Misiti, V., and Freda, C. (2008). Amorphous materials: Properties, structure, and durability: Oxidation state of iron in hydrous phono-tephritic melts. American Mineralogist, 93(10), 1493–1504.

Sehlke, A., and Whittington, A. G. (2015) Rheology of lava flows on Mercury: An analog experimental study. Journal of Geophysical Research: Planets, 120, 1924–1955.

Sehlke, A., and Whittington, A. G. (2016) The viscosity of planetary tholeiitic melts: A configurational entropy model. Geochimica et Cosmochimica Acta, 191, 277–299.

Shirey, S.B., (1997) Initial Os isotopic compositions of Munro Township, Ontario, komatiites revisited: Additional evidence for nearchondritic, late-Archean convecting mantle beneath the Superior Province, in Abstracts of the 7th Goldschmidt Conference: LPI Contribution 921, Abstract 2375.

Smith, P. M., and Asimow, P. D. (2005) Adiabat_1ph: A new public front-end to the MELTS, pMELTS, and HMELTS models. Geochemistry, Geophysics, Geosystems, 6, Q02004.

Soldati, A., Sehlke, A., Chigna, G., and Whittington, A. (2016) Field and experimental constraints on the rheology of arc basaltic lavas: The January 2014 eruption of Pacaya (Guatemala). Bulletin of Volcanology, 78(6), 43.

Spera, F. J., Borgia, A., Strimple, J., and Feigenson, M. (1988) Rheology of melts and magmatic suspensions: 1. Design and calibration of concentric cylinder viscometer with application to rhyolitic magma. Journal of Geophysical Research, 93(B9), 10,273–10,294.

Spina, L., Scheu, B., Cimarelli, C., Arciniega-Ceballos, A., and Dingwell, D. B. (2016) Time scales of foam stability in shallow conduits: Insights from analogue experiments. Geochemistry, Geophysics, Geosystems, 17, 4179–4194.

Stixrude, L., and Lithgow-Bertelloni, C. (2011) Thermodynamics of mantle minerals—II. Phase equilibria. Geophysical Journal International, 184(3), 1180–1213.

Udry, A., and Day, J. M. D. (2018) 1.34 billion-year-old magmatism on Mars evaluated from the co-genetic nakhlite and chassignite meteorites. Geochimica et Cosmochimica Acta, 238, 292–315.

Vaucher, J., Baratoux, D., Toplis, M. J., Pinet, P., Mangold, N., and Kurita, K. (2009) The morphologies of volcanic landforms at Central Elysium Planitia: Evidence for recent and fluid lavas on Mars. Icarus, 200(1), 39–51.

Vetere, F., Behrens, H., Botcharnikov, R., Holtz, F., and Fanara, S. (2014) The role of alkalis in the solubility of H_2O and CO_2 in silicate melts. Implication for phonotephritic magmas. Contributions to Mineralogy and Petrology, 167(5), 1014.

Vetere, F., Behrens, H., Holtz, F., and Neuville, D. R. (2006) Viscosity of andesitic melts—New experimental data and a revised calculation model. Chemical Geology, 228(4), 233–245.

Vetere, F., Iezzi, G., Behrens, H., Holtz, F., Ventura, G., Misiti, V., Cavallo, A., Mollo, S. and Dietrich, M., (2015) Glass forming ability and crystallisation behaviour of subalkaline silicate melts. Earth-Science Reviews, 150, 25–44.

Vetere, F., Rossi, S., Namur, O., Morgavi, D., Misiti, V., Mancinelli, P., Petrelli, M., Pauselli, C. and Perugini, D., (2017) Experimental constraints on the rheology, eruption, and emplacement dynamics of analog lavas comparable to Mercury's northern volcanic plains. Journal of Geophysical Research: Planets, 122, 1522–1538.

Vetere, F., Sato, H., Ishibashi, H., De Rosa, R., and Donato, P. (2013) Viscosity changes during crystallization of a shoshonitic magma: New insights on lava flow emplacement. Journal of Mineralogical and Petrological Sciences, 108(3), 144–160.

Vogel, H. (1921) The law of the relation between the viscosity of liquids and the temperature. Physikalische Zeitschrift, 22, 645–646.

Vona, A., and Romano, C. (2013) The effects of undercooling and deformation rates on the crystallization kinetics of Stromboli and Etna basalts. Contributions to Mineralogy and Petrology, 166(2), 491–509.

Vona, A., Romano, C., Dingwell, D. B., and Giordano, D. (2011) The rheology of crystal-bearing basaltic magmas from Stromboli and Etna. Geochimica et Cosmochimica Acta, 75(11), 3214–3236.

Williams, D. A., Kerr, R. C., Lesher, C. M., and Barnes, S. J. (2001) Analytical/numerical modeling of komatiite lava emplacement and thermal erosion at Perseverance, Western Australia. Journal of Volcanology and Geothermal Research, 110(1-2), 27–55.

Wilson, L., and Head, J. W. (1994) Mars: Review and analysis of volcanic eruption theory and relationships to observed landforms. Reviews of Geophysics, 32(3), 221–263.

Wilson, L., Mouginis-Mark, P. J., Tyson, S., Mackown, J., and Garbeil, H. (2009) Fissure eruptions in Tharsis, Mars: Implications for eruption conditions and magma sources. Journal of Volcanology and Geothermal Research, 185(1-2), 28–46.

APPENDIX IV. SUPPLEMENTARY MATERIALS

RAMAN ELASTIC GEOBAROMETRY FOR ANISOTROPIC MINERAL INCLUSIONS

Mara Murri[1], Mattia L. Mazzucchelli[1], Nicola Campomenosi[2], Andrey V. Korsakov[3], Mauro Prencipe[4], Boriana D. Mihailova[5], Marco Scambelluri[2], Ross J. Angel[1], Matteo Alvaro[1]

[1]*Department of Earth and Environmental Sciences, University of Pavia, Via A. Ferrata, 1 I-27100 4 Pavia, Italy*
[2]*Department of Earth Science, Environment & Life, University of Genoa, Corso Europa 26, 16132 Genoa, Italy*
[3]*V S Sobolev Institute of Geology and Mineralogy SB RAS, Novosibirsk*
[4]*Earth Sciences Department, University of Torino, Via Valperga Caluso 35 Italy*
[5]*Department of Earth Sciences, University of Hamburg, Grindelallee 48, D-20146 Hamburg, Germany*

Voigt notation

The band position under a strain $\boldsymbol{\varepsilon}$ is determined by the second-rank symmetric mode Grüneisen tensor $\boldsymbol{\gamma^m}$ (Ziman 1960, Key 1967, Cantrell 1980) for each Raman mode:

$$\frac{-\partial \omega}{\omega} = \gamma^m : \varepsilon \tag{1}$$

The ":" in equation (1) is a double-scalar product between the two tensors. Because both tensors are second-rank and symmetric this can be written out in full in Voigt (1910) notation as:

$$\frac{-\partial \omega}{\omega} = \gamma_1^m \varepsilon_1 + \gamma_2^m \varepsilon_2 + \gamma_3^m \varepsilon_3 + \gamma_4^m \varepsilon_4 + \gamma_5^m \varepsilon_5 + \gamma_6^m \varepsilon_6 \tag{2}$$

Note that under the Voigt convention here for strains, the values of the shear strains $\varepsilon_4, \varepsilon_5, \varepsilon_6$ are one-half of the values of the corresponding tensor components $\varepsilon_{23}, \varepsilon_{13}, \varepsilon_{12}$. Instead, γ_4^m, γ_5^m and γ_6^m are equal of the values of the corresponding tensor components $\gamma_{23}, \gamma_{13}, \gamma_{12}$.

This equation means that the changes in the Raman peak positions in general depend on all of the strains in three dimensions experienced by the crystal, not just the volume. In principle, the values of the six components, γ_i^m with $i = 1$ to 6, of a mode Grüneisen tensor may change with pressure and temperature, and with the magnitude of the strains. And, as we will show for quartz, the values of γ_i^m are different for different modes. The mode will be indicated by the superscript *m*, in various forms.

Because the mode Grüneisen tensor is a symmetric second-rank property tensor, it is subject to the same symmetry constraints on its component values as other second-rank property tensors, such as the thermal expansion and compressibility tensors. This is required to make the frequency shift given by (1) and (2) invariant under coordinate transformations. Thus, in all crystals with orthorhombic symmetry or higher, $\gamma_4^m = \gamma_5^m = \gamma_6^m = 0$. For uniaxial crystals in the standard setting $\gamma_1^m = \gamma_2^m$, and for cubic crystals and isotropic materials $\gamma_1^m = \gamma_2^m = \gamma_3^m$. Therefore, for the trigonal symmetry of quartz $\gamma_1^m = \gamma_2^m$. For the specific case of quartz inclusions in an isotropic host, such as garnet, the strain imposed by the garnet does not break the symmetry of the quartz crystal. Therefore, we are interested specifically in the cases when $\varepsilon_1 = \varepsilon_2$, for which the shift in the wave numbers of modes should be given by:

$$\frac{-\partial \omega}{\omega} = 2\gamma_1^m \varepsilon_1 + \gamma_3^m \varepsilon_3 \tag{3}$$

Computational details

The hybrid Hamiltonian WC1LYP is based on the generalized gradient approximation (GGA) exchange functional WC (Wu and Cohen 2006), mixed with 16% of the exact non-local Hartree–Fock exchange to correct for the self-interaction error (the interaction of an electron with itself), which is typical of both pure DFT local density (LDA) and generalized gradient approximation functionals. The Hamiltonian also includes the LYP correlation functional (Lee et al. 1988). The grid for the evaluation of the DFT exchange–correlation functionals was chosen by the keyword XLGRID of the CRYSTAL14 user manual (Dovesi et al. 2014) and corresponds to a total of 37547 points in the unit cell. A measure of the numerical accuracy provided by such a grid is the evaluation of the total number of electrons in the unit cell, by the numerical integration of the electron density over the cell volume. For quartz we obtained 90.00003 electrons out of 90 for the reference volume at 0K and 0GPa static pressure. The localised *contracted* atomic basis sets used were Si 86-311G** (Pascale et al. 2005) and 8-411G(2d) (Valenzano et al. 2006) for Si and O, respectively, which were successfully employed to calculate *ab initio* structures and properties of silicates (e.g. Stangarone et al. 2017). Within the CRYSTAL code the accuracy in evaluating the Coulomb and Hartree-Fock exchange series is controlled by the keyword TOLINTEG, for which we set the five parameters to 8 (T1, T2, T3 and T4) and 18 (T5) (Dovesi et al. 2014). The diagonalization of the Hamiltonian matrix was performed at 7 independent k vectors in the reciprocal space (Monkhorst net; Monkhorst and Pack 1976) by setting to 3 the shrinking factor IS (Dovesi et al. 2014). Cell parameters and fractional coordinates were optimized by analytical gradient methods, as implemented in CRYSTAL14 (Civalleri et al. 2001; Dovesi et al. 2014). Geometry optimization was considered converged when each component of the gradient (TOLDEG parameter in CRYSTAL14) was smaller than 0.00003 hartree/bohr and displacements (TOLDEX) were smaller than 0.00012 bohr with respect to the previous step. Lattice parameters and fractional coordinates were optimized at the WC1LYP level (static values: no zero point and thermal effects included), at the static pressures from 0 to 10 GPa (with step of 0.5 GPa from 0 to 5 GPa and then a simulation at 10 GPa). For the non-hydrostatic simulations, the cell parameters were fixed at the chosen strain conditions and only the fractional coordinates were optimized with the keyword ATOMONLY (Civalleri et al. 2001; Dovesi et al. 2014).

Vibrational wavenumbers of all of the normal modes were calculated at the Γ point within the limit of the harmonic approximation, by diagonalizing a mass-weighted Hessian matrix, whose elements are the second derivatives of the full potential of the crystal with respect to the mass-weighted atomic displacements (Pascale et al. 2004).

Residual plots from the fitting procedure

The Grüneisen tensor components for all modes were then determined by fitting Eqn (2) (in the main text) by least-squares to the wavenumber shifts at different strain states simulated by HF/DFT calculations. The maximum misfits (i.e. $\delta\omega_{obs}$-$\delta\omega_{calc}$) are -1.76 cm^{-1} and -3.41 cm^{-1}and for the 464 and 696 cm^{-1} bands, respectively, considering only the values in the black box because is where we could assume this surface to be planar (area of small strains). Outside from this box the misfit increases and therefore we did not include the other values in the fitting.

Raman spectroscopy details

Raman spectra were excited by the 514.532 nm line of a Coherent 90C Fred Ar$^+$ laser. The laser power on the sample surface was approximately 14 mW, while the laser spot on the sample surface was approximately 2 micrometers. Spectra were collected for 15 s averaging over 3 accumulations. These conditions were proven not to cause overheating of the sample. The spectrometer was calibrated to the silicon Raman peak at 520.5 cm^{-1}. The spectral resolution was 2 cm^{-1}, while the precision in measuring the peak positions was 0.35 cm^{-1}. In the case of the quartz inclusion i6, the angle between the c axis of the quartz inclusion and the polarization of the incident light was 30°. For the inclusion a series of spot

measurements were carried out along the two crystallographic axes. The OriginLab-Pro 2018 software package was used for data fitting and evaluation. The collected spectra were baseline corrected for the continuum luminescence background when necessary, temperature-reduced to account for the Bose-Einstein occupation factor (Kuzmany, 2009) and normalized to the acquisition time. Peak positions, full-widths at half maximum (FWHMs), and integrated intensities were determined from fits with pseudo-Voigt functions [PV = $(1 - q) \cdot$ Lorentz + $q \cdot$ Gauss, q is the weight coefficient]. The criterion for the maximum number of fitted peaks was $\Delta I < I/2$, where I and ΔI are the calculated magnitude and uncertainty of each peak intensity, respectively.

Figures
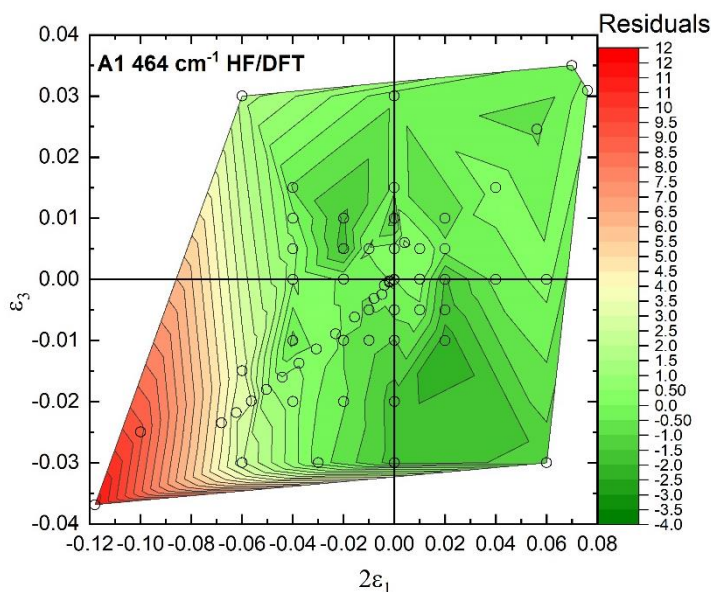
Figure S1. Residual plot from the fitting procedure for the Raman line near 464 cm^{-1}.
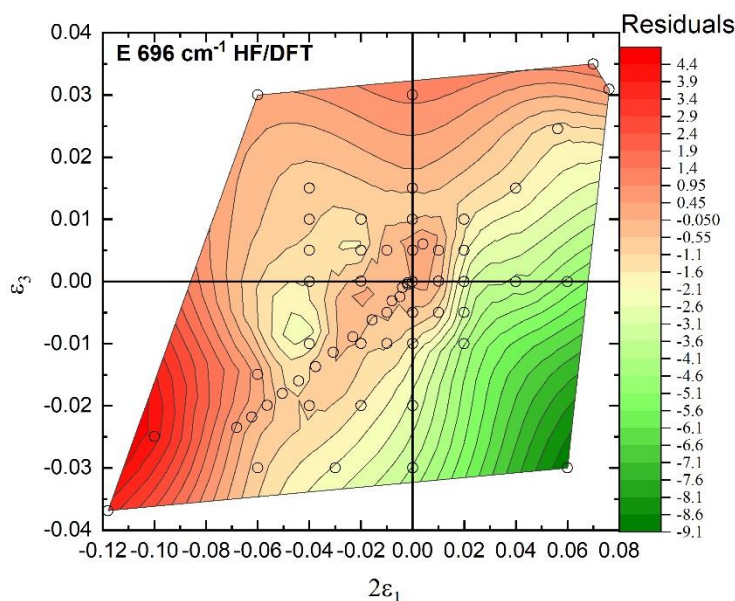
Figure S2. Residual plot from the fitting procedure for the Raman line near 696 cm^{-1}.
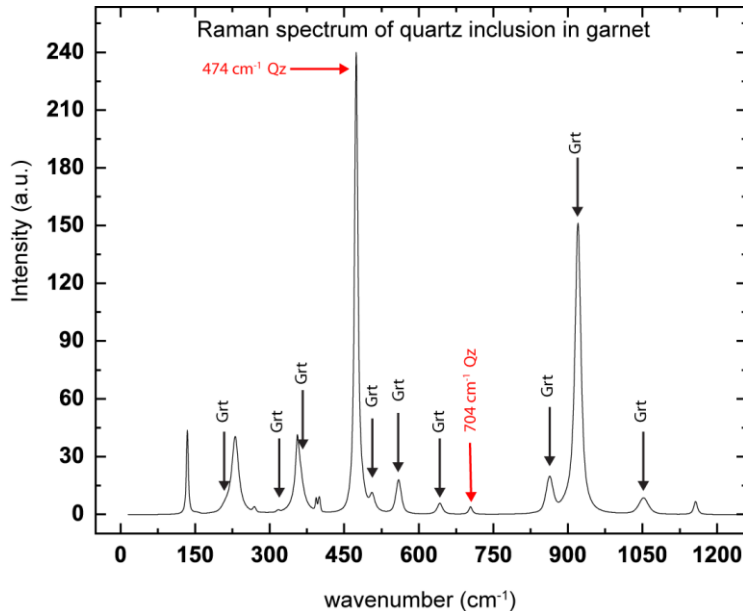
Figure S3. Raman spectrum of the quartz inclusion (i6) in the garnet host measured at the center of the inclusion. The two selected peaks of quartz are those at 474 and 704 cm^{-1} (highlighted in red). The peaks are shifted towards higher wavenumbers since the inclusion is strained. For un unstrained quartz they appear at 464 and 696 cm^{-1}. The non-labelled peaks are those of quartz.
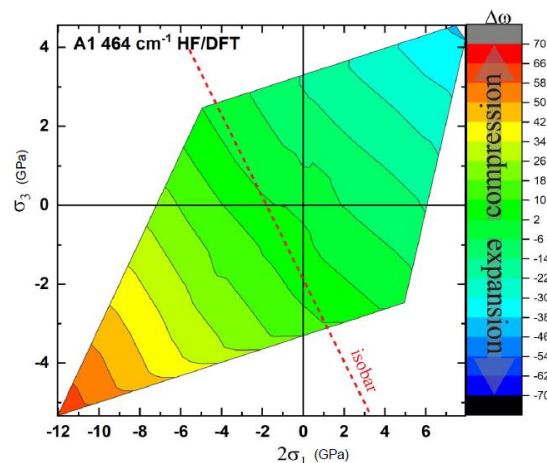
Figure S4. The iso-shift lines are not parallel to isobars, which are lines of equal pressure $(2\sigma_1+\sigma_3)/3\_-P$ (GPa), meaning that, in general, Raman shifts do not measure either pressures or stresses.

References

Cantrell Jr, J.H. (1980). Generalized Grüneisen tensor from solid nonlinearity parameters. Physical review B, 21(10), 4191.

Civalleri, B., D'Arco, P., Orlando, R., Saunders, V., and Dovesi, R. (2001) Hartree–Fock geometry optimisation of periodic systems with the CRYSTAL code. Chemical Physics Letters, 348, 131–138.

Dovesi, R., Orlando, R., Erba, A., Zicovich-Wilson, C. M., Civalleri, B., Casassa, S., ... & Noël, Y. (2014). CRYSTAL14: A program for the *ab initio* investigation of crystalline solids. International Journal of Quantum Chemistry, 114(19), 1287-1317.

Key, S.W. (1967). Grüneisen tensor for anisotropic materials. Journal of Applied Physics, 38(7), 2923-2928.

Kuzmany, H., 2009, Solid state spectroscopy, an introduction, second edition, cap-9 (185-200): 185-200 p., doi: 10.1007/978-3-642-01479-6.

Lee, C., Yang, W., and Parr, R.G. (1988) Development of the Colle-Salvetti correlation-energy formula into a functional of the electron density. Physical review B, 37, 785.

Monkhorst, H.J., and Pack, J.D. (1976) Special points for Brillouin-zone integrations. Physical Review B, 13, 5188.

Pascale, F., Zicovich-Wilson, C.M., Lopez Gejo, F., Civalleri, B., Orlando, R., and Dovesi, R. (2004) The calculation of the vibrational frequencies of crystalline compounds and its implementation in the CRYSTAL code. Journal of Computational Chemistry, 25, 888–897.

Pascale, F., Zicovich-Wilson, C. M., Orlando, R., Roetti, C., Ugliengo, P., & Dovesi, R. (2005). Vibration frequencies of Mg3Al2Si3O12 pyrope. An ab initio study with the CRYSTAL code. The Journal of Physical Chemistry B, 109(13), 6146-6152.

Stangarone, C., Böttger, U., Bersani, D., Tribaudino, M., & Prencipe, M. (2017). *Ab initio* simulations and experimental Raman spectra of Mg_2SiO_4 forsterite to simulate Mars surface environmental conditions. Journal of Raman Spectroscopy, 48(11), 1528-1535.

Valenzano, L., Torres, F. J., Doll, K., Pascale, F., Zicovich-Wilson, C. M., & Dovesi, R. (2006). Ab initio study of the vibrational spectrum and related properties of crystalline compounds; the case of CaCO3 calcite. Zeitschrift für Physikalische Chemie, 220(7/2006), 893-912.

Voigt W. Lehrbuch der Kristallphysik (B. G. Teubner. Berlin. 1910). p.754.

Wu, Z., and Cohen, R.E. (2006) More accurate generalized gradient approximation for solids. Physical Review B, 73, 235116.

Ziman, J.M. (1960). Electrons and phonons: the theory of transport phenomena in solids. Oxford University Press. p.469

THE EFFECTS OF NON-HYDROSTATIC STRESS ON THE STRUCTURE AND PROPERTIES OF ALPHA-QUARTZ

Mara Murri[1], Matteo Alvaro[1], Ross J. Angel[1], Mauro Prencipe[2], Boriana D. Mihailova[3]

[1]*Department of Earth and Environmental Sciences, University of Pavia, Via A. Ferrata, 1 I-27100 4 Pavia, Italy*
[2]*Earth Sciences Department, University of Torino, Via Valperga Caluso 35 Italy*
[3]*Department of Earth Sciences, University of Hamburg, Grindelallee 48, D-20146 Hamburg, Germany*

QUANTIFYING HEXAGONAL STACKING IN DIAMOND

Mara Murri,[1] Rachael L. Smith,[2] Kit McColl,[2] Martin Hart,[2] Matteo Alvaro,[1] Adrian P. Jones,[3] Péter Németh,[4] Christoph G. Salzmann,[2] Furio Corà,[2] Maria C. Domeneghetti,[1] Fabrizio Nestola,[5] Nikolay V. Sobolev,[6] Sergey A. Vishnevsky,[6] Alla M. Logvinova,[6] Paul F. McMillan[2]

[1]*Department of Earth and Environmental Sciences, University of Pavia, Via A. Ferrata, 1 27100 Pavia, Italy*
[2]*Department of Chemistry, University College London, 20 Gordon Street, London WC1H 0AJ, UK*
[3]*Department of Earth Sciences, University College London, WC1E 6BT, UK*
[4]*Institute of Materials and Environmental Chemistry, Research Centre for Natural Sciences-HAS, Magyar tudósok körútja 2, 1117 Budapest, Hungary*
[5]*Department of Geosciences, University of Padova, Via G. Gradenigo 6, I-35131 Padova, Italy*
[6]*V.S. Sobolev Institute of Geology and Mineralogy, Siberian Branch of Russian Academy of Sciences, Koptyug Ave., 3, Novosibirsk 90, 630090, Russia*

Contents

Preparation of the various diamond structures

Using our *Stacky* program (Playford et al. 2018), a range of stacking disordered diamond structures were created with 48 layers. *Stacky* requires the target 1st order stacking probabilities as input and then produces a closest possible structure ensuring periodicity across the unit cell boundary in the *c* direction of stacking. As described in Playford et al. (2018) in detail, the requirement for periodicity across the boundary of the unit cell imposes some restrictions with respect to the possible stacking sequences.

In addition to the stacking disordered structures, the structures of the regular 2H, 3C and 4H polytypes were also produced with *Stacky*. The structural details of all created structures are listed in Table S1. The *structures.zip* file contains the *cif* files of the various structures.

Table S1. Filenames, stacking probabilities and stacking sequences of the various diamond structures created with Stacky (Playford et al. 2018).

filename	Φ_c	Φ_{hc}	Φ_{cc}	stacking sequence (h = hexagonal, c = cubic)
diamond1.cif	0.25	0.25	0.25	hhhhhhhchhhcchhcchhchhchhhchhhhhchhhhhhhhchhhhcchh
diamond2.cif	0.5	0.5	0.5	hhcccchhcccchhcchhcccchhhhchhchhchhchchccccchhchcch
diamond3.cif	0.75	0.75	0.75	cchcccchhcccchhhccccccchcchcchchcccchccccccchcccc
diamond4.cif	0.5	0.25	0.75	hccccchhhhhhhhcchhcchhchccccccccchhhhhhhhhhhcccccc
diamond5.cif	0.5	0.75	0.25	hhcchhcchchchcchchchchcchhchhhchchhcchchchchchhcc
diamond6.cif	0.625	0.611	0.633	hhhcccchcchchcchchcchhccccchhchcccccccccchcccchchhh
diamond7.cif	0.875	0.833	0.881	cchcchcchcccccccccccccccccccchccccccccccccchhcccc
ccc.cif	1	1	1	ccc (cubic diamond)
hh.cif	0	0	0	hh (hexagonal diamond)
hchc.cif	0.5	1	0	hchc (4H polytype)

Calculated Raman spectra

The structures listed in Table S1 were used as starting structures for calculating the Raman spectra with CRYSTAL17 (Dovesi et al. 2018) as shown in Figure 3 in the main article. The calculated Raman spectra using Gaussian functions with 10 cm^{-1} half-widths as the profile functions are contained within *spectra.zip*. (https://www.nature.com/articles/s41598-019-46556-3#Sec12)

MCDIFFaX fitting of the X-ray patterns

The recorded X-ray diffraction patterns were baseline corrected using shifted Chebyshev background functions within the GSAS software (Larsen and Dreele 1985). Great care was taken to not subtract intensity in the angle ranges where stacking disorder leads to diffuse scattering. The diffraction data were then fitted with the MCDIFFaX software by refining up to 2nd order stacking probabilities, lattice parameters and peak-profile parameters (*u*, *v*, *w* and Gaussian / Lorentzian ratio) (Salzmann et al. 2015). During a typical refinement, a starting value of 0.5 was used for the zero-order stacking probability, and the 1st and 2nd order stacking probabilities were successively introduced during the refinement once the fits had converged using the lower-order stacking probabilities. Regarding the Cagliotti terms, the refinements were started by optimising *w* alone, whereas *u* and *v* were introduced during the later stages of the refinements. A detailed description of the MCDIFFaX program as well as the equations needed for the calculations of the 1st order stacking probabilities from the 2nd order stacking probabilities as well as the cubicity or hexagonality from the 1st order stacking probabilities are given in Salzmann et al. (2015). The determined stacking probabilities from all analysed Popigai diamond samples are listed in Table S2.

Table S2. Second and first-order stacking probabilities together with the resulting cubicities and hexagonalities of the various Popigai diamond samples.

sample	Φ_{ccc}	Φ_{hcc}	Φ_{chc}	Φ_{hhc}	Φ_{hc}	Φ_{cc}	Φ_{c}	Φ_{h}
POP1	0.865	0.330	0.786	0.665	0.756	0.709	0.722	0.278
POP2	0.873	0.471	0.822	0.969	0.845	0.788	0.799	0.201
POP3	0.932	0.337	0.847	0.883	0.852	0.832	0.835	0.165
POP4	0.563	0.695	0.789	0.449	0.680	0.614	0.638	0.362
POP5	0.934	0.330	0.815	0.907	0.830	0.834	0.833	0.167
POP6	0.842	0.901	0.817	0.895	0.830	0.851	0.848	0.152
POP10	0.786	0.367	0.616	0.842	0.687	0.632	0.651	0.349
POP11	0.931	0.748	0.613	1.000	0.721	0.915	0.895	0.105
POP12	0.781	0.359	0.459	0.766	0.586	0.621	0.607	0.393
POP13	0.912	0.343	0.765	0.963	0.804	0.796	0.797	0.203
POP16	0.822	0.833	0.832	0.724	0.811	0.824	0.822	0.178
POP17	0.773	0.916	1.000	0.907	1.000	0.802	0.834	0.166
POP20	0.849	0.916	0.950	0.831	0.943	0.858	0.869	0.131
POP21	0.809	0.880	1.000	0.898	1.000	0.821	0.848	0.152
POP23	0.783	0.914	0.920	0.854	0.914	0.808	0.827	0.173
POP24	0.778	0.844	0.975	0.926	0.973	0.792	0.824	0.176
POP25	0.798	0.893	0.955	0.921	0.953	0.816	0.838	0.162
POP27	0.936	0.876	1.000	0.878	1.000	0.932	0.936	0.064
POP29	0.381	0.743	0.796	0.981	0.828	0.545	0.645	0.355
POP31	0.796	0.889	0.970	0.902	0.968	0.813	0.838	0.162
POP32	0.959	0.860	1.000	0.789	1.000	0.955	0.957	0.043
POP34	0.802	0.396	0.794	0.948	0.822	0.666	0.711	0.289
POP35	0.761	0.426	0.685	0.892	0.739	0.641	0.673	0.327
POP36	0.786	0.898	0.941	0.727	0.924	0.807	0.828	0.172

Effect of hexagonality on the crystallographic *c/a* ratio

Within DIFFaX, the structure of a stacking disordered material is described by defining the structure of a single layer and then implementing the geometric recipes for stacking these layers together with the corresponding stacking probabilities (Treacy 1991). Since MCDIFFaX deals with individual layers, the *c* height of a layer needs to be multiplied by 2 before comparing the *c/a* ratio with the one of the ideal hexagonal close-packed structure for which $c/a = \sqrt{8}/3$. For fully cubic diamond, the *c/a* ratio is $\sqrt{8}/3$ by definition because of the cubic symmetry. Figure S1 shows the *c/a* ratios of the various Popigai diamond samples as determined with MCDIFFaX and plotted as a function of the hexagonality. Despite some considerable errors, it can be seen that the *c/a* ratio increases with increasing hexagonality. This implies that the repulsive interactions within the six-membered rings in boat conformation lead to slight separations of the stacked layers. The red line in Figure S1 shows the best linear fit to the data and the corresponding equation is shown in the legend. It is noted that the deviations from the fitted line do not seem to be connected with the deviations from random stacking, *i.e.* differences in the 1st order memory effects within the stacking sequences as shown in the stackogram in Figure 2B in the main article.
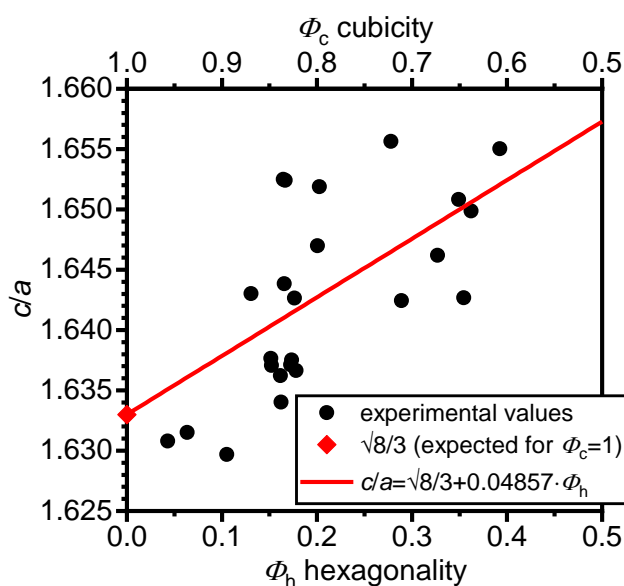
Figure S1. Crystallographic c/a ratios obtained from the MCDIFFaX fits of the Popigai diamonds. The red line represents the best linear fit to the data with the intercept value fixed to the expected c/a ratio of cubic diamond

.

References

Dovesi, R., Erba, A., Orlando, R., Zicovich-Wilson, C.M., Civalleri, B., Maschio, L., Rérat, M., Casassa, S., Baima, J., Salustro, S. and Kirtman, B. (2018) Quantum-mechanical condensed matter simulations with CRYSTAL. Wiley Interdisciplinary Reviews: Computational Molecular Science, 8(4), p.e1360.

Larsen, A. C., Von Dreele, R. B. (1985) GSAS - General Structure Analysis System, University of California.

Playford, H. Y., Whale, T. F., Murray, B., Tucker, M. G., and Salzmann, C. G. (2018) Analysis of stacking disorder in ice I using pair distribution functions. Journal of Applied Crystallography, 51(4).

Salzmann, C. G., Murray, B. J. and Shephard, J. J. (2015) Extent of stacking disorder in diamond. Diamond and Related Materials, 59, 69-72.

Treacy, M. M. J., Newsam, J. M., and Deem, M. W. (1991) A general recursion method for calculating diffracted intensities from crystals containing planar faults. Proceedings of the Royal Society of London. Series A: Mathematical and Physical Sciences, 433(1889), 499-520.

INTRACRYSTALLINE "GEOTHERMOMETRY" ASSESSED ON CLINO AND ORTHOPYROXENE BEARING SYNTHETIC ROCKS

Mara Murri[1], Fernando Cámara[2], John Adam[3], Maria C. Domeneghetti[1], Matteo Alvaro[1]

[1]*Department of Earth and Environmental Sciences, University of Pavia, Via A. Ferrata, 1 I-27100 4 Pavia, Italy*
[2]*Dipartimento di Scienze della Terra, Università degli Studi di Milano, Italy*
[3] *Department of Earth and Planetary Sciences, Macquarie University, Sydney, 2109, Australia*

	x	y	z	Uiso*/Ueq	Occ. (<1)	U11	U22	U33	U12	U13	U23
					CPX R80						
O1A	0.11513 (8)	0.08593 (9)	0.14067 (16)	0.01084 (15)	0.14(2)	0.0068 (3)	0.0146 (3)	0.0110 (3)	0.0015 (3)	0.0024 (3)	−0.0012 (3)
O1B	0.11513 (8)	0.08593 (9)	0.14067 (16)	0.01084 (15)	0.86(2)	0.0068 (3)	0.0146 (3)	0.0110 (3)	0.0015 (3)	0.0024 (3)	−0.0012 (3)
O2A	0.3621 (6)	0.2540 (5)	0.3182 (17)	0.0116 (6)	0.180(4)	0.0158 (7)	0.0082 (7)	0.0110 (14)	−0.0017 (5)	0.0045 (9)	−0.0003 (7)
O2B	0.3621 (6)	0.2540 (5)	0.3182 (17)	0.0116 (6)	0.66(4)	0.0158 (7)	0.0082 (7)	0.0110 (14)	−0.0017 (5)	0.0045 (9)	−0.0003 (7)
O2B1	0.3781 (18)	0.239 (2)	0.372 (6)	0.011 (2)*	0.16(4)						
O3A	0.35230 (8)	0.01763 (10)	0.00269 (16)	0.01284 (16)	0.29(3)	0.0084 (3)	0.0182 (4)	0.0121 (3)	0.0002 (3)	0.0035 (3)	−0.0056 (3)
O3B	0.35230 (8)	0.01763 (10)	0.00269 (16)	0.01284 (16)	0.71(3)	0.0084 (3)	0.0182 (4)	0.0121 (3)	0.0002 (3)	0.0035 (3)	−0.0056 (3)
SiA	0.28955 (3)	0.09241 (3)	0.23574 (6)	0.00702 (8)	0.52(2)	0.00614 (12)	0.00754 (13)	0.00796 (13)	−0.00026 (9)	0.00297 (9)	−0.00089 (9)
SiB	0.28955 (3)	0.09241 (3)	0.23574 (6)	0.00702 (8)	0.48(2)	0.00614 (12)	0.00754 (13)	0.00796 (13)	−0.00026 (9)	0.00297 (9)	−0.00089 (9)
M1A	0	0.90619 (5)	0.25	0.00641 (14)	0.089(3)	0.0060 (2)	0.0073 (2)	0.0059 (2)	0	0.00159 (14)	0
M1B	0	0.90619 (5)	0.25	0.00641 (14)	0.911(3)	0.0060 (2)	0.0073 (2)	0.0059 (2)	0	0.00159 (14)	0
M2A	0	0.30081 (18)	0.25	0.01145 (19)	0.659(4)	0.0140 (2)	0.0092 (5)	0.00872 (19)	0	−0.00037 (13)	0
M2B	0	0.2746 (13)	0.25	0.01145 (19)	0.290(3)	0.0140 (2)	0.0092 (5)	0.00872 (19)	0	−0.00037 (13)	0
M21A	0	0.2553 (14)	0.25	0.0090 (16)*	0.051(3)						

Table S1. Fractional atomic coordinates, equivalent isotropic displacement parameters, and anisotropic displacement parameters (Å^2) of crystals CPX R80, 1948 and 1950.

CPX 1948											
O1A	0.11555 (6)	0.08667 (6)	0.14125 (12)	0.01156 (10)	0.12(3)	0.0077 (2)	0.0147 (2)	0.0125 (2)	0.00142 (16)	0.00323 (17)	−0.00082 (17)
O1B	0.11555 (6)	0.08667 (6)	0.14125 (12)	0.01156 (10)	0.88(3)	0.0077 (2)	0.0147 (2)	0.0125 (2)	0.00142 (16)	0.00323 (17)	−0.00082 (17)
O2A	0.3621 (4)	0.2535 (3)	0.3192 (12)	0.0126 (4)	0.170(4)	0.0163 (5)	0.0091 (4)	0.0125 (10)	−0.0016 (3)	0.0046 (7)	−0.0004 (5)
O2B	0.3621 (4)	0.2535 (3)	0.3192 (12)	0.0126 (4)	0.65(3)	0.0163 (5)	0.0091 (4)	0.0125 (10)	−0.0016 (3)	0.0046 (7)	−0.0004 (5)
O2B1	0.3784 (11)	0.2405 (12)	0.372 (4)	0.0113 (11)*	0.18(3)						
O3A	0.35219 (6)	0.01855 (7)	0.00156 (11)	0.01412 (11)	0.21(3)	0.0091 (2)	0.0196 (3)	0.0137 (2)	0.00028 (18)	0.00339 (17)	−0.00619 (18)
O3B	0.35219 (6)	0.01855 (7)	0.00156 (11)	0.01412 (11)	0.79(3)	0.0091 (2)	0.0196 (3)	0.0137 (2)	0.00028 (18)	0.00339 (17)	−0.00619 (18)
SiA	0.28958 (2)	0.09233 (2)	0.23578 (4)	0.00828 (6)	0.58(2)	0.00732 (9)	0.00811 (9)	0.01007 (10)	−0.00034 (6)	0.00358 (6)	−0.00089 (6)
SiB	0.28958 (2)	0.09233 (2)	0.23578 (4)	0.00828 (6)	0.42(2)	0.00732 (9)	0.00811 (9)	0.01007 (10)	−0.00034 (6)	0.00358 (6)	−0.00089 (6)
M1A	0	0.90641 (3)	0.25	0.00847 (10)	0.112(2)	0.00831 (15)	0.00861 (15)	0.00846 (15)	0	0.00239 (10)	0
M1B	0	0.90641 (3)	0.25	0.00847 (10)	0.888(2)	0.00831 (15)	0.00861 (15)	0.00846 (15)	0	0.00239 (10)	0
M2A	0	0.30046 (10)	0.25	0.01233 (11)	0.702(4)	0.01466 (14)	0.0098 (3)	0.01034 (13)	0	0.00020 (8)	0
M2B	0	0.2686 (15)	0.25	0.01233 (11)	0.224(3)	0.01466 (14)	0.0098 (3)	0.01034 (13)	0	0.00020 (8)	0
M21A	0	0.2594 (13)	0.25	0.0137 (8)*	0.074(3)						

CPX 1950											
O1A	0.11600 (10)	0.08713 (10)	0.14211 (19)	0.01033 (17)	0.09(4)	0.0072 (3)	0.0128 (4)	0.0111 (4)	0.0013 (3)	0.0030 (3)	−0.0004 (3)
O1B	0.11600 (10)	0.08713 (10)	0.14211 (19)	0.01033 (17)	0.91(4)	0.0072 (3)	0.0128 (4)	0.0111 (4)	0.0013 (3)	0.0030 (3)	−0.0004 (3)
O2A	0.3626 (5)	0.2516 (4)	0.3220 (13)	0.0118 (6)	0.135(4)	0.0144 (7)	0.0088 (6)	0.0126 (13)	−0.0023 (5)	0.0047 (9)	−0.0012 (7)
O2B	0.3626 (5)	0.2516 (4)	0.3220 (13)	0.0118 (6)	0.77(3)	0.0144 (7)	0.0088 (6)	0.0126 (13)	−0.0023 (5)	0.0047 (9)	−0.0012 (7)
O2B1	0.383 (3)	0.234 (3)	0.385 (9)	0.011 (3)*	0.10(3)						
O3A	0.35172 (9)	0.01905 (11)	−0.00068 (18)	0.01213 (18)	0.20(4)	0.0084 (4)	0.0168 (4)	0.0113 (4)	−0.0001 (3)	0.0030 (3)	−0.0044 (3)
O3B	0.35172 (9)	0.01905 (11)	−0.00068 (18)	0.01213 (18)	0.80(4)	0.0084 (4)	0.0168 (4)	0.0113 (4)	−0.0001 (3)	0.0030 (3)	−0.0044 (3)
SiA	0.28887 (4)	0.09244 (4)	0.23421 (7)	0.00761 (9)	0.67(3)	0.00706 (14)	0.00744 (15)	0.00889 (15)	−0.00040 (10)	0.00319 (11)	−0.00072 (10)
SiB	0.28887 (4)	0.09244 (4)	0.23421 (7)	0.00761 (9)	0.33(3)	0.00706 (14)	0.00744 (15)	0.00889 (15)	−0.00040 (10)	0.00319 (11)	−0.00072 (10)
M1A	0	0.90674 (5)	0.25	0.00849 (16)	0.142(3)	0.0086 (2)	0.0084 (2)	0.0085 (2)	0	0.00246 (17)	0
M1B	0	0.90674 (5)	0.25	0.00849 (16)	0.858(3)	0.0086 (2)	0.0084 (2)	0.0085 (2)	0	0.00246 (17)	0
M2A	0	0.29995 (12)	0.25	0.01164 (16)	0.811(4)	0.0134 (2)	0.0098 (4)	0.0098 (2)	0	0.00030 (14)	0
M2B	0	0.273 (7)	0.25	0.01164 (16)	0.118(4)	0.0134 (2)	0.0098 (4)	0.0098 (2)	0	0.00030 (14)	0
M21A	0	0.248 (6)	0.25	0.0163 (19)*	0.072(4)						

	Table S2. Fractional atomic coordinates, equivalent isotropic displacement parameters, and anisotropic displacement parameters (Å^2) of crystals OPX R80, 1948, 1950 and 1949.										
					OPX R80						
	x	y	z	Uiso*/Ueq	Occ. (<1)	U11	U22	U33	U12	U13	U23
SiA	0.271282 (18)	0.34159 (4)	0.04772 (7)	0.00576 (7)	0.5	0.00538 (13)	0.00609 (14)	0.00580 (14)	−0.00058 (10)	0.00051 (10)	−0.00011 (10)
SiA+	0.271282 (18)	0.34159 (4)	0.04772 (7)	0.00576 (7)	0.5	0.00538 (13)	0.00609 (14)	0.00580 (14)	−0.00058 (10)	0.00051 (10)	−0.00011 (10)
SiB	0.473867 (18)	0.33731 (4)	0.79971 (7)	0.00614 (7)	0.5	0.00563 (13)	0.00629 (14)	0.00652 (14)	0.00032 (10)	−0.00019 (10)	0.00034 (10)
SiB+	0.473867 (18)	0.33731 (4)	0.79971 (7)	0.00614 (7)	0.5	0.00563 (13)	0.00629 (14)	0.00652 (14)	0.00032 (10)	−0.00019 (10)	0.00034 (10)
O1A	0.18307 (5)	0.33904 (10)	0.03714 (18)	0.00829 (15)	0.25	0.0058 (3)	0.0105 (4)	0.0086 (4)	0.0003 (3)	0.0000 (3)	0.0003 (3)
O1A-	0.18307 (5)	0.33904 (10)	0.03714 (18)	0.00829 (15)	0.75	0.0058 (3)	0.0105 (4)	0.0086 (4)	0.0003 (3)	0.0000 (3)	0.0003 (3)
O1B	0.56292 (5)	0.33804 (10)	0.80150 (18)	0.00862 (15)	0.25	0.0059 (3)	0.0111 (4)	0.0089 (4)	−0.0008 (3)	0.0000 (3)	0.0007 (3)
O1B-	0.56292 (5)	0.33804 (10)	0.80150 (18)	0.00862 (15)	0.75	0.0059 (3)	0.0111 (4)	0.0089 (4)	−0.0008 (3)	0.0000 (3)	0.0007 (3)
O2A	0.31061 (5)	0.50270 (10)	0.04425 (19)	0.00888 (15)	0.25	0.0097 (3)	0.0069 (3)	0.0100 (4)	−0.0018 (3)	−0.0002 (3)	0.0007 (3)
O2A-	0.31061 (5)	0.50270 (10)	0.04425 (19)	0.00888 (15)	0.75	0.0097 (3)	0.0069 (3)	0.0100 (4)	−0.0018 (3)	−0.0002 (3)	0.0007 (3)
O2B	0.43369 (5)	0.48526 (11)	0.69316 (19)	0.01110 (17)	0.25	0.0119 (4)	0.0103 (4)	0.0111 (4)	0.0024 (3)	0.0003 (3)	0.0024 (3)
O2B-	0.43369 (5)	0.48526 (11)	0.69316 (19)	0.01110 (17)	0.75	0.0119 (4)	0.0103 (4)	0.0111 (4)	0.0024 (3)	0.0003 (3)	0.0024 (3)
O3A	0.30252 (5)	0.22659 (11)	−0.17549 (19)	0.00972 (16)	0.25	0.0084 (3)	0.0124 (4)	0.0084 (3)	−0.0007 (3)	0.0007 (3)	−0.0043 (3)
O3A-	0.30252 (5)	0.22659 (11)	−0.17549 (19)	0.00972 (16)	0.75	0.0084 (3)	0.0124 (4)	0.0084 (3)	−0.0007 (3)	0.0007 (3)	−0.0043 (3)
O3B	0.44705 (5)	0.19772 (12)	0.60150 (19)	0.01042 (17)	0.25	0.0078 (3)	0.0128 (4)	0.0106 (4)	−0.0005 (3)	0.0001 (3)	−0.0044 (3)
O3B-	0.44705 (5)	0.19772 (12)	0.60150 (19)	0.01042 (17)	0.75	0.0078 (3)	0.0128 (4)	0.0106 (4)	−0.0005 (3)	0.0001 (3)	−0.0044 (3)
MgM1	0.37569 (2)	0.65413 (5)	0.86758 (8)	0.00717 (12)	0.924(2)	0.00728 (19)	0.00705 (19)	0.00718 (19)	0.00019 (12)	−0.00078 (12)	0.00019 (12)
FeM1	0.37569 (2)	0.65413 (5)	0.86758 (8)	0.00717 (12)	0.076(2)	0.00728 (19)	0.00705 (19)	0.00718 (19)	0.00019 (12)	−0.00078 (12)	0.00019 (12)
MgM2	0.378330 (19)	0.48254 (4)	0.36123 (7)	0.00983 (11)	0.761(2)	0.01011 (16)	0.01172 (17)	0.00767 (16)	−0.00187 (11)	−0.00195 (10)	−0.00111 (11)
FeM2	0.378330 (19)	0.48254 (4)	0.36123 (7)	0.00983 (11)	0.239(2)	0.01011 (16)	0.01172 (17)	0.00767 (16)	−0.00187 (11)	−0.00195 (10)	−0.00111 (11)

OPX 1948											
SiA	0.27129 (2)	0.34155 (5)	0.04792 (9)	0.00587 (11)	0.5	0.00555 (19)	0.0059 (2)	0.0061 (2)	−0.00026 (14)	0.00053 (14)	−0.00033 (15)
SiA+	0.27129 (2)	0.34155 (5)	0.04792 (9)	0.00587 (11)	0.5	0.00555 (19)	0.0059 (2)	0.0061 (2)	−0.00026 (14)	0.00053 (14)	−0.00033 (15)
SiB	0.47396 (2)	0.33734 (5)	0.79932 (9)	0.00628 (11)	0.5	0.00591 (19)	0.0059 (2)	0.0070 (2)	0.00023 (14)	−0.00013 (15)	0.00031 (15)
SiB+	0.47396 (2)	0.33734 (5)	0.79932 (9)	0.00628 (11)	0.5	0.00591 (19)	0.0059 (2)	0.0070 (2)	0.00023 (14)	−0.00013 (15)	0.00031 (15)
O1A	0.18313 (6)	0.33922 (14)	0.0371 (2)	0.0087 (2)	0.25	0.0059 (5)	0.0111 (5)	0.0092 (6)	0.0004 (4)	0.0009 (4)	0.0003 (4)
O1A-	0.18313 (6)	0.33922 (14)	0.0371 (2)	0.0087 (2)	0.75	0.0059 (5)	0.0111 (5)	0.0092 (6)	0.0004 (4)	0.0009 (4)	0.0003 (4)
O1B	0.56292 (7)	0.33817 (13)	0.8008 (3)	0.0088 (2)	0.25	0.0060 (5)	0.0103 (5)	0.0101 (6)	−0.0005 (4)	0.0001 (4)	0.0006 (4)
O1B-	0.56292 (7)	0.33817 (13)	0.8008 (3)	0.0088 (2)	0.75	0.0060 (5)	0.0103 (5)	0.0101 (6)	−0.0005 (4)	0.0001 (4)	0.0006 (4)
O2A	0.31055 (7)	0.50245 (14)	0.0444 (2)	0.0089 (2)	0.25	0.0101 (5)	0.0066 (5)	0.0100 (5)	−0.0015 (4)	−0.0002 (4)	0.0003 (4)
O2A-	0.31055 (7)	0.50245 (14)	0.0444 (2)	0.0089 (2)	0.75	0.0101 (5)	0.0066 (5)	0.0100 (5)	−0.0015 (4)	−0.0002 (4)	0.0003 (4)
O2B	0.43370 (7)	0.48521 (14)	0.6937 (3)	0.0110 (2)	0.25	0.0112 (5)	0.0095 (5)	0.0122 (6)	0.0024 (4)	0.0006 (4)	0.0028 (4)
O2B-	0.43370 (7)	0.48521 (14)	0.6937 (3)	0.0110 (2)	0.75	0.0112 (5)	0.0095 (5)	0.0122 (6)	0.0024 (4)	0.0006 (4)	0.0028 (4)
O3A	0.30257 (7)	0.22662 (14)	−0.1754 (2)	0.0100 (2)	0.25	0.0090 (5)	0.0122 (5)	0.0087 (5)	−0.0007 (4)	0.0010 (4)	−0.0048 (4)
O3A-	0.30257 (7)	0.22662 (14)	−0.1754 (2)	0.0100 (2)	0.75	0.0090 (5)	0.0122 (5)	0.0087 (5)	−0.0007 (4)	0.0010 (4)	−0.0048 (4)
O3B	0.44719 (7)	0.19800 (15)	0.6008 (3)	0.0109 (2)	0.25	0.0083 (5)	0.0128 (6)	0.0116 (6)	0.0001 (4)	0.0003 (4)	−0.0052 (4)
O3B-	0.44719 (7)	0.19800 (15)	0.6008 (3)	0.0109 (2)	0.75	0.0083 (5)	0.0128 (6)	0.0116 (6)	0.0001 (4)	0.0003 (4)	−0.0052 (4)
MgM1	0.37566 (3)	0.65419 (6)	0.86777 (10)	0.00726 (17)	0.923(3)	0.0078 (3)	0.0065 (3)	0.0075 (3)	0.00004 (17)	−0.00079 (18)	0.00026 (17)
FeM1	0.37566 (3)	0.65419 (6)	0.86777 (10)	0.00726 (17)	0.077(3)	0.0078 (3)	0.0065 (3)	0.0075 (3)	0.00004 (17)	−0.00079 (18)	0.00026 (17)
MgM2	0.37820 (2)	0.48253 (5)	0.36160 (9)	0.01032 (15)	0.754(3)	0.0104 (2)	0.0123 (2)	0.0083 (2)	−0.00193 (15)	−0.00183 (15)	−0.00128 (15)
FeM2	0.37820 (2)	0.48253 (5)	0.36160 (9)	0.01032 (15)	0.246(3)	0.0104 (2)	0.0123 (2)	0.0083 (2)	−0.00193 (15)	−0.00183 (15)	−0.00128 (15)

					OPX 1950						
SiA	0.271387 (16)	0.34133 (3)	0.04867 (6)	0.00564 (7)	0.5	0.00547 (12)	0.00587 (13)	0.00559 (13)	−0.00048 (9)	0.00047 (9)	−0.00012 (9)
SiA+	0.271387 (16)	0.34133 (3)	0.04867 (6)	0.00564 (7)	0.5	0.00547 (12)	0.00587 (13)	0.00559 (13)	−0.00048 (9)	0.00047 (9)	−0.00012 (9)
SiB	0.473851 (16)	0.33709 (3)	0.79854 (6)	0.00585 (7)	0.5	0.00537 (12)	0.00593 (13)	0.00626 (13)	0.00021 (9)	−0.00026 (9)	0.00022 (9)
SiB+	0.473851 (16)	0.33709 (3)	0.79854 (6)	0.00585 (7)	0.5	0.00537 (12)	0.00593 (13)	0.00626 (13)	0.00021 (9)	−0.00026 (9)	0.00022 (9)
O1A	0.18329 (4)	0.33923 (9)	0.03791 (16)	0.00783 (14)	0.25	0.0057 (3)	0.0094 (3)	0.0084 (3)	0.0002 (2)	0.0003 (2)	−0.0003 (3)
O1A-	0.18329 (4)	0.33923 (9)	0.03791 (16)	0.00783 (14)	0.75	0.0057 (3)	0.0094 (3)	0.0084 (3)	0.0002 (2)	0.0003 (2)	−0.0003 (3)
O1B	0.56277 (4)	0.33824 (9)	0.79986 (16)	0.00805 (14)	0.25	0.0062 (3)	0.0098 (3)	0.0082 (3)	−0.0008 (2)	0.0001 (2)	0.0007 (3)
O1B-	0.56277 (4)	0.33824 (9)	0.79986 (16)	0.00805 (14)	0.75	0.0062 (3)	0.0098 (3)	0.0082 (3)	−0.0008 (2)	0.0001 (2)	0.0007 (3)
O2A	0.31078 (4)	0.50206 (9)	0.04602 (16)	0.00841 (14)	0.25	0.0092 (3)	0.0068 (3)	0.0093 (3)	−0.0019 (2)	−0.0004 (2)	0.0010 (3)
O2A-	0.31078 (4)	0.50206 (9)	0.04602 (16)	0.00841 (14)	0.75	0.0092 (3)	0.0068 (3)	0.0093 (3)	−0.0019 (2)	−0.0004 (2)	0.0010 (3)
O2B	0.43358 (5)	0.48478 (10)	0.69310 (17)	0.01029 (15)	0.25	0.0108 (3)	0.0101 (3)	0.0100 (4)	0.0024 (3)	0.0009 (3)	0.0020 (3)
O2B-	0.43358 (5)	0.48478 (10)	0.69310 (17)	0.01029 (15)	0.75	0.0108 (3)	0.0101 (3)	0.0100 (4)	0.0024 (3)	0.0009 (3)	0.0020 (3)
O3A	0.30257 (4)	0.22697 (10)	−0.17490 (16)	0.00966 (15)	0.25	0.0082 (3)	0.0130 (4)	0.0078 (3)	−0.0009 (3)	0.0007 (2)	−0.0040 (3)
O3A-	0.30257 (4)	0.22697 (10)	−0.17490 (16)	0.00966 (15)	0.75	0.0082 (3)	0.0130 (4)	0.0078 (3)	−0.0009 (3)	0.0007 (2)	−0.0040 (3)
O3B	0.44726 (4)	0.19821 (10)	0.60005 (16)	0.01003 (15)	0.25	0.0082 (3)	0.0118 (3)	0.0100 (4)	−0.0006 (3)	0.0004 (3)	−0.0040 (3)
O3B-	0.44726 (4)	0.19821 (10)	0.60005 (16)	0.01003 (15)	0.75	0.0082 (3)	0.0118 (3)	0.0100 (4)	−0.0006 (3)	0.0004 (3)	−0.0040 (3)
MgM1	0.375669 (19)	0.65428 (4)	0.86841 (7)	0.00681 (11)	0.907(2)	0.00719 (16)	0.00687 (17)	0.00637 (17)	0.00009 (10)	−0.00048 (11)	0.00034 (11)
FeM1	0.375669 (19)	0.65428 (4)	0.86841 (7)	0.00681 (11)	0.093(2)	0.00719 (16)	0.00687 (17)	0.00637 (17)	0.00009 (10)	−0.00048 (11)	0.00034 (11)
MgM2	0.378171 (15)	0.48294 (3)	0.36223 (5)	0.00952 (9)	0.687(2)	0.00982 (13)	0.01136 (14)	0.00738 (13)	−0.00167 (9)	−0.00195 (9)	−0.00076 (9)
FeM2	0.378171 (15)	0.48294 (3)	0.36223 (5)	0.00952 (9)	0.313(2)	0.00982 (13)	0.01136 (14)	0.00738 (13)	−0.00167 (9)	−0.00195 (9)	−0.00076 (9)

OPX 1949											
SiA	0.271328 (13)	0.34146 (3)	0.04794 (5)	0.00596 (5)	0.5	0.00548 (10)	0.00670 (10)	0.00572 (10)	−0.00046 (6)	0.00047 (7)	−0.00025 (7)
SiA+	0.271328 (13)	0.34146 (3)	0.04794 (5)	0.00596 (5)	0.5	0.00548 (10)	0.00670 (10)	0.00572 (10)	−0.00046 (6)	0.00047 (7)	−0.00025 (7)
SiB	0.473874 (13)	0.33726 (3)	0.79934 (5)	0.00625 (6)	0.5	0.00564 (10)	0.00672 (10)	0.00640 (10)	0.00022 (6)	−0.00021 (7)	0.00038 (7)
SiB+	0.473874 (13)	0.33726 (3)	0.79934 (5)	0.00625 (6)	0.5	0.00564 (10)	0.00672 (10)	0.00640 (10)	0.00022 (6)	−0.00021 (7)	0.00038 (7)
O1A	0.18309 (3)	0.33913 (7)	0.03744 (13)	0.00842 (11)	0.25	0.0057 (2)	0.0105 (3)	0.0090 (2)	0.00027 (18)	0.00005 (19)	0.00044 (19)
O1A-	0.18309 (3)	0.33913 (7)	0.03744 (13)	0.00842 (11)	0.75	0.0057 (2)	0.0105 (3)	0.0090 (2)	0.00027 (18)	0.00005 (19)	0.00044 (19)
O1B	0.56292 (4)	0.33819 (7)	0.80091 (13)	0.00858 (11)	0.25	0.0061 (2)	0.0108 (3)	0.0087 (2)	−0.00068 (18)	−0.00005 (18)	0.00069 (19)
O1B-	0.56292 (4)	0.33819 (7)	0.80091 (13)	0.00858 (11)	0.75	0.0061 (2)	0.0108 (3)	0.0087 (2)	−0.00068 (18)	−0.00005 (18)	0.00069 (19)
O2A	0.31066 (4)	0.50248 (7)	0.04483 (13)	0.00916 (11)	0.25	0.0099 (2)	0.0075 (2)	0.0101 (3)	−0.00181 (19)	−0.00062 (19)	0.00071 (19)
O2A-	0.31066 (4)	0.50248 (7)	0.04483 (13)	0.00916 (11)	0.75	0.0099 (2)	0.0075 (2)	0.0101 (3)	−0.00181 (19)	−0.00062 (19)	0.00071 (19)
O2B	0.43365 (4)	0.48520 (8)	0.69319 (13)	0.01100 (11)	0.25	0.0114 (3)	0.0107 (3)	0.0108 (3)	0.0024 (2)	0.0003 (2)	0.0024 (2)
O2B-	0.43365 (4)	0.48520 (8)	0.69319 (13)	0.01100 (11)	0.75	0.0114 (3)	0.0107 (3)	0.0108 (3)	0.0024 (2)	0.0003 (2)	0.0024 (2)
O3A	0.30261 (3)	0.22673 (8)	−0.17524 (13)	0.01005 (11)	0.25	0.0084 (2)	0.0134 (3)	0.0084 (2)	−0.0003 (2)	0.00048 (18)	−0.0042 (2)
O3A-	0.30261 (3)	0.22673 (8)	−0.17524 (13)	0.01005 (11)	0.75	0.0084 (2)	0.0134 (3)	0.0084 (2)	−0.0003 (2)	0.00048 (18)	−0.0042 (2)
O3B	0.44710 (4)	0.19766 (8)	0.60126 (13)	0.01062 (11)	0.25	0.0084 (2)	0.0130 (3)	0.0104 (3)	−0.0008 (2)	0.0003 (2)	−0.0047 (2)
O3B-	0.44710 (4)	0.19766 (8)	0.60126 (13)	0.01062 (11)	0.75	0.0084 (2)	0.0130 (3)	0.0104 (3)	−0.0008 (2)	0.0003 (2)	−0.0047 (2)
MgM1	0.375683 (15)	0.65419 (3)	0.86783 (6)	0.00717 (9)	0.9243(18)	0.00739 (13)	0.00746 (14)	0.00665 (14)	0.00010 (8)	−0.00074 (8)	0.00029 (8)
FeM1	0.375683 (15)	0.65419 (3)	0.86783 (6)	0.00717 (9)	0.0757(18)	0.00739 (13)	0.00746 (14)	0.00665 (14)	0.00010 (8)	−0.00074 (8)	0.00029 (8)
MgM2	0.378283 (13)	0.48265 (3)	0.36156 (5)	0.01002 (8)	0.7440(19)	0.01013 (11)	0.01210 (12)	0.00784 (11)	−0.00187 (7)	−0.00191 (7)	−0.00101 (7)
FeM2	0.378283 (13)	0.48265 (3)	0.36156 (5)	0.01002 (8)	0.2560(19)	0.01013 (11)	0.01210 (12)	0.00784 (11)	−0.00187 (7)	−0.00191 (7)	−0.00101 (7)

COOLING HISTORY AND EMPLACEMENT OF A PYROXENITIC LAVA AS PROXY FOR UNDERSTANDING MARTIAN LAVA FLOWS

Mara Murri[1], Maria C. Domeneghetti[1], Anna M. Fioretti[2], Fabrizio Nestola[3], Francesco Vetere[4,5], Diego Perugini[4], Alessandro Pisello[4], Manuele Faccenda[3], Matteo Alvaro[1*]

[1]*Department of Earth and Environmental Sciences, University of Pavia, Via A. Ferrata, 1 27100 Pavia, Italy*
[2]*Istituto di Geoscienze e Georisorse CNR, Padova, Italy*
[3]*Department of Geosciences, University of Padova, Via G. Gradenigo 6, 35131 Padova, Italy*
[4]*Department of Physics and Geology, University of Perugia, piazza Università 1, 06123 Perugia, Italy.*
[5]*Institute of Mineralogy, Leibniz Universität Hannover, Callinstr. 3, D-30167, Hannover, Germany.*

Table S1. Unit cell parameters for clinopyroxenes TSC 3.9, 3.12_1, 3.12_2, 3.22, 3.31_1 and 3.31_2 and information on data collection and structural refinement.

	CPX 3.9	CPX 3.12_1	CPX 3.12_2	CPX 3.22_1	CPX 3.31_1	CPX 3.31_2
a (Å)	9.74318 (17)	9.74290 (14)	9.7434 (2)	9.74870 (18)	9.74221 (12)	9.74248 (13)
b (Å)	8.92390 (13)	8.92082 (11)	8.92133 (19)	8.92808 (13)	8.92235 (10)	8.92335 (10)
c (Å)	5.25403 (11)	5.25360 (8)	5.25381 (14)	5.2566 (1)	5.25425 (7)	5.25463 (8)
β (°)	106.233 (2)	106.2359 (16)	106.174 (3)	106.2034 (19)	106.3216 (13)	106.2884 (15)
V (Å^3)	438.61 (1)	438.40 (1)	438.61 (2)	439.35 (1)	438.31 (1)	438.48 (1)
θ_{max} - θ_{min} (°)	57-3.2	56.6-3.2	56.6-3.2	56.6-3.2	56.6-3.2	56.6-3.2
$refl.no$	27691	21124	31302	31261	29141	29352
I_{ind}	3011	2977	2988	2990	2990	2981
R_{int}	0.031	0.022	0.077	0.041	0.026	0.027
R_{all}	0.018	0.016	0.155	0.021	0.018	0.015
R_w	0.041	0.039	0.423	0.05	0.043	0.039
S	1.04	1.13	2.08	1.06	1.18	1.1
m.a.n. M1	13.51 (1)	13.35 (1)	13.38 (8)	14.02 (1)	13.68 (1)	13.58 (1)
m.a.n. (M2+M21)	20 (3)	19.89 (3)	20.05 (8)	20.16 (3)	20.05 (4)	20.07 (3)
m.a.n. (M1+M2+M21)	33.51 (3)	33.24 (4)	33.43 (11)	34.18 (3)	33.72 (4)	33.65 (4)

Standard deviations are given in parentheses. *refl.no.* is the number of unique reflections; I_{ind} is the number of independent reflections used for structure refinement; $R_{int} = \Sigma \left| F_o^2 - F_o^2 \text{(mean)} \right| / \Sigma [F_o^2]$ where F_o and F_c are the observed and calculated structure factors; $R_{all} = \Sigma \left| \left| F_o^2 \right| - F_c^2 \right| / \Sigma [F_o^2]$; $R_w = \{ \Sigma [w(F_o^2 - F_c^2)^2] / \Sigma [w(F_o^2)^2] \}^{1/2}$; $S = [\Sigma [w(F_o^2 - F_c^2)^2]/(n-p)]^{0.5}$, where n is the number of reflections and p is the total number of parameters refined. [a] m.a.n. is the mean atomic number (in electrons per formula unit) before introducing the chemical constraints. Crystal system monoclinic $C2/c$; radiation type Mo$K\alpha$.

Table S2. Site population for clinopyroxenes TSC 3.9, 3.12_1, 3.12_2, 3.22, 3.31_1 and 3.31_2 obtained from structure refinements using chemical constraints.

		CPX 3.9		CPX 3.12_1		CPX 3.12_2		CPX 3.22		CPX 3.31_1		CPX 3.31_2	
Site													
T	Si	1.948		1.952		1.952		1.971		1.967		1.971	
	Al	0.052		0.048		0.048		0.029		0.033		0.029	
M1	Mg	0.885	(1)	0.897	(1)	0.895	(3)	0.832	(3)	0.848	(3)	0.855	(3)
	Fe	0.050	(2)	0.042	(2)	0.044	(4)	0.130	(3)	0.105	(5)	0.102	(5)
	Fe3+	0.032		0.029		0.029		0.004		0.005		0.003	
	Al	0.0000		0.000		0.000		0.018		0.027		0.026	
	Cr	0.025		0.025		0.024		0.004		0.002		0.002	
	Ti	0.007		0.006		0.006		0.008		0.010		0.010	
	Mn	0.002		0.001		0.002		0.003		0.003		0.003	
M2	Mg	0.061	(2)	0.067	(2)	0.061	(7)	0.046	(2)	0.059	(4)	0.052	(3)
	Fe	0.092	(1)	0.088	(1)	0.097	(7)	0.104	(2)	0.117	(2)	0.113	(2)
	Ca	0.823		0.825		0.822		0.833		0.799		0.809	
	Mn	0.006		0.003		0.004		0.003		0.004		0.004	
	Na	0.018		0.017		0.017		0.014		0.021		0.021	
	XFe	0.15		0.14		0.15		0.21		0.20		0.19	
	Fs	9		8		9		12		12		12	
	k_D	0.038	(2)	0.036	(2)	0.031	(4)	0.069	(4)	0.062	(5)	0.055	(4)
T_c(°C)		645	(10)	637	(12)	608	(25)	791	(15)	764	(20)	734	(19)

Note: $k_D = [(Fe^{2+}{}_{M1})(Mg_{M2})/(Fe^{2+}{}_{M2})(Mg_{M1})]$. The site occupancy values represent atoms per six oxygen atoms. Chemical constraints introduced are based on the chemical analysis (see Table S3).

Table S3. Electron microprobe analysis for clinopyroxenes TSC 3.9, 3.12_1, 3.12_2, 3.22, 3.31_1 and 3.31_2 and formula in atoms per formula unit (apfu) based on six oxygen atoms.

	CPX 3.9		CPX 3.12_1		CPX 3.12_2		CPX 3.22		CPX 3.31_1		CPX 3.31_2	
	(averaged 10 spots)		(averaged 13 spots)		(averaged 16 spots)		(averaged 10 spots)		(averaged 25 spots)		(averaged 38 spots)	
wt%												
SiO2	53.59	(20)	53.72	(13)	53.76	(27)	54.30	(31)	53.74	(55)	53.74	(55)
TiO2	0.25	(2)	0.21	(2)	0.22	(3)	0.30	(3)	0.37	(6)	0.37	(6)
Al2O3	1.18	(7)	1.07	(8)	1.10	(14)	1.27	(8)	1.61	(29)	1.61	(29)
Cr2O3	0.89	(11)	0.86	(7)	0.84	(9)	0.15	(4)	0.08	(5)	0.08	(5)
Fe2O3	0.00	(0)	0.00	(0)	0.00	(0)	0.00	(0)	0.00	(0)	0.00	(0)
FeO	5.31	(20)	4.95	(29)	5.31	(60)	6.85	(28)	8.19	(80)	8.19	(80)
MnO	0.16	(7)	0.13	(2)	0.17	(11)	0.16	(4)	0.19	(3)	0.19	(3)
MgO	18.17	(21)	18.24	(21)	17.98	(47)	16.95	(28)	16.59	(61)	16.59	(61)
CaO	20.86	(16)	21.16	(16)	21.15	(11)	20.98	(19)	20.15	(25)	20.15	(25)
Na2O	0.26	(2)	0.24	(2)	0.24	(2)	0.20	(2)	0.24	(6)	0.24	(6)
K2O	0.00	(0)	0.00	(0)	0.00	(0)	0.00	(0)	0.00	(0)	0.00	(0)
Totale	100.68	(32)	100.58	(18)	100.77	(26)	101.17	(36)	101.18	(53)	101.18	(53)
FeO	4.33	(21)	4.07	(23)	4.39	(65)	6.85	(30)	7.89	(65)	7.89	(65)
Fe2O3	1.09	(11)	0.97	(17)	1.02	(17)	0.00	(18)	0.33	(46)	0.33	(46)
Totale	100.79	(31)	100.68	(19)	100.88	(25)	101.17	(36)	101.21	(54)	101.21	(54)
a.p.f.u												
Si	1.944	(5)	1.949	(3)	1.949	(6)	1.971	(5)	1.958	(13)	1.958	(13)
Ti	0.007	(1)	0.006	(1)	0.006	(1)	0.008	(1)	0.010	(2)	0.010	(2)
Al	0.050	(3)	0.046	(4)	0.047	(6)	0.054	(4)	0.069	(13)	0.069	(13)
Cr	0.026	(3)	0.025	(2)	0.024	(3)	0.004	(1)	0.002	(1)	0.002	(1)
Fe3+	0.030	(3)	0.027	(5)	0.028	(5)	0.000	(5)	0.009	(13)	0.009	(13)
Fe2+	0.131	(6)	0.124	(7)	0.133	(20)	0.208	(9)	0.240	(21)	0.240	(21)
Mn	0.005	(2)	0.004	(1)	0.005	(3)	0.005	(1)	0.006	(1)	0.006	(1)
Mg	0.983	(10)	0.987	(11)	0.972	(22)	0.917	(13)	0.901	(30)	0.901	(30)
Ca	0.811	(7)	0.822	(6)	0.822	(4)	0.816	(7)	0.787	(9)	0.787	(9)
Na	0.019	(1)	0.017	(2)	0.017	(1)	0.014	(2)	0.017	(4)	0.017	(4)
K	0.000	(0)	0.000	(0)	0.000	(0)	0.000	(0)	0.000	(0)	0.000	(0)
Totale	4.005	(3)	4.006	(3)	4.004	(2)	3.998	(3)	4.000	(2)	4.000	(2)
Al IV	0.050	(3)	0.046	(3)	0.047	(6)	0.029	(5)	0.042	(13)	0.042	(13)
Al VI	0.000	(1)	0.000	(1)	0.000	(0)	0.025	(5)	0.027	(6)	0.027	(6)
m.a.n*	33.29	(15)	33.21	(11)	33.32	(32)	33.63	(15)	34.00	(38)	34.00	(38)

m.a.n.*: calculated total mean atomic number for $M1$, $M2$ and $M21$ sites, in electrons per formula unit. Standard deviations are given in parentheses.

	ρ (g/cm^3)	cp (J/Kg/K)	Th.cond (W m^{-1} K^{-1})
Peridotite	3.19	1000	3
Pyroxenite	3.2	750	4.3
Gabbro-Pyroxenite	2.9	500	2.5

Table S4. Physical properties of the three lithologies (density, heat capacity and thermal conductivity).

VISCOSITY OF PYROXENITE MELT AND ITS EVOLUTION
DURING COOLING

F. Vetere[1,2], M. Murri[3], M. Alvaro[3], M. C. Domeneghetti[3], S. Rossi[1], A. Pisello[1],
D. Perugini[1], and F. Holtz[2]

[1]*Department of Physics and Geology, University of Perugia, Perugia, Italy*
[2]*Institute of Mineralogy, Leibniz Universität Hannover, Hannover, Germany*
[3]*Department of Earth and Environmental Sciences, University of Pavia, Pavia, Italy*

Introduction

The rheological behavior of melts undergo crystallization is of paramount importance to understand magmatic environments. In fact, magmatic and volcanic systems need to be studied under non-equilibrium conditions and, as consequence, scientists need to focus on physical magma properties and their evolutions from a dynamic point of view. Melt viscosity measurements were performed at different shear rates (from 13 to 20 s^{-1}) allowing us to prove the Newtonian behavior of such a melt under the investigated shear rates. Also, the subliquidus temperature viscosity measurements were performed at shear rate of 0.1 and 1 s^{-1} in order to investigate 1) the behavior of such system during crystallization processes at constant shear rate and 2) growth rate of solid phases. This work is one of the few studying magma evolution under variable applied cooling and shear rates and it provides new insights on the viscosity evolution via experimental approach. To support this approach, here we show details on the viscosity and relative velocities of magma flows as they are subjected to Earth or Mars gravity as well as to different shear stress and variable terrain slopes.

Figure S1 reports Raman spectra on the Theo's Glass, proving the amorphous state of the starting material. The shape of the spectrum is typically that of a silicate glass presenting: a low wavenumber region (LW ~250–650 cm^{-1}), the mid-wavenumber region (MW ~650–850 cm^{-1}) and a high-wavenumber region (HW ~850–1250 cm^{-1}) [Neuville et al. 2014]. The fact that LW region is way weaker than HW region, is typical of a mafic composition. Within HW, it is known that peaks at ~980 cm^{-1}, 1050 and 1150 cm^{-1} are relatable to Q3 species, Q4i species and Q4ii species, respectively. By observing the figure, it is clear how the peak at ~980 cm^{-1} is dominant, while peaks at 1050 and 1150 cm^{-1} are just shoulders or hardly visible. This means that the glass is strongly non-polymerized and Q3 species are dominant [Di Genova et al. 2015].

Figure S2 and S3 report Continuous velocity variation for 1, 5 and 10 m thick lavas flowing on 0.1, 1 and 10 ° terrain slopes on Mars and on Earth, respectively.

Tables S1 to S2 report Electron Microprobe analyses on the composition of solid phases (112 Clinopyroxenes and 18 Fe-Ti Oxides). Table S3 reports experimental apparent viscosity data obtained by using the concentric cylinder method. Tables S4-Earth and S4-Mars report details on the calculated lava velocities applying iteratively equations 4, 5 and 6 as explained into the main text. Finally, Table S5 shows calculated max distance for a lava on Mars surface as the terrain slope varies from 0.1 to 5 °by using viscosity data reported in Figure 7 and Table 2 and S3.
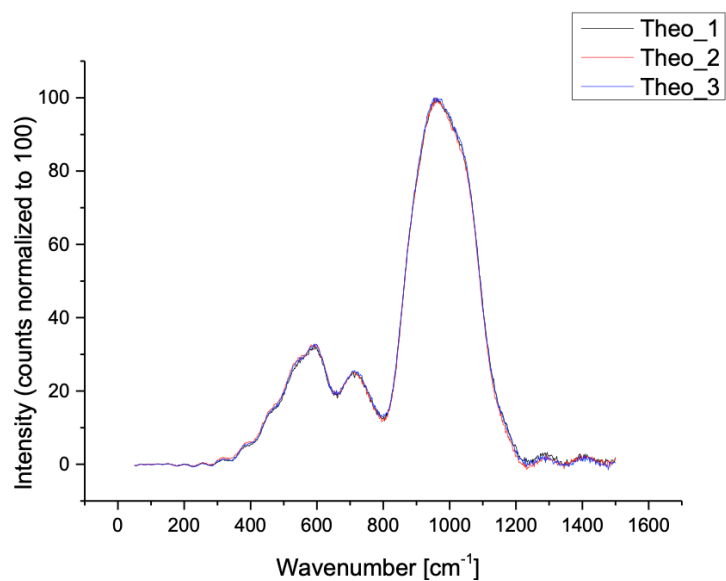
Figure S1. Superimposed spectra of three Raman analyses performed at different points on a fragment of one Theo's glass. Acquisition was performed by micro-Raman spectrometer (HORIBA; XploRa-Raman-System). Green argon ion laser (532 nm, ca. 2.5 mW), was used through the 100× objective to a ~1 μm spot, over a wavenumber range from 150 to 1500 cm^{-1}. Other parameters used for the acquisition: grating 1800T, confocal hole 300 μm, slit 200 μm exposure time 60 seconds. Silicon standard was used for calibration. Acquired spectra have been corrected for the wavelength of excitation source after Long (1977) approaches. Finally, a background subtraction after Di Genova et al. (2015) was performed by subtracting a baseline whose nodes are anchored in two areas where spectral response is not expected: from 50 to ~250 and from ~1250 to 1500 cm^{-1}.
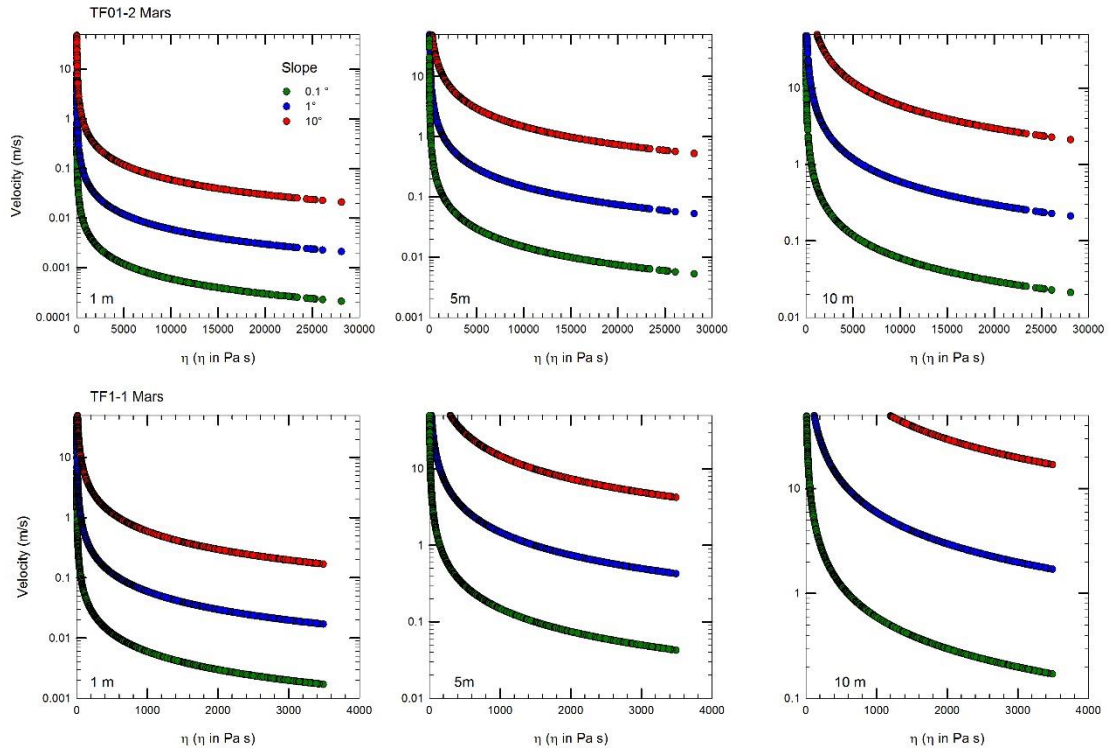
Figure S2. Continuous velocity variation for 1, 5 and 10 m thick lavas flowing on 0.1, 1 and 10 °
terrain slopes on Mars. Velocities are determined by using equation 7 and viscosity data presented in
Figures 6 and 7, Table 2 and S3.
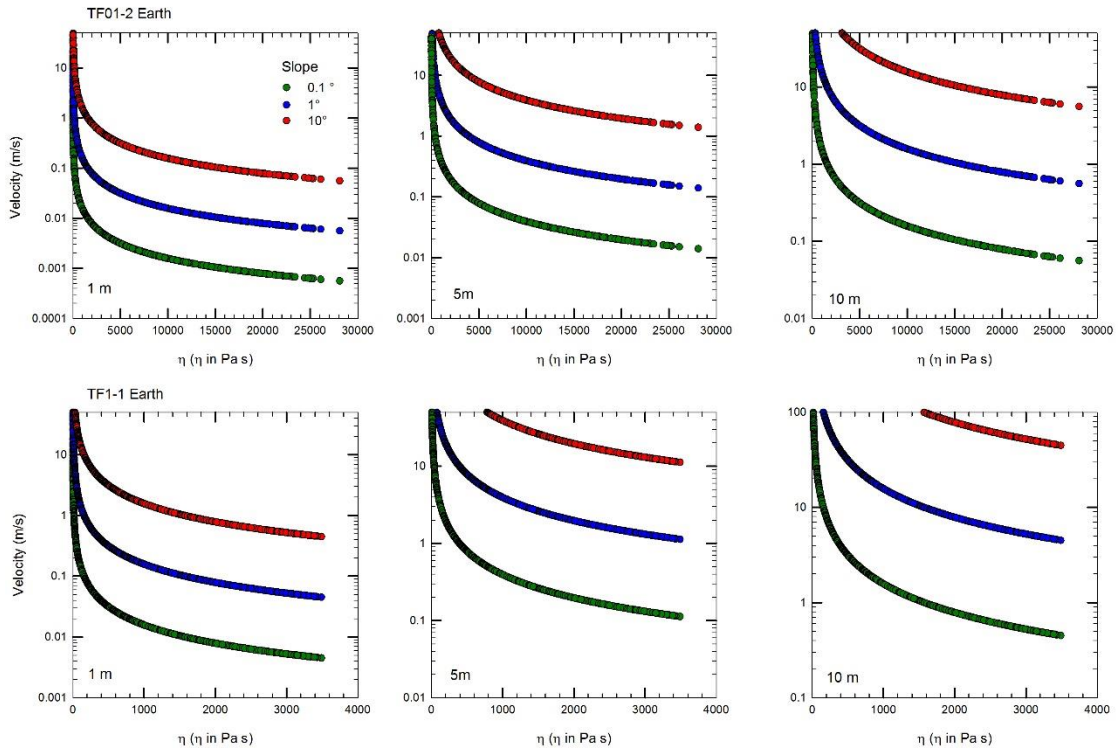
Figure S3. Continuous velocity variation for 1, 5 and 10 m thick lavas flowing on 0.1, 1 and 10 ° terrain slopes on Earth. Velocities are determined by using equation 7 and viscosity data presented in Figures 6 and 7, Table 2 and S3.

Table S1. Chemical analyses and relative Wo, En and Fs components for pyroxenes. Details on measurement conditions are provided in the main text.

TF01-1

	Cpx										core	rim			core	rim	
SiO$_2$	51.94	51.68	47.69	52.00	52.31	54.75	51.96	49.21	51.84	51.49	50.02	51.85	51.13	51.10	50.61	51.98	48.15
TiO$_2$	0.26	0.28	0.57	0.21	0.25	0.17	0.27	0.45	0.21	0.23	0.39	0.25	0.32	0.25	0.37	0.23	0.34
Al$_2$O$_3$	1.94	2.28	3.84	2.06	1.92	1.35	1.92	2.76	2.09	2.10	2.53	1.80	2.59	2.22	2.62	2.17	3.18
Cr$_2$O$_3$	0.08	0.00	0.03	0.05	0.10	0.00	0.10	0.00	0.00	0.03	0.09	0.01	0.00	0.05	0.05	0.02	0.01
FeO	6.05	6.89	10.34	5.78	5.95	4.51	6.25	8.01	6.61	6.45	7.42	6.07	7.17	6.63	7.34	6.47	9.75
MnO	0.00	0.00	0.00	0.00	0.00	0.00	0.00	0.00	0.00	0.00	0.00	0.00	0.00	0.00	0.00	0.00	0.00
MgO	20.67	19.61	15.93	19.56	20.92	24.72	20.23	18.05	20.17	18.98	18.69	20.88	19.00	19.56	19.30	20.71	16.55
CaO	18.48	19.26	20.46	20.03	17.98	14.00	19.10	18.20	18.17	20.19	18.72	18.43	19.43	18.78	19.45	17.93	20.63
Na$_2$O	0.24	0.27	0.45	0.21	0.30	0.22	0.30	0.34	0.26	0.38	0.26	0.32	0.48	0.36	0.28	0.26	0.39
K$_2$O	0.01	0.00	0.00	0.01	0.02	0.01	0.00	0.01	0.00	0.01	0.02	0.01	0.00	0.01	0.01	0.01	0.01
Wo	35.60	37.14	40.52	38.74	34.79	26.97	36.69	36.79	35.39	39.16	37.12	35.34	37.82	36.75	37.45	34.66	40.39
En	55.43	52.64	43.89	52.65	56.34	66.27	54.07	50.77	54.69	51.23	51.57	55.72	51.48	53.27	51.72	55.71	45.09
Fs	8.97	10.22	15.59	8.61	8.87	6.75	9.24	12.44	9.92	9.62	11.31	8.94	10.70	9.98	10.83	9.64	14.53

													core	rim			
SiO$_2$	50.69	51.47	50.89	51.76	48.19	51.62	51.16	52.28	52.58	52.39	52.29	51.83	50.10	51.72	51.13	50.85	49.54
TiO$_2$	0.31	0.29	0.27	0.21	0.82	0.28	0.27	0.23	0.17	0.19	0.18	0.24	0.29	0.26	0.24	0.30	0.29
Al$_2$O$_3$	2.34	2.64	2.52	2.19	4.79	2.10	2.21	1.81	1.55	1.49	1.70	2.07	2.63	2.16	2.27	2.51	2.95
Cr$_2$O$_3$	0.01	0.06	0.09	0.04	0.00	0.03	0.10	0.02	0.02	0.06	0.02	0.05	0.07	0.07	0.00	0.01	0.06
FeO	7.32	6.70	6.01	5.95	10.32	6.45	6.77	5.77	5.35	5.20	5.71	6.50	7.73	5.55	6.55	6.47	8.41
MnO	0.00	0.00	0.00	0.00	0.00	0.00	0.00	0.00	0.00	0.00	0.00	0.00	0.00	0.00	0.00	0.00	0.00
MgO	18.42	19.59	19.39	19.91	14.42	20.27	18.52	20.59	20.64	19.04	20.50	20.58	18.29	19.72	19.05	18.76	17.73
CaO	20.24	19.03	19.17	20.09	20.10	18.45	20.69	18.50	18.47	19.60	18.92	18.14	19.90	20.05	20.00	19.87	19.46
Na$_2$O	0.30	0.29	0.30	0.35	0.54	0.42	0.28	0.35	0.26	0.29	0.29	0.31	0.30	0.25	0.33	0.28	0.34
K$_2$O	0.00	0.01	0.00	0.01	0.03	0.00	0.00	0.01	0.00	0.00	0.01	0.02	0.00	0.00	0.00	0.00	0.00
Wo	39.31	36.99	37.75	38.36	41.80	35.75	40.05	35.85	35.98	39.10	36.49	35.04	38.81	38.74	38.80	39.01	38.48
En	49.78	52.99	53.15	52.91	41.71	54.64	49.89	55.53	55.96	52.86	55.02	55.31	49.63	53.02	51.43	51.23	48.77
Fs	10.91	10.02	9.11	8.72	16.49	9.61	10.06	8.62	8.05	8.04	8.49	9.65	11.56	8.25	9.76	9.76	12.74

TF1-1

	dark	bright															
SiO$_2$	52.62	50.18	50.30	50.33	51.62	52.66	52.40	52.54	53.81	52.03	50.90	51.17	51.89	48.56	48.67	48.48	48.45
TiO$_2$	0.19	0.31	0.28	0.26	0.28	0.16	0.14	0.18	0.17	0.25	0.27	0.29	0.24	0.44	0.40	0.44	0.40
Al$_2$O$_3$	1.45	2.59	2.44	2.31	2.02	1.44	1.23	1.71	0.98	1.94	2.07	2.20	1.79	3.17	3.00	3.10	3.08
Cr$_2$O$_3$	0.00	0.01	0.00	0.04	0.05	0.00	0.02	0.08	0.00	0.07	0.00	0.06	0.00	0.00	0.07	0.00	0.00
FeO	5.52	7.79	7.46	7.15	5.88	4.21	4.21	4.67	3.29	5.24	6.39	5.86	5.77	9.22	8.97	8.77	9.19
MnO	0.00	0.00	0.00	0.00	0.00	0.00	0.00	0.00	0.00	0.00	0.00	0.00	0.00	0.00	0.00	0.00	0.00
MgO	21.92	18.05	18.44	18.67	19.63	20.48	20.00	20.88	22.68	19.97	19.07	19.55	20.98	16.90	17.16	16.67	17.02
CaO	17.13	19.64	19.66	19.88	19.71	19.52	19.84	18.69	17.87	20.16	19.95	19.93	17.48	20.10	19.84	19.98	20.95
Na$_2$O	0.26	0.31	0.27	0.35	0.29	0.23	0.24	0.26	0.18	0.28	0.26	0.22	0.30	0.38	0.37	0.33	0.40
K$_2$O	0.03	0.02	0.01	0.01	0.01	0.00	0.01	0.00	0.01	0.00	0.00	0.00	0.01	0.01	0.01	0.02	0.01
Wo	33.02	38.70	38.52	38.72	38.23	38.07	38.96	36.40	34.38	38.78	38.81	38.59	34.19	39.68	39.23	40.04	40.58
En	58.78	49.51	50.26	50.61	52.99	55.58	54.64	56.58	60.72	53.46	51.63	52.68	57.11	46.42	47.22	46.51	45.87
Fs	8.20	11.78	11.22	10.67	8.78	6.35	6.40	7.02	4.90	7.75	9.55	8.73	8.70	13.90	13.55	13.45	13.54

SiO$_2$	52.15	53.79	53.52	50.50	49.63	50.98	53.40	52.31	51.98	49.88	49.56	51.63	50.52	50.59	52.86	51.27	50.63
TiO$_2$	0.21	0.14	0.16	0.39	0.23	0.19	0.13	0.21	0.21	0.40	0.39	0.21	0.23	0.27	0.14	0.25	0.23
Al$_2$O$_3$	1.76	1.01	0.96	2.34	3.16	2.11	1.48	1.32	1.55	2.60	2.55	2.11	1.76	2.05	1.46	1.91	1.93
Cr$_2$O$_3$	0.06	0.01	0.00	0.06	0.00	0.01	0.07	0.03	0.00	0.09	0.00	0.02					
FeO	4.89	3.86	3.88	6.80	7.91	6.35	5.39	4.47	4.80	7.54	7.66	6.02	5.18	6.01	5.08	5.56	5.67
MnO	0.00	0.00	0.00	0.00	0.00	0.00	0.00	0.00	0.00	0.00	0.00	0.00	0.00	0.00	0.00	0.00	0.00
MgO	20.00	23.99	23.44	19.75	17.09	18.81	23.29	21.30	20.50	17.40	18.03	18.63	20.67	19.56	23.09	19.91	19.09
CaO	19.57	15.74	16.42	18.83	19.64	19.96	15.78	17.19	19.63	19.93	19.47	19.54	18.22	19.03	16.02	19.90	20.61
Na$_2$O	0.28	0.24	0.18	0.32	0.37	0.33	0.24	0.34	0.30	0.32	0.30	0.25	0.29	0.25	0.26	0.30	0.23
K$_2$O	0.00	0.01	0.00	0.01	0.02	0.01	0.02	0.08	0.00	0.01	0.00	0.00	0.00	0.00	0.00	0.02	0.01
Wo	38.24	30.20	31.56	36.55	39.67	39.13	30.14	34.18	37.86	39.91	38.60	39.00	35.75	37.42	30.77	38.36	40.00
En	54.38	64.06	62.68	53.33	48.04	51.30	61.91	58.94	55.02	48.48	49.74	51.72	56.44	53.50	61.70	53.41	51.55
Fs	7.38	5.73	5.76	10.12	12.29	9.57	7.95	6.88	7.12	11.61	11.66	9.29	7.81	9.08	7.53	8.23	8.45

SiO_2	53.54	50.75	50.31	49.92	50.01	54.68	51.19
TiO_2	0.16	0.25	0.22	0.25	0.30	0.12	0.30
Al_2O_3	1.08	1.81	2.05	1.88	2.28	0.78	2.00
Cr_2O_3							
FeO	3.67	5.04	5.80	5.69	6.09	3.39	5.75
MnO	0.00	0.00	0.00	0.00	0.00	0.00	0.00
MgO	23.40	19.69	19.49	19.56	18.92	25.95	19.95
CaO	17.06	20.20	19.87	19.75	19.91	14.70	19.39
Na_2O	0.18	0.28	0.30	0.41	0.26	0.13	0.27
K_2O	0.02	0.01	0.00	0.30	0.00	0.00	0.00
Wo	32.52	39.25	38.64	38.50	39.10	27.50	37.60
En	62.08	53.23	52.72	53.04	51.72	67.59	53.84
Fs	5.40	7.52	8.64	8.46	9.18	4.90	8.56

PhasePlot simulation

SiO_2	52.33
TiO_2	0.21
Al_2O_3	2.69
Cr_2O_3	0.00
FeO	7.28
MnO	0.00
MgO	18.61
CaO	18.73
Na_2O	0.15
K_2O	0.00
Wo	37.25
En	51.51
Fs	11.24

Table S2. Chemical analyses of Fe-Mg-Ti oxides. Details on measurement conditions are provided into the main text.

TF01-1

SiO_2	2.87	0.17	0.10	0.48	0.13	0.13	0.11	0.15
TiO_2	0.91	0.87	0.85	0.84	0.85	0.82	0.84	0.86
Al_2O_3	4.41	3.50	3.47	3.60	3.70	3.80	3.88	3.65
FeO	70.50	75.47	75.66	74.59	74.09	74.08	73.53	74.16
MnO	0.00	0.00	0.00	0.05	0.00	0.01	0.08	0.04
MgO	11.78	12.56	12.46	13.07	13.60	13.70	13.46	12.70
CaO	0.71	0.17	0.20	0.42	0.15	0.12	0.26	0.13

TF01-2

SiO_2	0.11	0.12	0.13	0.12	0.71
TiO_2	0.58	0.54	0.54	0.66	0.53
Al_2O_3	2.99	3.24	3.16	3.04	3.47
FeO	75.04	75.04	73.43	74.36	73.59
MnO	0.05	0.04	0.07	0.02	0.05
MgO	12.98	13.56	14.13	12.59	13.27
CaO	0.16	0.19	0.23	0.23	0.53

TF1-1

SiO_2	3.40	0.18	0.19	1.00	0.09
TiO_2	0.66	0.63	0.60	0.67	0.60
Al_2O_3	3.72	3.56	3.44	3.54	3.50
FeO	71.02	72.64	71.87	71.36	71.91
MnO	0.00	0.00	0.06	0.05	0.07

Table S3. Apparent viscosity experimental data as in Figure 7. Temperature interval goes from 1510 K to quenching temperature. See the main text for details.

TF01-2						TF1-1					
Time [s]	Viscosity [Pa-s]	Shear Rate [1/s]	Shear Stress [Pa]	Torque [mNm]	Temperatrue K	Time [s]	Viscosity [Pa-s]	Shear Rate [1/s]	Shear Stress [Pa]	Torque [mNm]	Temperatrue K
13000	162	0.1	16.20	0.09	1501	9570	38	1.0	38.40	0.20	1510
13010	163	0.1	16.30	0.09	1501	9580	41	1.0	40.80	0.22	1510
13020	165	0.1	16.50	0.09	1501	9590	40	1.0	39.70	0.21	1510
13030	168	0.1	16.80	0.09	1501	9600	39	1.0	38.70	0.21	1510
13040	182	0.1	18.20	0.10	1501	9610	40	1.0	40.40	0.22	1510
13050	191	0.1	19.10	0.10	1501	9620	42	1.0	41.70	0.22	1510
13060	191	0.1	19.10	0.10	1501	9630	41	1.0	40.80	0.22	1510
13070	194	0.1	19.37	0.10	1501	9640	42	1.0	42.20	0.22	1510
13080	195	0.1	19.50	0.10	1501	9650	43	1.0	42.90	0.23	1510
13090	200	0.1	20.04	0.11	1501	9660	42	1.0	42.20	0.22	1510
13100	210	0.1	21.00	0.11	1501	9670	44	1.0	44.30	0.24	1510
13110	213	0.1	21.33	0.11	1501	9680	46	1.0	46.40	0.25	1510
13120	229	0.1	22.86	0.12	1501	9690	45	1.0	44.60	0.24	1510
13130	231	0.1	23.14	0.09	1501	9700	45	1.0	44.50	0.24	1510
13140	231	0.1	23.15	0.10	1501	9710	47	1.0	47.40	0.25	1510
13150	244	0.1	24.39	0.13	1501	9720	47	1.0	47.40	0.25	1510
13160	245	0.1	24.55	0.13	1501	9730	47	1.0	46.80	0.25	1510
13170	254	0.1	25.40	0.14	1500	9740	48	1.0	48.30	0.26	1510
13180	259	0.1	25.88	0.14	1500	9750	51	1.0	51.20	0.27	1510
13190	262	0.1	26.20	0.14	1500	9760	50	1.0	50.10	0.27	1510
13200	267	0.1	26.70	0.14	1500	9770	49	1.0	49.30	0.26	1510
13210	267	0.1	26.70	0.14	1500	9780	53	1.0	53.10	0.28	1510
13220	274	0.1	27.40	0.15	1500	9790	53	1.0	52.70	0.28	1510
13230	277	0.1	27.70	0.15	1500	9800	51	1.0	50.80	0.27	1510
13240	281	0.1	28.10	0.15	1500	9810	52	1.0	52.40	0.28	1510
13250	284	0.1	28.38	0.15	1500	9820	55	1.0	54.80	0.29	1510
13260	284	0.1	28.40	0.15	1500	9830	54	1.0	53.60	0.29	1510
13270	291	0.1	29.10	0.16	1500	9840	55	1.0	55.20	0.29	1510
13280	293	0.1	29.30	0.16	1500	9850	53	1.0	53.30	0.28	1510
13290	304	0.1	30.40	0.16	1500	9860	53	1.0	53.30	0.28	1510
13300	308	0.1	30.76	0.16	1500	9870	57	1.0	57.00	0.30	1510
13310	314	0.1	31.40	0.17	1500	9880	59	1.0	59.40	0.32	1510
13320	316	0.1	31.60	0.17	1500	9890	57	1.0	56.80	0.30	1510
13330	318	0.1	31.80	0.17	1500	9900	59	1.0	58.90	0.31	1510
13340	322	0.1	32.20	0.17	1500	9910	60	1.0	60.00	0.32	1510
13350	333	0.1	33.30	0.18	1500	9920	62	1.0	62.20	0.33	1510
13360	339	0.1	33.90	0.18	1500	9930	60	1.0	60.40	0.32	1509
13370	350	0.1	35.00	0.19	1500	9940	63	1.0	62.70	0.33	1509
13380	360	0.1	36.00	0.19	1500	9950	61	1.0	61.30	0.33	1509
13390	361	0.1	36.10	0.19	1500	9960	57	1.0	56.50	0.30	1509
13400	366	0.1	36.60	0.20	1500	9970	62	1.0	61.50	0.33	1509
13410	374	0.1	37.40	0.20	1500	9980	65	1.0	64.80	0.34	1509
13420	376	0.1	37.60	0.20	1500	9990	62	1.0	62.40	0.33	1509
13430	384	0.1	38.40	0.20	1500	10000	63	1.0	63.30	0.34	1509
13440	394	0.1	39.40	0.21	1500	10010	66	1.0	65.90	0.35	1509
13450	395	0.1	39.50	0.21	1500	10020	67	1.0	67.20	0.36	1509
13460	398	0.1	39.80	0.21	1500	10030	70	1.0	70.30	0.37	1509
13470	409	0.1	40.90	0.22	1500	10040	68	1.0	68.40	0.36	1509
13480	423	0.1	42.30	0.23	1500	10050	72	1.0	71.50	0.38	1509
13490	418	0.1	41.80	0.22	1500	10060	68	1.0	68.40	0.36	1509
13500	437	0.1	43.70	0.23	1500	10070	71	1.0	70.70	0.38	1509
13500	471	0.1	47.10	0.25	1500	10080	73	1.0	72.50	0.39	1509
13510	484	0.1	48.40	0.26	1500	10090	71	1.0	70.70	0.38	1509
13520	526	0.1	52.60	0.28	1500	10100	75	1.0	75.00	0.40	1509
13530	532	0.1	53.20	0.28	1499	10110	74	1.0	74.00	0.39	1509
13540	484	0.1	48.35	0.26	1499	10120	75	1.0	75.30	0.40	1509
13550	525	0.1	52.50	0.28	1499	10130	75	1.0	75.30	0.40	1509
13560	511	0.1	51.10	0.27	1499	10140	77	1.0	76.60	0.41	1509
13570	524	0.1	52.40	0.28	1499	10150	76	1.0	75.70	0.40	1509
13580	554	0.1	55.40	0.30	1499	10160	78	1.0	78.00	0.42	1509
13590	536	0.1	53.60	0.29	1499	10170	82	1.0	81.70	0.43	1509
13600	541	0.1	54.10	0.29	1499	10180	84	1.0	83.60	0.44	1509
13610	493	0.1	49.30	0.26	1499	10190	79	1.0	79.10	0.42	1509
13620	551	0.1	55.04	0.29	1499	10200	82	1.0	81.80	0.44	1509
13630	623	0.1	62.24	0.33	1499	10210	85	1.0	85.30	0.45	1509

13640	642	0.1	64.20	0.34	1499	10220	88	1.0	87.60	0.47	1509
13650	680	0.1	67.93	0.36	1499	10230	87	1.0	87.00	0.46	1509
13660	670	0.1	67.00	0.36	1499	10240	91	1.0	90.80	0.48	1509
13670	679	0.1	67.90	0.36	1499	10250	91	1.0	90.70	0.48	1509
13680	711	0.1	71.10	0.38	1499	10260	87	1.0	87.20	0.46	1509
13690	681	0.1	68.10	0.36	1499	10270	92	1.0	91.70	0.49	1509
13700	611	0.1	61.10	0.33	1499	10280	95	1.0	94.80	0.50	1509
13710	655	0.1	65.50	0.35	1499	10290	93	1.0	92.80	0.49	1508
13720	664	0.1	66.40	0.35	1499	10300	89	1.0	89.40	0.48	1508
13730	637	0.1	63.64	0.34	1499	10310	89	1.0	88.90	0.47	1508
13740	697	0.1	69.70	0.37	1499	10320	92	1.0	91.60	0.49	1508
13750	662	0.1	66.20	0.35	1499	10330	94	1.0	94.00	0.50	1508
13760	665	0.1	66.43	0.35	1499	10340	95	1.0	94.80	0.50	1508
13770	774	0.1	77.25	0.41	1499	10350	96	1.0	96.10	0.51	1508
13780	826	0.1	82.43	0.44	1499	10360	95	1.0	94.70	0.50	1508
13790	785	0.1	78.42	0.42	1499	10370	99	1.0	99.20	0.53	1508
13800	677	0.1	67.70	0.36	1499	10380	99	1.0	99.20	0.53	1508
13810	740	0.1	74.00	0.39	1499	10390	98	1.0	97.90	0.52	1508
13820	837	0.1	83.62	0.44	1499	10400	102	1.0	102	0.54	1508
13830	722	0.1	72.20	0.38	1499	10410	108	1.0	108	0.57	1508
13840	674	0.1	67.40	0.36	1499	10420	105	1.0	105	0.56	1508
13850	634	0.1	63.40	0.34	1499	10430	111	1.0	112	0.59	1508
13860	689	0.1	68.90	0.37	1499	10440	112	1.0	112	0.60	1508
13870	636	0.1	63.54	0.34	1499	10450	116	1.0	116	0.62	1508
13880	704	0.1	70.40	0.37	1499	10460	110	1.0	110	0.59	1508
13890	664	0.1	66.40	0.35	1498	10470	110	1.0	110	0.59	1508
13900	702	0.1	70.20	0.37	1498	10480	110	1.0	110	0.59	1508
13910	791	0.1	79.10	0.42	1498	10490	119	1.0	119	0.64	1508
13920	778	0.1	77.80	0.41	1498	10500	121	1.0	121	0.64	1508
13930	836	0.1	83.60	0.44	1498	10510	120	1.0	120	0.64	1508
13940	876	0.1	87.60	0.47	1498	10520	119	1.0	119	0.63	1508
13950	815	0.1	81.50	0.43	1498	10530	125	1.0	125	0.67	1508
13960	824	0.1	82.24	0.44	1498	10540	124	1.0	124	0.66	1508
13970	925	0.1	92.41	0.49	1498	10550	127	1.0	127	0.67	1508
13980	867	0.1	86.70	0.46	1498	10560	128	1.0	128	0.68	1508
13990	818	0.1	81.80	0.44	1498	10570	128	1.0	128	0.68	1508
14000	775	0.1	77.50	0.41	1498	10580	130	1.0	130	0.69	1508
14010	792	0.1	79.20	0.42	1498	10590	129	1.0	129	0.69	1508
14020	790	0.1	79.00	0.42	1498	10600	134	1.0	134	0.72	1508
14030	792	0.1	79.12	0.42	1498	10610	139	1.0	139	0.74	1508
14040	924	0.1	92.22	0.49	1498	10620	136	1.0	136	0.72	1508
14050	1020	0.1	101.90	0.54	1498	10630	142	1.0	142	0.76	1508
14060	1060	0.1	105.89	0.56	1498	10640	138	1.0	138	0.73	1508
14070	1060	0.1	106.00	0.57	1498	10650	138	1.0	138	0.74	1507
14080	984	0.1	98.30	0.52	1498	10660	140	1.0	140	0.75	1507
14090	974	0.1	97.30	0.52	1498	10670	134	1.0	134	0.71	1507
14100	1060	0.1	106.00	0.56	1498	10680	147	1.0	147	0.78	1507
14110	1000	0.1	100.00	0.53	1498	10690	144	1.0	144	0.76	1507
14120	932	0.1	93.11	0.49	1498	10700	151	1.0	151	0.80	1507
14130	853	0.1	85.21	0.45	1498	10710	147	1.0	147	0.78	1507
14140	848	0.1	84.80	0.45	1498	10720	146	1.0	146	0.78	1507
14150	873	0.1	87.30	0.46	1498	10730	154	1.0	154	0.82	1507
14160	894	0.1	89.22	0.47	1498	10740	154	1.0	154	0.82	1507
14170	941	0.1	94.01	0.50	1498	10750	155	1.0	155	0.83	1507
14180	953	0.1	95.20	0.51	1498	10760	159	1.0	159	0.85	1507
14190	1130	0.1	113.00	0.60	1498	10770	159	1.0	159	0.85	1507
14200	1060	0.1	106.00	0.56	1498	10780	157	1.0	157	0.84	1507
14210	1160	0.1	116.00	0.62	1498	10790	158	1.0	158	0.84	1507
14220	1050	0.1	104.90	0.56	1498	10800	157	1.0	157	0.83	1507
14230	1130	0.1	113.00	0.60	1498	10810	154	1.0	154	0.82	1507
14240	1170	0.1	116.77	0.62	1498	10820	163	1.0	163	0.87	1507
14250	1030	0.1	102.90	0.55	1497	10830	170	1.0	170	0.90	1507
14260	1020	0.1	102.00	0.54	1497	10840	164	1.0	164	0.87	1507
14270	967	0.1	96.70	0.51	1497	10850	167	1.0	167	0.89	1507
14280	974	0.1	97.40	0.52	1497	10860	169	1.0	169	0.90	1507
14290	936	0.1	93.60	0.50	1497	10870	175	1.0	175	0.93	1507
14300	956	0.1	95.50	0.51	1497	10880	162	1.0	162	0.86	1507
14310	922	0.1	92.20	0.49	1497	10890	171	1.0	171	0.91	1507
14320	992	0.1	99.10	0.53	1497	10900	177	1.0	177	0.94	1507

14330	1020	0.1	101.90	0.54	1497	10910	176	1.0	176	0.94	1507
14340	1090	0.1	109.00	0.58	1497	10920	175	1.0	175	0.93	1507
14350	1050	0.1	104.90	0.56	1497	10930	176	1.0	176	0.93	1507
14360	1040	0.1	104.00	0.55	1497	10940	181	1.0	181	0.96	1507
14370	1190	0.1	118.88	0.63	1497	10950	181	1.0	181	0.96	1507
14380	1130	0.1	113.00	0.60	1497	10960	182	1.0	182	0.97	1507
14390	1110	0.1	111.00	0.59	1497	10970	189	1.0	189	1.01	1507
14400	1070	0.1	107.00	0.57	1497	10980	180	1.0	180	0.95	1507
14410	1090	0.1	109.00	0.58	1497	10990	188	1.0	188	1.00	1507
14420	1000	0.1	100.00	0.53	1497	11000	189	1.0	189	1.00	1507
14430	1010	0.1	101.00	0.54	1497	11010	194	1.0	194	1.03	1506
14440	1020	0.1	102.00	0.54	1497	11020	194	1.0	194	1.03	1506
14450	1030	0.1	103.00	0.55	1497	11030	194	1.0	194	1.03	1506
14460	1050	0.1	105.00	0.56	1497	11040	193	1.0	193	1.02	1506
14470	1030	0.1	103.00	0.55	1497	11050	198	1.0	198	1.05	1506
14480	1220	0.1	121.88	0.65	1497	11060	195	1.0	195	1.04	1506
14490	1310	0.1	131.00	0.70	1497	11070	198	1.0	198	1.05	1506
14500	1200	0.1	119.88	0.64	1497	11080	201	1.0	201	1.07	1506
14510	1130	0.1	112.77	0.60	1497	11090	200	1.0	200	1.07	1506
14520	1190	0.1	118.88	0.63	1497	11100	204	1.0	204	1.08	1506
14530	1130	0.1	113.00	0.60	1497	11110	197	1.0	197	1.05	1506
14540	1230	0.1	123.00	0.65	1497	11120	206	1.0	206	1.09	1506
14550	1120	0.1	111.89	0.59	1497	11130	204	1.0	204	1.08	1506
14560	1060	0.1	105.89	0.56	1497	11140	218	1.0	218	1.16	1506
14570	1160	0.1	115.77	0.61	1497	11150	207	1.0	207	1.10	1506
14580	1110	0.1	111.00	0.59	1497	11160	209	1.0	209	1.11	1506
14590	1090	0.1	108.89	0.58	1497	11170	206	1.0	206	1.10	1506
14600	1040	0.1	104.00	0.55	1497	11180	213	1.0	213	1.13	1506
14610	1190	0.1	119.00	0.63	1496	11190	218	1.0	218	1.16	1506
14620	1110	0.1	110.89	0.59	1496	11200	218	1.0	218	1.16	1506
14630	1180	0.1	117.88	0.63	1496	11210	221	1.0	221	1.17	1506
14640	1140	0.1	114.00	0.61	1496	11220	227	1.0	227	1.21	1506
14650	1160	0.1	116.00	0.62	1496	11230	221	1.0	221	1.18	1506
14660	1190	0.1	119.00	0.63	1496	11240	214	1.0	214	1.14	1506
14670	1150	0.1	115.00	0.61	1496	11250	219	1.0	219	1.17	1506
14680	1160	0.1	116.00	0.62	1496	11260	224	1.0	224	1.19	1506
14690	1160	0.1	115.88	0.61	1496	11270	218	1.0	218	1.16	1506
14700	1150	0.1	115.00	0.61	1496	11280	231	1.0	231	1.23	1506
14710	1170	0.1	117.00	0.62	1496	11290	222	1.0	222	1.18	1506
14720	1170	0.1	117.00	0.62	1496	11300	230	1.0	230	1.22	1506
14730	1170	0.1	117.00	0.63	1496	11310	232	1.0	232	1.23	1506
14740	1150	0.1	114.77	0.61	1496	11320	232	1.0	232	1.23	1506
14750	1130	0.1	113.00	0.60	1496	11330	235	1.0	235	1.25	1506
14760	1180	0.1	117.76	0.63	1496	11340	233	1.0	232	1.24	1506
14770	1180	0.1	118.00	0.63	1496	11350	236	1.0	236	1.25	1506
14780	1190	0.1	119.00	0.63	1496	11360	233	1.0	233	1.24	1506
14790	1290	0.1	128.87	0.69	1496	11370	240	1.0	240	1.27	1505
14800	1350	0.1	134.87	0.72	1496	11380	229	1.0	229	1.22	1505
14810	1380	0.1	138.00	0.73	1496	11390	235	1.0	235	1.25	1505
14820	1300	0.1	129.87	0.69	1496	11400	245	1.0	245	1.30	1505
14830	1150	0.1	115.00	0.61	1496	11410	237	1.0	237	1.26	1505
14840	1330	0.1	132.73	0.71	1496	11420	251	1.0	251	1.33	1505
14850	1270	0.1	127.00	0.68	1496	11430	246	1.0	246	1.31	1505
14860	1250	0.1	124.88	0.67	1496	11440	247	1.0	247	1.31	1505
14870	1290	0.1	128.87	0.68	1496	11450	243	1.0	243	1.29	1505
14880	1430	0.1	143.00	0.76	1496	11460	248	1.0	248	1.32	1505
14890	1490	0.1	149.00	0.79	1496	11470	254	1.0	253	1.35	1505
14900	1480	0.1	147.85	0.79	1496	11480	248	1.0	248	1.32	1505
14910	1450	0.1	144.86	0.77	1496	11490	246	1.0	246	1.31	1505
14920	1400	0.1	140.00	0.75	1496	11500	247	1.0	247	1.31	1505
14930	1400	0.1	139.86	0.74	1496	11510	253	1.0	253	1.34	1505
14940	1300	0.1	130.00	0.69	1496	11520	248	1.0	248	1.32	1505
14950	1500	0.1	149.70	0.79	1496	11530	258	1.0	258	1.37	1505
14960	1380	0.1	138.00	0.73	1496	11540	247	1.0	247	1.31	1505
14970	1460	0.1	146.00	0.78	1495	11550	260	1.0	260	1.38	1505
14980	1460	0.1	146.00	0.78	1495	11560	267	1.0	267	1.42	1505
14990	1420	0.1	142.00	0.76	1495	11570	276	1.0	276	1.47	1505
15000	1460	0.1	146.00	0.78	1495	11580	256	1.0	256	1.36	1505
15010	1450	0.1	145.00	0.77	1495	11590	269	1.0	269	1.43	1505

15020	1730	0.1	173.00	0.92	1495	11600	262	1.0	262	1.39	1505
15030	1560	0.1	156.00	0.83	1495	11610	262	1.0	262	1.39	1505
15040	1570	0.1	157.00	0.84	1495	11620	261	1.0	261	1.39	1505
15050	1610	0.1	160.84	0.86	1495	11630	267	1.0	267	1.42	1505
15060	1610	0.1	161.00	0.86	1495	11640	265	1.0	265	1.41	1505
15070	1550	0.1	155.00	0.82	1495	11650	262	1.0	262	1.39	1505
15080	1540	0.1	154.00	0.82	1495	11660	268	1.0	268	1.42	1505
15090	1440	0.1	144.00	0.76	1495	11670	277	1.0	277	1.47	1505
15100	1510	0.1	151.00	0.80	1495	11680	265	1.0	265	1.41	1505
15110	1490	0.1	148.85	0.79	1495	11690	275	1.0	275	1.46	1505
15120	1470	0.1	146.85	0.78	1495	11700	276	1.0	276	1.47	1505
15130	1670	0.1	167.00	0.89	1495	11710	278	1.0	278	1.48	1505
15140	1570	0.1	156.84	0.84	1495	11720	272	1.0	272	1.45	1505
15150	1510	0.1	151.00	0.81	1495	11730	274	1.0	274	1.46	1504
15160	1650	0.1	165.00	0.88	1495	11740	282	1.0	282	1.50	1504
15170	1690	0.1	169.00	0.90	1495	11750	274	1.0	274	1.45	1504
15180	1610	0.1	160.84	0.86	1495	11760	281	1.0	281	1.49	1504
15190	1700	0.1	170.00	0.91	1495	11770	273	1.0	273	1.45	1504
15200	1580	0.1	158.00	0.84	1495	11780	282	1.0	282	1.50	1504
15210	1640	0.1	164.00	0.87	1495	11790	279	1.0	279	1.48	1504
15220	1630	0.1	163.00	0.87	1495	11800	282	1.0	282	1.50	1504
15230	1640	0.1	164.00	0.87	1495	11810	287	1.0	287	1.52	1504
15240	1510	0.1	151.00	0.80	1495	11820	286	1.0	286	1.52	1504
15250	1550	0.1	154.85	0.82	1495	11830	284	1.0	284	1.51	1504
15260	1680	0.1	168.00	0.89	1495	11840	281	1.0	281	1.49	1504
15270	1660	0.1	166.00	0.88	1495	11850	289	1.0	289	1.54	1504
15280	1730	0.1	173.00	0.92	1495	11860	290	1.0	290	1.54	1504
15290	1610	0.1	160.84	0.85	1495	11870	289	1.0	289	1.54	1504
15300	1680	0.1	168.00	0.89	1495	11880	294	1.0	294	1.56	1504
15310	1910	0.1	191.00	1.01	1495	11890	297	1.0	297	1.58	1504
15320	1620	0.1	162.00	0.86	1495	11900	304	1.0	304	1.62	1504
15330	1750	0.1	175.00	0.93	1494	11910	293	1.0	293	1.56	1504
15340	1770	0.1	177.00	0.94	1494	11920	304	1.0	304	1.62	1504
15350	1750	0.1	175.00	0.93	1494	11930	292	1.0	292	1.55	1504
15360	1720	0.1	171.83	0.91	1494	11940	302	1.0	302	1.60	1504
15370	1730	0.1	173.00	0.92	1494	11950	300	1.0	300	1.59	1504
15380	1660	0.1	166.00	0.88	1494	11960	299	1.0	299	1.59	1504
15390	1790	0.1	179.00	0.95	1494	11970	304	1.0	304	1.62	1504
15400	1840	0.1	184.00	0.98	1494	11980	320	1.0	320	1.70	1504
15410	1830	0.1	182.82	0.97	1494	11990	306	1.0	306	1.62	1504
15420	1860	0.1	185.81	0.99	1494	12000	316	1.0	316	1.68	1504
15430	1880	0.1	188.00	1.00	1494	12010	312	1.0	312	1.66	1504
15440	1780	0.1	178.00	0.94	1494	12020	312	1.0	312	1.66	1504
15450	1840	0.1	184.00	0.98	1494	12030	310	1.0	310	1.65	1504
15460	1840	0.1	183.82	0.98	1494	12040	314	1.0	314	1.67	1504
15470	1840	0.1	183.82	0.98	1494	12050	307	1.0	307	1.63	1504
15480	1770	0.1	177.00	0.94	1494	12060	318	1.0	318	1.69	1504
15490	1980	0.1	197.80	1.05	1494	12070	328	1.0	328	1.74	1504
15500	1840	0.1	183.82	0.98	1494	12080	321	1.0	321	1.71	1504
15510	1900	0.1	190.00	1.01	1494	12090	320	1.0	320	1.70	1503
15520	1890	0.1	189.00	1.00	1494	12100	312	1.0	312	1.66	1503
15530	1950	0.1	194.81	1.04	1494	12110	324	1.0	324	1.72	1503
15540	2230	0.1	222.78	1.18	1494	12120	318	1.0	318	1.69	1503
15550	1960	0.1	196.00	1.04	1494	12130	313	1.0	313	1.66	1503
15560	1890	0.1	189.00	1.01	1494	12140	309	1.0	309	1.64	1503
15570	2100	0.1	210.00	1.11	1494	12150	329	1.0	329	1.75	1503
15580	1960	0.1	195.80	1.04	1494	12160	326	1.0	326	1.73	1503
15590	2030	0.1	203.00	1.08	1494	12170	329	1.0	329	1.75	1503
15600	2020	0.1	201.80	1.07	1494	12180	341	1.0	341	1.81	1503
15610	2010	0.1	200.80	1.07	1494	12190	327	1.0	327	1.74	1503
15620	2060	0.1	206.00	1.10	1494	12200	321	1.0	321	1.70	1503
15630	1970	0.1	197.00	1.05	1494	12210	325	1.0	325	1.73	1503
15640	2110	0.1	210.79	1.12	1494	12220	336	1.0	336	1.78	1503
15650	2000	0.1	200.00	1.06	1494	12230	325	1.0	325	1.73	1503
15660	1910	0.1	191.00	1.02	1494	12240	346	1.0	346	1.84	1503
15670	1930	0.1	192.81	1.03	1494	12250	327	1.0	327	1.74	1503
15680	2150	0.1	214.79	1.14	1494	12260	326	1.0	326	1.73	1503
15690	1970	0.1	197.00	1.05	1493	12270	342	1.0	342	1.82	1503
15700	1920	0.1	192.00	1.02	1493	12280	330	1.0	330	1.75	1503

15710	2120	0.1	212.00	1.13	1493	12290	344	1.0	344	1.83	1503
15720	2060	0.1	206.00	1.10	1493	12300	334	1.0	334	1.77	1503
15730	2190	0.1	219.00	1.16	1493	12310	355	1.0	355	1.88	1503
15740	2160	0.1	215.78	1.15	1493	12320	333	1.0	333	1.77	1503
15750	2220	0.1	222.00	1.18	1493	12330	334	1.0	334	1.77	1503
15760	2090	0.1	208.79	1.11	1493	12340	348	1.0	348	1.85	1503
15770	2330	0.1	232.53	1.23	1493	12350	337	1.0	337	1.79	1503
15780	2400	0.1	240.00	1.28	1493	12360	341	1.0	341	1.81	1503
15790	2000	0.1	200.00	1.07	1493	12370	349	1.0	349	1.85	1503
15800	2300	0.1	229.54	1.22	1493	12380	352	1.0	352	1.87	1503
15810	2300	0.1	230.00	1.23	1493	12390	347	1.0	347	1.84	1503
15820	2140	0.1	213.79	1.14	1493	12400	331	1.0	331	1.76	1503
15830	2210	0.1	221.00	1.18	1493	12410	348	1.0	348	1.85	1503
15840	2260	0.1	226.00	1.20	1493	12420	348	1.0	348	1.85	1503
15850	2160	0.1	216.00	1.15	1493	12430	357	1.0	357	1.90	1503
15860	2220	0.1	222.00	1.18	1493	12440	342	1.0	342	1.82	1503
15870	2350	0.1	234.53	1.25	1493	12450	349	1.0	349	1.85	1502
15880	2410	0.1	241.00	1.28	1493	12460	357	1.0	357	1.90	1502
15890	2350	0.1	234.77	1.25	1493	12470	355	1.0	355	1.89	1502
15900	2330	0.1	232.77	1.24	1493	12480	353	1.0	353	1.88	1502
15910	2470	0.1	247.00	1.31	1493	12490	349	1.0	349	1.86	1502
15920	2450	0.1	245.00	1.30	1493	12500	354	1.0	354	1.88	1502
15930	2240	0.1	224.00	1.19	1493	12510	368	1.0	368	1.96	1502
15940	2310	0.1	231.00	1.23	1493	12520	359	1.0	359	1.91	1502
15950	2500	0.1	249.75	1.33	1493	12530	372	1.0	372	1.98	1502
15960	2370	0.1	237.00	1.26	1493	12540	357	1.0	357	1.90	1502
15970	2450	0.1	244.51	1.30	1493	12550	369	1.0	369	1.96	1502
15980	2430	0.1	242.76	1.29	1493	12560	363	1.0	363	1.93	1502
15990	2300	0.1	229.54	1.22	1493	12570	356	1.0	356	1.89	1502
16000	2470	0.1	246.75	1.31	1493	12580	359	1.0	359	1.91	1502
16010	2670	0.1	267.00	1.42	1493	12590	369	1.0	369	1.96	1502
16020	2520	0.1	251.75	1.34	1493	12600	372	1.0	372	1.98	1502
16030	2770	0.1	276.45	1.47	1493	12610	373	1.0	373	1.98	1502
16040	2710	0.1	271.00	1.44	1493	12620	362	1.0	362	1.92	1502
16050	2970	0.1	297.00	1.58	1492	12630	380	1.0	380	2.02	1502
16060	2670	0.1	266.73	1.42	1492	12640	378	1.0	378	2.01	1502
16070	2460	0.1	246.00	1.31	1492	12650	366	1.0	366	1.94	1502
16080	2490	0.1	248.75	1.32	1492	12660	371	1.0	371	1.97	1502
16090	2520	0.1	251.50	1.34	1492	12670	368	1.0	368	1.96	1502
16100	2590	0.1	259.00	1.38	1492	12680	358	1.0	358	1.90	1502
16110	2530	0.1	253.00	1.35	1492	12690	371	1.0	371	1.97	1502
16120	2700	0.1	269.73	1.43	1492	12700	378	1.0	378	2.01	1502
16130	2690	0.1	268.73	1.43	1492	12710	376	1.0	376	2.00	1502
16140	2590	0.1	258.74	1.37	1492	12720	387	1.0	387	2.06	1502
16150	2440	0.1	244.00	1.29	1492	12730	385	1.0	385	2.04	1502
16160	2620	0.1	261.74	1.39	1492	12740	371	1.0	371	1.97	1502
16170	2740	0.1	273.45	1.45	1492	12750	385	1.0	385	2.05	1502
16180	2520	0.1	252.00	1.34	1492	12760	382	1.0	382	2.03	1502
16190	2780	0.1	277.72	1.47	1492	12770	385	1.0	385	2.05	1502
16200	3020	0.1	302.00	1.61	1492	12780	372	1.0	372	1.98	1502
16210	2830	0.1	283.00	1.51	1492	12790	368	1.0	368	1.95	1502
16220	2980	0.1	297.40	1.58	1492	12800	384	1.0	384	2.04	1502
16230	2790	0.1	278.72	1.48	1492	12810	394	1.0	394	2.09	1501
16240	2600	0.1	260.00	1.38	1492	12820	387	1.0	387	2.06	1501
16250	2740	0.1	273.45	1.46	1492	12830	380	1.0	380	2.02	1501
16260	2800	0.1	280.00	1.49	1492	12840	389	1.0	389	2.07	1501
16270	2920	0.1	291.42	1.55	1492	12850	393	1.0	393	2.09	1501
16280	3000	0.1	299.40	1.59	1492	12860	382	1.0	382	2.03	1501
16290	3030	0.1	302.70	1.61	1492	12870	397	1.0	397	2.11	1501
16300	3210	0.1	320.36	1.70	1492	12880	396	1.0	396	2.11	1501
16310	3080	0.1	307.69	1.64	1492	12890	380	1.0	380	2.02	1501
16320	2910	0.1	290.71	1.55	1492	12900	389	1.0	389	2.06	1501
16330	2790	0.1	279.00	1.48	1492	12910	388	1.0	388	2.06	1501
16340	3190	0.1	318.36	1.69	1492	12920	397	1.0	396	2.11	1501
16350	3000	0.1	299.70	1.59	1492	12930	399	1.0	399	2.12	1501
16360	3330	0.1	332.67	1.77	1492	12940	393	1.0	393	2.09	1501
16370	3270	0.1	326.67	1.73	1492	12950	383	1.0	383	2.04	1501
16380	3070	0.1	307.00	1.63	1492	12960	398	1.0	399	2.12	1501
16390	3200	0.1	320.00	1.70	1492	12970	396	1.0	396	2.10	1501

16400	2830	0.1	282.72	1.50	1492	12980	405	1.0	406	2.15	1501
16410	3120	0.1	311.69	1.66	1491	12990	392	1.0	392	2.08	1501
16420	3110	0.1	311.00	1.65	1491	13000	399	1.0	398	2.12	1501
16430	2860	0.1	285.71	1.52	1491	13010	401	1.0	401	2.13	1501
16440	3090	0.1	309.00	1.64	1491	13020	390	1.0	390	2.07	1501
16450	2900	0.1	289.71	1.54	1491	13030	396	1.0	396	2.10	1501
16460	2810	0.1	281.00	1.49	1491	13040	414	1.0	414	2.20	1501
16470	2870	0.1	286.71	1.52	1491	13050	402	1.0	402	2.14	1501
16480	2980	0.1	297.70	1.58	1491	13060	397	1.0	397	2.11	1501
16490	2880	0.1	288.00	1.53	1491	13070	407	1.0	407	2.16	1501
16500	2970	0.1	297.00	1.58	1491	13080	400	1.0	400	2.13	1501
16510	3190	0.1	318.36	1.69	1491	13090	412	1.0	412	2.19	1501
16520	3130	0.1	312.69	1.66	1491	13100	399	1.0	399	2.12	1501
16530	2980	0.1	298.00	1.59	1491	13110	417	1.0	416	2.21	1501
16540	3020	0.1	302.00	1.61	1491	13120	403	1.0	403	2.14	1501
16550	3070	0.1	306.39	1.63	1491	13130	407	1.0	407	2.16	1501
16560	3070	0.1	307.00	1.63	1491	13140	412	1.0	411	2.19	1501
16570	3050	0.1	305.00	1.62	1491	13150	420	1.0	420	2.23	1501
16580	3020	0.1	302.00	1.60	1491	13160	418	1.0	418	2.22	1501
16590	3460	0.1	345.65	1.84	1491	13170	410	1.0	410	2.18	1500
16600	3080	0.1	308.00	1.64	1491	13180	426	1.0	426	2.26	1500
16610	2760	0.1	276.00	1.47	1491	13190	411	1.0	411	2.18	1500
16620	3030	0.1	302.70	1.61	1491	13200	421	1.0	421	2.24	1500
16630	3260	0.1	326.00	1.73	1491	13210	418	1.0	418	2.22	1500
16640	2870	0.1	287.00	1.53	1491	13220	414	1.0	414	2.20	1500
16650	3000	0.1	300.00	1.60	1491	13230	422	1.0	422	2.24	1500
16660	2940	0.1	294.00	1.56	1491	13240	420	1.0	420	2.23	1500
16670	2480	0.1	248.00	1.32	1491	13250	421	1.0	421	2.24	1500
16680	2710	0.1	271.00	1.44	1491	13260	421	1.0	421	2.24	1500
16690	3150	0.1	314.37	1.67	1491	13270	439	1.0	438	2.33	1500
16700	3420	0.1	341.32	1.81	1491	13280	412	1.0	412	2.19	1500
16710	2810	0.1	281.00	1.49	1491	13290	425	1.0	425	2.26	1500
16720	2940	0.1	294.00	1.56	1491	13300	428	1.0	428	2.27	1500
16730	3030	0.1	302.70	1.61	1491	13310	424	1.0	424	2.26	1500
16740	2900	0.1	290.00	1.54	1491	13320	429	1.0	429	2.28	1500
16750	3200	0.1	319.68	1.70	1491	13330	420	1.0	420	2.23	1500
16760	3150	0.1	315.00	1.67	1491	13340	426	1.0	426	2.26	1500
16770	3080	0.1	307.69	1.64	1490	13350	431	1.0	431	2.29	1500
16780	3470	0.1	346.65	1.84	1490	13360	426	1.0	425	2.26	1500
16790	3330	0.1	332.33	1.77	1490	13370	432	1.0	432	2.29	1500
16800	3140	0.1	313.69	1.67	1490	13380	421	1.0	420	2.23	1500
16810	2830	0.1	283.00	1.50	1490	13390	420	1.0	420	2.23	1500
16820	3310	0.1	330.34	1.76	1490	13400	449	1.0	449	2.38	1500
16830	3090	0.1	309.00	1.64	1490	13410	434	1.0	434	2.31	1500
16840	3030	0.1	302.70	1.61	1490	13420	427	1.0	427	2.27	1500
16850	3180	0.1	317.68	1.69	1490	13430	432	1.0	431	2.29	1500
16860	3100	0.1	310.00	1.65	1490	13440	439	1.0	439	2.33	1500
16870	3170	0.1	316.68	1.68	1490	13450	438	1.0	438	2.33	1500
16880	2780	0.1	277.44	1.47	1490	13460	447	1.0	447	2.38	1500
16890	3080	0.1	307.69	1.64	1490	13470	429	1.0	429	2.28	1500
16900	3340	0.1	334.00	1.77	1490	13480	453	1.0	453	2.41	1500
16910	3250	0.1	325.00	1.73	1490	13490	441	1.0	441	2.34	1500
16920	3090	0.1	308.69	1.64	1490	13500	441	1.0	441	2.34	1500
16930	3200	0.1	319.04	1.69	1490	13510	438	1.0	438	2.33	1500
16940	3300	0.1	330.00	1.75	1490	13520	441	1.0	441	2.34	1500
16950	3340	0.1	334.00	1.77	1490	13530	437	1.0	437	2.32	1499
16960	3690	0.1	369.00	1.96	1490	13540	448	1.0	448	2.38	1499
16970	3270	0.1	327.00	1.74	1490	13550	453	1.0	453	2.41	1499
16980	3620	0.1	361.64	1.92	1490	13560	449	1.0	449	2.39	1499
16990	3570	0.1	357.00	1.90	1490	13570	459	1.0	459	2.44	1499
17000	3160	0.1	315.37	1.68	1490	13580	437	1.0	437	2.32	1499
17010	3060	0.1	306.00	1.63	1490	13590	437	1.0	437	2.32	1499
17020	3200	0.1	319.68	1.70	1490	13600	450	1.0	450	2.39	1499
17030	2950	0.1	295.00	1.57	1490	13610	430	1.0	430	2.29	1499
17040	2930	0.1	293.00	1.56	1490	13620	466	1.0	466	2.47	1499
17050	2660	0.1	266.00	1.41	1490	13630	465	1.0	465	2.47	1499
17060	2710	0.1	270.73	1.44	1490	13640	432	1.0	432	2.29	1499
17070	3040	0.1	304.00	1.62	1490	13650	460	1.0	460	2.44	1499
17080	3110	0.1	310.69	1.65	1490	13660	449	1.0	449	2.39	1499

17090	3150	0.1	314.37	1.67	1490	13670	458	1.0	458	2.44	1499
17100	3260	0.1	326.00	1.73	1490	13680	440	1.0	440	2.34	1499
17110	3220	0.1	322.00	1.71	1490	13690	456	1.0	456	2.42	1499
17120	3050	0.1	304.70	1.62	1490	13700	471	1.0	471	2.50	1499
17130	3260	0.1	326.00	1.73	1489	13710	440	1.0	439	2.33	1499
17140	3060	0.1	306.00	1.63	1489	13720	457	1.0	457	2.43	1499
17150	3370	0.1	335.65	1.78	1489	13730	460	1.0	460	2.44	1499
17160	2710	0.1	271.00	1.44	1489	13740	459	1.0	459	2.44	1499
17170	2800	0.1	280.00	1.49	1489	13750	462	1.0	462	2.45	1499
17180	3140	0.1	313.69	1.66	1489	13760	461	1.0	461	2.45	1499
17190	2800	0.1	280.00	1.49	1489	13770	450	1.0	450	2.39	1499
17200	3160	0.1	315.68	1.68	1489	13780	475	1.0	475	2.52	1499
17210	3100	0.1	309.69	1.64	1489	13790	472	1.0	472	2.51	1499
17220	3170	0.1	316.37	1.68	1489	13800	468	1.0	468	2.49	1499
17230	3120	0.1	311.38	1.65	1489	13810	469	1.0	469	2.49	1499
17240	3460	0.1	346.00	1.84	1489	13820	468	1.0	468	2.49	1499
17250	3370	0.1	337.00	1.79	1489	13830	473	1.0	473	2.51	1499
17260	3760	0.1	376.00	2.00	1489	13840	478	1.0	478	2.54	1499
17270	3310	0.1	331.00	1.76	1489	13850	473	1.0	473	2.51	1499
17280	3460	0.1	346.00	1.84	1489	13860	473	1.0	472	2.51	1499
17290	3050	0.1	304.39	1.62	1489	13870	458	1.0	458	2.43	1499
17300	3050	0.1	304.39	1.62	1489	13880	470	1.0	470	2.50	1499
17310	3660	0.1	366.00	1.95	1489	13890	466	1.0	465	2.47	1498
17320	3400	0.1	340.00	1.81	1489	13900	473	1.0	472	2.51	1498
17330	3370	0.1	336.33	1.79	1489	13910	480	1.0	480	2.55	1498
17340	3430	0.1	343.00	1.82	1489	13920	471	1.0	471	2.50	1498
17350	3510	0.1	351.00	1.87	1489	13930	483	1.0	483	2.57	1498
17360	3680	0.1	368.00	1.96	1489	13940	472	1.0	472	2.51	1498
17370	3630	0.1	362.64	1.93	1489	13950	464	1.0	464	2.47	1498
17380	3550	0.1	354.65	1.89	1489	13960	489	1.0	489	2.60	1498
17390	3860	0.1	384.84	2.04	1489	13970	483	1.0	483	2.57	1498
17400	3820	0.1	382.00	2.03	1489	13980	480	1.0	480	2.55	1498
17410	3590	0.1	359.00	1.91	1489	13990	481	1.0	481	2.56	1498
17420	3370	0.1	337.00	1.79	1489	14000	494	1.0	494	2.63	1498
17430	3220	0.1	322.00	1.71	1489	14010	488	1.0	488	2.59	1498
17440	3330	0.1	333.00	1.77	1489	14020	481	1.0	481	2.56	1498
17450	3890	0.1	389.00	2.07	1489	14030	478	1.0	478	2.54	1498
17460	3870	0.1	386.23	2.05	1489	14040	484	1.0	483	2.57	1498
17470	3640	0.1	364.00	1.94	1489	14050	490	1.0	490	2.60	1498
17480	3630	0.1	363.00	1.93	1489	14060	504	1.0	504	2.68	1498
17490	3780	0.1	377.24	2.00	1488	14070	488	1.0	488	2.59	1498
17500	3640	0.1	363.64	1.93	1488	14080	479	1.0	479	2.54	1498
17510	4060	0.1	405.59	2.16	1488	14090	483	1.0	483	2.57	1498
17520	3470	0.1	346.65	1.84	1488	14100	497	1.0	497	2.64	1498
17530	4030	0.1	403.00	2.14	1488	14110	479	1.0	479	2.55	1498
17540	3780	0.1	377.62	2.00	1488	14120	499	1.0	499	2.65	1498
17550	3660	0.1	366.00	1.95	1488	14130	482	1.0	481	2.56	1498
17560	3730	0.1	373.00	1.98	1488	14140	496	1.0	496	2.63	1498
17570	3850	0.1	385.00	2.05	1488	14150	490	1.0	490	2.60	1498
17580	3860	0.1	385.61	2.05	1488	14160	470	1.0	470	2.50	1498
17590	3850	0.1	385.00	2.05	1488	14170	492	1.0	492	2.62	1498
17600	3860	0.1	385.61	2.05	1488	14180	487	1.0	487	2.59	1498
17610	4180	0.1	417.58	2.22	1488	14190	503	1.0	503	2.67	1498
17620	3840	0.1	382.85	2.03	1488	14200	481	1.0	481	2.56	1498
17630	3690	0.1	368.63	1.96	1488	14210	488	1.0	488	2.59	1498
17640	3740	0.1	373.25	1.98	1488	14220	500	1.0	500	2.66	1498
17650	3740	0.1	374.00	1.99	1488	14230	521	1.0	520	2.77	1498
17660	3430	0.1	341.97	1.82	1488	14240	507	1.0	508	2.70	1498
17670	4080	0.1	407.18	2.17	1488	14250	512	1.0	512	2.72	1497
17680	3870	0.1	386.23	2.05	1488	14260	497	1.0	497	2.64	1497
17690	3640	0.1	364.00	1.94	1488	14270	503	1.0	503	2.67	1497
17700	3520	0.1	352.00	1.87	1488	14280	503	1.0	503	2.67	1497
17710	3710	0.1	369.52	1.96	1488	14290	514	1.0	514	2.73	1497
17720	3720	0.1	371.63	1.97	1488	14300	498	1.0	498	2.65	1497
17730	3660	0.1	365.27	1.94	1488	14310	511	1.0	511	2.71	1497
17740	4090	0.1	409.00	2.17	1488	14320	488	1.0	489	2.60	1497
17750	3470	0.1	346.31	1.84	1488	14330	489	1.0	489	2.60	1497
17760	3840	0.1	383.62	2.04	1488	14340	511	1.0	511	2.72	1497
17770	3810	0.1	380.24	2.02	1488	14350	492	1.0	492	2.61	1497

17780	3510	0.1	351.00	1.86	1488	14360	509	1.0	509	2.71	1497
17790	3660	0.1	366.00	1.95	1488	14370	496	1.0	495	2.63	1497
17800	3590	0.1	358.64	1.90	1488	14380	513	1.0	513	2.73	1497
17810	3690	0.1	369.00	1.96	1488	14390	514	1.0	513	2.73	1497
17820	3700	0.1	369.63	1.96	1488	14400	500	1.0	500	2.65	1497
17830	4150	0.1	415.00	2.21	1488	14410	518	1.0	518	2.75	1497
17840	4120	0.1	411.18	2.18	1488	14420	499	1.0	498	2.65	1497
17850	3990	0.1	398.20	2.11	1487	14430	499	1.0	499	2.65	1497
17860	3900	0.1	390.00	2.07	1487	14440	509	1.0	509	2.70	1497
17870	3830	0.1	382.23	2.03	1487	14450	516	1.0	516	2.74	1497
17880	3860	0.1	385.23	2.05	1487	14460	507	1.0	507	2.69	1497
17890	4370	0.1	436.56	2.32	1487	14470	514	1.0	514	2.73	1497
17900	4070	0.1	406.19	2.16	1487	14480	511	1.0	511	2.72	1497
17910	4290	0.1	428.57	2.28	1487	14490	518	1.0	518	2.75	1497
17920	3970	0.1	397.00	2.11	1487	14500	521	1.0	521	2.77	1497
17930	3840	0.1	384.00	2.04	1487	14510	535	1.0	534	2.84	1497
17940	4380	0.1	437.12	2.33	1487	14520	516	1.0	516	2.74	1497
17950	4730	0.1	472.05	2.51	1487	14530	521	1.0	521	2.77	1497
17960	4440	0.1	444.00	2.36	1487	14540	522	1.0	521	2.77	1497
17970	3890	0.1	389.00	2.07	1487	14550	522	1.0	522	2.77	1497
17980	4480	0.1	447.55	2.38	1487	14560	511	1.0	511	2.72	1497
17990	3850	0.1	385.00	2.04	1487	14570	543	1.0	543	2.89	1497
18000	4070	0.1	407.00	2.16	1487	14580	535	1.0	535	2.84	1497
18010	4530	0.1	453.00	2.41	1487	14590	533	1.0	533	2.83	1497
18020	4840	0.1	484.00	2.58	1487	14600	526	1.0	526	2.79	1497
18030	4500	0.1	448.65	2.39	1487	14610	528	1.0	528	2.80	1496
18040	4180	0.1	417.58	2.22	1487	14620	547	1.0	547	2.91	1496
18050	4250	0.1	424.58	2.25	1487	14630	538	1.0	538	2.86	1496
18060	4270	0.1	427.00	2.27	1487	14640	541	1.0	541	2.88	1496
18070	4540	0.1	454.00	2.41	1487	14650	519	1.0	519	2.76	1496
18080	4870	0.1	485.54	2.58	1487	14660	535	1.0	534	2.84	1496
18090	3910	0.1	390.22	2.08	1487	14670	547	1.0	546	2.90	1496
18100	4160	0.1	416.00	2.21	1487	14680	529	1.0	529	2.81	1496
18110	4160	0.1	416.00	2.21	1487	14690	532	1.0	532	2.82	1496
18120	4310	0.1	431.00	2.29	1487	14700	547	1.0	547	2.91	1496
18130	4300	0.1	430.00	2.29	1487	14710	554	1.0	553	2.94	1496
18140	4040	0.1	404.00	2.15	1487	14720	538	1.0	538	2.86	1496
18150	4450	0.1	444.56	2.36	1487	14730	543	1.0	543	2.88	1496
18160	4390	0.1	439.00	2.34	1487	14740	552	1.0	552	2.93	1496
18170	5050	0.1	505.00	2.69	1487	14750	539	1.0	539	2.87	1496
18180	4180	0.1	417.58	2.22	1487	14760	534	1.0	534	2.84	1496
18190	4780	0.1	476.57	2.53	1487	14770	533	1.0	533	2.83	1496
18200	4850	0.1	485.00	2.58	1487	14780	550	1.0	550	2.92	1496
18210	4430	0.1	442.56	2.35	1486	14790	545	1.0	545	2.90	1496
18220	4160	0.1	415.58	2.21	1486	14800	562	1.0	562	2.99	1496
18230	4010	0.1	400.60	2.13	1486	14810	537	1.0	537	2.85	1496
18240	4550	0.1	453.64	2.41	1486	14820	539	1.0	539	2.86	1496
18250	4670	0.1	465.13	2.47	1486	14830	541	1.0	541	2.87	1496
18260	4440	0.1	444.00	2.36	1486	14840	567	1.0	567	3.01	1496
18270	4230	0.1	423.00	2.25	1486	14850	549	1.0	549	2.92	1496
18280	4140	0.1	414.00	2.20	1486	14860	551	1.0	551	2.93	1496
18290	3840	0.1	384.00	2.04	1486	14870	549	1.0	549	2.92	1496
18300	5050	0.1	504.50	2.68	1486	14880	563	1.0	563	2.99	1496
18310	4630	0.1	462.07	2.46	1486	14890	550	1.0	550	2.92	1496
18320	4120	0.1	411.59	2.19	1486	14900	561	1.0	562	2.98	1496
18330	4060	0.1	406.00	2.16	1486	14910	556	1.0	556	2.95	1496
18340	4170	0.1	417.00	2.22	1486	14920	562	1.0	562	2.99	1496
18350	4440	0.1	443.56	2.35	1486	14930	523	1.0	522	2.78	1496
18360	4240	0.1	423.15	2.25	1486	14940	547	1.0	547	2.91	1496
18370	4270	0.1	426.15	2.26	1486	14950	551	1.0	551	2.93	1496
18380	4400	0.1	439.56	2.34	1486	14960	550	1.0	550	2.92	1496
18390	4420	0.1	442.00	2.35	1486	14970	549	1.0	549	2.92	1495
18400	4700	0.1	469.53	2.50	1486	14980	559	1.0	559	2.97	1495
18410	4650	0.1	464.54	2.47	1486	14990	540	1.0	540	2.87	1495
18420	4390	0.1	439.00	2.34	1486	15000	557	1.0	557	2.96	1495
18430	4860	0.1	485.51	2.58	1486	15010	580	1.0	580	3.08	1495
18440	4650	0.1	465.00	2.47	1486	15020	582	1.0	582	3.09	1495
18450	4390	0.1	438.56	2.33	1486	15030	565	1.0	565	3.00	1495
18460	5260	0.1	526.00	2.79	1486	15040	555	1.0	555	2.95	1495

18470	5080	0.1	508.00	2.70	1486	15050	572	1.0	572	3.04	1495
18480	4810	0.1	480.52	2.56	1486	15060	555	1.0	555	2.95	1495
18490	4780	0.1	478.00	2.54	1486	15070	577	1.0	577	3.07	1495
18500	5040	0.1	504.00	2.68	1486	15080	565	1.0	565	3.00	1495
18510	4320	0.1	431.57	2.29	1486	15090	589	1.0	589	3.13	1495
18520	4570	0.1	456.54	2.42	1486	15100	563	1.0	563	2.99	1495
18530	4900	0.1	490.00	2.61	1486	15110	577	1.0	577	3.07	1495
18540	4990	0.1	498.00	2.65	1486	15120	584	1.0	584	3.10	1495
18550	4870	0.1	487.00	2.59	1486	15130	569	1.0	569	3.02	1495
18560	5190	0.1	517.96	2.76	1486	15140	563	1.0	563	2.99	1495
18570	5330	0.1	531.93	2.83	1485	15150	571	1.0	570	3.03	1495
18580	4950	0.1	495.00	2.63	1485	15160	565	1.0	565	3.00	1495
18590	5300	0.1	529.47	2.82	1485	15170	583	1.0	583	3.10	1495
18600	5240	0.1	524.00	2.78	1485	15180	601	1.0	601	3.19	1495
18610	4730	0.1	472.53	2.51	1485	15190	574	1.0	574	3.05	1495
18620	5310	0.1	531.00	2.82	1485	15200	585	1.0	585	3.11	1495
18630	4620	0.1	461.08	2.45	1485	15210	596	1.0	595	3.16	1495
18640	4910	0.1	491.00	2.61	1485	15220	573	1.0	573	3.04	1495
18650	4810	0.1	479.56	2.55	1485	15230	571	1.0	571	3.04	1495
18660	4800	0.1	480.00	2.55	1485	15240	600	1.0	600	3.19	1495
18670	5260	0.1	524.95	2.79	1485	15250	589	1.0	589	3.13	1495
18680	4780	0.1	477.04	2.54	1485	15260	579	1.0	579	3.08	1495
18690	5410	0.1	539.38	2.86	1485	15270	563	1.0	563	2.99	1495
18700	5250	0.1	525.00	2.79	1485	15280	596	1.0	596	3.17	1495
18710	4600	0.1	459.54	2.44	1485	15290	579	1.0	579	3.07	1495
18720	5220	0.1	520.43	2.77	1485	15300	580	1.0	580	3.08	1495
18730	4700	0.1	470.00	2.50	1485	15310	569	1.0	569	3.02	1495
18740	4620	0.1	462.00	2.45	1485	15320	601	1.0	601	3.20	1495
18750	5400	0.1	540.00	2.87	1485	15330	577	1.0	577	3.06	1494
18760	5430	0.1	541.37	2.88	1485	15340	593	1.0	593	3.15	1494
18770	6080	0.1	607.39	3.23	1485	15350	591	1.0	591	3.14	1494
18780	5250	0.1	523.95	2.78	1485	15360	580	1.0	580	3.08	1494
18790	5650	0.1	564.44	3.00	1485	15370	581	1.0	581	3.09	1494
18800	5590	0.1	559.00	2.97	1485	15380	600	1.0	600	3.19	1494
18810	5280	0.1	528.00	2.80	1485	15390	582	1.0	582	3.09	1494
18820	5180	0.1	517.48	2.75	1485	15400	575	1.0	575	3.05	1494
18830	5890	0.1	589.00	3.13	1485	15410	600	1.0	600	3.19	1494
18840	5010	0.1	501.00	2.67	1485	15420	579	1.0	579	3.08	1494
18850	6010	0.1	599.80	3.19	1485	15430	602	1.0	603	3.20	1494
18860	5740	0.1	572.85	3.04	1485	15440	588	1.0	589	3.13	1494
18870	5150	0.1	515.00	2.73	1485	15450	579	1.0	579	3.08	1494
18880	5170	0.1	516.48	2.75	1485	15460	605	1.0	605	3.21	1494
18890	5380	0.1	538.00	2.86	1485	15470	592	1.0	591	3.14	1494
18900	5330	0.1	531.93	2.82	1485	15480	609	1.0	609	3.23	1494
18910	5550	0.1	555.00	2.96	1485	15490	601	1.0	602	3.20	1494
18920	4840	0.1	483.52	2.57	1485	15500	602	1.0	602	3.20	1494
18930	5430	0.1	543.00	2.89	1484	15510	608	1.0	608	3.23	1494
18940	5530	0.1	553.00	2.95	1484	15520	581	1.0	581	3.09	1494
18950	5340	0.1	534.00	2.84	1484	15530	604	1.0	604	3.21	1494
18960	5510	0.1	549.90	2.92	1484	15540	610	1.0	610	3.24	1494
18970	5340	0.1	533.47	2.83	1484	15550	613	1.0	613	3.26	1494
18980	5420	0.1	539.83	2.87	1484	15560	603	1.0	602	3.20	1494
18990	5350	0.1	534.47	2.84	1484	15570	606	1.0	606	3.22	1494
19000	5700	0.1	570.00	3.03	1484	15580	606	1.0	606	3.22	1494
19010	6180	0.1	617.38	3.28	1484	15590	611	1.0	611	3.24	1494
19020	5750	0.1	574.43	3.05	1484	15600	628	1.0	628	3.33	1494
19030	5690	0.1	567.86	3.02	1484	15610	608	1.0	608	3.23	1494
19040	5490	0.1	547.90	2.91	1484	15620	604	1.0	604	3.21	1494
19050	5300	0.1	529.47	2.82	1484	15630	596	1.0	596	3.17	1494
19060	5310	0.1	531.00	2.82	1484	15640	607	1.0	607	3.22	1494
19070	6120	0.1	610.16	3.24	1484	15650	617	1.0	617	3.28	1494
19080	6660	0.1	665.33	3.54	1484	15660	601	1.0	601	3.19	1494
19090	5620	0.1	560.88	2.98	1484	15670	607	1.0	607	3.22	1494
19100	5840	0.1	582.83	3.09	1484	15680	616	1.0	616	3.27	1494
19110	5440	0.1	542.91	2.89	1484	15690	610	1.0	610	3.24	1493
19120	5510	0.1	549.90	2.92	1484	15700	604	1.0	604	3.21	1493
19130	6190	0.1	619.00	3.29	1484	15710	599	1.0	599	3.18	1493
19140	5230	0.1	521.43	2.77	1484	15720	618	1.0	618	3.29	1493
19150	5800	0.1	580.00	3.08	1484	15730	626	1.0	625	3.32	1493

19160	5060	0.1	506.00	2.69	1484	15740	610	1.0	610	3.24	1493
19170	6080	0.1	608.00	3.23	1484	15750	621	1.0	621	3.30	1493
19180	5410	0.1	541.00	2.88	1484	15760	634	1.0	634	3.37	1493
19190	6060	0.1	604.18	3.21	1484	15770	625	1.0	625	3.32	1493
19200	4930	0.1	493.00	2.62	1484	15780	614	1.0	614	3.26	1493
19210	5530	0.1	553.00	2.94	1484	15790	627	1.0	627	3.33	1493
19220	5680	0.1	566.30	3.01	1484	15800	643	1.0	643	3.42	1493
19230	5300	0.1	528.94	2.81	1484	15810	630	1.0	630	3.35	1493
19240	5540	0.1	553.45	2.94	1484	15820	641	1.0	641	3.41	1493
19250	5600	0.1	560.00	2.98	1484	15830	625	1.0	625	3.32	1493
19260	6210	0.1	620.38	3.30	1484	15840	623	1.0	623	3.31	1493
19270	5680	0.1	566.30	3.01	1484	15850	646	1.0	646	3.43	1493
19280	5700	0.1	570.00	3.03	1484	15860	611	1.0	611	3.25	1493
19290	6130	0.1	612.39	3.26	1483	15870	638	1.0	639	3.39	1493
19300	5450	0.1	544.46	2.89	1483	15880	614	1.0	614	3.26	1493
19310	5710	0.1	571.00	3.04	1483	15890	606	1.0	605	3.22	1493
19320	6150	0.1	615.00	3.27	1483	15900	638	1.0	638	3.39	1493
19330	6590	0.1	659.00	3.50	1483	15910	622	1.0	622	3.31	1493
19340	5770	0.1	575.85	3.06	1483	15920	647	1.0	647	3.44	1493
19350	5240	0.1	523.48	2.78	1483	15930	631	1.0	631	3.35	1493
19360	5330	0.1	533.00	2.83	1483	15940	639	1.0	639	3.40	1493
19370	5630	0.1	561.87	2.99	1483	15950	630	1.0	630	3.35	1493
19380	5860	0.1	584.83	3.11	1483	15960	673	1.0	672	3.57	1493
19390	6630	0.1	663.00	3.53	1483	15970	656	1.0	656	3.48	1493
19400	6550	0.1	653.04	3.47	1483	15980	632	1.0	632	3.36	1493
19410	5180	0.1	518.00	2.76	1483	15990	624	1.0	624	3.31	1493
19420	6360	0.1	634.09	3.37	1483	16000	644	1.0	644	3.42	1493
19430	6420	0.1	640.72	3.40	1483	16010	636	1.0	636	3.38	1493
19440	6350	0.1	635.00	3.38	1483	16020	641	1.0	641	3.40	1493
19450	6190	0.1	619.00	3.29	1483	16030	630	1.0	630	3.35	1493
19460	6340	0.1	633.37	3.37	1483	16040	646	1.0	646	3.43	1493
19470	6050	0.1	604.40	3.21	1483	16050	645	1.0	645	3.43	1492
19480	5770	0.1	577.00	3.06	1483	16060	635	1.0	635	3.38	1492
19490	5690	0.1	569.00	3.03	1483	16070	629	1.0	629	3.34	1492
19500	5580	0.1	556.88	2.96	1483	16080	651	1.0	650	3.46	1492
19510	5230	0.1	523.00	2.78	1483	16090	653	1.0	653	3.47	1492
19520	5660	0.1	563.74	2.99	1483	16100	670	1.0	670	3.56	1492
19530	5610	0.1	559.32	2.97	1483	16110	646	1.0	646	3.43	1492
19540	5590	0.1	556.76	2.96	1483	16120	663	1.0	663	3.52	1492
19550	6060	0.1	603.58	3.21	1483	16130	663	1.0	663	3.52	1492
19560	5880	0.1	588.00	3.12	1483	16140	656	1.0	656	3.49	1492
19570	6250	0.1	623.75	3.31	1483	16150	648	1.0	648	3.44	1492
19580	6730	0.1	672.33	3.57	1483	16160	641	1.0	641	3.41	1492
19590	5940	0.1	594.00	3.16	1483	16170	654	1.0	654	3.48	1492
19600	6270	0.1	627.00	3.33	1483	16180	663	1.0	663	3.52	1492
19610	6230	0.1	623.00	3.32	1483	16190	664	1.0	664	3.53	1492
19620	5840	0.1	582.83	3.10	1483	16200	658	1.0	657	3.49	1492
19630	6410	0.1	640.36	3.40	1483	16210	667	1.0	667	3.54	1492
19640	5840	0.1	584.00	3.10	1483	16220	668	1.0	668	3.55	1492
19650	6540	0.1	653.35	3.47	1482	16230	654	1.0	654	3.48	1492
19660	6210	0.1	619.76	3.29	1482	16240	667	1.0	667	3.54	1492
19670	6060	0.1	606.00	3.22	1482	16250	672	1.0	672	3.57	1492
19680	6730	0.1	673.00	3.57	1482	16260	653	1.0	654	3.47	1492
19690	5890	0.1	587.23	3.12	1482	16270	687	1.0	688	3.66	1492
19700	6090	0.1	608.39	3.23	1482	16280	669	1.0	669	3.55	1492
19710	6080	0.1	606.78	3.23	1482	16290	674	1.0	674	3.58	1492
19720	6330	0.1	632.37	3.36	1482	16300	679	1.0	679	3.61	1492
19730	6590	0.1	657.68	3.49	1482	16310	671	1.0	671	3.56	1492
19740	6780	0.1	676.64	3.59	1482	16320	687	1.0	686	3.65	1492
19750	6750	0.1	675.00	3.59	1482	16330	680	1.0	680	3.62	1492
19760	6590	0.1	659.00	3.50	1482	16340	680	1.0	680	3.61	1492
19770	6160	0.1	615.38	3.27	1482	16350	680	1.0	680	3.61	1492
19780	5650	0.1	565.00	3.00	1482	16360	682	1.0	682	3.62	1492
19790	5920	0.1	592.00	3.15	1482	16370	684	1.0	684	3.64	1492
19800	6060	0.1	606.00	3.22	1482	16380	672	1.0	673	3.57	1492
19810	6260	0.1	624.75	3.32	1482	16390	702	1.0	702	3.73	1492
19820	6160	0.1	614.77	3.27	1482	16400	658	1.0	658	3.50	1492
19830	5860	0.1	586.00	3.12	1482	16410	692	1.0	691	3.67	1491
19840	6730	0.1	672.33	3.57	1482	16420	689	1.0	689	3.66	1491

19850	6650	0.1	664.34	3.53	1482	16430	675	1.0	675	3.59	1491
19860	6870	0.1	685.63	3.64	1482	16440	681	1.0	681	3.62	1491
19870	6920	0.1	690.62	3.67	1482	16450	709	1.0	709	3.77	1491
19880	7550	0.1	754.25	4.01	1482	16460	696	1.0	696	3.70	1491
19890	6670	0.1	667.00	3.55	1482	16470	692	1.0	692	3.68	1491
19900	7010	0.1	700.30	3.72	1482	16480	694	1.0	694	3.69	1491
19910	6400	0.1	640.00	3.41	1482	16490	689	1.0	689	3.66	1491
19920	5710	0.1	569.86	3.03	1482	16500	693	1.0	693	3.68	1491
19930	6360	0.1	635.36	3.38	1482	16510	700	1.0	701	3.72	1491
19940	7240	0.1	723.28	3.84	1482	16520	715	1.0	715	3.80	1491
19950	7220	0.1	722.00	3.84	1482	16530	702	1.0	702	3.73	1491
19960	6250	0.1	625.00	3.32	1482	16540	695	1.0	695	3.69	1491
19970	5760	0.1	575.42	3.06	1482	16550	692	1.0	692	3.68	1491
19980	6480	0.1	646.70	3.44	1482	16560	718	1.0	717	3.81	1491
19990	7190	0.1	718.28	3.82	1482	16570	684	1.0	685	3.64	1491
20000	7100	0.1	707.87	3.76	1482	16580	706	1.0	706	3.75	1491
20010	7560	0.1	755.24	4.01	1481	16590	707	1.0	706	3.75	1491
20020	6240	0.1	624.00	3.33	1481	16600	715	1.0	714	3.80	1491
20030	7470	0.1	746.25	3.97	1481	16610	698	1.0	698	3.71	1491
20040	8050	0.1	804.20	4.27	1481	16620	679	1.0	679	3.61	1491
20050	7690	0.1	769.00	4.09	1481	16630	696	1.0	696	3.70	1491
20060	6900	0.1	689.31	3.66	1481	16640	697	1.0	697	3.71	1491
20070	6420	0.1	642.00	3.41	1481	16650	706	1.0	706	3.75	1491
20080	5650	0.1	564.44	3.00	1481	16660	709	1.0	709	3.77	1491
20090	6740	0.1	671.98	3.57	1481	16670	726	1.0	726	3.86	1491
20100	6780	0.1	676.64	3.60	1481	16680	717	1.0	717	3.81	1491
20110	6630	0.1	663.00	3.52	1481	16690	710	1.0	710	3.77	1491
20120	7190	0.1	719.00	3.82	1481	16700	693	1.0	692	3.68	1491
20130	8060	0.1	803.58	4.27	1481	16710	680	1.0	680	3.61	1491
20140	7670	0.1	767.00	4.07	1481	16720	717	1.0	717	3.81	1491
20150	7410	0.1	739.52	3.93	1481	16730	704	1.0	704	3.74	1491
20160	7340	0.1	734.00	3.90	1481	16740	726	1.0	725	3.85	1491
20170	6840	0.1	683.32	3.63	1481	16750	736	1.0	736	3.91	1491
20180	7440	0.1	743.26	3.95	1481	16760	707	1.0	707	3.76	1491
20190	8050	0.1	804.20	4.27	1481	16770	729	1.0	729	3.87	1490
20200	6700	0.1	667.99	3.55	1481	16780	718	1.0	717	3.81	1490
20210	7560	0.1	754.25	4.01	1481	16790	708	1.0	709	3.77	1490
20220	6700	0.1	670.00	3.56	1481	16800	727	1.0	726	3.86	1490
20230	6590	0.1	659.00	3.50	1481	16810	732	1.0	731	3.88	1490
20240	7710	0.1	768.69	4.09	1481	16820	744	1.0	744	3.95	1490
20250	8010	0.1	801.00	4.26	1481	16830	740	1.0	739	3.93	1490
20260	6960	0.1	695.30	3.69	1481	16840	714	1.0	714	3.79	1490
20270	7220	0.1	721.28	3.83	1481	16850	719	1.0	719	3.82	1490
20280	6210	0.1	620.38	3.30	1481	16860	733	1.0	733	3.89	1490
20290	6920	0.1	689.92	3.67	1481	16870	729	1.0	730	3.88	1490
20300	6640	0.1	664.00	3.53	1481	16880	727	1.0	727	3.86	1490
20310	7520	0.1	752.00	4.00	1481	16890	742	1.0	741	3.94	1490
20320	6710	0.1	669.66	3.56	1481	16900	724	1.0	724	3.84	1490
20330	7020	0.1	700.60	3.72	1481	16910	744	1.0	744	3.95	1490
20340	6750	0.1	674.33	3.59	1481	16920	747	1.0	748	3.97	1490
20350	7520	0.1	750.50	3.99	1481	16930	742	1.0	743	3.95	1490
20360	7590	0.1	759.00	4.04	1481	16940	724	1.0	724	3.85	1490
20370	6250	0.1	625.00	3.32	1480	16950	748	1.0	748	3.98	1490
20380	7230	0.1	722.28	3.84	1480	16960	754	1.0	754	4.01	1490
20390	7190	0.1	718.28	3.82	1480	16970	722	1.0	722	3.84	1490
20400	6600	0.1	658.68	3.50	1480	16980	748	1.0	747	3.97	1490
20410	6880	0.1	687.31	3.65	1480	16990	739	1.0	739	3.93	1490
20420	6940	0.1	692.61	3.68	1480	17000	758	1.0	757	4.02	1490
20430	6650	0.1	664.34	3.53	1480	17010	737	1.0	737	3.92	1490
20440	6820	0.1	680.64	3.61	1480	17020	768	1.0	769	4.08	1490
20450	6900	0.1	690.00	3.67	1480	17030	749	1.0	749	3.98	1490
20460	6930	0.1	692.31	3.68	1480	17040	764	1.0	764	4.06	1490
20470	6910	0.1	691.00	3.67	1480	17050	760	1.0	760	4.04	1490
20480	6700	0.1	670.00	3.56	1480	17060	769	1.0	768	4.08	1490
20490	6640	0.1	663.34	3.53	1480	17070	755	1.0	755	4.01	1490
20500	7980	0.1	798.00	4.24	1480	17080	748	1.0	748	3.98	1490
20510	7320	0.1	732.00	3.89	1480	17090	739	1.0	739	3.93	1490
20520	7490	0.1	748.25	3.98	1480	17100	802	1.0	801	4.26	1490
20530	7660	0.1	766.00	4.07	1480	17110	758	1.0	758	4.03	1490

20540	7430	0.1	743.00	3.95	1480	17120	755	1.0	755	4.01	1490
20550	7920	0.1	789.62	4.20	1480	17130	746	1.0	746	3.96	1489
20560	7890	0.1	786.63	4.18	1480	17140	749	1.0	749	3.98	1489
20570	6600	0.1	659.34	3.50	1480	17150	746	1.0	746	3.96	1489
20580	8120	0.1	810.38	4.31	1480	17160	731	1.0	731	3.88	1489
20590	7440	0.1	744.00	3.96	1480	17170	748	1.0	748	3.98	1489
20600	8700	0.1	867.39	4.61	1480	17180	773	1.0	772	4.10	1489
20610	8390	0.1	838.16	4.46	1480	17190	768	1.0	768	4.08	1489
20620	8930	0.1	893.00	4.74	1480	17200	787	1.0	787	4.18	1489
20630	8390	0.1	836.48	4.45	1480	17210	795	1.0	795	4.23	1489
20640	8030	0.1	803.00	4.27	1480	17220	773	1.0	773	4.11	1489
20650	7830	0.1	781.43	4.15	1480	17230	766	1.0	766	4.07	1489
20660	8280	0.1	825.52	4.39	1480	17240	810	1.0	810	4.31	1489
20670	7630	0.1	762.24	4.05	1480	17250	762	1.0	761	4.04	1489
20680	7540	0.1	753.25	4.01	1480	17260	741	1.0	741	3.94	1489
20690	7410	0.1	741.00	3.94	1480	17270	780	1.0	780	4.14	1489
20700	6790	0.1	676.28	3.59	1480	17280	770	1.0	770	4.09	1489
20710	7010	0.1	699.60	3.72	1480	17290	757	1.0	757	4.02	1489
20720	7180	0.1	716.56	3.81	1480	17300	775	1.0	774	4.11	1489
20730	7140	0.1	713.29	3.79	1479	17310	766	1.0	766	4.07	1489
20740	6920	0.1	689.92	3.66	1479	17320	788	1.0	788	4.19	1489
20750	8170	0.1	817.00	4.34	1479	17330	765	1.0	765	4.06	1489
20760	7570	0.1	757.00	4.02	1479	17340	783	1.0	783	4.16	1489
20770	7120	0.1	712.00	3.79	1479	17350	789	1.0	789	4.19	1489
20780	6000	0.1	600.00	3.19	1479	17360	771	1.0	771	4.10	1489
20790	6900	0.1	690.00	3.67	1479	17370	797	1.0	797	4.23	1489
20800	8140	0.1	813.19	4.32	1479	17380	780	1.0	780	4.14	1489
20810	7470	0.1	747.00	3.98	1479	17390	769	1.0	769	4.08	1489
20820	7410	0.1	739.52	3.93	1479	17400	794	1.0	794	4.22	1489
20830	7750	0.1	775.00	4.13	1479	17410	785	1.0	785	4.17	1489
20840	6710	0.1	670.33	3.56	1479	17420	771	1.0	771	4.10	1489
20850	7670	0.1	767.00	4.07	1479	17430	799	1.0	799	4.24	1489
20860	8480	0.1	845.46	4.49	1479	17440	781	1.0	781	4.15	1489
20870	7480	0.1	748.00	3.97	1479	17450	769	1.0	769	4.08	1489
20880	6500	0.1	650.00	3.46	1479	17460	825	1.0	825	4.38	1489
20890	7320	0.1	731.27	3.89	1479	17470	798	1.0	798	4.24	1489
20900	7610	0.1	760.24	4.04	1479	17480	809	1.0	809	4.30	1489
20910	6960	0.1	696.60	3.70	1479	17490	827	1.0	827	4.40	1488
20920	7500	0.1	750.00	3.98	1479	17500	810	1.0	809	4.30	1488
20930	7390	0.1	738.26	3.92	1479	17510	792	1.0	792	4.21	1488
20940	6290	0.1	629.00	3.34	1479	17520	807	1.0	807	4.29	1488
20950	8020	0.1	800.40	4.25	1479	17530	845	1.0	845	4.49	1488
20960	8380	0.1	838.00	4.46	1479	17540	825	1.0	826	4.39	1488
20970	7140	0.1	713.29	3.79	1479	17550	831	1.0	831	4.42	1488
20980	8360	0.1	836.00	4.44	1479	17560	798	1.0	799	4.24	1488
20990	7380	0.1	736.52	3.91	1479	17570	817	1.0	817	4.34	1488
21000	7340	0.1	734.00	3.90	1479	17580	816	1.0	816	4.34	1488
21010	8810	0.1	881.00	4.69	1479	17590	808	1.0	809	4.30	1488
21020	8620	0.1	860.28	4.57	1479	17600	816	1.0	816	4.34	1488
21030	8360	0.1	834.33	4.44	1479	17610	820	1.0	821	4.36	1488
21040	7990	0.1	799.00	4.24	1479	17620	791	1.0	791	4.20	1488
21050	8790	0.1	879.00	4.67	1479	17630	826	1.0	826	4.39	1488
21060	8490	0.1	849.00	4.51	1479	17640	813	1.0	812	4.32	1488
21070	8030	0.1	803.00	4.27	1479	17650	806	1.0	806	4.28	1488
21080	7280	0.1	726.54	3.86	1479	17660	851	1.0	852	4.53	1488
21090	8120	0.1	811.19	4.31	1478	17670	843	1.0	843	4.48	1488
21100	7210	0.1	719.56	3.83	1478	17680	819	1.0	819	4.35	1488
21110	8720	0.1	871.13	4.63	1478	17690	826	1.0	826	4.39	1488
21120	8850	0.1	884.12	4.70	1478	17700	837	1.0	836	4.44	1488
21130	7920	0.1	792.00	4.21	1478	17710	835	1.0	835	4.44	1488
21140	8420	0.1	839.47	4.46	1478	17720	807	1.0	807	4.29	1488
21150	8320	0.1	831.17	4.41	1478	17730	825	1.0	825	4.38	1488
21160	8080	0.1	807.19	4.29	1478	17740	802	1.0	802	4.26	1488
21170	9730	0.1	971.05	5.16	1478	17750	844	1.0	843	4.48	1488
21180	8740	0.1	873.13	4.64	1478	17760	824	1.0	825	4.38	1488
21190	8780	0.1	877.12	4.66	1478	17770	840	1.0	840	4.46	1488
21200	8490	0.1	847.30	4.50	1478	17780	810	1.0	810	4.31	1488
21210	8770	0.1	876.12	4.66	1478	17790	832	1.0	832	4.42	1488
21220	7380	0.1	738.00	3.92	1478	17800	833	1.0	833	4.43	1488

21230	7880	0.1	787.21	4.18	1478	17810	820	1.0	820	4.36	1488
21240	7130	0.1	713.00	3.79	1478	17820	830	1.0	830	4.41	1488
21250	7600	0.1	759.24	4.04	1478	17830	819	1.0	819	4.35	1488
21260	8700	0.1	869.13	4.62	1478	17840	864	1.0	864	4.59	1488
21270	8220	0.1	820.36	4.36	1478	17850	838	1.0	836	4.44	1487
21280	8250	0.1	824.18	4.38	1478	17860	872	1.0	872	4.64	1487
21290	8890	0.1	886.33	4.71	1478	17870	843	1.0	843	4.48	1487
21300	7810	0.1	778.66	4.14	1478	17880	844	1.0	844	4.49	1487
21310	6910	0.1	688.93	3.66	1478	17890	868	1.0	868	4.61	1487
21320	7840	0.1	784.00	4.17	1478	17900	867	1.0	867	4.61	1487
21330	8080	0.1	807.19	4.29	1478	17910	813	1.0	813	4.32	1487
21340	9030	0.1	902.10	4.79	1478	17920	853	1.0	853	4.53	1487
21350	8040	0.1	803.20	4.27	1478	17930	843	1.0	843	4.48	1487
21360	8090	0.1	809.00	4.30	1478	17940	825	1.0	825	4.39	1487
21370	7810	0.1	781.00	4.15	1478	17950	830	1.0	830	4.41	1487
21380	8840	0.1	884.00	4.70	1478	17960	850	1.0	850	4.52	1487
21390	7870	0.1	787.00	4.19	1478	17970	855	1.0	856	4.55	1487
21400	8650	0.1	863.27	4.59	1478	17980	847	1.0	847	4.50	1487
21410	8320	0.1	832.00	4.42	1478	17990	853	1.0	853	4.53	1487
21420	8800	0.1	879.12	4.67	1478	18000	839	1.0	839	4.46	1487
21430	8050	0.1	805.00	4.28	1478	18010	877	1.0	877	4.66	1487
21440	8410	0.1	838.48	4.46	1478	18020	866	1.0	866	4.60	1487
21450	9370	0.1	933.25	4.96	1477	18030	881	1.0	881	4.68	1487
21460	8090	0.1	806.57	4.29	1477	18040	852	1.0	852	4.53	1487
21470	8680	0.1	868.00	4.61	1477	18050	884	1.0	884	4.70	1487
21480	7620	0.1	761.24	4.05	1477	18060	855	1.0	854	4.54	1487
21490	8470	0.1	844.46	4.49	1477	18070	858	1.0	858	4.56	1487
21500	8040	0.1	804.00	4.27	1477	18080	839	1.0	838	4.46	1487
21510	9270	0.1	927.00	4.94	1477	18090	879	1.0	880	4.67	1487
21520	10200	0.1	1017.96	5.39	1477	18100	867	1.0	867	4.61	1487
21530	6980	0.1	698.00	3.71	1477	18110	847	1.0	846	4.50	1487
21540	8490	0.1	848.15	4.51	1477	18120	887	1.0	887	4.71	1487
21550	9140	0.1	913.09	4.85	1477	18130	861	1.0	861	4.58	1487
21560	8840	0.1	884.00	4.70	1477	18140	884	1.0	883	4.69	1487
21570	8040	0.1	801.59	4.26	1477	18150	877	1.0	877	4.66	1487
21580	8250	0.1	825.00	4.39	1477	18160	854	1.0	854	4.54	1487
21590	9440	0.1	944.00	5.02	1477	18170	845	1.0	845	4.49	1487
21600	8910	0.1	891.00	4.73	1477	18180	873	1.0	874	4.64	1487
21610	8620	0.1	860.28	4.57	1477	18190	890	1.0	890	4.73	1487
21620	8500	0.1	849.15	4.51	1477	18200	909	1.0	910	4.83	1487
21630	8540	0.1	854.00	4.54	1477	18210	896	1.0	896	4.76	1486
21640	9250	0.1	925.00	4.92	1477	18220	876	1.0	876	4.65	1486
21650	8350	0.1	834.17	4.43	1477	18230	880	1.0	880	4.68	1486
21660	8680	0.1	867.13	4.61	1477	18240	866	1.0	866	4.60	1486
21670	9410	0.1	940.06	5.00	1477	18250	898	1.0	899	4.77	1486
21680	8610	0.1	861.00	4.58	1477	18260	868	1.0	869	4.62	1486
21690	8650	0.1	863.27	4.59	1477	18270	872	1.0	872	4.63	1486
21700	8510	0.1	850.15	4.52	1477	18280	899	1.0	899	4.78	1486
21710	8830	0.1	882.12	4.68	1477	18290	911	1.0	911	4.84	1486
21720	9430	0.1	942.06	5.01	1477	18300	867	1.0	867	4.61	1486
21730	10600	0.1	1060.00	5.65	1477	18310	910	1.0	909	4.83	1486
21740	8880	0.1	885.34	4.70	1477	18320	913	1.0	912	4.85	1486
21750	9020	0.1	902.00	4.80	1477	18330	881	1.0	881	4.68	1486
21760	9270	0.1	927.00	4.93	1477	18340	871	1.0	870	4.62	1486
21770	9870	0.1	985.03	5.23	1477	18350	897	1.0	897	4.77	1486
21780	8430	0.1	842.16	4.48	1477	18360	886	1.0	887	4.71	1486
21790	9650	0.1	964.04	5.12	1477	18370	863	1.0	864	4.59	1486
21800	9380	0.1	937.06	4.98	1477	18380	954	1.0	954	5.07	1486
21810	9410	0.1	941.00	5.01	1476	18390	900	1.0	899	4.78	1486
21820	9880	0.1	987.01	5.24	1476	18400	897	1.0	897	4.77	1486
21830	9610	0.1	960.04	5.10	1476	18410	930	1.0	931	4.95	1486
21840	7670	0.1	767.00	4.08	1476	18420	916	1.0	916	4.87	1486
21850	8230	0.1	818.89	4.35	1476	18430	924	1.0	924	4.91	1486
21860	9240	0.1	922.15	4.90	1476	18440	923	1.0	923	4.90	1486
21870	8220	0.1	821.18	4.37	1476	18450	888	1.0	888	4.72	1486
21880	10300	0.1	1027.94	5.45	1476	18460	943	1.0	944	5.01	1486
21890	10300	0.1	1028.97	5.44	1476	18470	889	1.0	888	4.72	1486
21900	9530	0.1	950.14	5.05	1476	18480	917	1.0	918	4.88	1486
21910	8750	0.1	872.38	4.63	1476	18490	937	1.0	936	4.98	1486

21920	10500	0.1	1048.95	5.56	1476	18500	895	1.0	895	4.76	1486
21930	9820	0.1	980.04	5.21	1476	18510	914	1.0	914	4.86	1486
21940	8940	0.1	894.00	4.75	1476	18520	944	1.0	944	5.01	1486
21950	9160	0.1	916.00	4.86	1476	18530	922	1.0	922	4.90	1486
21960	10000	0.1	998.00	5.33	1476	18540	908	1.0	908	4.82	1486
21970	10000	0.1	999.00	5.31	1476	18550	896	1.0	896	4.76	1486
21980	9010	0.1	900.10	4.78	1476	18560	907	1.0	907	4.82	1486
21990	9090	0.1	909.00	4.83	1476	18570	960	1.0	960	5.10	1485
22000	7900	0.1	787.63	4.19	1476	18580	980	1.0	979	5.20	1485
22010	9790	0.1	978.02	5.20	1476	18590	965	1.0	965	5.13	1485
22020	10300	0.1	1030.00	5.45	1476	18600	958	1.0	958	5.09	1485
22030	10800	0.1	1078.92	5.75	1476	18610	976	1.0	975	5.18	1485
22040	9690	0.1	969.00	5.15	1476	18620	982	1.0	981	5.21	1485
22050	10700	0.1	1067.86	5.67	1476	18630	966	1.0	966	5.13	1485
22060	9350	0.1	935.00	4.97	1476	18640	898	1.0	899	4.78	1485
22070	9980	0.1	998.00	5.31	1475	18650	946	1.0	947	5.03	1485
22080	10700	0.1	1067.86	5.70	1476	18660	930	1.0	930	4.94	1485
22090	10100	0.1	1010.00	5.37	1476	18670	991	1.0	991	5.27	1485
22100	10300	0.1	1026.91	5.44	1476	18680	994	1.0	994	5.28	1485
22110	10300	0.1	1027.94	5.48	1476	18690	962	1.0	962	5.11	1485
22120	9050	0.1	904.10	4.81	1476	18700	959	1.0	959	5.10	1485
22130	10500	0.1	1050.00	5.60	1476	18710	919	1.0	919	4.88	1485
22140	8950	0.1	895.00	4.76	1476	18720	939	1.0	939	4.99	1485
22150	9400	0.1	938.12	4.99	1476	18730	927	1.0	926	4.92	1485
22160	11300	0.1	1128.87	5.98	1476	18740	970	1.0	970	5.16	1485
22170	11600	0.1	1158.84	6.16	1475	18750	973	1.0	972	5.17	1485
22180	10500	0.1	1050.00	5.58	1475	18760	941	1.0	940	5.00	1485
22190	10100	0.1	1007.98	5.33	1475	18770	933	1.0	932	4.95	1485
22200	11600	0.1	1160.00	6.14	1475	18780	896	1.0	896	4.76	1485
22210	8240	0.1	824.00	4.38	1475	18790	965	1.0	964	5.12	1485
22220	8550	0.1	853.29	4.54	1475	18800	931	1.0	931	4.95	1485
22230	10300	0.1	1030.00	5.49	1475	18810	980	1.0	980	5.21	1485
22240	9650	0.1	965.00	5.13	1475	18820	952	1.0	952	5.06	1485
22250	9560	0.1	954.09	5.07	1475	18830	946	1.0	945	5.02	1485
22260	9600	0.1	959.04	5.09	1475	18840	961	1.0	959	5.10	1485
22270	10000	0.1	999.00	5.32	1475	18850	955	1.0	954	5.07	1485
22280	9830	0.1	981.03	5.22	1475	18860	931	1.0	930	4.94	1485
22290	9970	0.1	997.00	5.30	1475	18870	917	1.0	917	4.87	1485
22300	10500	0.1	1050.00	5.58	1475	18880	1010	1.0	1010	5.36	1485
22310	9990	0.1	997.00	5.30	1475	18890	994	1.0	994	5.28	1485
22320	10200	0.1	1018.98	5.43	1475	18900	989	1.0	990	5.26	1485
22330	9900	0.1	990.00	5.26	1475	18910	980	1.0	980	5.21	1485
22340	8760	0.1	874.25	4.65	1475	18920	957	1.0	957	5.08	1485
22350	9870	0.1	986.01	5.24	1475	18930	984	1.0	984	5.23	1484
22360	9860	0.1	985.01	5.23	1475	18940	983	1.0	984	5.23	1484
22370	10800	0.1	1077.84	5.72	1475	18950	994	1.0	994	5.28	1484
22380	9850	0.1	984.02	5.23	1475	18960	966	1.0	966	5.13	1484
22390	10300	0.1	1030.00	5.48	1475	18970	989	1.0	988	5.25	1484
22400	10300	0.1	1030.00	5.48	1475	18980	998	1.0	998	5.30	1484
22410	10900	0.1	1090.00	5.81	1475	18990	982	1.0	981	5.21	1484
22420	9360	0.1	935.06	4.97	1475	19000	990	1.0	990	5.26	1484
22430	9780	0.1	977.02	5.19	1475	19010	990	1.0	990	5.26	1484
22440	9030	0.1	901.19	4.79	1475	19020	1040	1.0	1040	5.54	1484
22450	10100	0.1	1008.99	5.35	1475	19030	979	1.0	979	5.20	1484
22460	9720	0.1	970.06	5.16	1475	19040	1040	1.0	1040	5.52	1484
22470	9460	0.1	945.05	5.02	1475	19050	1010	1.0	1010	5.34	1484
22480	10700	0.1	1067.86	5.66	1475	19060	1020	1.0	1020	5.42	1484
22490	10500	0.1	1047.90	5.59	1475	19070	965	1.0	964	5.12	1484
22500	10800	0.1	1080.00	5.74	1475	19080	972	1.0	972	5.17	1484
22510	9920	0.1	991.01	5.27	1475	19090	975	1.0	975	5.18	1484
22520	11000	0.1	1100.00	5.87	1475	19100	1010	1.0	1010	5.37	1484
22530	11200	0.1	1117.76	5.93	1474	19110	1000	1.0	1000	5.33	1484
22540	12400	0.1	1240.00	6.61	1474	19120	1010	1.0	1010	5.38	1484
22550	11700	0.1	1170.00	6.22	1474	19130	1010	1.0	1010	5.35	1484
22560	9480	0.1	945.16	5.02	1474	19140	1010	1.0	1020	5.40	1484
22570	9520	0.1	951.05	5.05	1474	19150	1040	1.0	1040	5.51	1484
22580	10300	0.1	1030.00	5.49	1474	19160	1040	1.0	1040	5.52	1484
22590	10700	0.1	1067.86	5.67	1474	19170	1010	1.0	1010	5.38	1484
22600	9150	0.1	914.09	4.86	1474	19180	1010	1.0	1010	5.36	1484

22610	9760	0.1	974.05	5.18	1474	19190	1010	1.0	1010	5.38	1484
22620	11900	0.1	1190.00	6.33	1474	19200	1020	1.0	1020	5.42	1484
22630	9690	0.1	969.00	5.16	1474	19210	1040	1.0	1040	5.52	1484
22640	12000	0.1	1197.60	6.35	1474	19220	1010	1.0	1010	5.36	1484
22650	11500	0.1	1150.00	6.13	1474	19230	1040	1.0	1040	5.51	1484
22660	10700	0.1	1070.00	5.68	1474	19240	999	1.0	999	5.31	1484
22670	11200	0.1	1118.88	5.97	1474	19250	1040	1.0	1040	5.53	1484
22680	11100	0.1	1110.00	5.90	1474	19260	1110	1.0	1110	5.89	1484
22690	12100	0.1	1207.58	6.40	1474	19270	1020	1.0	1020	5.44	1484
22700	11100	0.1	1108.89	5.88	1474	19280	1100	1.0	1100	5.83	1484
22710	10500	0.1	1048.95	5.57	1474	19290	1080	1.0	1080	5.72	1483
22720	11000	0.1	1098.90	5.82	1474	19300	1120	1.0	1120	5.94	1483
22730	11700	0.1	1170.00	6.21	1474	19310	1060	1.0	1060	5.64	1483
22740	12200	0.1	1217.56	6.49	1474	19320	1120	1.0	1120	5.94	1483
22750	11000	0.1	1100.00	5.86	1474	19330	1100	1.0	1100	5.87	1483
22760	14000	0.1	1398.60	7.45	1474	19340	1080	1.0	1080	5.74	1483
22770	11900	0.1	1187.62	6.32	1474	19350	1090	1.0	1100	5.82	1483
22780	11900	0.1	1190.00	6.35	1474	19360	1080	1.0	1080	5.73	1483
22790	12000	0.1	1200.00	6.39	1474	19370	1120	1.0	1130	5.98	1483
22800	12000	0.1	1198.80	6.39	1474	19380	1140	1.0	1140	6.03	1483
22810	12600	0.1	1258.74	6.67	1474	19390	1110	1.0	1110	5.91	1483
22820	12700	0.1	1270.00	6.76	1474	19400	1080	1.0	1080	5.76	1483
22830	13000	0.1	1298.70	6.91	1474	19410	1100	1.0	1100	5.82	1483
22840	12300	0.1	1227.54	6.54	1474	19420	1130	1.0	1130	5.99	1483
22850	12600	0.1	1260.00	6.71	1474	19430	1100	1.0	1100	5.85	1483
22860	13000	0.1	1298.70	6.91	1474	19440	1150	1.0	1150	6.10	1483
22870	12200	0.1	1220.00	6.46	1474	19450	1180	1.0	1180	6.26	1483
22880	12100	0.1	1210.00	6.42	1474	19460	1120	1.0	1120	5.97	1483
22890	11900	0.1	1188.81	6.31	1473	19470	1110	1.0	1110	5.92	1483
22900	13500	0.1	1350.00	7.18	1473	19480	1120	1.0	1120	5.98	1483
22910	14900	0.1	1488.51	7.90	1473	19490	1110	1.0	1110	5.91	1483
22920	14400	0.1	1440.00	7.67	1473	19500	1130	1.0	1130	6.03	1483
22930	13500	0.1	1350.00	7.17	1473	19510	1130	1.0	1140	6.03	1483
22940	14200	0.1	1420.00	7.53	1473	19520	1060	1.0	1060	5.65	1483
22950	13400	0.1	1340.00	7.12	1473	19530	1120	1.0	1120	5.95	1483
22960	13900	0.1	1388.61	7.36	1473	19540	1180	1.0	1190	6.30	1483
22970	13500	0.1	1350.00	7.15	1473	19550	1170	1.0	1170	6.20	1483
22980	14300	0.1	1430.00	7.58	1473	19560	1090	1.0	1090	5.79	1483
22990	13900	0.1	1385.83	7.37	1473	19570	1230	1.0	1230	6.52	1483
23000	14000	0.1	1400.00	7.42	1473	19580	1130	1.0	1130	6.01	1483
23010	13700	0.1	1367.26	7.25	1473	19590	1130	1.0	1120	5.97	1483
23020	14400	0.1	1440.00	7.64	1473	19600	1180	1.0	1170	6.24	1483
23030	14100	0.1	1410.00	7.47	1473	19610	1160	1.0	1160	6.18	1483
23040	12900	0.1	1290.00	6.84	1473	19620	1200	1.0	1200	6.36	1483
23050	15700	0.1	1570.00	8.36	1473	19630	1170	1.0	1170	6.23	1483
23060	15500	0.1	1550.00	8.26	1473	19640	1200	1.0	1200	6.40	1483
23070	16100	0.1	1610.00	8.53	1473	19650	1180	1.0	1180	6.28	1482
23080	15400	0.1	1538.46	8.18	1473	19660	1140	1.0	1140	6.03	1482
23090	16100	0.1	1610.00	8.58	1473	19670	1110	1.0	1110	5.92	1482
23100	15800	0.1	1578.42	8.37	1473	19680	1200	1.0	1200	6.37	1482
23110	15400	0.1	1536.92	8.14	1473	19690	1160	1.0	1150	6.14	1482
23120	15200	0.1	1520.00	8.08	1473	19700	1140	1.0	1140	6.06	1482
23130	15800	0.1	1578.42	8.41	1473	19710	1220	1.0	1220	6.47	1482
23140	14600	0.1	1460.00	7.75	1473	19720	1220	1.0	1220	6.48	1482
23150	15800	0.1	1580.00	8.40	1473	19730	1210	1.0	1210	6.43	1482
23160	15800	0.1	1578.42	8.40	1473	19740	1260	1.0	1260	6.72	1482
23170	16500	0.1	1645.05	8.74	1473	19750	1170	1.0	1170	6.22	1482
23180	15600	0.1	1560.00	8.30	1473	19760	1260	1.0	1260	6.70	1482
23190	16900	0.1	1688.31	8.98	1473	19770	1220	1.0	1220	6.49	1482
23200	15600	0.1	1560.00	8.33	1473	19780	1240	1.0	1240	6.57	1482
23210	14600	0.1	1458.54	7.74	1473	19790	1230	1.0	1230	6.55	1482
23220	15900	0.1	1590.00	8.46	1473	19800	1290	1.0	1290	6.84	1482
23230	17600	0.1	1760.00	9.39	1473	19810	1300	1.0	1300	6.93	1482
23240	19000	0.1	1900.00	10.10	1473	19820	1300	1.0	1290	6.87	1482
23250	17200	0.1	1720.00	9.13	1472	19830	1270	1.0	1280	6.78	1482
23260	16900	0.1	1688.31	8.97	1472	19840	1270	1.0	1270	6.76	1482
23270	19300	0.1	1930.00	10.30	1472	19850	1230	1.0	1230	6.55	1482
23280	16600	0.1	1660.00	8.80	1472	19860	1250	1.0	1250	6.63	1482
23290	18400	0.1	1840.00	9.78	1472	19870	1290	1.0	1290	6.85	1482

23300	17700	0.1	1770.00	9.39	1472	19880	1300	1.0	1300	6.90	1482
23310	20300	0.1	2027.97	10.80	1472	19890	1240	1.0	1240	6.60	1482
23320	18900	0.1	1890.00	10.00	1472	19900	1260	1.0	1260	6.71	1482
23330	18300	0.1	1828.17	9.73	1472	19910	1290	1.0	1290	6.86	1482
23340	17600	0.1	1758.24	9.35	1472	19920	1280	1.0	1280	6.82	1482
23350	17400	0.1	1738.26	9.22	1472	19930	1310	1.0	1300	6.92	1482
23360	18400	0.1	1836.32	9.75	1472	19940	1320	1.0	1320	6.99	1482
23370	19500	0.1	1950.00	10.40	1472	19950	1240	1.0	1240	6.60	1482
23380	19500	0.1	1950.00	10.40	1472	19960	1350	1.0	1340	7.13	1482
23390	19700	0.1	1970.00	10.50	1472	19970	1400	1.0	1400	7.43	1482
23400	18000	0.1	1800.00	9.57	1472	19980	1320	1.0	1320	7.01	1482
23410	20500	0.1	2050.00	10.90	1472	19990	1340	1.0	1340	7.11	1482
23420	18300	0.1	1830.00	9.74	1472	20000	1300	1.0	1300	6.91	1482
23430	21400	0.1	2140.00	11.40	1472	20010	1370	1.0	1370	7.26	1481
23440	19600	0.1	1960.00	10.40	1472	20020	1300	1.0	1300	6.91	1481
23450	20100	0.1	2010.00	10.70	1472	20030	1390	1.0	1390	7.37	1481
23460	18100	0.1	1808.19	9.58	1472	20040	1280	1.0	1280	6.81	1481
23470	19800	0.1	1978.02	10.50	1472	20050	1370	1.0	1370	7.29	1481
23480	21400	0.1	2140.00	11.40	1472	20060	1380	1.0	1380	7.32	1481
23490	18900	0.1	1890.00	10.10	1472	20070	1420	1.0	1420	7.54	1481
23500	19400	0.1	1940.00	10.30	1472	20080	1340	1.0	1340	7.13	1481
23510	21700	0.1	2170.00	11.50	1472	20090	1380	1.0	1380	7.32	1481
23520	19900	0.1	1990.00	10.60	1472	20100	1350	1.0	1350	7.18	1481
23530	21900	0.1	2190.00	11.70	1472	20110	1380	1.0	1380	7.34	1481
23540	23100	0.1	2307.69	12.20	1472	20120	1430	1.0	1430	7.60	1481
23550	20300	0.1	2030.00	10.80	1472	20130	1330	1.0	1330	7.05	1481
23560	20400	0.1	2035.92	10.80	1472	20140	1330	1.0	1330	7.08	1481
23570	22100	0.1	2210.00	11.80	1472	20150	1470	1.0	1470	7.80	1481
23580	21900	0.1	2190.00	11.60	1472	20160	1460	1.0	1460	7.76	1481
23590	20200	0.1	2017.98	10.70	1472	20170	1410	1.0	1410	7.49	1481
23600	25200	0.1	2514.96	13.30	1472	20180	1390	1.0	1390	7.41	1481
23610	21200	0.1	2120.00	11.30	1471	20190	1390	1.0	1390	7.39	1481
23620	22500	0.1	2250.00	12.00	1471	20200	1400	1.0	1390	7.41	1481
23630	21700	0.1	2167.83	11.50	1471	20210	1370	1.0	1370	7.26	1481
23640	25300	0.1	2530.00	13.40	1471	20220	1490	1.0	1490	7.94	1481
23650	26100	0.1	2610.00	13.90	1471	20230	1440	1.0	1440	7.65	1481
23660	23000	0.1	2300.00	12.20	1471	20240	1420	1.0	1420	7.53	1481
23670	20600	0.1	2057.94	10.90	1471	20250	1460	1.0	1460	7.76	1481
23680	25000	0.1	2500.00	13.30	1471	20260	1460	1.0	1460	7.76	1481
23690	20200	0.1	2013.94	10.70	1471	20270	1390	1.0	1390	7.40	1481
23700	20700	0.1	2070.00	11.00	1471	20280	1430	1.0	1430	7.59	1481
23710	24900	0.1	2490.00	13.30	1471	20290	1410	1.0	1410	7.50	1481
23720	22600	0.1	2257.74	12.00	1471	20300	1450	1.0	1450	7.69	1481
23730	23400	0.1	2340.00	12.40	1471	20310	1430	1.0	1430	7.60	1481
23740	24400	0.1	2440.00	13.00	1471	20320	1400	1.0	1400	7.46	1481
23750	25100	0.1	2507.49	13.30	1471	20330	1410	1.0	1410	7.49	1481
23760	19700	0.1	1970.00	10.50	1471	20340	1430	1.0	1430	7.61	1481
23770	22500	0.1	2250.00	12.00	1471	20350	1500	1.0	1500	7.95	1481
23780	28100	0.1	2810.00	14.90	1471	20360	1450	1.0	1450	7.70	1481
23790	24800	0.1	2480.00	13.20	1471	20370	1380	1.0	1380	7.33	1480
23800	23400	0.1	2340.00	12.40	1471	20380	1390	1.0	1390	7.40	1480
23810	24400	0.1	2440.00	13.00	1471	20390	1470	1.0	1470	7.80	1480
23820	25100	0.1	2507.49	13.30	1471	20400	1520	1.0	1510	8.04	1480
23830	19700	0.1	1970.00	10.50	1471	20410	1520	1.0	1520	8.08	1480
23840	22500	0.1	2250.00	12.00	1471	20420	1490	1.0	1490	7.91	1480
23850	28100	0.1	2810.00	14.90	1471	20430	1560	1.0	1560	8.28	1480
23860	30800	0.1	3080.00	15.00	1471	20440	1520	1.0	1520	8.08	1480
23870	31400	0.1	3140.00	15.10	1471	20450	1540	1.0	1540	8.16	1480
23880	32100	0.1	3210.00	14.10	1470	20460	1590	1.0	1590	8.47	1480
23890	32000	0.1	3200.00	14.50	1470	20470	1440	1.0	1440	7.64	1480
						20480	1540	1.0	1540	8.16	1480
						20490	1550	1.0	1550	8.22	1480
						20500	1530	1.0	1530	8.11	1480
						20510	1530	1.0	1530	8.12	1480
						20520	1490	1.0	1490	7.94	1480
						20530	1570	1.0	1570	8.33	1480
						20540	1430	1.0	1440	7.63	1480
						20550	1540	1.0	1540	8.16	1480
						20560	1530	1.0	1530	8.14	1480

20570	1510	1.0	1500	8.00	1480
20580	1520	1.0	1520	8.09	1480
20590	1540	1.0	1540	8.17	1480
20600	1550	1.0	1550	8.23	1480
20610	1540	1.0	1540	8.17	1480
20620	1570	1.0	1570	8.34	1480
20630	1540	1.0	1540	8.17	1480
20640	1540	1.0	1540	8.17	1480
20650	1530	1.0	1530	8.14	1480
20660	1630	1.0	1630	8.66	1480
20670	1550	1.0	1550	8.23	1480
20680	1640	1.0	1640	8.71	1480
20690	1640	1.0	1640	8.72	1480
20700	1570	1.0	1570	8.32	1480
20710	1550	1.0	1550	8.22	1480
20720	1550	1.0	1550	8.26	1480
20730	1570	1.0	1570	8.33	1479
20740	1630	1.0	1630	8.65	1479
20750	1580	1.0	1580	8.42	1479
20760	1610	1.0	1610	8.53	1479
20770	1630	1.0	1630	8.67	1479
20780	1620	1.0	1620	8.62	1479
20790	1650	1.0	1650	8.76	1479
20800	1680	1.0	1690	8.97	1479
20810	1640	1.0	1640	8.72	1479
20820	1610	1.0	1610	8.58	1479
20830	1700	1.0	1700	9.04	1479
20840	1670	1.0	1670	8.86	1479
20850	1650	1.0	1650	8.78	1479
20860	1690	1.0	1690	8.98	1479
20870	1660	1.0	1660	8.81	1479
20880	1660	1.0	1660	8.83	1479
20890	1690	1.0	1680	8.95	1479
20900	1680	1.0	1680	8.95	1479
20910	1780	1.0	1780	9.46	1479
20920	1830	1.0	1830	9.70	1479
20930	1810	1.0	1810	9.63	1479
20940	1750	1.0	1750	9.27	1479
20950	1720	1.0	1720	9.15	1479
20960	1810	1.0	1810	9.60	1479
20970	1710	1.0	1710	9.08	1479
20980	1770	1.0	1770	9.40	1479
20990	1710	1.0	1710	9.11	1479
21000	1790	1.0	1790	9.50	1479
21010	1750	1.0	1740	9.27	1479
21020	1720	1.0	1720	9.13	1479
21030	1840	1.0	1830	9.75	1479
21040	1810	1.0	1820	9.65	1479
21050	1720	1.0	1720	9.14	1479
21060	1700	1.0	1700	9.05	1479
21070	1830	1.0	1830	9.74	1479
21080	1740	1.0	1730	9.21	1479
21090	1770	1.0	1770	9.43	1478
21100	1780	1.0	1770	9.43	1478
21110	1820	1.0	1820	9.65	1478
21120	1740	1.0	1740	9.23	1478
21130	1790	1.0	1790	9.50	1478
21140	1740	1.0	1740	9.27	1478
21150	1820	1.0	1820	9.66	1478
21160	1770	1.0	1770	9.39	1478
21170	1780	1.0	1780	9.48	1478
21180	1800	1.0	1800	9.56	1478
21190	1820	1.0	1820	9.68	1478
21200	1850	1.0	1850	9.83	1478
21210	1870	1.0	1870	9.95	1478
21220	1830	1.0	1830	9.70	1478
21230	1880	1.0	1880	9.98	1478
21240	1790	1.0	1790	9.49	1478
21250	1950	1.0	1950	10.40	1478

21260	1830	1.0	1830	9.74	1478
21270	1860	1.0	1860	9.90	1478
21280	1830	1.0	1830	9.72	1478
21290	1890	1.0	1890	10.00	1478
21300	1860	1.0	1860	9.88	1478
21310	1870	1.0	1870	9.96	1478
21320	1850	1.0	1850	9.82	1478
21330	1850	1.0	1850	9.81	1478
21340	1940	1.0	1930	10.30	1478
21350	1870	1.0	1870	9.92	1478
21360	1830	1.0	1830	9.72	1478
21370	1860	1.0	1860	9.89	1478
21380	1940	1.0	1940	10.30	1478
21390	1880	1.0	1880	9.98	1478
21400	1880	1.0	1880	9.97	1478
21410	2050	1.0	2050	10.90	1478
21420	1950	1.0	1950	10.40	1478
21430	1930	1.0	1940	10.30	1478
21440	1970	1.0	1970	10.50	1478
21450	2030	1.0	2030	10.80	1477
21460	1920	1.0	1920	10.20	1477
21470	1930	1.0	1930	10.30	1477
21480	1930	1.0	1930	10.30	1477
21490	2050	1.0	2060	10.90	1477
21500	1980	1.0	1980	10.50	1477
21510	2000	1.0	2000	10.60	1477
21520	1990	1.0	1980	10.50	1477
21530	1970	1.0	1970	10.50	1477
21540	2060	1.0	2070	11.00	1477
21550	2090	1.0	2090	11.10	1477
21560	1930	1.0	1930	10.20	1477
21570	2010	1.0	2010	10.70	1477
21580	2030	1.0	2030	10.80	1477
21590	1920	1.0	1930	10.20	1477
21600	2010	1.0	2010	10.70	1477
21610	1990	1.0	1990	10.60	1477
21620	2000	1.0	2000	10.60	1477
21630	2080	1.0	2080	11.00	1477
21640	1960	1.0	1960	10.40	1477
21650	1960	1.0	1960	10.40	1477
21660	1950	1.0	1950	10.30	1477
21670	2110	1.0	2110	11.20	1477
21680	2000	1.0	2000	10.60	1477
21690	1960	1.0	1950	10.40	1477
21700	2040	1.0	2040	10.90	1477
21710	2070	1.0	2060	11.00	1477
21720	2080	1.0	2080	11.00	1477
21730	2020	1.0	2020	10.70	1477
21740	2160	1.0	2160	11.50	1477
21750	2000	1.0	2000	10.60	1477
21760	2130	1.0	2130	11.30	1477
21770	2190	1.0	2190	11.70	1477
21780	2080	1.0	2080	11.00	1477
21790	2010	1.0	2010	10.70	1477
21800	2100	1.0	2090	11.10	1477
21810	2080	1.0	2070	11.00	1476
21820	2080	1.0	2070	11.00	1476
21830	2120	1.0	2120	11.30	1476
21840	2180	1.0	2180	11.60	1476
21850	2020	1.0	2020	10.70	1476
21860	2250	1.0	2250	12.00	1476
21870	2150	1.0	2150	11.40	1476
21880	2070	1.0	2060	11.00	1476
21890	2250	1.0	2240	11.90	1476
21900	2270	1.0	2270	12.00	1476
21910	2100	1.0	2100	11.10	1476
21920	2000	1.0	2000	10.60	1476
21930	2100	1.0	2100	11.20	1476
21940	2060	1.0	2060	10.90	1476

214

21950	2020	1.0	2020	10.70	1476
21960	2160	1.0	2160	11.50	1476
21970	2160	1.0	2160	11.50	1476
21980	2160	1.0	2160	11.50	1476
21990	2280	1.0	2280	12.10	1476
22000	2220	1.0	2220	11.80	1476
22010	2130	1.0	2120	11.30	1476
22020	2250	1.0	2250	12.00	1476
22030	2250	1.0	2250	11.90	1476
22040	2140	1.0	2140	11.40	1476
22050	2160	1.0	2170	11.50	1476
22060	2230	1.0	2230	11.90	1476
22070	2250	1.0	2250	12.00	1476
22080	2100	1.0	2100	11.10	1476
22090	2210	1.0	2210	11.70	1476
22100	2280	1.0	2280	12.10	1476
22110	2290	1.0	2290	12.20	1476
22120	2200	1.0	2200	11.70	1476
22130	2340	1.0	2340	12.40	1476
22140	2200	1.0	2190	11.70	1476
22150	2270	1.0	2270	12.10	1476
22160	2330	1.0	2330	12.40	1476
22170	2290	1.0	2290	12.20	1475
22180	2320	1.0	2310	12.30	1475
22190	2420	1.0	2420	12.80	1475
22200	2320	1.0	2320	12.30	1475
22210	2230	1.0	2230	11.80	1475
22220	2360	1.0	2360	12.50	1475
22230	2230	1.0	2230	11.80	1475
22240	2260	1.0	2260	12.00	1475
22250	2320	1.0	2320	12.30	1475
22260	2290	1.0	2280	12.10	1475
22270	2280	1.0	2280	12.10	1475
22280	2350	1.0	2350	12.50	1475
22290	2360	1.0	2360	12.50	1475
22300	2340	1.0	2340	12.50	1475
22310	2370	1.0	2370	12.60	1475
22320	2250	1.0	2250	12.00	1475
22330	2410	1.0	2410	12.80	1475
22340	2430	1.0	2420	12.90	1475
22350	2410	1.0	2410	12.80	1475
22360	2450	1.0	2450	13.00	1475
22370	2530	1.0	2520	13.40	1475
22380	2410	1.0	2410	12.80	1475
22390	2360	1.0	2360	12.50	1475
22400	2460	1.0	2460	13.10	1475
22410	2330	1.0	2330	12.40	1475
22420	2340	1.0	2340	12.40	1475
22430	2370	1.0	2360	12.60	1475
22440	2390	1.0	2390	12.70	1475
22450	2280	1.0	2280	12.10	1475
22460	2420	1.0	2410	12.80	1475
22470	2390	1.0	2390	12.70	1475
22480	2350	1.0	2340	12.50	1475
22490	2420	1.0	2420	12.90	1475
22500	2420	1.0	2420	12.90	1475
22510	2470	1.0	2470	13.10	1475
22520	2490	1.0	2490	13.20	1475
22530	2470	1.0	2470	13.10	1474
22540	2400	1.0	2400	12.70	1474
22550	2400	1.0	2400	12.80	1474
22560	2380	1.0	2380	12.60	1474
22570	2560	1.0	2560	13.60	1474
22580	2430	1.0	2430	12.90	1474
22590	2460	1.0	2470	13.10	1474
22600	2620	1.0	2620	13.90	1474
22610	2540	1.0	2540	13.50	1474
22620	2540	1.0	2530	13.50	1474
22630	2530	1.0	2530	13.40	1474

22640	2410	1.0	2410	12.80	1474
22650	2610	1.0	2610	13.90	1474
22660	2680	1.0	2680	14.30	1474
22670	2570	1.0	2570	13.70	1474
22680	2640	1.0	2650	14.10	1474
22690	2670	1.0	2670	14.20	1474
22700	2480	1.0	2480	13.20	1474
22710	2600	1.0	2600	13.80	1474
22720	2610	1.0	2600	13.80	1474
22730	2540	1.0	2530	13.50	1474
22740	2550	1.0	2550	13.50	1474
22750	2620	1.0	2620	13.90	1474
22760	2690	1.0	2690	14.30	1474
22770	2500	1.0	2500	13.30	1474
22780	2730	1.0	2740	14.50	1474
22790	2690	1.0	2690	14.30	1474
22800	2750	1.0	2750	14.60	1474
22810	2610	1.0	2610	13.90	1474
22820	2680	1.0	2680	14.20	1474
22830	2780	1.0	2780	14.80	1474
22840	2630	1.0	2630	14.00	1474
22850	2720	1.0	2720	14.50	1474
22860	2760	1.0	2760	14.70	1474
22870	2850	1.0	2850	15.20	1474
22880	2650	1.0	2650	14.10	1474
22890	2820	1.0	2820	15.00	1473
22900	2810	1.0	2810	14.90	1473
22910	2610	1.0	2610	13.90	1473
22920	2760	1.0	2750	14.60	1473
22930	2640	1.0	2640	14.00	1473
22940	2800	1.0	2800	14.90	1473
22950	2740	1.0	2740	14.60	1473
22960	2730	1.0	2730	14.50	1473
22970	2730	1.0	2730	14.50	1473
22980	2700	1.0	2700	14.40	1473
22990	2740	1.0	2740	14.60	1473
23000	2760	1.0	2760	14.70	1473
23010	2860	1.0	2850	15.20	1473
23020	2950	1.0	2950	15.70	1473
23030	2840	1.0	2840	15.10	1473
23040	2840	1.0	2840	15.10	1473
23050	2870	1.0	2880	15.30	1473
23060	2790	1.0	2790	14.80	1473
23070	2950	1.0	2950	15.70	1473
23080	2900	1.0	2900	15.40	1473
23090	2940	1.0	2940	15.60	1473
23100	2860	1.0	2860	15.20	1473
23110	2860	1.0	2860	15.20	1473
23120	2990	1.0	2990	15.90	1473
23130	2900	1.0	2890	15.40	1473
23140	3000	1.0	3000	15.90	1473
23150	2910	1.0	2910	15.50	1473
23160	2870	1.0	2870	15.30	1473
23170	3130	1.0	3130	16.60	1473
23180	2910	1.0	2910	15.40	1473
23190	3000	1.0	2990	15.90	1473
23200	2960	1.0	2960	15.70	1473
23210	2900	1.0	2900	15.40	1473
23220	3100	1.0	3100	16.50	1473
23230	2910	1.0	2910	15.50	1473
23240	3000	1.0	3000	15.90	1473
23250	3120	1.0	3120	16.60	1472
23260	2880	1.0	2880	15.30	1472
23270	3150	1.0	3150	16.70	1472
23280	2930	1.0	2930	15.60	1472
23290	2970	1.0	2980	15.80	1472
23300	3150	1.0	3150	16.80	1472
23310	3210	1.0	3210	17.00	1472
23320	3020	1.0	3020	16.10	1472

23330	3000	1.0	3000	15.90	1472
23340	2960	1.0	2960	15.70	1472
23350	2950	1.0	2940	15.60	1472
23360	3020	1.0	3020	16.00	1472
23370	2990	1.0	2990	15.90	1472
23380	3110	1.0	3110	16.50	1472
23390	3010	1.0	3000	16.00	1472
23400	3060	1.0	3060	16.30	1472
23410	3060	1.0	3060	16.30	1472
23420	3070	1.0	3070	16.30	1472
23430	3080	1.0	3070	16.30	1472
23440	3090	1.0	3100	16.40	1472
23450	3100	1.0	3100	16.50	1472
23460	3000	1.0	3000	15.90	1472
23470	3090	1.0	3090	16.40	1472
23480	3170	1.0	3170	16.80	1472
23490	3010	1.0	3010	16.00	1472
23500	3130	1.0	3130	16.60	1472
23510	3140	1.0	3140	16.70	1472
23520	2990	1.0	2990	15.90	1472
23530	3240	1.0	3240	17.20	1472
23540	3290	1.0	3290	17.50	1472
23550	3070	1.0	3070	16.30	1472
23560	3170	1.0	3170	16.80	1472
23570	3160	1.0	3160	16.80	1472
23580	3160	1.0	3150	16.80	1472
23590	3120	1.0	3120	16.60	1472
23600	3340	1.0	3340	17.70	1472
23610	3240	1.0	3240	17.20	1471
23620	3310	1.0	3310	17.60	1471
23630	3320	1.0	3330	17.70	1471
23640	3250	1.0	3240	17.20	1471
23650	3300	1.0	3290	17.50	1471
23660	3150	1.0	3150	16.70	1471
23670	3390	1.0	3380	18.00	1471
23680	3240	1.0	3240	17.20	1471
23690	3200	1.0	3190	17.00	1471
23700	3490	1.0	3490	18.50	1471
23710	3220	1.0	3220	17.10	1471
23720	3110	1.0	3110	16.50	1471
23730	3290	1.0	3290	17.50	1471
23740	3230	1.0	3220	17.10	1471
23750	3170	1.0	3160	16.80	1471
23760	3140	1.0	3140	16.70	1471
23770	3430	1.0	3430	18.20	1471
23780	3330	1.0	3320	17.60	1471
23790	3240	1.0	3240	17.20	1471
23800	3380	1.0	3380	18.00	1471
23810	3280	1.0	3280	17.40	1471
23820	3170	1.0	3170	16.80	1471
23830	3410	1.0	3410	18.10	1471
23840	3390	1.0	3390	18.00	1471
23850	3300	1.0	3300	17.50	1471
23860	3200	1.0	3200	17.00	1471
23870	3230	1.0	3230	17.10	1471
23880	3160	1.0	3160	16.80	1470
23890	3150	1.0	3150	16.70	1470

Table S4. Velocities (v), Reynold's number (Re) and lava friction coefficient (λ) values by solving iteratively equations 4, 5 and 6. S4-Earth and S4-Mars refer to Earth and Martian environments, respectively.

Table S4-Earth

m/s²	g	9.81			g	9.81			g	9.81			g	9.81			g	9.81	
lava flow thickness (m)	h	1			h	1			h	5			h	5			h	10	
lava bulk density (Kg/m³)	ρ	2698			ρ	2698			ρ	2698			ρ	2698			ρ	2698	
dynamic viscosity in Pa s	η	2			η	8			η	2			η	8			η	2	
Reynolds number	Re																		
lava friction coefficient	λ																		

(Additional parameter columns: g 9.81, h 10, ρ 2698, η 8)

slope	velocity (m/s)	Re	λ	velocity (m/s)	Re	λ	velocity (m/s)	Re	λ	velocity (m/s)	Re	λ	velocity (m/s)	Re	λ	velocity (m/s)	Re	λ
0.1	1.245	3291.924	0.044	0.894	602.234	0.086	1.473	9931	0.032	1.131	1897.861	0.054	1.631	21319.438	0.026	1.305	4401.826	0.040
0.2	1.891	5144.963	0.038	1.395	943.175	0.070	2.201	14850	0.028	1.724	2907.633	0.046	2.433	32803.704	0.023	1.965	6628.601	0.035
0.3	2.398	6460.984	0.036	1.800	1218.389	0.063	2.779	18741	0.027	2.199	3706.746	0.042	3.064	41586.340	0.022	2.492	8403.243	0.033
0.4	2.839	7656.400	0.034	2.150	1447.076	0.059	3.277	22105	0.025	2.610	4400.256	0.040	3.604	48786.221	0.021	2.947	9936.766	0.032
0.5	3.234	8722.808	0.033	2.469	1665.013	0.056	3.723	25117	0.025	2.979	5024.132	0.039	4.086	55104.151	0.020	3.354	11312.428	0.030
0.6	3.596	9694.464	0.032	2.761	1861.425	0.054	4.131	27863	0.024	3.318	5595.824	0.037	4.527	60941.305	0.020	3.728	12572.640	0.030
0.7	3.934	10617.837	0.031	3.033	2044.663	0.052	4.510	30416	0.024	3.633	6125.570	0.036	4.937	66473.009	0.020	4.075	13744.078	0.029
0.8	4.252	11483.643	0.030	3.291	2219.786	0.051	4.866	32820	0.023	3.930	6624.365	0.035	5.323	71745.515	0.019	4.402	14844.917	0.028
0.9	4.551	12281.853	0.030	3.534	2382.909	0.049	5.202	35086	0.023	4.212	7101.667	0.035	5.687	76751.972	0.019	4.711	15886.923	0.028
1.0	4.836	13035.588	0.029	3.768	2540.938	0.048	5.523	37249	0.022	4.480	7555.526	0.034	6.034	81486.335	0.019	5.005	16879.805	0.027
1.1	5.110	13774.075	0.029	3.991	2692.511	0.047	5.829	39316	0.022	4.736	7984.397	0.034	6.365	85962.010	0.019	5.287	17830.538	0.027
1.2	5.374	14499.859	0.028	4.206	2835.968	0.046	6.124	41303	0.022	4.983	8403.510	0.033	6.683	90213.126	0.018	5.558	18743.930	0.027
1.3	5.628	15196.304	0.028	4.413	2975.808	0.046	6.407	43219	0.022	5.222	8805.163	0.033	6.989	94284.775	0.018	5.819	19624.415	0.026
1.4	5.874	15854.162	0.028	4.615	3113.372	0.045	6.681	45067	0.021	5.452	9194.415	0.032	7.284	98220.546	0.018	6.071	20475.883	0.026
1.5	6.111	16482.874	0.027	4.810	3245.180	0.044	6.947	46859	0.021	5.676	9569.986	0.032	7.570	102053.498	0.018	6.316	21301.136	0.026
1.6	6.342	17098.927	0.027	4.999	3371.558	0.044	7.205	48597	0.021	5.893	9936.451	0.032	7.848	105802.790	0.018	6.554	22102.424	0.025
1.7	6.567	17709.612	0.027	5.184	3496.231	0.043	7.456	50290	0.021	6.104	10293.100	0.031	8.119	109474.604	0.018	6.785	22882.005	0.025
1.8	6.786	18309.941	0.027	5.364	3618.669	0.043	7.700	51940	0.021	6.310	10640.334	0.031	8.382	113065.994	0.018	7.010	23641.861	0.025
1.9	7.000	18891.695	0.027	5.540	3736.918	0.042	7.939	53546	0.021	6.511	10980.142	0.031	8.640	116570.328	0.017	7.230	24383.405	0.025
2.0	7.209	19452.948	0.026	5.712	3852.106	0.042	8.172	55116	0.020	6.708	11310.988	0.030	8.891	119982.289	0.017	7.445	25107.809	0.025
2.1	7.413	19999.093	0.026	5.881	3966.198	0.042	8.399	56654	0.020	6.900	11635.439	0.030	9.136	123300.640	0.017	7.655	25816.347	0.025
2.2	7.613	20536.604	0.026	6.046	4078.842	0.041	8.622	58158	0.020	7.089	11953.171	0.030	9.376	126529.624	0.017	7.861	26510.263	0.024
2.3	7.810	21067.528	0.026	6.208	4188.296	0.041	8.841	59631	0.020	7.273	12264.757	0.030	9.611	129678.258	0.017	8.062	27190.508	0.024
2.4	8.002	21589.739	0.026	6.367	4294.881	0.041	9.055	61077	0.020	7.455	12570.618	0.030	9.841	132758.338	0.017	8.260	27857.804	0.024
2.5	8.191	22100.955	0.025	6.524	4400.346	0.040	9.265	62495	0.020	7.633	12870.581	0.029	10.067	135782.210	0.017	8.455	28512.867	0.024
2.6	8.377	22601.564	0.025	6.677	4504.609	0.040	9.472	63888	0.020	7.808	13165.318	0.029	10.289	138760.421	0.017	8.645	29156.461	0.024
2.7	8.560	23093.861	0.025	6.829	4606.448	0.040	9.675	65258	0.020	7.980	13455.591	0.029	10.508	141700.198	0.017	8.833	29789.258	0.024
2.8	8.739	23579.260	0.025	6.977	4705.985	0.039	9.875	66606	0.020	8.149	13741.412	0.029	10.723	144604.915	0.017	9.018	30411.770	0.024
2.9	8.916	24057.076	0.025	7.124	4804.497	0.039	10.071	67931	0.020	8.316	14022.025	0.029	10.934	147474.285	0.017	9.199	31024.452	0.023
3.0	9.090	24526.302	0.025	7.268	4902.442	0.039	10.265	69237	0.019	8.480	14299.256	0.029	11.142	150305.513	0.017	9.378	31627.820	0.023
3.1	9.262	24987.767	0.025	7.411	4998.931	0.039	10.456	70524	0.019	8.641	14571.795	0.028	11.347	153094.661	0.016	9.554	32222.406	0.023
3.2	9.431	25443.870	0.025	7.551	5093.355	0.038	10.644	71791	0.019	8.801	14840.511	0.028	11.550	155838.112	0.016	9.728	32808.623	0.023
3.3	9.598	25896.048	0.025	7.689	5186.448	0.038	10.829	73041	0.019	8.958	15105.872	0.028	11.749	158533.841	0.016	9.900	33386.753	0.023
3.4	9.763	26342.919	0.024	7.826	5278.980	0.038	11.012	74274	0.019	9.114	15367.455	0.028	11.945	161182.053	0.016	10.069	33957.066	0.023
3.5	9.925	26781.753	0.024	7.961	5370.411	0.038	11.192	75492	0.019	9.267	15626.557	0.028	12.139	163785.330	0.016	10.236	34519.921	0.023
3.6	10.086	27212.098	0.024	8.095	5460.128	0.038	11.370	76693	0.019	9.418	15881.846	0.028	12.330	166348.256	0.016	10.401	35075.712	0.023
3.7	10.244	27637.180	0.024	8.226	5548.626	0.037	11.546	77879	0.019	9.568	16133.803	0.028	12.519	168876.531	0.016	10.563	35624.753	0.023
3.8	10.401	28060.610	0.024	8.357	5636.614	0.037	11.720	79052	0.019	9.716	16383.271	0.028	12.706	171376.001	0.016	10.724	36167.245	0.023
3.9	10.556	28481.837	0.024	8.485	5723.900	0.037	11.892	80211	0.019	9.862	16628.747	0.027	12.890	173851.718	0.016	10.883	36703.353	0.023
4.0	10.709	28896.385	0.024	8.613	5809.691	0.037	12.062	81356	0.019	10.006	16872.948	0.027	13.072	176307.137	0.016	11.040	37233.309	0.022

4.1	10.860	29301.983	0.024	8.739	5894.146	0.037	12.229	82487	0.019	10.149	17113.883	0.027	13.252	178743.719	0.016	11.196	37757.406	0.022
4.2	11.010	29702.866	0.024	8.863	5978.232	0.037	12.396	83608	0.019	10.290	17351.059	0.027	13.431	181161.002	0.016	11.349	38275.896	0.022
4.3	11.158	30104.421	0.024	8.987	6061.885	0.036	12.560	84716	0.019	10.430	17585.670	0.027	13.607	183556.936	0.016	11.502	38788.930	0.022
4.4	11.305	30503.672	0.024	9.109	6144.185	0.036	12.722	85812	0.019	10.569	17821.893	0.027	13.782	185928.569	0.016	11.652	39296.613	0.022
4.5	11.450	30893.138	0.023	9.230	6225.259	0.036	12.883	86897	0.019	10.706	18052.822	0.027	13.955	188272.926	0.016	11.801	39799.090	0.022
4.6	11.594	31277.306	0.023	9.350	6306.172	0.036	13.042	87972	0.018	10.841	18280.681	0.027	14.126	190587.728	0.016	11.949	40296.581	0.022
4.7	11.736	31666.626	0.023	9.469	6386.850	0.036	13.200	89036	0.018	10.976	18507.625	0.027	14.295	192871.987	0.016	12.095	40789.305	0.022
4.8	11.877	32043.898	0.023	9.586	6466.029	0.036	13.356	90089	0.018	11.109	18732.287	0.027	14.462	195126.353	0.016	12.239	41277.411	0.022
4.9	12.017	32421.753	0.023	9.703	6544.846	0.036	13.511	91132	0.018	11.241	18953.999	0.027	14.628	197353.032	0.016	12.383	41760.980	0.022
5.0	12.155	32795.015	0.023	9.819	6622.401	0.035	13.664	92167	0.018	11.371	19176.643	0.026	14.793	199555.446	0.016	12.525	42240.096	0.022
5.1	12.292	33167.212	0.023	9.933	6699.419	0.035	13.816	93192	0.018	11.501	19393.433	0.026	14.956	201737.671	0.016	12.666	42714.889	0.022
5.2	12.429	33535.256	0.023	10.047	6776.110	0.035	13.967	94207	0.018	11.629	19608.218	0.026	15.117	203903.668	0.016	12.805	43185.521	0.022
5.3	12.563	33899.996	0.023	10.159	6852.377	0.035	14.116	95214	0.018	11.757	19823.533	0.026	15.277	206056.595	0.016	12.944	43652.123	0.022
5.4	12.697	34261.412	0.023	10.271	6928.066	0.035	14.264	96212	0.018	11.883	20041.342	0.026	15.436	208198.304	0.015	13.081	44114.783	0.022
5.5	12.830	34619.511	0.023	10.382	7002.967	0.035	14.411	97202	0.018	12.008	20247.487	0.026	15.593	210329.057	0.015	13.217	44573.587	0.022
5.6	12.961	34974.331	0.023	10.492	7076.982	0.035	14.557	98183	0.018	12.132	20457.104	0.026	15.749	212447.581	0.015	13.352	45028.650	0.021
5.7	13.092	35325.942	0.023	10.601	7150.221	0.035	14.701	99157	0.018	12.256	20668.782	0.026	15.904	214551.467	0.015	13.486	45480.090	0.021
5.8	13.221	35674.438	0.023	10.709	7222.947	0.035	14.844	100123	0.018	12.378	20873.621	0.026	16.058	216637.739	0.015	13.618	45927.985	0.021
5.9	13.349	36019.938	0.023	10.816	7295.392	0.034	14.986	101082	0.018	12.499	21077.868	0.026	16.210	218703.561	0.015	13.750	46372.372	0.021
6.0	13.477	36362.579	0.023	10.923	7367.591	0.034	15.127	102033	0.018	12.620	21281.303	0.026	16.362	220746.979	0.015	13.881	46813.311	0.021
6.1	13.603	36702.512	0.023	11.029	7439.346	0.034	15.267	102977	0.018	12.739	21479.108	0.026	16.512	222767.404	0.015	14.011	47250.922	0.021
6.2	13.729	37039.894	0.022	11.134	7510.391	0.034	15.406	103913	0.018	12.858	21684.532	0.026	16.660	224765.858	0.015	14.139	47685.343	0.021
6.3	13.853	37374.880	0.022	11.239	7580.608	0.034	15.544	104843	0.018	12.976	21882.622	0.026	16.808	226744.874	0.015	14.267	48116.662	0.021
6.4	13.977	37707.619	0.022	11.342	7650.152	0.034	15.681	105766	0.018	13.093	22077.631	0.026	16.955	228707.995	0.015	14.394	48544.881	0.021
6.5	14.100	38038.247	0.022	11.445	7719.337	0.034	15.817	106683	0.018	13.209	22276.087	0.025	17.100	230659.127	0.015	14.520	48970.004	0.021
6.6	14.222	38366.880	0.022	11.547	7788.386	0.034	15.951	107593	0.018	13.325	22471.633	0.025	17.245	232601.734	0.015	14.646	49392.114	0.021
6.7	14.343	38693.608	0.022	11.649	7857.233	0.034	16.085	108496	0.018	13.439	22661.601	0.025	17.388	234538.039	0.015	14.770	49811.358	0.021
6.8	14.463	39018.497	0.022	11.750	7925.572	0.034	16.218	109394	0.018	13.553	22857.254	0.025	17.531	236468.568	0.015	14.893	50227.834	0.021
6.9	14.583	39341.582	0.022	11.850	7993.135	0.034	16.351	110286	0.018	13.666	23042.110	0.025	17.673	238391.996	0.015	15.016	50641.535	0.021
7.0	14.702	39662.868	0.022	11.950	8059.961	0.033	16.482	111171	0.018	13.778	23234.116	0.025	17.813	240305.431	0.015	15.138	51052.440	0.021
7.1	14.820	39982.334	0.022	12.049	8126.393	0.033	16.612	112050	0.018	13.890	23421.990	0.025	17.953	242205.168	0.015	15.259	51460.619	0.021
7.2	14.937	40299.936	0.022	12.147	8192.763	0.033	16.742	112925	0.018	14.001	23608.209	0.025	18.092	244087.609	0.015	15.379	51866.216	0.021
7.3	15.054	40615.610	0.022	12.245	8259.055	0.033	16.871	113793	0.018	14.111	23795.050	0.025	18.230	245950.257	0.015	15.499	52269.323	0.021
7.4	15.170	40929.282	0.022	12.342	8324.895	0.033	16.999	114656	0.017	14.220	23978.620	0.025	18.367	247792.584	0.015	15.617	52669.921	0.021
7.5	15.285	41240.877	0.022	12.438	8389.938	0.033	17.126	115514	0.017	14.329	24161.325	0.025	18.503	249616.323	0.015	15.735	53067.975	0.021
7.6	15.399	41550.325	0.022	12.534	8454.276	0.033	17.252	116366	0.017	14.437	24345.959	0.025	18.638	251425.324	0.015	15.853	53463.547	0.021
7.7	15.513	41857.574	0.022	12.630	8518.390	0.033	17.378	117212	0.017	14.545	24523.777	0.025	18.773	253224.612	0.015	15.969	53856.767	0.021
7.8	15.626	42162.598	0.022	12.725	8582.610	0.033	17.503	118055	0.017	14.652	24707.564	0.025	18.906	255019.099	0.015	16.085	54247.700	0.021
7.9	15.738	42465.405	0.022	12.819	8646.685	0.033	17.627	118892	0.017	14.758	24885.925	0.025	19.039	256812.176	0.015	16.201	54636.337	0.021
8.0	15.850	42766.044	0.022	12.913	8710.042	0.033	17.750	119724	0.017	14.864	25064.185	0.025	19.171	258604.433	0.015	16.315	55022.699	0.021
8.1	15.961	43064.605	0.022	13.006	8772.544	0.033	17.873	120552	0.017	14.969	25241.606	0.025	19.303	260393.261	0.015	16.429	55406.845	0.020
8.2	16.071	43361.223	0.022	13.099	8834.774	0.033	17.995	121374	0.017	15.073	25417.156	0.025	19.434	262173.275	0.015	16.542	55788.795	0.020
8.3	16.181	43656.071	0.022	13.191	8897.270	0.033	18.116	122191	0.017	15.177	25591.949	0.025	19.564	263937.999	0.015	16.655	56168.553	0.020
8.4	16.290	43949.349	0.022	13.283	8959.661	0.032	18.236	123005	0.017	15.281	25765.865	0.025	19.693	265682.132	0.015	16.767	56546.225	0.020
8.5	16.399	44241.268	0.022	13.374	9021.125	0.032	18.356	123813	0.017	15.383	25940.276	0.024	19.821	267403.906	0.015	16.878	56921.921	0.020
8.6	16.507	44532.032	0.022	13.465	9081.787	0.032	18.476	124619	0.017	15.486	26113.093	0.024	19.948	269106.551	0.015	16.989	57295.558	0.020
8.7	16.614	44821.811	0.021	13.555	9142.716	0.032	18.594	125418	0.017	15.587	26283.690	0.024	20.075	270798.147	0.015	17.099	57667.048	0.020
8.8	16.721	45110.711	0.021	13.645	9203.967	0.032	18.712	126214	0.017	15.688	26453.949	0.024	20.202	272488.786	0.015	17.209	58036.599	0.020
8.9	16.828	45398.750	0.021	13.735	9264.185	0.032	18.830	127005	0.017	15.789	26622.993	0.024	20.327	274186.356	0.015	17.318	58404.342	0.020
9.0	16.933	45685.831	0.021	13.824	9323.449	0.032	18.946	127792	0.017	15.889	26796.353	0.024	20.452	275891.533	0.015	17.426	58770.038	0.020
9.1	17.039	45971.727	0.021	13.912	9383.576	0.032	19.062	128575	0.017	15.988	26956.379	0.024	20.577	277595.212	0.015	17.534	59133.780	0.020
9.2	17.144	46256.084	0.021	14.000	9443.498	0.032	19.178	129355	0.017	16.088	27129.162	0.024	20.700	279280.885	0.015	17.641	59495.864	0.020
9.3	17.248	46538.453	0.021	14.088	9501.488	0.032	19.293	130130	0.017	16.187	27300.933	0.024	20.823	280933.608	0.015	17.748	59855.969	0.020
9.4	17.351	46818.356	0.021	14.175	9561.270	0.032	19.407	130901	0.017	16.285	27461.697	0.024	20.946	282553.066	0.015	17.854	60214.213	0.020
9.5	17.454	47095.421	0.021	14.262	9619.246	0.032	19.521	131668	0.017	16.382	27623.361	0.024	21.067	284162.473	0.015	17.960	60570.770	0.020
9.6	17.557	47369.589	0.021	14.348	9677.707	0.032	19.634	132432	0.017	16.479	27788.022	0.024	21.188	285799.271	0.015	18.065	60925.681	0.020
9.7	17.659	47641.427	0.021	14.434	9735.613	0.032	19.747	133192	0.017	16.576	27948.672	0.024	21.309	287476.129	0.015	18.170	61278.688	0.020
9.8	17.760	47912.585	0.021	14.520	9793.321	0.032	19.859	133948	0.017	16.672	28113.356	0.024	21.429	289127.853	0.015	18.274	61630.101	0.020
9.9	17.862	48186.423	0.021	14.605	9850.746	0.032	19.970	134700	0.017	16.768	28276.221	0.024	21.548	290645.241	0.015	18.378	61979.786	0.020
10.0	17.963	48468.873	0.021	14.690	9907.908	0.032	20.081	135449	0.017	16.863	28435.616	0.024	21.667	292299.095	0.015	18.481	62327.810	0.020

Table S4-Mars

	Block 1		Block 2		Block 3		Block 4		Block 5		Block 6	
m/s²	g	3.72	g	3.72	g	3.72	g	3.72	g	3.72	g	3.72
lava flow thickness (m)	h	1	h	1	h	5	h	5	h	10	h	10
lava bulk density (Kg/m³)	ρ	2698	ρ	2698	ρ	2698	ρ	2698	ρ	2698	ρ	2698
dynamic viscosity in Pa s	η	2	η	8	η	2	η	8	η	2	η	8
Reynolds number	Re											
lava friction coefficient	λ											

slope	velocity (m/s)	Re	λ	velocity (m/s)	Re	λ	velocity (m/s)	Re	λ	velocity (m/s)	Re	λ	velocity (m/s)	Re	λ	velocity (m/s)	Re	λ
0.1	0.695	1875	0.054	0.468	315	0.118	0.835	5631	0.037	0.621	1046	0.067	0.938	12653	0.030	0.730	2460	0.049
0.2	1.059	2856	0.046	0.746	503	0.093	1.254	8458	0.033	0.956	1611	0.057	1.398	18865	0.027	1.107	3732	0.042
0.3	1.350	3643	0.043	0.972	656	0.082	1.588	10710	0.031	1.225	2066	0.052	1.764	23795	0.025	1.409	4751	0.039
0.4	1.603	4324	0.040	1.170	789	0.076	1.876	12654	0.030	1.459	2460	0.049	2.079	28040	0.024	1.670	5632	0.037
0.5	1.830	4936	0.039	1.348	909	0.071	2.134	14395	0.028	1.670	2816	0.047	2.360	31837	0.023	1.904	6423	0.036
0.6	2.038	5498	0.038	1.513	1020	0.068	2.371	15990	0.028	1.863	3142	0.045	2.618	35311	0.023	2.120	7148	0.035
0.7	2.232	6021	0.036	1.666	1124	0.065	2.590	17472	0.027	2.044	3446	0.044	2.857	38538	0.022	2.320	7824	0.034
0.8	2.414	6513	0.036	1.812	1222	0.063	2.797	18865	0.027	2.214	3733	0.042	3.081	41566	0.022	2.508	8458	0.033
0.9	2.587	6979	0.035	1.949	1315	0.061	2.992	20183	0.026	2.375	4004	0.041	3.294	44430	0.022	2.686	9060	0.032
1.0	2.752	7424	0.034	2.081	1404	0.060	3.178	21438	0.026	2.528	4263	0.041	3.496	47157	0.021	2.856	9633	0.032
1.1	2.909	7850	0.034	2.208	1489	0.059	3.357	22640	0.025	2.676	4512	0.040	3.689	49764	0.021	3.019	10182	0.031
1.2	3.061	8259	0.033	2.330	1571	0.057	3.528	23794	0.025	2.817	4751	0.039	3.875	52269	0.021	3.176	10710	0.031
1.3	3.208	8654	0.033	2.447	1651	0.056	3.693	24907	0.025	2.954	4981	0.039	4.054	54682	0.021	3.327	11219	0.030
1.4	3.349	9036	0.032	2.561	1728	0.055	3.852	25983	0.024	3.086	5205	0.038	4.226	57015	0.020	3.473	11712	0.030
1.5	3.487	9407	0.032	2.672	1802	0.055	4.007	27026	0.024	3.215	5421	0.038	4.394	59274	0.020	3.614	12189	0.030
1.6	3.620	9767	0.032	2.780	1875	0.054	4.157	28038	0.024	3.340	5632	0.037	4.556	61466	0.020	3.752	12653	0.030
1.7	3.750	10117	0.031	2.885	1946	0.053	4.303	29023	0.024	3.461	5836	0.037	4.715	63599	0.020	3.886	13104	0.029
1.8	3.876	10459	0.031	2.987	2015	0.052	4.445	29982	0.024	3.580	6036	0.036	4.869	65676	0.020	4.016	13544	0.029
1.9	4.000	10792	0.031	3.087	2082	0.052	4.584	30919	0.023	3.695	6231	0.036	5.019	67703	0.020	4.143	13974	0.029
2.0	4.121	11118	0.031	3.185	2149	0.051	4.720	31834	0.023	3.809	6422	0.036	5.165	69682	0.019	4.268	14393	0.028
2.1	4.239	11437	0.030	3.281	2213	0.051	4.852	32728	0.023	3.919	6609	0.035	5.309	71618	0.019	4.390	14804	0.028
2.2	4.355	11750	0.030	3.375	2277	0.050	4.982	33605	0.023	4.028	6792	0.035	5.449	73513	0.019	4.509	15206	0.028
2.3	4.468	12056	0.030	3.468	2339	0.050	5.109	34463	0.023	4.134	6971	0.035	5.587	75369	0.019	4.626	15600	0.028
2.4	4.580	12356	0.030	3.558	2400	0.049	5.234	35306	0.023	4.239	7147	0.035	5.722	77190	0.019	4.740	15987	0.028
2.5	4.689	12652	0.030	3.647	2460	0.049	5.357	36133	0.023	4.341	7320	0.034	5.855	78977	0.019	4.853	16367	0.028
2.6	4.797	12942	0.029	3.735	2519	0.048	5.477	36945	0.022	4.442	7490	0.034	5.985	80733	0.019	4.964	16740	0.027
2.7	4.902	13227	0.029	3.821	2577	0.048	5.596	37744	0.022	4.541	7657	0.034	6.113	82458	0.019	5.073	17107	0.027
2.8	5.006	13508	0.029	3.906	2635	0.048	5.712	38529	0.022	4.639	7822	0.034	6.238	84155	0.019	5.180	17468	0.027
2.9	5.109	13784	0.029	3.989	2691	0.047	5.827	39303	0.022	4.735	7984	0.034	6.362	85825	0.019	5.285	17824	0.027
3.0	5.210	14056	0.029	4.072	2746	0.047	5.940	40064	0.022	4.829	8144	0.033	6.484	87470	0.019	5.389	18174	0.027
3.1	5.309	14324	0.029	4.153	2801	0.047	6.051	40814	0.022	4.923	8301	0.033	6.604	89090	0.018	5.491	18519	0.027
3.2	5.407	14589	0.028	4.233	2855	0.046	6.161	41554	0.022	5.015	8456	0.033	6.722	90686	0.018	5.592	18859	0.027
3.3	5.504	14850	0.028	4.312	2909	0.046	6.269	42283	0.022	5.105	8609	0.033	6.839	92260	0.018	5.692	19195	0.026
3.4	5.599	15107	0.028	4.390	2961	0.046	6.376	43003	0.022	5.195	8760	0.033	6.954	93813	0.018	5.790	19526	0.026
3.5	5.694	15361	0.028	4.468	3013	0.045	6.481	43713	0.022	5.284	8909	0.033	7.068	95346	0.018	5.887	19853	0.026
3.6	5.787	15612	0.028	4.544	3065	0.045	6.585	44414	0.022	5.371	9057	0.032	7.180	96859	0.018	5.982	20176	0.026
3.7	5.879	15860	0.028	4.619	3116	0.045	6.687	45107	0.021	5.457	9202	0.032	7.291	98353	0.018	6.077	20494	0.026
3.8	5.969	16105	0.028	4.693	3166	0.045	6.789	45791	0.021	5.543	9346	0.032	7.400	99829	0.018	6.170	20809	0.026
3.9	6.059	16348	0.028	4.767	3215	0.045	6.889	46468	0.021	5.627	9488	0.032	7.508	101287	0.018	6.263	21121	0.026
4.0	6.148	16587	0.027	4.840	3265	0.044	6.988	47136	0.021	5.710	9629	0.032	7.615	102729	0.018	6.354	21429	0.026
4.1	6.236	16824	0.027	4.912	3313	0.044	7.086	47797	0.021	5.793	9768	0.032	7.721	104154	0.018	6.444	21733	0.026

4.2	6.323	17058	0.027	4.983	3361	0.044	7.183	48451	0.021	5.874	9906	0.032	7.825	105564	0.018	6.534	22035	0.026
4.3	6.409	17290	0.027	5.054	3409	0.044	7.279	49098	0.021	5.955	10042	0.031	7.929	106959	0.018	6.622	22333	0.025
4.4	6.494	17520	0.027	5.124	3456	0.043	7.374	49738	0.021	6.035	10177	0.031	8.031	108339	0.018	6.710	22628	0.025
4.5	6.578	17747	0.027	5.193	3503	0.043	7.468	50372	0.021	6.114	10310	0.031	8.132	109705	0.018	6.796	22920	0.025
4.6	6.661	17972	0.027	5.262	3549	0.043	7.561	51000	0.021	6.193	10443	0.031	8.233	111057	0.018	6.882	23209	0.025
4.7	6.744	18195	0.027	5.330	3595	0.043	7.653	51621	0.021	6.270	10574	0.031	8.332	112396	0.018	6.967	23495	0.025
4.8	6.826	18416	0.027	5.397	3640	0.043	7.745	52237	0.021	6.347	10703	0.031	8.430	113722	0.018	7.051	23779	0.025
4.9	6.907	18634	0.027	5.464	3685	0.043	7.835	52846	0.021	6.424	10832	0.031	8.528	115036	0.017	7.134	24060	0.025
5.0	6.987	18851	0.027	5.530	3730	0.042	7.924	53450	0.021	6.499	10959	0.031	8.624	116337	0.017	7.217	24339	0.025
5.1	7.067	19066	0.026	5.595	3774	0.042	8.013	54049	0.021	6.574	11086	0.031	8.720	117627	0.017	7.299	24615	0.025
5.2	7.146	19279	0.026	5.660	3818	0.042	8.101	54643	0.021	6.648	11211	0.030	8.814	118905	0.017	7.380	24889	0.025
5.3	7.224	19490	0.026	5.725	3861	0.042	8.188	55231	0.020	6.722	11335	0.030	8.908	120172	0.017	7.460	25160	0.025
5.4	7.302	19700	0.026	5.789	3905	0.042	8.275	55814	0.020	6.795	11458	0.030	9.001	121429	0.017	7.540	25429	0.025
5.5	7.379	19907	0.026	5.852	3947	0.042	8.361	56393	0.020	6.868	11580	0.030	9.094	122674	0.017	7.619	25696	0.025
5.6	7.455	20113	0.026	5.915	3990	0.041	8.446	56966	0.020	6.939	11702	0.030	9.185	123910	0.017	7.698	25961	0.024
5.7	7.531	20318	0.026	5.978	4032	0.041	8.530	57535	0.020	7.011	11822	0.030	9.276	125135	0.017	7.776	26223	0.024
5.8	7.606	20521	0.026	6.040	4074	0.041	8.614	58100	0.020	7.081	11941	0.030	9.366	126350	0.017	7.853	26484	0.024
5.9	7.680	20722	0.026	6.102	4115	0.041	8.697	58660	0.020	7.152	12059	0.030	9.456	127556	0.017	7.930	26742	0.024
6.0	7.754	20922	0.026	6.163	4157	0.041	8.779	59216	0.020	7.221	12177	0.030	9.544	128753	0.017	8.006	26999	0.024
6.1	7.828	21120	0.026	6.223	4198	0.041	8.861	59768	0.020	7.291	12294	0.030	9.632	129941	0.017	8.081	27254	0.024
6.2	7.901	21317	0.026	6.284	4238	0.041	8.942	60316	0.020	7.359	12409	0.030	9.720	131119	0.017	8.156	27507	0.024
6.3	7.973	21512	0.026	6.343	4279	0.041	9.023	60859	0.020	7.427	12524	0.030	9.806	132289	0.017	8.231	27758	0.024
6.4	8.045	21706	0.026	6.403	4319	0.040	9.103	61399	0.020	7.495	12639	0.030	9.893	133451	0.017	8.304	28007	0.024
6.5	8.117	21899	0.026	6.462	4359	0.040	9.182	61935	0.020	7.562	12752	0.029	9.978	134604	0.017	8.378	28254	0.024
6.6	8.188	22090	0.025	6.521	4398	0.040	9.261	62467	0.020	7.629	12865	0.029	10.063	135749	0.017	8.451	28500	0.024
6.7	8.258	22280	0.025	6.579	4437	0.040	9.340	62995	0.020	7.695	12976	0.029	10.147	136886	0.017	8.523	28744	0.024
6.8	8.328	22469	0.025	6.637	4476	0.040	9.417	63520	0.020	7.761	13088	0.029	10.231	138015	0.017	8.595	28986	0.024
6.9	8.397	22656	0.025	6.694	4515	0.040	9.495	64042	0.020	7.827	13198	0.029	10.314	139136	0.017	8.666	29227	0.024
7.0	8.466	22843	0.025	6.751	4554	0.040	9.571	64559	0.020	7.892	13308	0.029	10.397	140250	0.017	8.737	29466	0.024
7.1	8.535	23028	0.025	6.808	4592	0.040	9.648	65074	0.020	7.956	13417	0.029	10.479	141357	0.017	8.808	29704	0.024
7.2	8.603	23212	0.025	6.864	4630	0.040	9.724	65585	0.020	8.021	13525	0.029	10.560	142457	0.017	8.878	29940	0.024
7.3	8.671	23394	0.025	6.921	4668	0.039	9.799	66093	0.020	8.084	13632	0.029	10.641	143549	0.017	8.947	30175	0.024
7.4	8.738	23576	0.025	6.976	4706	0.039	9.874	66598	0.020	8.148	13739	0.029	10.722	144635	0.017	9.017	30408	0.024
7.5	8.805	23756	0.025	7.032	4743	0.039	9.948	67100	0.020	8.211	13846	0.029	10.802	145714	0.017	9.085	30640	0.024
7.6	8.872	23936	0.025	7.087	4780	0.039	10.022	67598	0.020	8.274	13951	0.029	10.881	146786	0.017	9.154	30870	0.023
7.7	8.938	24114	0.025	7.142	4817	0.039	10.095	68094	0.020	8.336	14056	0.029	10.960	147852	0.017	9.222	31099	0.023
7.8	9.004	24292	0.025	7.196	4854	0.039	10.169	68586	0.020	8.398	14161	0.029	11.039	148911	0.017	9.289	31327	0.023
7.9	9.069	24468	0.025	7.250	4890	0.039	10.241	69076	0.019	8.459	14265	0.029	11.117	149964	0.017	9.356	31553	0.023
8.0	9.134	24643	0.025	7.304	4927	0.039	10.313	69563	0.019	8.521	14368	0.029	11.194	151010	0.017	9.423	31778	0.023
8.1	9.198	24817	0.025	7.358	4963	0.039	10.385	70047	0.019	8.582	14471	0.028	11.271	152051	0.016	9.489	32002	0.023
8.2	9.263	24991	0.025	7.411	4999	0.039	10.456	70528	0.019	8.642	14573	0.028	11.348	153086	0.016	9.555	32225	0.023
8.3	9.327	25163	0.025	7.464	5034	0.039	10.527	71007	0.019	8.702	14674	0.028	11.424	154114	0.016	9.621	32446	0.023
8.4	9.390	25334	0.025	7.517	5070	0.038	10.598	71483	0.019	8.762	14775	0.028	11.500	155137	0.016	9.686	32666	0.023
8.5	9.453	25505	0.025	7.569	5105	0.038	10.668	71956	0.019	8.822	14876	0.028	11.576	156155	0.016	9.751	32885	0.023
8.6	9.516	25674	0.025	7.621	5141	0.038	10.738	72427	0.019	8.881	14975	0.028	11.651	157166	0.016	9.815	33103	0.023
8.7	9.579	25843	0.025	7.673	5176	0.038	10.807	72895	0.019	8.940	15075	0.028	11.725	158173	0.016	9.880	33319	0.023
8.8	9.641	26011	0.024	7.725	5210	0.038	10.876	73361	0.019	8.999	15174	0.028	11.799	159173	0.016	9.943	33534	0.023
8.9	9.703	26178	0.024	7.776	5245	0.038	10.945	73824	0.019	9.057	15272	0.028	11.873	160169	0.016	10.007	33749	0.023
9.0	9.764	26344	0.024	7.827	5279	0.038	11.013	74285	0.019	9.115	15370	0.028	11.947	161159	0.016	10.070	33962	0.023
9.1	9.825	26509	0.024	7.878	5314	0.038	11.081	74743	0.019	9.173	15467	0.028	12.020	162144	0.016	10.133	34174	0.023
9.2	9.886	26673	0.024	7.929	5348	0.038	11.149	75199	0.019	9.230	15564	0.028	12.092	163124	0.016	10.196	34385	0.023
9.3	9.947	26837	0.024	7.979	5382	0.038	11.216	75653	0.019	9.287	15660	0.028	12.164	164099	0.016	10.258	34595	0.023
9.4	10.007	26999	0.024	8.029	5416	0.038	11.283	76104	0.019	9.344	15756	0.028	12.236	165069	0.016	10.320	34803	0.023
9.5	10.067	27161	0.024	8.079	5449	0.038	11.350	76553	0.019	9.401	15852	0.028	12.308	166034	0.016	10.381	35011	0.023
9.6	10.127	27322	0.024	8.129	5483	0.038	11.416	77000	0.019	9.457	15947	0.028	12.379	166994	0.016	10.443	35218	0.023
9.7	10.186	27483	0.024	8.178	5516	0.037	11.482	77445	0.019	9.513	16041	0.028	12.450	167950	0.016	10.504	35424	0.023
9.8	10.245	27642	0.024	8.227	5549	0.037	11.548	77888	0.019	9.569	16135	0.028	12.520	168900	0.016	10.564	35629	0.023
9.9	10.304	27801	0.024	8.276	5582	0.037	11.613	78328	0.019	9.624	16229	0.028	12.591	169847	0.016	10.625	35832	0.023
10.0	10.363	27959	0.024	8.325	5615	0.037	11.678	78767	0.019	9.680	16322	0.028	12.660	170788	0.016	10.685	36035	0.023

Table S5. Magma travel distances calculated from viscosity data provided in Figure 7 as from Table 2 and Table S3. S5-Earth and S5-Mars refer to Earth and Martian environments, respectively.

h	ρ	g	slope	Lava travel distance	
				TF01-2	TF1-1
m	Kg/m^3	m/s^2	(°)	Km	Km
1	2698	3.7	5	375	296
1	2698	3.7	1	75	59
1	2698	3.7	0.1	8	6

References

Long, D. A., and Long, D. A. (1977) Raman spectroscopy (Vol. 276). New York: McGraw-Hill.

Di Genova, D., Morgavi, D., Hess, K. U., Neuville, D. R., Borovkov, N., Perugini, D., and Dingwell, D. B. (2015) Approximate chemical analysis of volcanic glasses using Raman spectroscopy. Journal of Raman Spectroscopy, 46(12), 1235-1244.

Neuville, D. R., de Ligny, D., and Henderson, G. S. (2014) Advances in Raman spectroscopy applied to earth and material sciences. Reviews in Mineralogy and Geochemistry, 78(1), 509-541.

APPENDIX V. OTHER ACTIVITIES

Fellowships and grants
- The Barringer Family Fund for Meteorite Impact Research to support the research project entitled: "Stacking Disorder in Diamonds as a Tool for Investigating Impact Craters." ($5000) Principal Investigator. (2016- Present)
- Grant AIC at the Italian Crystallographic Association (AIC) 26th-29th June 2017, Perugia
- Europlanet 2020 RI: Cathodoluminescence as a Tool for Unravelling Shock Features of Diamonds from Impact Craters, for a Europlanet Transnational Access (TA) project to use the Petrology-Mineralogy Characterisation Facility (PMCF) at the Natural History Museum, London. (8th – 12th October 2018). Principal investigator
- Grant to attend the XIV National Congress of Planetary Sciences 5th -9th February 2018, Bormio
- Grant AIC to attend the SGI-SIMP congress 11th -14th September 2018, Catania
- EPSC 2018 Early Career Researcher (ECR) Bursary Application (450€) to attend the European Planetary Science Congress (EPSC) 16th – 21st September 2018, Berlin
- Grant SIMP to attend the XV National Congress of Planetary Sciences 4th -8th February 2019, Firenze
- Grant SIMP to attend the 9th European Conference on Mineralogy and Spectroscopy 10th -13th September 2019, Prague.

Supervision activities
- *Giulia Miracca (B.Sc. February 2019).* Thesis topic: Natural impact diamonds from Popigai crater
- *Kira Musyachenko (M.Sc).* Thesis topic: Ab initio calculations and Raman measurements of inclusions in garnets (2019-2020)

Teaching activities
- Cultore della Materia for Mineralogy (2017- Present)
- Teaching support for Mineralogy: optics & crystallography (B.Sc, 12 CFU) Geological Sciences, University of Pavia. (2017 – 2018)
- Teaching support for Mineralogy: optics & crystallography (B.Sc, 12 CFU) Geological Sciences, University of Pavia.(2018-2019)

Organization of scientific meetings:
- Co-convener for the session: "Planetary evolution: new insights from remote sensing, in-situ, terrestrial analogues and meteorite studies" at SIMP-SGI-SOGEI 16th -19th September 2019, Parma

Commissions of trust
- Reviewer for Lithos (2018- Present)

Courses and fieldtrips:
- Elasticity course (30 hours, October 2016 - February 2017) held by R.J Angel (University of Padova)
- Density Functional Theory course (23rd-27th January 2017), held by M. Prencipe within the framework of the PhD program at the University of Torino (7,5 CFU)
- Course of Raman and IR spectroscopy of solids (20th -24th March 2017), held by B. Mihailova at the University of Hamburg
- Adamello field trip within the framework of the PhD program at the University of Pavia (11th -13th July 2017)
- Scientific communication course (12 hours, February 2018- May 2018) held by R.J Angel (University of Pavia)

- Asinara field trip within the framework of the PhD program at the University of Pavia (17th -20th June 2018)
- Single crystal X-ray diffraction course (20 hours, October 2018- January 2019) held by R.J Angel (University of Pavia)

Participation to meetings, conferences, seminars and workshops as presenting author:
2017.

1. **Murri M.,** Mazzucchelli M.L., Prencipe M., Mihailova B., Scambelluri M., Campomenosi N., Angel R.J., Alvaro M. *Ab initio simulation on Quartz (SiO$_2$) under hydrostatic stress vs isotropic strain.* Italian Crystallographic Association (AIC) 26th-29th June 2017, Perugia

2. **Murri M.,** Jones A.P., McMillan P.F., Salzmann C.G., Alvaro M., Domeneghetti M.C., Nestola F., Prencipe M., Dobson D., Hazael R., Moore M., Vishnevsky S., Logvinova A.M., Sobolev N.V. *Structure characterization of impact natural diamond from Popigai crater.* 80th Annual Meeting of the Meteoritical Society 23rd-28th July 2017, Santa Fe, New Mexico

3. **Murri M.,** Mazzucchelli M.L., Prencipe M., Mihailova B., Scambelluri M., Campomenosi N., Angel R.J., Alvaro M. *How does Quartz respond to deviatoric stresses? Ab initio calculations on SiO$_2$ tectosilicate.* Joint congress AIV-SGI-SIMP-SOGEI 3rd-6th September 2017, Pisa

4. **Murri M.**, Cámara F., Adam J., Domeneghetti M.C., Alvaro M. *Intracrystalline "geothermometry" assessed on clino- orthopyroxenes bearing synthetic rocks.* Joint congress AIV-SGI-SIMP-SOGEI 3rd-6th September 2017, Pisa.

2018.

5. **Murri M.,** Jones A.P., McMillan P.F., Salzmann C.G., Alvaro M., Domeneghetti M.C., Nestola F., Prencipe M., Dobson D., Hazael R., Moore M., Vishnevsky S., Logvinova A.M., Sobolev N.V. *Crystal structure characterization of impact diamonds.* International Diamond School "Diamonds: Geology, Gemology and Exploration". 29th January -2nd February 2018, Brixen.

6. **Murri M.,** Jones A.P., McMillan P.F., Salzmann C.G., Alvaro M., Domeneghetti M.C., Nestola F., Prencipe M., Dobson D., Hazael R., Moore M., Vishnevsky S., Logvinova A.M., Sobolev N.V. *XRD structure characterization of impact diamonds from Popigai crater.* XIV National Congress of Planetary Sciences 5th -9th February 2018, Bormio.

7. **Murri M.** *Raman spectroscopy: a tool for elastic geobarometry.* PhD congress, Department of Earth and Environmental Sciences, 10th-11th May 2018, University of Pavia.

8. **Murri M.,** Prencipe M., Angel R.J., Mihailova B., Alvaro M. *The role of the phonon Grüneisen tensor in the application of Raman spectroscopy for geobarometry.* XIII GeoRaman Conference 10th-15th June 2018, Catania.

9. **Murri M.,** Mazzucchelli M.L., Campomenosi N., Korsakov A.V., Prencipe M., Mihailova B.D., Scambelluri M., Ange1 R.J., Alvaro M. *Raman elastic geobarometry for anisotropic mineral inclusions.* SGI-SIMP Conference 12th -14th September 2018, Catania.

10. **Murri M.,** Cámara F., Domeneghetti M.C., Alvaro M. *Intracrystalline geothermometers validated on synthetic clino and orthopyroxenes and applied to a terrestrial analogue.* European Planetary Science Congress, 16th -21th September 2018, Berlin.

11. **Murri M.** *Natural impact diamonds from Popigai crater.* 8th October 2018, Natural History Museum (London). *Invited talk.*

12. **Murri M.** *Crateri da impatto terrestri e colate laviche marziane: cosa ci raccontano i minerali.* Settimana del Pianeta Terra, 18th October 2018, Pavia. *Invited seminar*

2019.

13. **Murri M.**, Cámara F., Domeneghetti M.C., Alvaro M. *Intracrystalline geothermometry applied to a Martian analogue.* XV National Congress of Planetary Sciences, 4th -8th February 2019, Firenze, Italy

14. **Murri M.** *Application of the Raman elastic geobarometry to host-inclusion systems from UHPM rocks.* PhD congress, Department of Earth and Environmental Sciences, 7th-8th March 2019 Pavia, Italy.

15. **Murri M.**, Korsakov A.V., Angel R.J., Prencipe M., Mihailova B. D., Alvaro M. *Raman elastic geobarometry to infer unique P-T conditions of host-inclusion systems from UHPM rocks.* Goldschmidt Conference 2019, 18th- 23rd August 2019, Barcelona, Spain.

16. **Murri M.**, Stangarone C., Korsakov A.V., Angel R.J., Prencipe M., Mihailova B.D., Alvaro M. *How to determine a unique entrapment condition of host-inclusion systems from UHPM rocks using Raman elastic geobarometry.* 9th European Conference on Mineralogy and Spectroscopy 2019, 10th – 13th September 2019, Prague, Czech Republic.